UNIVERSITY OF CRETE

DEPARTMENT OF MATERIALS SCIENCE AND TECHNOLOGY

DEVELOPMENT OF PROTOCOLS FOR INVESTIGATING LINEAR, BRANCHED AND SUPRAMOLECULAR POLYMERS UNDERGOING SHEAR

A DISSERTATION
submitted in partial fulfillment of
the requirements for the degree of
DOCTOR OF PHILOSOPHY

By
SALVATORE COSTANZO

Heraklion, Greece,
24 February 2017

ΠΑΝΕΠΙΣΤΗΜΙΟ ΚΡΗΤΗΣ
ΣΧΟΛΗ ΘΕΤΙΚΩΝ ΚΑΙ ΤΕΧΝΟΛΟΓΙΚΩΝ ΕΠΙΣΤΗΜΩΝ
ΤΜΗΜΑ ΕΠΙΣΤΗΜΗΣ ΚΑΙ ΤΕΧΝΟΛΟΓΙΑΣ ΥΛΙΚΩΝ

ΠΡΑΚΤΙΚΟ ΔΗΜΟΣΙΑΣ ΠΑΡΟΥΣΙΑΣΗΣ ΚΑΙ ΕΞΕΤΑΣΗΣ ΤΗΣ ΔΙΔΑΚΤΟΡΙΚΗΣ ΔΙΑΤΡΙΒΗΣ ΤΟΥ

κ. Costanzo Salvatore

ΥΠΟΨΗΦΙΟΥ ΔΙΔΑΚΤΟΡΑ ΤΟΥ ΤΜΗΜΑΤΟΣ ΕΠΙΣΤΗΜΗΣ ΚΑΙ ΤΕΧΝΟΛΟΓΙΑΣ ΥΛΙΚΩΝ

Η Επταμελής Επιτροπή της Διδακτορικής Διατριβής του κ Costanzo Salvatore η οποία ορίσθηκε στην 74η Γ.Σ.Ε.Σ. στις 04/11/2016, εκλήθη την Παρασκευή 24 Φεβρουαρίου 2017 να εξετάσει την σύμφωνα με το Νόμο υποστήριξη της διατριβής του υποψηφίου με τίτλο:

«Development of Protocols for Investigating Linear, Branched and Supramolecular Polymers Undergoing Shear»

Τα παρόντα μέλη της επταμελούς Επιτροπής εκφράζουν ομόφωνα την πλήρη ικανοποίησή τους για την υψηλή ποιότητα του περιεχομένου και της υποστήριξης της διατριβής.
Τα ερευνητικά αποτελέσματα της εργασίας του **κ. Costanzo Salvatore** είναι σημαντικά, πρωτότυπα και διευρύνουν το πεδίο της έρευνας στην Επιστήμη και Τεχνολογία Υλικών.
Ως εκ τούτου η Εξεταστική Επιτροπή προτείνει ομόφωνα την απονομή του Διδακτορικού Διπλώματος στον κ. Costanzo Salvatore.

Τα μέλη της επταμελούς επιτροπής για την αξιολόγηση της Διδακτορικής Διατριβής του κ. Costanzo Salvatore.

<u>Η Επταμελής Επιτροπή</u>:

Βλασσόπουλος Δημήτριος, (Επιβλέπων)
Καθηγητής, ΤΕΤΥ, Παν/μιο Κρήτης

Πετεκίδης Γεώργιος,
Αναπληρωτής καθηγητής ΤΕΤΥ, Παν/μιο Κρήτης

Benoit Loppinet,
Ερευνητής Β', ΙΤΕ, Ηράκλειο Κρήτης

Χαρμανδάρης Ευάγγελος
Επίκουρος Καθηγητής, ΤΕΜ, Παν/μιο Κρήτης

Βαμβακάκη Μαρία
Αναπληρώτρια καθηγήτρια, ΤΕΤΥ, Παν/μιο Κρήτης

van Ruymbeke Evelyne
Professor, University Catholique de Louvain, Belgium — E van Ruymbeke

Ianniruberto Giovanni
Associate Professor, University Napoli Federico II, Italy

Περίληψη

Ο στόχος της παρούσας διατριβής είναι να ρίξει φως στη μή-γραμμική ρεολογική συμπεριφορά σύνθετων πολυμερικών δομών με τη χρήση προχωρημένων τεχνικών τελευταίας τεχνολογίας και με ιδιαίτερη εστίαση στην ρεολογία διάτμησης. Ισχυρά μή-γραμμικά φαινόμενα ροής είναι πανταχού παρόντα στις διαδικασίες κατεργασίας πολυμερών, επομένως η κατανόησή τους είναι θεμελιώδους σημασίας για τεχνολογικές εφαρμογές. Από την άλλη πλευρά, η πρόοδος στην μή-γραμμική ρεολογία εξαρτάται από την επίλυση σοβαρών πειραματικών προβλημάτων που σχετίζονται με αστάθειες ροής. Η ανάπτυξη πειραματικών εργαλείων για την επίλυση αυτών των ζητημάτων είναι μια εξαιρετικά χρονοβόρα και επίπονη πρόκληση. Ξεπερνώντας αστάθειες ροής στην μή-γραμμική πειραματική ρεολογία θα οδηγήσει τον τομέα σε νέες κατευθύνσεις όπως η ακριβής και ποσοτική μοντελοποίηση, η αποκωδικοποίηση των μηχανισμών κίνησης μακρομορίων, και ο σχεδιασμός μακρομοριακών συστημάτων με επιθυμητές ιδιότητες που θα δύνανται να καθοριστούν. Ιδιαίτερα, σε σχέση με τους μοριακούς μηχανισμούς, η γνώση της μή-γραμμικής ροής είναι μάλλον περιορισμένη, ειδικά στη διάτμηση. Σε αυτό το πλαίσιο, το έργο αυτής της διατριβής επιχειρεί να απαντήσει σε δύο καίρια ερωτήματα: i) πώς θα αποκτήσουμε αξιόπιστες μετρήσεις σε παροδική (χρονικά μεταβαλλόμενη) διάτμηση; ii) ποιός είναι ο ρόλος των εμπλοκών, των διακλαδώσεων και των ελκτικών αλληλεπιδράσεων (συνενώσεων) στον καθορισμό της μή-γραμμικής ρεολογίας σύνθετων πολυμερικών συστημάτων; Είναι σαφές ότι η απάντηση στο πρώτο ερώτημα είναι αναγκαία για να αντιμετωπιστεί το δεύτερο. Ως εκ τούτου, στο πρώτο μέρος της διατριβής παρουσιάζουμε το σχεδιασμό και την υλοποίηση μιας γεωμετρίας κώνου-διαιρεμένης πλάκας (CPP) που θα μπορεί να προσαρμοστεί στο ρεόμετρο ARES και επιτρέπει ακριβείς μετρήσεις στη μή-γραμμική περιοχή της διάτμησης. Στο δεύτερο μέρος, εφαρμόζουμε τη τεχνική CPP και την ομοαξονική ρεομετρία εφελκυσμού για να διερευνηθεί η απόκριση πρότυπων συστημάτων, που περιλαμβάνουν γραμμικά κυκλικά, δενδριτικά και δενδροποιημένα υπερδιακλαδωμένα πολυμερή, προκειμένου να απαντηθούν τα προαναφερθέντα ερωτήματα.

to Angela and Margherita

Abstract

The aim of the present thesis is to shed light into the nonlinear rheological behavior of complex polymeric structures by means of state-of-the-art instrumentation, particularly focusing on shear rheology. Strong nonlinear flows are ubiquitous in polymer processing, therefore their understanding is fundamental for technological applications. On the other hand, the progress in nonlinear rheology has been halted by experimental issues associated with flow instabilities, rendering rheometric experiments problematic. The development of experimental tools to resolve these issues is a timely, outstanding challenge. Overcoming flow instabilities in nonlinear experimental rheology will advance the field in different directions such as accurate modeling development, decoding molecular mechanisms of motion, designing macromolecular systems with desired, tunable properties. Particularly, in relation to molecular mechanisms, knowledge of polymer dynamics in nonlinear flows is rather limited, especially in shear. In such a context, this thesis work attempts to answer two key questions: i) How can we obtain reliable measurements in transient shear? ii) What is the interplay of entanglements, branching and associations in determining the nonlinear rheology of complex systems? It is clear that answering the first question is necessary in order to address the second one. Therefore, in the first part of this thesis we present the design and implementation of a cone-partitioned-plate (CPP) geometry for ARES rheometer that allows for accurate, artifact-free measurements in nonlinear transient shear. In the second part, we apply CPP and uniaxial extensional rheometry to investigate model systems including linear, ring, Cayley-tree and dendronized polymers, in order to address the above-mentioned questions.

Contents

List of Figures

Chapter 1

INTRODUCTION

1.1 Rheology of polymers: an overview

The large-scale production of polymer materials in modern society has led many scientists to define our times as *the Polymer Age* [1]. Polymers are ubiquitous in nature and society. They have always been part of human life, and Man learnt to exploit polymer properties well before their study developed as a modern science. The use of polymer materials is documented in the history of different civilizations all over the world. For example, it is reported in the Bible that Noah used pitch, the heaviest part of crude oil, to make the Ark waterproof; ancient Incas used to play ritual games with heavy rubber balls; Chinese were among the first to condition the environment of silkworms to enhance the production of natural protein fibers for clothing and old natives of South America observed that natural rubber, the so-called *caoutchouc*, becomes harder if left in air for some time, an analogous process to modern vulcanization where oxygen has been replaced by sulfur [2, 3]. In all aforementioned examples, as well as in many others from ancient history, the polymeric nature of such materials was unknown and their use limited. The production of polymers developed to large scale only in the last 150 years, due to the industrial progress and advent of oil industry. After the Second World War, polymeric materials gradually replaced steel in most applications. Oil extraction provided raw materials for polymerization processes in quantities never available before. Concomitantly, scientific progress in synthetic chemistry promoted new routes for efficient large-scale production of polymeric materials [4]. In this context, the study of mechanical properties of soft matter became fundamental and paved the way for the development of rheology as the most relevant science for technological progress. As mechanical properties of polymer systems were discovered, the advantages from their use compared to other materials became apparent: their elastic properties and strength can be comparable to metals but they are much lighter and they can be easily processed and shaped. Nowadays, the world consumption of conventional polymer materials exceeds 150 billions of tons and it is destined to increase to more than 350 billions in the next twenty years [5]. Certainly, such a massive usage posed many relevant questions regarding environmental sustainability of polymeric materials. It is well-known that conventional polymers are not biodegradable and polymer thermosets such as cross-linked rubbers, cannot be re-used. This issue pushed researchers to find new ways to enhance mechanical properties of polymers and simultaneously develop more eco-friendly materials. A recent step forward in this direction is offered by the so-called supramolecular polymers, where the reversibility of bonds provides the basis for recyclable materials [6, 7].

The increasing demand of polymer-based products in developed countries encouraged fast processing in polymer industry. In modern plants, polymer melts and solutions are pumped and extruded at extremely high deformation rates, with polymer chains being deformed beyond their equilibrium conformations. When this happens, the flow is referred to as nonlinear. At low deformation rates (i.e., in linear flows), mechanical properties of materials depend only on temperature. Conversely, nonlinear flows are characterized by the fact that the rheological properties of materials depend on the deformation rate, apart from temperature. In most cases, fast processing brings also advantages in terms of energy required for industrial unit operations, thanks to the fact that the viscosity decreases upon shear rate increase in nonlinear flows, a feature known as *rate thinning*. Thereby, in spite of the fact that the first approach to study mechanical and flow properties of a soft material is linear rheology, knowledge of nonlinear properties of polymeric materials appear highly desirable for a reliable design of processing units. In addition, fast flows in advanced polymer processing are rather complex combinations of both extensional and shear flows. A good example thereof is blow molding, where a polymer melt is extruded into a mold and pushed against the cavity walls by air blown from the inside. Once the nonlinear behavior of a polymeric system is known in simple flows such as shear or uniaxial extension, constitutive equations can be derived [8, 9]. Then, computational rheology software (i.e., ANSYS Fluent, COMSOL Multiphysics) can simulate the flow behavior in complex geometries based on information from the aforementioned simple flows. Regarding uniaxial extension, carrying out experiments in a controlled fashion is possible and bench-top stretching rheometers are currently available (i.e., VADER 1000, Rheo Filament ApS USA). On the other hand, despite the relative simplicity in implementing steady shear flow in modern rotational rheometers, nonlinear measurements are more challenging due to flow instabilities under shear. These include shear banding, wall-slip, die swell, Weissenberg effect, edge fracture and viscous heating [10]. Such flow instabilities are related to shear stresses and the peculiarity of polymer systems (especially melts) to develop substantial stresses. Among shear instabilities, edge fracture is a serious issue in steady shear rotational measurements. As it develops at the rim of the sample, shear fracture eventually penetrates into the measurement volume. The formed voids immediately affect torque and normal force measurements. A way to overcome this issue consists in restricting the measurement volume to the inner part of the sample through the use of a cone-partitioned-plate geometry (CPP). Such measuring system provides reliable data for assessing flow properties of polymers in nonlinear conditions, therefore it represents a very useful tool for understanding rheological properties of polymers at lab-scale. The functioning and advantages of CPP geometry will be extensively discussed in the third chapter of this thesis. Indeed, we have advanced the implementation of CPP on commercial, rotational strain-controlled ARES rheometer (TA, USA). When carried out in a reliable way, nonlinear shear rheology has proven to be a valuable tool to investigate the flow properties of conventional polymer systems as well as the emerging class of supramolecular polymers. As mentioned before, associating polymers are a class of responsive soft materials with versatile properties that can be tailored molecularly via molar mass, molecular structure and bonding interactions. Nowadays they are used in numerous applications because reversibility of supramolecular bonds makes them good candidates for recyclable materials. One can also obtain an enhancement of mechanical properties of classic polymers, thanks to the additional contribution of supramolecular interactions to entropic elasticity of molecules provided by topological constraints (*entanglements*); moreover, supramolecular interactions can be dissociated upon temperature increase, hence promoting the recovery of flow properties.

The scope of this thesis is to develop reliable protocols for nonlinear shear rheology in order to address some open questions regarding nonlinear dynamics of complex systems, whose understanding has been sofar hindered by experimental issues associated with flow instabilities. Such questions include: which are the molecular parameters controlling nonlinear flow or how does nonlinear extensional rheology of polymer melts and solutions with the same number of entanglements compare to their nonlinear shear properties? Concerning the role of molecular structure (architecture), which are the key experimental features of nonlinear shear rheology of ring polymers? And how does the relaxation of branched systems from steady state in extensional flow compare to their counterpart in shear? Finally, how do we understand the dynamics of complex hyperbranched macromolecules such as dendronized polymers, where topological constraints are coupled with supramolecular interactions? In order to address this challenge, we start from the simple picture of linear entangled polymers with a brief digression on ring polymers where the classic relaxation mechanism due to free ends is absent. Then, the role of branching is examined by decoding the nonlinear response of symmetric Caley-tree polymers. Finally, a complex combination of topological constraints, molecular thickness and supramolecular interactions is investigated through the unique molecular architecture of dendronized polymers.

1.2 The molecular origin of elasticity in polymers

Polymeric materials are viscoelastic. This means that their mechanical properties are intermediate between two archetypes: the purely viscous liquid and the purely elastic solid. The former is described by Newton's law of viscosity,

$$\sigma = \eta\dot{\gamma} \tag{1.1}$$

where η is the viscosity, σ is the shear stress and $\dot{\gamma}$ is the shear rate. A viscous liquid has a purely dissipative behavior: all energy spent for deformation is dissipated into friction between molecules and transforms into heat. The purely elastic solid obeys Hooke's law,

$$\sigma = G\gamma \tag{1.2}$$

where γ is the deformation strain and G the elastic shear modulus. Equation (1.2) describes a purely conservative behavior: all energy spent to deform the material is released back as soon as the imposed force field that induces the deformation is removed. Viscoelastic materials are characterized by the fact that the mechanical response to an external strain or stress depends on the timescale during which the mechanical behavior is considered. At long times, a viscoelastic material will flow and dissipate all energy transferred to it. However, at short times, it will react as an elastic solid, yielding back part of the energy spent for its deformation. From a microscopic point of view, transient elasticity is described with a molecular structure. A typical case is that of long flexible polymer chains. In a polymer melt, chains are intermingled with each other and the motion of a single chain is hindered by the topological entropic constraints imposed by the surrounding molecules, as illustrated in figure 1.1

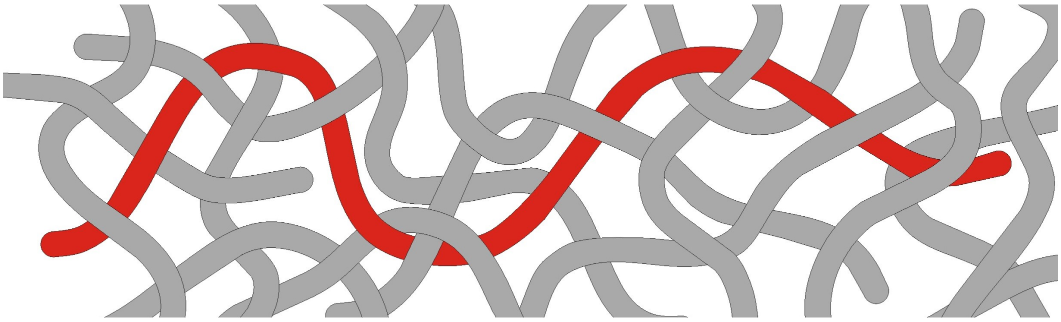

Figure 1.1: Schematic illustration of polymer chains in a melt. A single chain (highlighted in red) is confined in a tube-like region by the surrounding chains.

These topological constraints are usually referred to as *entanglements*. Entanglements confine a polymer chain in a tube-like region. At long time scales the chain can diffuse curvilinearly along the tube, akin to a snake motion. This diffusion mechanism is thereby called *reptation*. Reptation is a dissipative, diffusive mechanism [11, 12]. However, when a polymer melt is subjected to very fast deformation, chains do not have time to relax stress by diffusing past each other through reptation. At short time scales, entanglements act as fixed constraints between molecules, akin to permanent cross-links in rubber networks. The temporary network formed by entanglements is responsible for the transient elastic properties of polymers. Polymer chains in amorphous polymers at rest are random coils in their unperturbed configurations. The function $W(\mathbf{r})$ describing the end-to-end chain vector $\mathbf{r}$ is Gaussian and its distribution is given by [1]:

$$W(\mathbf{r}) = \left(\frac{3}{2}\pi\langle r^2\rangle_0\right)^{3/2} \exp\left[-\left(\frac{3}{2}\langle r^2\rangle_0\right) r^2\right] \tag{1.3}$$

where $\langle r^2\rangle_0$ is the mean square magnitude of $\mathbf{r}$ averaged over all possible spatial configurations. The Helmholtz free energy of the chain, A is given as a function of the displacement length $r \equiv |\mathbf{r}|$ by:

$$A(\mathbf{r}) \;=\; A^0(T) - kT\ln W(\mathbf{r}) \;=\; A^0(T) + (3kT/2\langle r^2\rangle_0)r^2 \qquad (1.4)$$

By differentiating equation (1.4) with respect to r one obtains a simple tension-displacement relation [1, 13]

$$f \;=\; \frac{3kT}{\langle r^2\rangle_0}r \qquad (1.5)$$

where f is the magnitude of the tensile force and r is the average distance between ends of the chain. The relation (1.5) is analogous to Hooke's law for elastic spring $f = K\delta r$ where the proportionality constant, K between the force f and the displacement δr is given by $3kT/\langle r^2\rangle_0$. Therefore, when the network is deformed, the random coils are deformed as well and polymer chains act as molecular springs at short time scales. Furthermore, we note that elasticity is purely entropic here. It arises exclusively from the tendency of a chain to relax from an oriented state by adopting conformations of maximum randomness. Assuming that the transient network undergoes affine deformation, the elastic free energy of the whole network is given integrating equation (1.4) over all chains in the network. From a macroscopic point of view, the elastic properties of the transient polymer network are described by the elastic plateau modulus G_N^0, whose magnitude is directly related to the number density of the cross-linking points of the network i.e., entanglements. The density of entanglements is governed by two length parameters: the step length of the Gaussian chain, also defined as Kuhn length b and the lateral distance between chains, determining the amount of chain strands per volume, a quantity directly related to the tube diameter a. Such quantities depend on the chemical structure therefore, the plateau modulus is fixed for a given polymer and defined as [1, 13]:

$$G_N^0 = \nu kT \;= \frac{4}{5}\frac{\rho RT}{M_0}\frac{b^2}{a^2} \qquad (1.6)$$

where ν is the number density of entanglements, k the Boltzmann constant and T the absolute temperature, R the gas constant and M_0 the molecular weight of the Kuhn segment. Equation (1.6) relates macroscopic elastic properties of polymers to their microstructure and it is in good agreement with experimental data [14]

1.3 Linear and nonlinear rheology of molten polymers

As underlined in section 1.2, the stress response of viscoelastic materials to any imposed deformation is time-dependent. For example, the stress in a polymeric material subjected to a step-strain is constant and proportional to the applied strain, akin to elastic solids, but it decays and eventually approaches zero at long times, as for a viscous liquid. The study of complex behavior of soft matter promoted the establishment of a new discipline in the early 1900s, known as rheology (from the statement of the Greek philosopher Heraclitus, τα Πάντα ῥεῖ, *everything flows*). Rheology was thought as a new branch of material science derived from mechanics of continuous media, aimed to provide the tools for describing the flow behavior of viscoelastic materials and relate their macroscopic mechanical properties to their molecular structure. The time-dependence of materials response is rationalized in rheology through the concept of Deborah number [15] (symbol De), a dimensionless quantity defined as follows

$$De = \frac{\text{time of relaxation}}{\text{time of observation}} \tag{1.7}$$

The Deborah number is fundamental to discriminate between the liquid-like and solid-like (elastic) response of a material. Large values of De imply that the characteristic relaxation time, τ of the material is much larger than that of the observation, therefore the material will not relax over the duration of observation and behave as elastic solid. Conversely, small values of De correspond to viscous liquid behavior. The Deborah number is relevant for transient experiments where elastic properties of the material change as a function of time. However such number is identically zero in steady flows where the stretch history of the material (and hence its elasticity) remains constant [16]. In this respect, it is useful to define another dimensionless number, the Weissenberg number (symbol, Wi), defined as the product of the characteristic relaxation time of the material, τ by the shear rate $\dot{\gamma}$, $Wi = \tau\dot{\gamma}$. The value of Wi provides a way to define the linearity conditions in steady flow experiments, such as simple shear and uniaxial extension [17].

In general, linear conditions can be defined both macroscopically and microscopically. From a microstructural point of view, linearity is preserved as long as the molecules are only slightly perturbed from their equilibrium configurations upon applying a deformation. Within the hyphotesis of affine deformation, such a situation is possible in the limit of small applied strains. From a macro-rheological point of view, small strains imply that the rheological parameters such as moduli and compliances are independent on the magnitude of the applied strain and stress, respectively. On the other hand, if the strain value is increased beyond the linear regime, molecular conformations are strongly altered with respect to their equilibrium values. Consequently, rheological properties tend to be different from equilibrium. In the following, we introduce the main rheological parameters used to describe the flow properties of viscoelastic materials both in linear and nonlinear regime. Such parameters are defined starting from simple shear flow experiments presented below.

Stress relaxation

During stress relaxation tests (also called step-strain), a constant strain γ is applied for a certain time Δt and the evolution of the stress σ in the material is measured. Figure 1.2 shows the rheological response to step strain of purely viscous liquids (L) and purely elastic solids (S) along with that of viscoelastic materials (VE). A viscous liquid obeys Newton's law $\sigma = \eta\dot{\gamma}$. The shear rate $\dot{\gamma}$ is the derivative of the step-

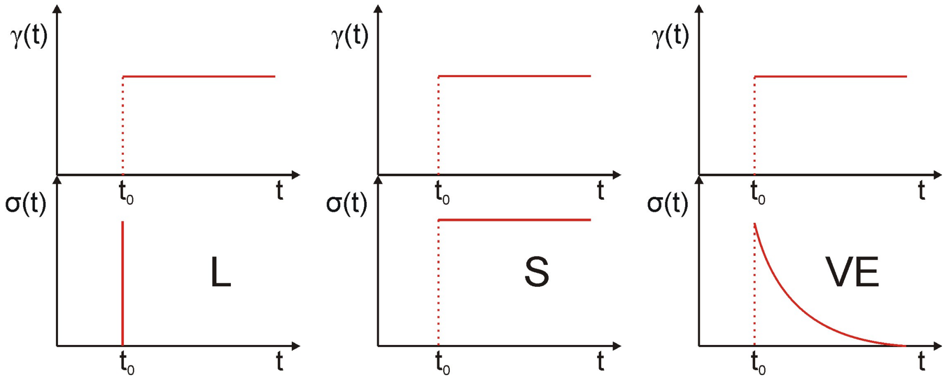

Figure 1.2: Stress relaxation test (L, liquid; S, solid; VE, viscoelastic).

strain, and therefore is a Dirac delta function. A viscous liquid reacts to step-strain deformation with an infinite stress pulse which decays to zero instantaneously. Elastic solids obey Hooke's law $\sigma = G\gamma$ therefore, the response to step-strain is a step-stress whose value is given by $\sigma = G\gamma$. Viscoleastic materials have intermediate response: at short times, the stress raises instantaneously to a finite value (elastic response) and then it gradually decays to zero. In linear regime, the level of the stress curve $\sigma = \sigma(t)$ is proportional to the applied strain γ therefore, it is straightforward to overcome the strain dependence of the results by defining the so-called *relaxation modulus*, $G(t)$, defined as follows

$$G(t) = \frac{\sigma(t)}{\gamma} \tag{1.8}$$

In light of the above, the relaxation modulus $G(t)$ is a strain-independent quantity in linear regime. At larger strains, nonlinear conditions are approached and $G(t)$ becomes lower and lower as the strain γ increases, therefore the strain dependence is recovered $(G = G(t, \gamma))$ as described in figure 1.3 From the shape of the curves in figure 1.3, one can observe that the function $G = G(t, \gamma)$ can be factorized as follows

$$G(t, \gamma) = G(t)h(\gamma) \qquad t > \tau \tag{1.9}$$

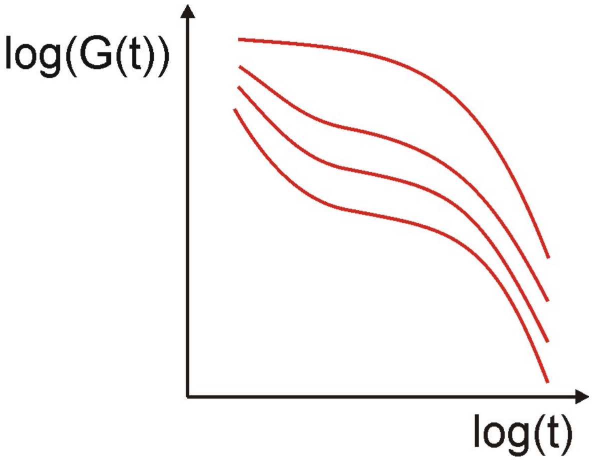

Figure 1.3: Relaxation modulus of viscoelastic materials in nonlinear regime. Strain γ increases from top to bottom.

where $h(\gamma)$ is the so-called damping function and τ is a characteristic time of the material [18]. This principle is also called time-strain separability [19]. For some systems, the Deborah number based on τ is smaller than unity and $G(t, \gamma)$ can be factorized over the whole experimental time.

Creep

The creep test consists in applying a constant stress σ to a material for a certain time Δt and measuring the temporal evolution of the strain. Figure 1.4 depicts the material response of model materials to creep experiments.

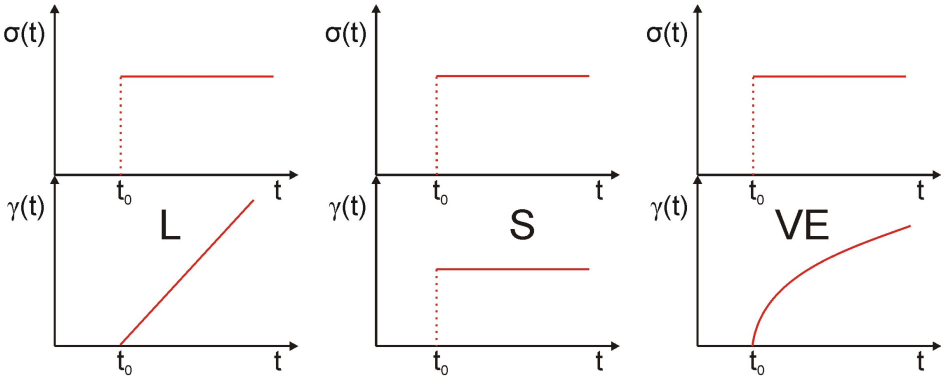

Figure 1.4: Material response to creep test (L, liquid; S, solid; VE, viscoelastic).

For a purely viscous liquid (L) following Newton's law, the strain increases linearly starting from the time t_0 at which stress is applied. The slope of the curve has a value identical to the Newtonian viscosity. Conversely, solid materials (S) respond to constant stress σ with a constant strain given by the ratio of the stress over the elastic shear modulus, $\gamma = \sigma/G$. Viscoelastic material are characterized by intermediate response between elastic solids and viscous liquids, depending on the time scale of observation. At short times viscoelastic materials respond to creep flow with an instantaneous deformation which tends to be constant over a brief time (elastic response). Subsequently, flow behavior is approached, and the curve of $\gamma = \gamma(t)$ tends to a straight line on a linear-linear plot, with a slope given by the zero shear viscosity. The level of the strain function $\gamma = \gamma(t)$ is directly proportional to the stress σ applied. In order to avoid σ dependence of the data, a rheological parameter is defined for creep, referred to as creep compliance, $J(t)$, given by

$$J(t) = \frac{\gamma(t)}{\sigma} \tag{1.10}$$

In the linear regime, i.e., for small values of σ, the creep compliance is strain-independent and the approximate relation $G(t) = 1/J(t)$ holds fairly well. When nonlinear conditions are approached, the compliance curves become stress-dependent $J = J(t, \sigma)$ and they are shifted towards larger values as the applied stress increases.

Frequency response

During frequency response test, a sinusoidal strain (or stress, in a stress-controlled mode) is applied $\gamma(t) = \gamma_0 \sin(\omega t)$, and the stress (or strain, in a stress-controlled mode) response is measured. Under the assumption of small strains, the response to a sinusoidal strain-wave is a sinusoidal stress wave $\sigma(t) = \sigma_0 \sin(\omega t + \delta)$. For a viscous liquid (L) the response wave is shifted at $\delta = \pi/2$ with respect to the strain-wave. Such a phase shift derives from the Newton's law: the stress is in phase with the shear rate, given by the derivative of the sinusoidal strain. Therefore, the stress is a cosinusoidal function. For purely elastic solids (S), application of Hooke's law yields $\delta = 0$ therefore stress and strain waves are in phase. The stress response of viscoelastic materials has a phase shift between 0 and $\pi/2$ with respect to the strain-wave. Figure 1.5 shows the frequency response of the three aforemetioned materials.

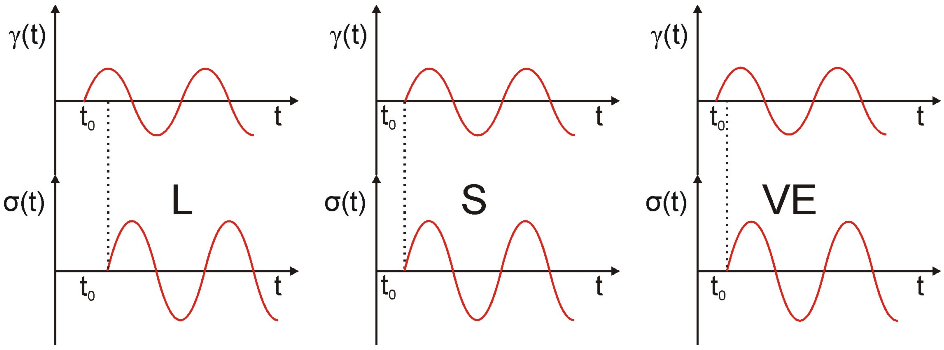

Figure 1.5: Material frequency response.

The frequency response of viscoelastic materials can be decomposed as follows

$$\sigma(t) = \sigma_0 \sin(\omega t + \delta) \tag{1.11}$$

$$\sigma(t) = \sigma_0 \left[\sin(\omega t)\cos(\delta) + \cos(\omega t)\sin(\delta)\right] \tag{1.12}$$

$$\frac{\sigma(t)}{\gamma_0} = \frac{\sigma_0 \cos(\delta)}{\gamma_0}\sin(\omega t) + \frac{\sigma_0 \sin(\delta)}{\gamma_0}\cos(\omega t) \tag{1.13}$$

$$\frac{\sigma(t)}{\gamma_0} = G' \sin(\omega t) + G'' \cos(\omega t) \tag{1.14}$$

In equation (1.14) the elastic modulus $G' = (\sigma_0 \cos(\delta))/\gamma_0$ and the viscous modulus $G'' = (\sigma_0 \sin(\delta))/\gamma_0$ are defined. In general, G' is a measure of the amount of energy stored during an oscillation cycle while G'' is a measure of the amount of energy dissipated. Given the proportionality between σ_0 and γ_0 in the linear regime, the viscoelastic moduli are strain-independent. As the strain is increased beyond linearity limits, different situations are possible, according to the nature of the particular viscoelastic material observed [20]. Such possibilities are reported in figure 1.6.

In the nonlinear regime, the stress wave is still periodic but not sinusoidal, the shape depending on the particular material. An efficient technique to study nonlinear

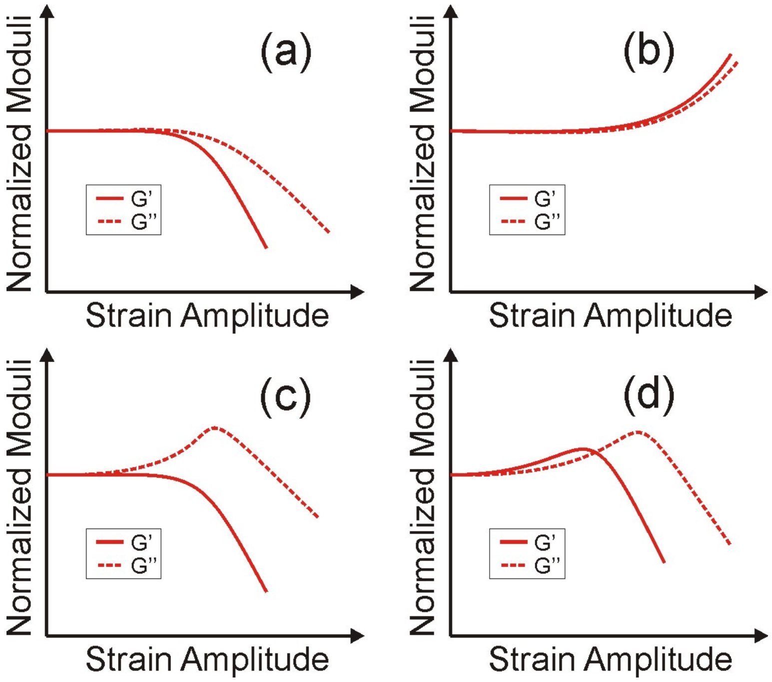

Figure 1.6: Large amplitude oscillatory shear behavior of viscoelastic materials (a, shear thinning; b, shear thickening; c, weak overshoot; d, strong overshoot).

behavior of materials is to perform frequency tests with a strain amplitude such that nonlinear conditions are approached. Then, the analysis of the material response is carried out through a Fourier transformation of the stress wave and the study of the characteristics of higher harmonics [21]. However, such technique remains to date purely phenomenological. Amorphous polymers follow a shear thinning behavior as reported in figure 1.6(a) From oscillatory experiments is it possible to obtain a complex viscosity as follows

$$\eta^*(\omega) = \frac{\sqrt{G'^2 + G''^2}}{\omega} \tag{1.15}$$

For most of the amorphous polymers, it has been empirically demonstrated that the complex viscosity is numerically identical to the shear viscosity if the shear rate $\dot{\gamma}$ is numerically equal to the frequency ω:

$$\eta^*(\omega) = \eta(\dot{\gamma})|_{\omega=\dot{\gamma}} \tag{1.16}$$

Such empirical observation is referred to as Cox-Merz rule [22].

Transient start-up shear

Shear start-up tests (also referred to as step-rate tests) consist in applying a constant shear rate to a material for a time Δt and measure the evolution of the stress over time. The stress response of viscous liquids, elastic solids and viscoelastic materials to start-up shear is reported in figure 1.7.

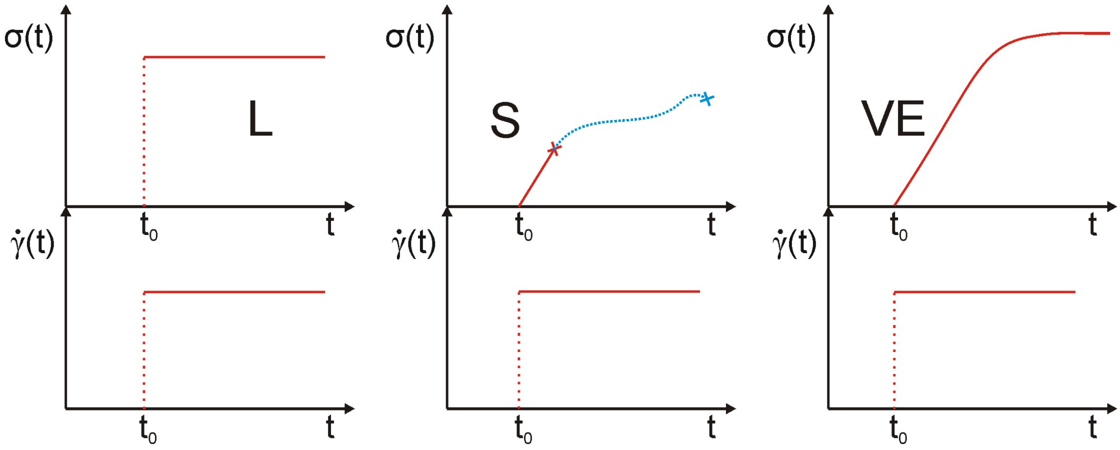

Figure 1.7: Start-up shear response of materials (L, liquid; S, solid; VE, viscoelastic).

Viscous liquids (L) react to constant shear rate with an instantaneous constant stress. The ratio of the stress and the applied shear rate yields the Newtonian viscosity $\eta_0 = \sigma/\dot{\gamma}$. The viscosity of viscous liquids is only function of the temperature T and pressure P, $\eta = \eta(T, P)$. At constant shear rate, the strain increases linearly with time. Hence, the stress in elastic solids subjected to step shear increases linearly, according to Hooke's law. If the solid is brittle, failure occurs when the strain level reaches the nonlinear limit as indicated by the red cross in figure 1.7(S). On the other hand, if the solid is ductile, beyond linear regime the structure yields but it is still able to withstand some deformation before breakage (S, blue curve).The response of viscoelastic materials is intermediate between viscous liquids and elastic solids, depending on the time scale of observation. When a constant shear rate is applied in the linear regime, the stress in a viscoelastic material starts to increase quasi-linearly with a slope given by a characteristic value of the elastic modulus. At longer times, the stress approaches a plateau value. The ratio of the stress plateau $\sigma(t)$ over the applied shear rate $\dot{\gamma}_0$ gives the transient viscosity $\eta(t)$. For shear rate experiments on viscoelastic polymer materials, linear conditions are defined according to the values of shear rate $\dot{\gamma}$ rather than strain γ. This is due to the fact that the microstructure of polymer materials is not *static* as for solid lattices. Polymer chains in molten state diffuse past each other due to thermal motion. If the characteristic time of the flow is longer than the characteristic time for diffusion, the polymer chain have the possibility to diffuse while sheared. In such a case, the flow does not affect the conformation of the transient network, i.e., the entanglements density. Therefore, even if the strain increases indefinitely, the flow is in linear regime. However, when the characteristic time of shear is shorter than the reptation time, diffusion cannot occur over the typical experimental time. In this case, entanglements act as permanent crosslinks at short time scales, inducing strong orientation and stretch of the coils. At longer time scales the system reaches a new equilibrium state characterized by a lower density of entanglements and lower viscosity. Strong orientation and stretch of the polymer coils define nonlinear shear flow regime. In linear regime, the relaxation from steady state upon flow cessation involves only the recovery of random coil configuration from oriented state. In this case the relaxation is in general exponential with a single mode. In nonlinear regime the relaxation upon flow cessation involves recovery from stretch and orientation and it is usually a multimode exponential process. In view of this picture, the viscosity of viscoelastic materials is not function of the sole temperature and pressure but also of the shear rate, $\eta = \eta(T, P, \dot{\gamma})$. The shear rate dependence comes into play when the value of the shear rate is larger than the inverse of the maximum relaxation time of the system, τ_D. In other words, if the Weissenberg number, $Wi = \dot{\gamma}\tau_D$ is larger than unity, the viscosity of the viscoelastic materials is also function of the shear rate.

For amorphous polymeric materials, the viscosity decreases upon shear rate increase in nonlinear regime. This behavior is known as shear thinning. The trend of transient viscosity in nonlinear regime is depicted in figure 1.8.

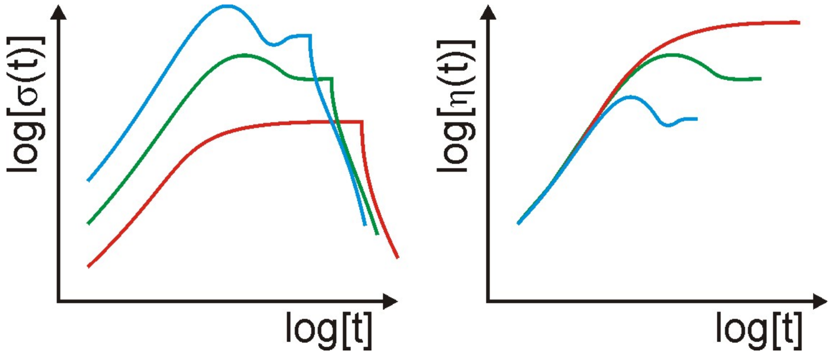

Figure 1.8: Linear and nonlinear shear response of a viscoelastic material.

Figure 1.8 reports the evolution of the transient shear stress (left panel) upon application of a step shear rate for a certain time Δt, at three shear rates corresponding to three different regimes (red, linear; green, moderately nonlinear; blue, strongly nonlinear). Relaxation of the stress upon flow cessation is also depicted. The corresponding temporal evolution of viscosity is reported in the right panel. Under linear conditions (red curve) the stress increases and then reaches a plateau value. Moreover, as the flow is stopped the stress relaxes to zero. This situation corresponds to $Wi < 1$. When $Wi > 1$ the stress curve displays an overshoot before reaching steady state. As mentioned above, the peak of the stress involves strong orientation and stretch of the coils. The plateau value of the stress depends on the shear rate in nonlinear regime. In strong nonlinear conditions (blue curve) the coils are oriented and possibly stretched. At high rates an undershoot following overshoot appears. The molecular origin of the undershoot will be clarified in the next chapters.

1.4 Normal stresses and flow instabilities

So far stress σ, strain γ and shear rate, $\dot{\gamma}$ have been treated as scalar quantities. This is possible for given directions of the stress and the flow field. In a more general case

σ, γ and $\dot{\gamma}$ in particular directions are components of the stress tensor $\boldsymbol{\sigma}$, the strain tensor $\boldsymbol{\gamma}$ and the velocity gradient tensor $\dot{\boldsymbol{\gamma}}$, respectively. Throughout the text, tensors are indicated by small bold Greek letters or capital bold Latin letters whereas vectors are indicated by small bold Latin letters. A tensor is a linear mathematical operator which acts on a vector $\boldsymbol{a}$ to yield a vector $\boldsymbol{b}$. For example, once a Cartesian reference system is established in a point p of a material, the vector $\boldsymbol{a}$ could be a unit vector, defining a certain surface S encompassing p through its normal direction, while the vector $\boldsymbol{b}$ could consist of three components of the stress on the surface S along the three directions of the Cartesian system. If one is able to define a tensor $\boldsymbol{\sigma}$ which can trasform $\boldsymbol{a}$ in $\boldsymbol{b}$, the stress in the point p of the material acting on a generic surface would be known as soon as the surface A is defined through the normal unit vector. Such a tensor $\boldsymbol{\sigma}$ would include all necessary information to define the state of stress in a point p of the material on a generic surface. In order to demonstrate that it is possible to define a tensor $\boldsymbol{\sigma}$ with the aforementioned characteristics, let us consider a generic point p in a material and a Cartesian reference system with origin in p as depicted in figure 1.9.

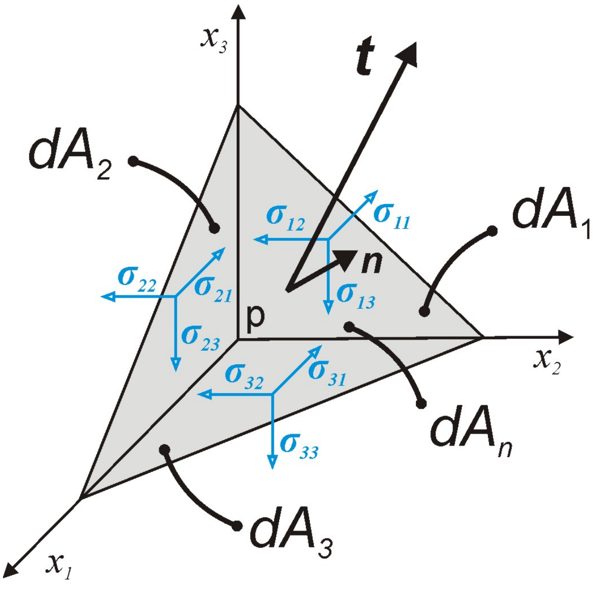

Figure 1.9: Definition of the stress tensor components.

Let us focus on the rectangular tetrahedron of figure 1.9. The quantities dA_i define the $i-th$ surface normal to the direction i. The unit vector $\boldsymbol{n}$ is normal to the surface dA_n. Let σ_{ij} be the component of the stress acting on the surface of normal direction i along the direction j. If the components σ_{ij} with $i, j = 1, ..., 3$ on the three surfaces dA_i are known, the stress components of the vector $\boldsymbol{t} = (t_1, t_2, t_3)$ acting on the surface defined by $\boldsymbol{n}$ along the directions x_1, x_2 and x_3 are known. In order to demonstrate it, let us note that

$$dA_i = \ dA_n(\boldsymbol{e_i} \cdot \boldsymbol{n}) \quad i = 1, ..., 3 \tag{1.17}$$

Apart from surface forces, a volume (body) force will be acting on the tetrahedron volume $\boldsymbol{f} = (f_1, f_2, f_3)$ For translational equilibrium of the tetrahedron to translation along the $i-th$ direction we have

$$\sigma_{1,i} dA_1 + \sigma_{2,i} dA_2 + \sigma_{3,i} dA3 - t_i dA_n + f_i dV = 0 \tag{1.18}$$

As the tetrahedron approaches infinitesimal dimensions, $dV/dA_i \rightarrow 0$ therefore the volume force is negligible:

$$\sigma_{1,i} dA_1 + \sigma_{2,i} dA_2 + \sigma_{3,i} dA_3 = t_i dA_n \tag{1.19}$$

Introducing equation (1.17) into equation (1.19) leads to the following

$$\sigma_{1,i} dA_n(\boldsymbol{e_1} \cdot \boldsymbol{n}) + \sigma_{2,i} dA_n(\boldsymbol{e_2} \cdot \boldsymbol{n}) + \sigma_{3,i} dA_n(\boldsymbol{e_3} \cdot \boldsymbol{n}) = t_i dA_n \tag{1.20}$$

$$(\sigma_{1,i}\boldsymbol{e_1} + \sigma_{2,i}\boldsymbol{e_2} + \sigma_{3,i}\boldsymbol{e_3}) \cdot \boldsymbol{n} = t_i \tag{1.21}$$

For the three directions $1, 2, 3$, in matrix notation we have:

$$\begin{pmatrix} \sigma_{11} & \sigma_{12} & \sigma_{13} \\ \sigma_{21} & \sigma_{22} & \sigma_{23} \\ \sigma_{31} & \sigma_{32} & \sigma_{33} \end{pmatrix} \cdot \boldsymbol{n} \ = \ \boldsymbol{\sigma} \cdot \boldsymbol{n} = \boldsymbol{t} \tag{1.22}$$

Equation (1.22) is known as Cauchy's law [23]. The nine components $\sigma_i j$ with $i, j = 1, 2, 3$ define the stress tensor $\boldsymbol{\sigma}$. The stress tensor $\boldsymbol{\sigma}$ describes the state of stress in the generic point p of a material. For rotational equilibrium, the tensor is necessarily symmetric, therefore $\sigma_{ij} = \sigma_{ji}$. We note that the components of $\boldsymbol{\sigma}$ out of the diagonal are shear stresses while the components in diagonal are normal stresses. For incompressible fluids, if the components σ_{ii} with $i = (1, ..., 3)$ are equal in modulus, no flow will occur. In order to induce motion, the important quantities are therefore the differences of normal stresses in the different directions. The difference $N_1 = \sigma_{11} - \sigma_{22}$ is referred to as first normal stress difference while the quantity $N_2 = \sigma_{22} - \sigma_{33}$ defines the second normal stress difference. In the definition of N_1 and N_2 we follow the generally accepted convention for the direction of normal stress differences: if the material moves only along direction 1 and the velocity varies only along direction 2, the first normal stress difference is the difference between σ_{11} and σ_{22} while the second normal stress difference is the difference between σ_{22} and the normal stress acting along the third independent direction σ_{33}. In the definition above, we considered tensile stresses as positive and compression stresses as negative. In the analysis of motion in cone and plate shear rheometry spherical coordinates are more suitable than Cartesian reference (figure 1.10). In such coordinates, normal stress differences are defined as $N_1 = \sigma_{\phi\phi} - \sigma_{\theta\theta}$ and $N_2 = \sigma_{\theta\theta} - \sigma_{rr}$, according to the above-defined convention.

A peculiarity of polymer materials is that they develop normal stresses when subjected to simple shear in strong nonlinear conditions. These stresses are responsible for flow instabilities. Examples of such instabilities are reported in figure 1.11. The

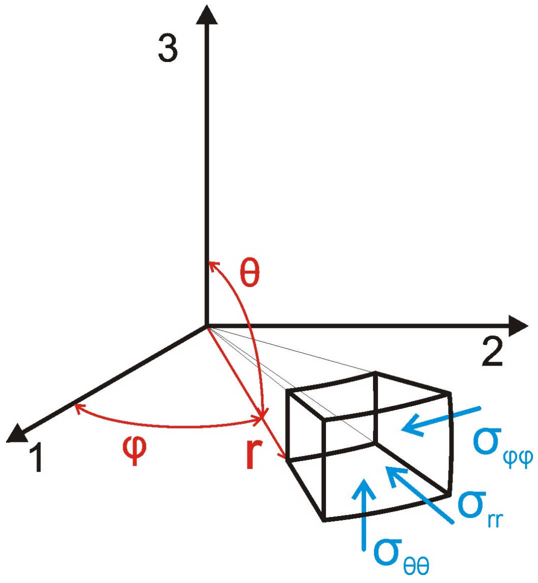

Figure 1.10: Definition of the stress tensor components in spherical coordinates.

Weissenberg effect (figure 1.11.a), also referred to as rod-climbing, describes the ability of some polymeric materials subjected to strong stirring to climb the stirring rod. The second normal stress difference has been indicated to be the cause of such effect. Die swell (figure 1.11.b) is an extrusion instability which occurs when a molten polymer is ejected from a die. If the shear rate of extrusion is high compared to the characteristic relaxation time of the material, the diameter of the extrudated filament swells with respect to the diameter of the extruder tube [27]. Sharkskin (figure1.11.c) is another flow instability occurring during extrusion, characterized by fractures around the extruded filament, which look like the openings on the skin of a shark [28]. Such instability is due to stick-slip mechanism of the molten polymer flowing in the extruder cavity. Edge fracture (picture 1.11.d) occurs in rotational reometry. At high values of the Weissenberg number the second normal stress difference overcomes the interfacial tension of the ideally spherical surface of the sample. The original shape is therefore distorted. As the flow proceeds, the corrugated surface develops a fracture which grows in time and penetrates into the sample [26]. In extreme conditions, the polymer is rolled up between the two plates and eventually expelled from the measuring system.

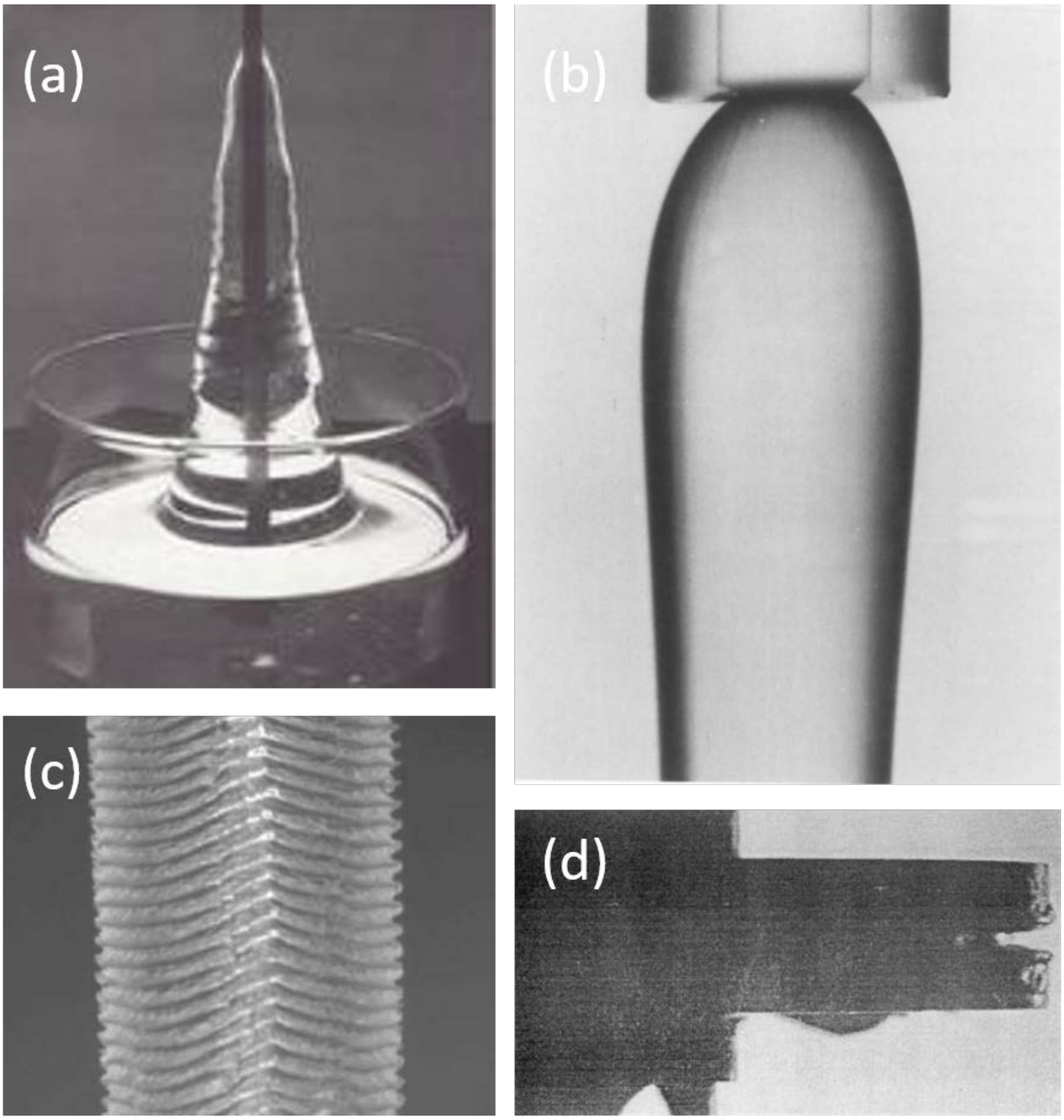

Figure 1.11: Flow instabilities (a, Weissenberg effect (picture from ref.[24]); b, die swell (picture from ref.[24]); c, sharkskin (picture from ref.[25]); d, edge fracture (picture from ref.[26]).

1.5 The concept of cone-partitioned plate geometry

Shear fracture is a serious issue hindering reliable measurements in start-up rotational shear flow of viscoelastic materials. The phenomenon has been intensively studied since the early work of Tanner and Keentok [29] who indicated that shear fracture in rotational rheometry is caused by the second normal stress difference. As shear fracture cannot be avoided in rotational measurements, it poses experimental challenges to properly measure torque and axial force. The main problem is that edge fracture penetrates into the sample creating voids inside the measurement volume. Such voids significantly reduce the torque and axial force readings with respect to the ideal values (with no fracture occurring). The most effective solution to overcome such problem was initially found by Pollett [30] and pioneered by Meissner and coworkers [31] who implemented a so-called cone-partitioned plate geometry (CPP) on a rotational RMS800 rheometer. The idea of such geometry is to measure only the innermost part of the sample disc which is not affected by edge fracture. Figure 1.12(a) shows a schematic of the working principle of the CPP. The transducer senses only the inner portion of the sample while an outer non-measuring partition covers the remaining part of the fluid. The gap between the inner and outer partition is a small fraction of millimeter.

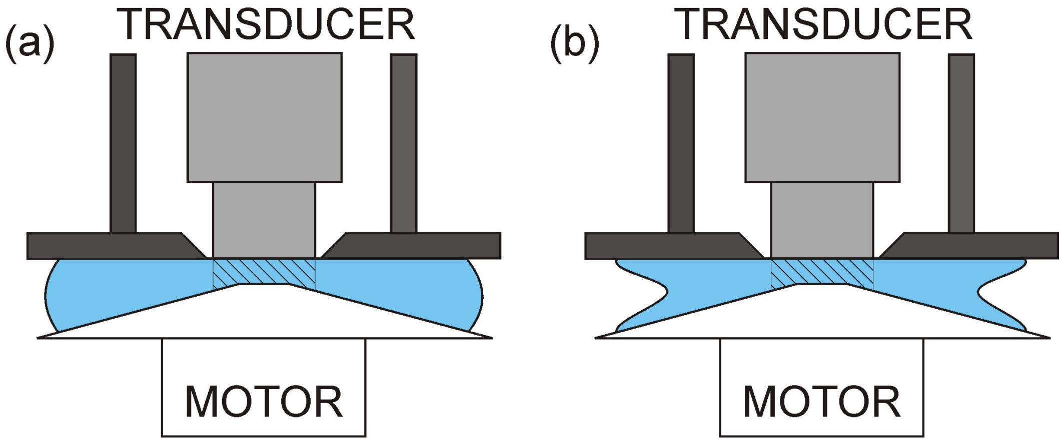

Figure 1.12: Schematic of cone partitioned plate geometry (white, bottom cone attached to the motor; light gray, upper plate attached to the transducer; dark gray, non measuring partition; blue, sample; the shaded area is the measured part of the sample.

When edge fracture occurs during a start-up shear experiment (figure 1.12(b)), some time is needed until it propagates inward to such an extent that it penetrates into the measured volume. During this time, reliable measurements of torque and axial force are still possible. A remark is in order about the normal force measurements with CPP geometry. In simple cone-plate geometry, N_1 coincides with the double of the axial force F divided by the area of the measuring plate ($N_1 = 2F/(\pi R^2)$, with R being the radius of the sample) hence it is directly measured . In CPP geometry, due to sample overfilling (i.e. the ratio of the radius of the measured sample R_i with respect to the external radius R), the measured N_1 is an apparent one $N_{1,app}$, because of the contribution to the normal stress distribution of the non-measured part of the sample. Depending on the overfilling, the difference between the effective value of the normal force and the apparent one can be very significant. Moreover, the normal force distribution is affected by edge fracture therefore the axial force signal is unavoidably affected by error. However, when fracture induces only a slight disturbance of the free surface, such an error is generally lower than 5% [32]. By means of CPP geometry, N_2 can be also obtained, as reported in chapter 3 [30, 31, 33]. Similarly to N_1, N_2 is also affected by some error as soon as fracture occurs. Even in this case however, if the fracture does not become catastrophic, the error is negligible. As explained in chapter 3, reliable measurements of N_1 and N_2 can be detected only for the steady state values as axial compliance induces delay in the axial force signal that is not easily quantified.

1.6 Linear and ring polymers

As mentioned above, the dynamics of linear polymers have been analysed within the framework of the tube model that allows to reduce the many body problem of chain motion in an ensemble of chains comprising a polymer melt, to a single body problem, i.e. the motion of a test chain confined in a tube-like region. The main relaxation mechanism of the test chain is reptation, namely curvilinear diffusion along the tube. In the original formulation of the tube model, reptation was the only relaxation mechanism [11]. Such model predicts a cubic dependence of the zero shear viscosity η_0 on molecular weight M_w whereas the experimental dependence indicates that:

$$\eta_0 \propto M_w^{3.4} \tag{1.23}$$

For this reason, the tube model underwent several refinements and other relaxation mechanism were introduced, such as contour length fluctuations (CLF)[34], thermal constraint release (TCR) and convective constraint release (CCR), the latter being relevant for nonlinear flows[35, 36]. The CLF mechanism explains the 3.4 exponent in the relation (1.23). Such mechanism takes into account the fact that the relaxation of the chain ends is faster compared to the internal monomers, as they can freely fluctuate and shorten the tube length instantaneously. The CCR mechanism considers the fact that chains making the tube, can convectively diffuse in fast shear flows and remove some of the tube constraints, changing the tube conformation. Such mechanism is useful to correctly predict the transient evolution of the stress in shear flow and relaxation of polymers after flow cessation. Stress overshoot in transient shear experiments can be explained in terms of chain orientation and stretch while the stress reduction following the undershoot can be interpreted in terms of partial disentanglement due to CCR [37]. Further refinements of tube model pointed out that, due to partial disentanglement, linear chains can undergo tumbling in transient shear flows [38]. Moreover, tumbling can be directly related to stress undershoot following the overshoot in transient startup shear [39].

The success of the tube model relies on the effective interpretation of free-ends dynamics. In absence of free ends, mechanisms such as reptation and CLF are not possible. An effective strategy to avoid free chain ends is to synthesize ring polymers. Ring molecules can be made in dilute environment [40]. However, the separation of rings

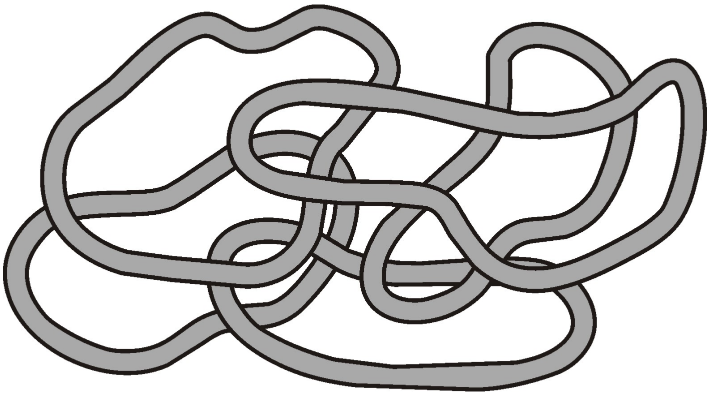

Figure 1.13: schematic representation of molten ring polymers.

from the unlinked linear precursors is challenging. On the other hand, small fractions of linear contaminants dramatically affect the rheological behavior [41]. Recently, a very efficient separation method consisting in Liquid Chromatography at the Critical Condition (LCCC) was employed to obtain high purity ring polymers with a fraction of linear contaminant below 5% [42]. From the study of the linear rheology of highly purified ring polymers [41, 43], it was found that no plateau of the storage modulus is detectable from the dynamic mastercurves, conversely to linear polymers [43]. Moreover, stress relaxation experiments on rings showed that the stress decays as a power-law over an extended range of time scales [41]. Several theoretical studies have been carried out in order to describe the dynamics of ring polymers. The two most relevant models are the Rouse model extended to ring polymers [44] and the lattice-animal model [45]. The first model consists in solving the equation of motion for a bead-spring ring chain. Because of the absence of free ends, all segments of the chain are equivalent. Therefore, the orientational anisotropy during creep is the same for all segments and independent of time, conversely to linear polymers where free ends relax faster compared to the inner segments of the chain. In other words, no retardation occurs for the segment anisotropy in ring polymers. However, the ring chain exhibits retardation behavior in its creep strain. The conformational analysis indicates that this retardation of the ring chain corresponds to growth of the orientational correlation of different segments with time. The lattice-animal model analyses the conformation of a ring polymer in a lattice of fixed obstacles. Topological constraints of entangled rings force them to adopt *lattice-animal-like* conformations comprising double-folded loops that relax stress by sliding along the contour of other loops. However, both models are in disagreement with experimental data on rings, most likely because of multiple threading of ring loops which interpenetrate each other [41, 46].

Nonlinear experimental shear rheology of ring polymers is a virtually unexplored field because of the very low amount of samples available compared to quantities required for nonlinear measurements. Our homemade CPP geometry, with the inner radius of 6mm allowed us to perform nonlinear start-up shear experiments on ring systems. Results of such experiments will be presented in chapter 4 along with nonlinear rheology of linear polymers.

1.7 Hyperbranched and dendronized polymers

The category of branched polymers encompasses a wide range of different polymer architectures. The common feature of these systems is that the structure includes at least one monomer from which three or more chains originate. Figure 1.14 shows a cartoon illustration of the most common branched architectures.

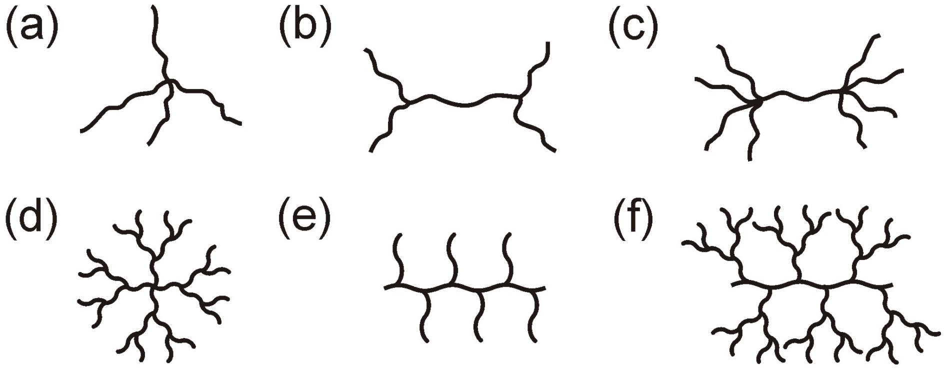

Figure 1.14: Cartoon illustration of different branched polymer architectures (a, star; b, H polymers; c, pom-pom; d, dendrimer; e, comb/bottlebrush; f, dendronized.

Star polymers are the simplest branched structure. The number of arms, also referred to as functionality f, ranges from a minimum of 3 up to several hundreds. The main feature of molecular dynamics of entangled star polymers is the fact that one end of the arm is effectively forzen, i.e., the core acts as a stagnation point. In order to diffuse along its tube, a single arm will fluctuate from the periphery (free end) to the center. This would translate into a huge entropic penalty [47]. Therefore, the main relaxation mechanism of such polymers is arm-retraction, a Rouse-like mechanism similar to countour length fluctuations: in order to release the stress, an arm has to retract along its tube and then move to a new configuration involving a new section of the tube. Thereby, the memory of the old configuration and the stress associated with it are lost. The characteristic stress-relaxation time τ_a of star polymers increases exponentially upon the number of entanglements per arm, $Z_a = M_a/M_e$ where M_a is the molecular weight of a single arm. For $f \leq 32$, the time τ_a is not dependent on the functionality f [48]. Concerning the frequency response of star polymers, the frequency spectrum of the dynamic moduli indicates a much broader relaxation compared to linear polymers of comparable M_w ($M_{w,linear} = 2 \times M_a$), reflecting the entropic barrier to retraction (relaxation process). Moreover, the loss modulus G' keeps increasing with frequency after the terminal crossover frequency ω_c. Such characteristics are associated with the relaxation process of the star arms. The viscosity is also independent on the number of arms and increases exponentially upon Z_a according to the following equation:

$$\eta_0 \simeq A \exp\left(B Z_a\right) \tag{1.24}$$

where A and B are constant independent on the length of the arm [1]. Each chain end of a star polymer can be grafted with two or more branches in order to obtain the so-called dendrimers (or dendritics, figure 1.14(d)). The grafting process can be carried out up to different generations so that more complex and bulky structures are obtained. Relaxation process of dendrimers is a hierarchical process [49]. Relaxation starts by arm retraction of the the outermost branches. Once they have relaxed they act as diluent for the inner branches, speeding up the relaxation/retraction of the latter. Correspondingly, the loss factor $tan(\delta) = G''/G'$ as a function of frequency ω is characterized by several peaks which correspond to the relaxation of the different generations [50]. A useful simplified model for branched polymers is the so-called pom-pom model (figure 1.14(c)). Such architecture consists in a linear backbone where both chain ends are branched, with more than two arms originating from each end [51]. The pom-pom model through hierarchical relaxation explains the nonlinear rheological features of hyperbranched polymers such as long chain branched polyethylenes, i.e. strain hardening in extension and shear thinning under shear. Hierarchical relaxation applies also to comb polymers (fig. 1.14(e)). Such systems are characterized by short branches randomly grafted on a linear backbone. The simplest case of comb polymers is represented by the so-called H polymers (figure 1.14(d)). At times shorter than the retraction/relaxation time of the single branch, τ_a the backbone is frozen in its tube whereas relaxation of the side branches occurs [51–53]. At time scales larger than τ_a the relaxation of the outer branches is completed and the backbone can reptate along its tube [54]. Backbone reptation proceeds by the hopping of the branching points with relaxed arms. In this case, $\tan(\delta) = \tan(\delta(\omega))$ indicates two processes: a high frequency one, corresponding to the relaxation of the side branches, and a low frequency one, corresponding to the relaxation of the backbone [48].

Starting from the paradigm of comb polymers, the grafting density of side branches on the backbone can be increased up to one arm per repeating unit. Simultaneously, the length of the branches can be also increased. Such systems are referred to as bottlebrush polymers [55, 56]. Moreover, if the side arms of these densely branched polymers are grown dendritically, such systems are referred to as dendronized polymers [57, 58] (figure 1.14(f)). Bottlebrush and dendronized polymers are characterized by high steric crowding around the linear backbone. This feature includes them in the category of *thick* polymers, described in section 1.9. The rheology of bottlebrush and dendronized polymers possess some characteristic of highly branched systems, such as the continuous decreasing of the elastic modulus G' in the intermediate frequency range corresponding to the relaxation of the side branches. However, molecular dynamics of these categories are rather complex and described by a combination of hierarchical relaxations of the side groups with extremely slow dynamics of the backbones. Molecular thickness strongly affects the possibility of the backbone to form entanglements (as explained in section 1.9, even at very large values of the molecular weight of the backbone.

1.8 Associating polymers

In the past 25 years, technological and environmental challenges coupled with the need of functional and stimuli-responsive polymers for a wide range of applications, have led to the development of the so-called supramolecular chemistry [6, 7]. The category of supramolecular polymers encompasses polimeric materials with very different chemistry and structure, with the common ability to form stable aggregates beyond the single molecule via secondary, highly-directional, reversible non-covalent interactions [59]. Supramolecular polymers can self-assemble from functionalized monomers [60]. Such molecules possess a relatively low viscosity at high temperature which confers them a high processability with low energy costs. On the other hand, if these systems are brought to low temperature, supramolecular bonds are formed. The latter give rise to strong elastic networks resulting only from supramolecular associations in the case of small molecules, or from a combination of supramolecular association and topological interactions (i.e., entanglements) in the case of large molecules. In principle, the breaking/reformation process of the supramolecular networks upon temperature variation can be repeated for infinite times, making supramolecular polymers recyclable, akin to thermoplastics. On the other hand, the strength of supramolecular

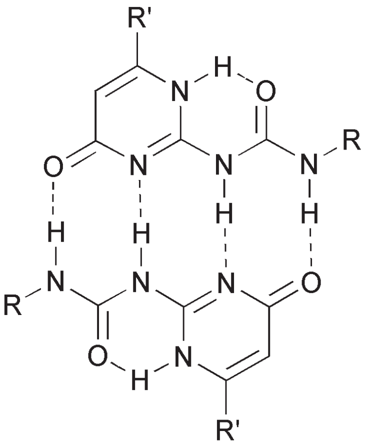

Figure 1.15: dimerization of ureido-pyrimidinone (picture from ref. [62]).

networks can be comparable with the mechanical properties of the thermosets. The strong temperature dependence of the mechanical properties is a unique characteristic of supramolecular networks insofar as breaking/reformation of bonds introduces additional relaxation mechanisms to that of ordinary polymers. Such versatility has made supramolecular polymers good candidates in applications such as coatings for sensitive materials, cosmetics, foodstuff, and elastomers. Moreover, thanks to fast formation/breaking kinetics of associating systems, some supramolecular polymers also possess unique characteristics such as the self-healing ability [61].

Supramolecular interactions involve very different types of noncovalent bonds, i.e. hydrogen bonding (HB), metal-ligand bonding, $\pi - \pi$ stacking, etc. Among them, hydrogen bonding is the most frequently used in supramolecular chemistry. Such popularity is due to the high reversibility of HB interactions and the large availability of HB groups in organic chemistry [60, 62, 63], i.e., ethyl, carbonyl, carboxil and amide- units. The relatively low strength of HB interaction has been compensated by the synthesis of new functional groups capable of forming arrays of multiple hydrogen bonds [64]. In this regard, the synthesis of Ureido-Pyrimidinone group (UPy, figure1.15) has been a remarkable achievement [63]. Such a functional group can form an array of four hydrogen bonds with an exceptionally strong dimerization constant in chloroform [65]. The effect of UPy incorporation into ordinary polymers on the mechanical properties has been widely studied, starting from the simple scenario of linear unentangled polymers [66–68]. The rheology of HB systems reflects the role of supramolecular interactions. Increasing UPy concentration in a linear backbone provides a number density of bonds which can be larger than that of analogous well-entangled polymers. This induces an enhancement of the elastic properties of unentangled systems with respect to entangled ones. Moreover, it is possible to combine both entanglements and supramolecular interactions to obtain very stiff materials with longer relaxation time compared to the non-interacting analogous. Theoretical models have been proposed to study such systems, invoking coupling of reptation with bonding kinetics as relaxation mechanisms [69]. Decoding molecular dynamics of supramoleuclar systems is further complicated when supramolecular groups are inserted more complex structures than linear polymers, i.e., stars or hyperbranched systems. As a case study, in chapter 6 and 7 of the present work, we are going to examine the effect of supramolecular interaction of the mechanical properties of dendronized polymers with both weak and strong hydrogen bonding groups.

1.9 Molecular thickness and packing length

Since the development of modern polymer science, polymer chains have been considered as curvilinear, one-dimensional objects. However, recent progress in chemistry has opened the route to the synthesis of molecules such as bottlebrushes and dendronized polymers, introducing a dense molecular crowding in the region around the linear backbone. Consequently, questions were rised about the role of molecular thickness in determining the elastic properties of polymer melts. In particular, the attention of researchers focused on how molecular thickness would affect the capacity of polymer systems to form entanglements. The question was first examined by Kavassalis and Noolandi who revisited the concept of entanglements [70, 71]. They assumed that the entanglement molecular weight decreases upon increase of the polymer chain length. Moreover, for a given chain length, the ability to form entanglements is dictated by a geometrical parameter, the coordination number $\tilde{N}$. For a given chain length, the lower the coordination number the smaller the entanglement molecular weight.

Fetters and coworkers came up with the concept of packing length [14, 72]. The packing length parameter, p is defined as follows

$$p = \frac{M}{\langle r^2 \rangle_0 \rho N_a} \tag{1.25}$$

where, $\langle r^2 \rangle_0$ is the mean square end-to-end distance, M is the molecular weight of the chain, ρ is the density and N_a is the Avogadro's number. The packing length p can be linked to the molecular diameter. Indeed, the quantity $v = M/(\rho N_a)$ is the molecular volume occupied by a polymer chain. If we consider the polymer chain as a cylinder with length $l = \langle r^2 \rangle_0$, the ratio of molecular volume to its length v/l yields a cross-sectional area. Therefore, the smaller is p, the slender is the polymer chain. According to the work of Fetters *et al.*, the packing length is directly related to the entanglement molecular weight M_e and therefore to the plateau modulus. The following relations exist between p, M_e and G_N^0:

$$\frac{M_e}{\rho} \propto p^3 \tag{1.26}$$

$$\frac{G_N^0}{T} \propto p^{-3} \tag{1.27}$$

From equations (1.26) and (1.27) one can immediately infer that the packing length affects the ability to form entanglements. In particular, the larger is the packing length, the larger M_e. This is demonstrated in figure 1.16 where M_e is plotted as a function of p for different polymer systems.

For fixed total molecular weight M_w, the larger is M_e, the smaller the number

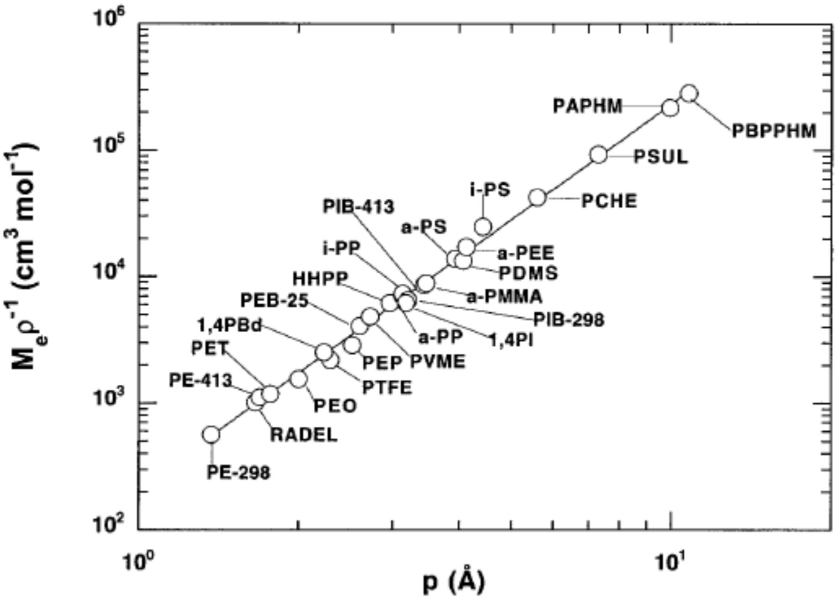

Figure 1.16: Entanglement molecular weight, M_e as a function of the packing length, p for different polymer melts [73].

of entanglements per chain $Z = M/M_e$. Therefore, bulky chains tend to form less entanglements and the resulting elastic plateau modulus is lower, as stated in equation (1.27). Such characteristic is apparent for bottlebrush polymers but it is also present in dendronized polymers, as we shall observe in chapter 6.

1.10 Summary

To date, material science and rheology have made remarkable steps forward in decoding the linear mechanical properties of polymeric materials whereas, some aspect of polymer dynamics in nonlinear flows are still an open challenge. On the other hand, the large distribution of polymer products induced fast industrial processing which posed the problem of studying the mechanical nonlinear flow properties of polymers in deep detail. Experimental work on nonlinear properties of polymers is complicated by flow instabilities, particularly in rotational shear flows. Among such instabilities, edge fracture is the most serious issue hindering reliable measurements in shear. The development of Cone-Partitioned plate fixture for rotational rheometers allowed to overcome experimental artefacts associated with fracture. In addition, proper implementation of CPP geometry allows to extract all the viscometric functions of a specific system, i.e., viscosity and first and second normal stress differences as functions of the deformation rate. The present work is between the necessity of decoding nonlinear flow properties of novel systems such as dendronized polymers as well as addressing some open challenges in nonlinear rheology of simple molecules, and the possibility to obtain reliable measurements in rotational shear flows. In this respect, one of the main achievements of this work is the design and implementation of a new CPP fixture for ARES rheometer which allowed us to study nonlinear start-up shear of model systems even with very small amounts of samples. We used such geometry to explore the interplay of topological constraints and supramolecular interactions in determining the flow properties of model systems. We started from the simple picture of linear polymers, attempting at unrevealing the molecular origin of rheological features of linear polymers in start-up shear, such as the stress undershoot following the overshoot at very high values of Wi. Moreover, we investigated the nonlinear shear rheology of ring polymers, for the first time from experimental perspective, aimed to elucidate the possibility of such systems to form entanglements. Topological complexity has been also addressed by studying nonlinear rheology of hyperbranched systems, such as Caley-Tree polymers. Dendronized polymers which couple topological interactions with the ability to form hydrogen bonding have been investigated as well. The role of hydrogen-bonding in determining the mechanical properties of dendronized polymers is studied in depth by incorporating UPy groups on the outermost branches of these systems.

Chapter 2

MATERIALS AND METHODS

2.1 Materials

2.1.1 Linear Polystyrene melts and solutions

In order to elucidate molecular aspects of the transient nonlinear rheology of linear polymers, we used four polystyrene (PS) samples of different weight-average molar masses M_w = 2000, 133000, 185000, and 285000 g/mol, coded as PS2k, PS133k, PS185k and PS285k, respectively. The oligomer PS2k is a commercial sample purchased from Sigma-Aldrich, Germany (with polydispersity index, i.e., ratio of weight to number-average molar mass, $PDI = M_w/M_n = 1.01$. PS133k (PDI = 1.01) and PS185k (PDI = 1.03) are commercial samples purchased from Polymer Laboratories, UK. Sample PS285k (PDI = 1.09) was identical to that used by Huang et al. [74]. Two PS solutions were prepared by diluting PS285k in PS2k in order to match the number of entanglements of the PS133k and PS185k melts. To maintain consistently with previous studies, [74–76] we used M_e = 13.3 kg/mol. Consequently, PS133k has a number of entanglements $Z = M_w/M_e = 10$ while PS185k has Z = 13.9. The entanglement molar mass of a polymer solution is given by [74]

$$M_e(\phi) = M_e(1)\phi^{-\alpha} \tag{2.1}$$

where $M_e(\phi)$ is the entanglement molar mass of the solution, $M_e(1)$ that of the melt and α the dilution exponent (here taken to be 1.0). Using equation (2.1), we calculated the amount of PS2k that needs to be added to PS285k in order to obtain two solutions with the same Z of the corresponding melts. The results are shown in table 2.1. In order to prepare homogeneous solutions, appropriate amounts of PS285k and PS2k were added to pre-weighted toluene in a glass vial under gentle stirring for 48 h. Subsequently, the solvent was slowly evaporated at room temperature in a hood over the course of 8 days and finally in a vacuum oven at 100°C for 2 days in order to strip the residual toluene. Toluene removal was monitored by keeping track of the weight loss of the sample. In the final solutions the amount of residual toluene is less than 0.5% wt.

sample	ϕ	Z
PS133k	1	10
PS185k	1	13.9
PS285k/2k-47	0.47	10
PS285k/2k-65	0.65	13.9

Table 2.1: Polymer volume fraction ϕ and number Z of entanglements in the four samples used.

2.1.2 Ring Polystyrene melts and Ring/Linear blends

The PS ring samples were made by prof. Taihyun Chang and coworkers at the Pohang University of Science and Technology (Korea). They are synthesized by ring closure of telechelic PS which was prepared in THF by anionic polymerization using potassium naphthalenide as an initiator. The synthetic scheme is shown in Scheme 2.1. The

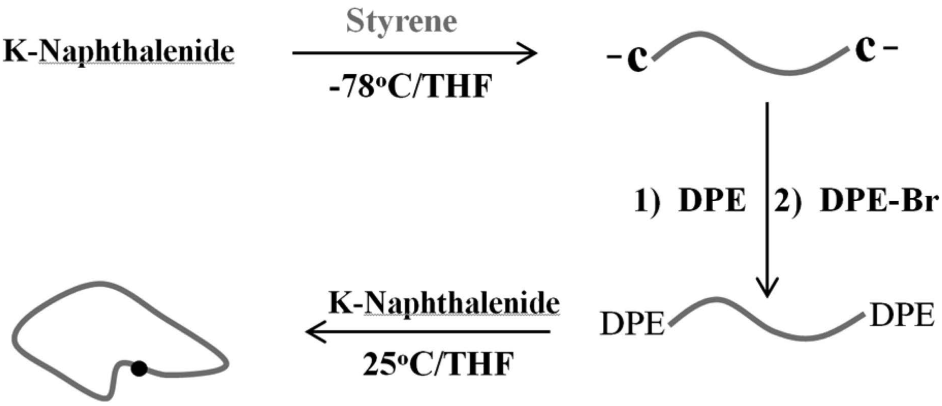

Figure 2.1: Synthetic scheme of PS rings.

anionic ends of PS were end-capped with diphenylethylene (DPE) first and then further reacted with 1-(4-(3-bromopropyl)- phenyl)-1-phenylethylene (DPE-Br) to make a telechelic DPE-ended PS. DPE-Br was prepared and purified according the procedure in the literature [77]. The ring closure of the telechelic PS was carried out in dilute THF solution (0.1% w/v) by potassium naphthalenide [78]. As-synthesized ring PS contains a significant amount of byproducts (various linear adducts as well as multiple rings), and it is purified by fractional precipitation first to remove most of the high M_w adducts. Then it is subjected to liquid chromatography at the critical condition (LCCC) fractionation to obtain single ring PS with high purity. The ring polymer is very sensitive to the linear contamination. A tiny amount of linear component added to ring systems will induce a dramatic change in their rheological behavior [41]. On the other hand, the conventional liquid chromatography cannot effectively purify the ring sample. Here, the ring sample is purified by LCCC fractionation [42]. The LCCC technique can effectively purify the ring sample, making the residual linear contamination hardly detectable in any analysis techniques including SEC and MALDI-MS [42, 79]. The SEC chromatogram in Figure 2.2.a shows the comparison between the elution curves before and after LCCC fractionation for a ring PS. The results clearly indicate a very effective purification of the ring polymer from the residual linear precursor. Figure 2.2.b shows the comparison between the chromatograms of the fractions

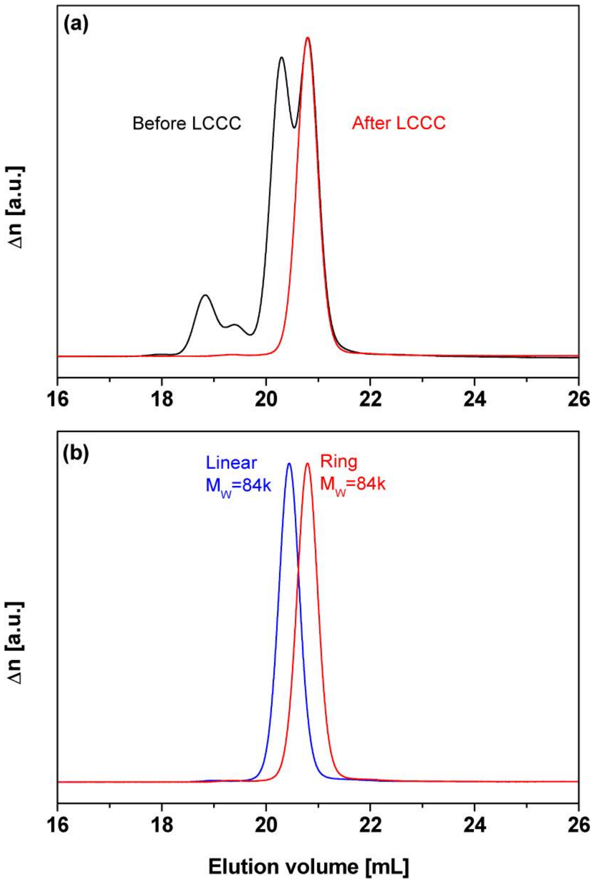

Figure 2.2: (a) SEC chromatograms of ring products before (black) and after (red) LCCC fractionation. (b) SEC chromatograms of linear precursor (blue) and pure ring (red) after LCCC fractionation.

of ring polymer and its linear precursor that had been separated by LCCC. The elution peak of the ring sample corresponds to a larger value of the elution volume with respect to the linear sample. This corroborates the known fact that, due to molecular structure, ring polymers have smaller size compared to linear polymers of the same M_w. The weight-average molar mass, M_w, and the polydispersity, M_w/M_n, of the ring polymer PS (coded as ring PS84k) determined by SEC-light scattering detection were 84 kg/mol and 1.003, respectively. In addition to ring PS84k, we also used a ring PS with M_w=185k, prepared with the same procedure as the former (coded as ring PS185k). For comparison we also investigated the linear polystyrene precursors (same molar mass), with code lin PS-84k and lin PS-185k. In addition, we prepared two blends of ring and linear polystyrenes: (i) molar mass 84 kg/mol for both components, with the fraction of the linear being 85% (code lin/ring PS84k); (ii) molar mass 185 kg/mol for both components with the fraction of linear being 75% (code lin/ring PS185k). The reason for using the blends is to test the response of a network formed by linear chains threading rings when their fraction is extremely small [41].

2.1.3 Cayley-tree polymers

We used Cayley-tree PMMA of generation 3 (code G3) and 4 (code G4). These dendritically branched macromolecules were synthesized by Hirao and coworkers [80–84] using benzyl bromide moieties as coupling agents. Earlier rheological investigations were presented by van Ruymbeke *et al.* [50] who studied the linear and nonlinear extensional properties. Each tree polymer consists of equal segments between generations (or with a free end at the highest generation). The number average molar mass of each segment is $M_n = 11000$ g/mol (i.e., 2.4 entanglements) and the polydispersity index $M_w/M_n = 1.02$. Figure 2.3 provides cartoon illustrations of the molecular structures of G3 and G4. Characterization of G3 and G4 can be found in [50] and [83, 84]. We performed size exclusion chromatography in fresh and used (after first

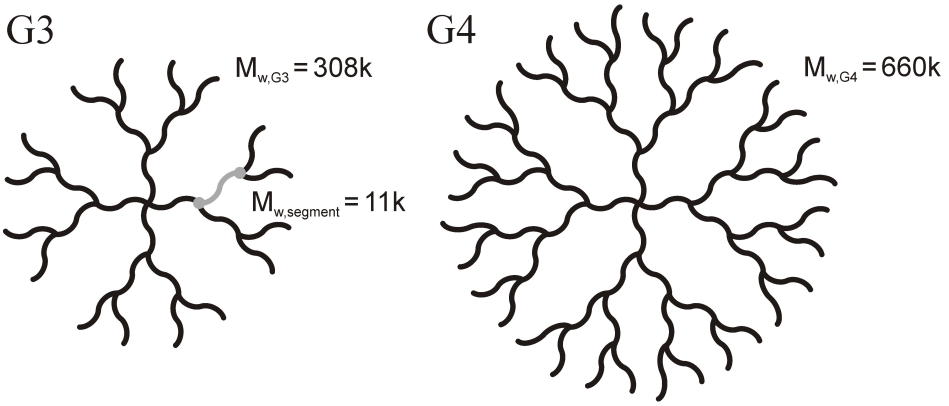

Figure 2.3: Illustration of Cayley-tree polymers of 3 (G3) and 4 (G4) generations.

stretching experiment) sample G4. The results from the analysis with the RI detector (not shown) show that there is a small fraction (about 6%) of larger molecules, which we call side-products, with an average molar mass of about 1349000 g/mol, i.e., double than that of the main target product (see also [83, 84]). Whereas these side-products have an influence on the LVE at very long times [50], at this small amount they do not affect the terminal response of the target dendritic molecules. This is also supported by earlier extensive work on structural and rheological analysis of branched polymers [50, 54, 85]. Furthermore, the used samples appear to contain slightly larger fraction of side-products (10%) but they were perfectly soluble in chloroform, a good solvent. These facts, along with evidence from literature (for fractions of 15% lower we can ignore their contribution to a first approach [54]), give confidence about the appropriateness of these samples for the present investigation.

2.1.4 Dendronized polymers

The synthesis of all dendronized polymers in this work was carried out by dr. Leon F. Serc under the supervision of prof. Dieter A. Schlüter at the Swiss Federal Institute of Technology (ETH), Zurich. The molecular structures of the herein investigated DPs are illustrated in figure 2.4. The first-generation PG1 dendronized polymers were prepared via controlled radical polymerization of the corresponding methacrylate monomers with

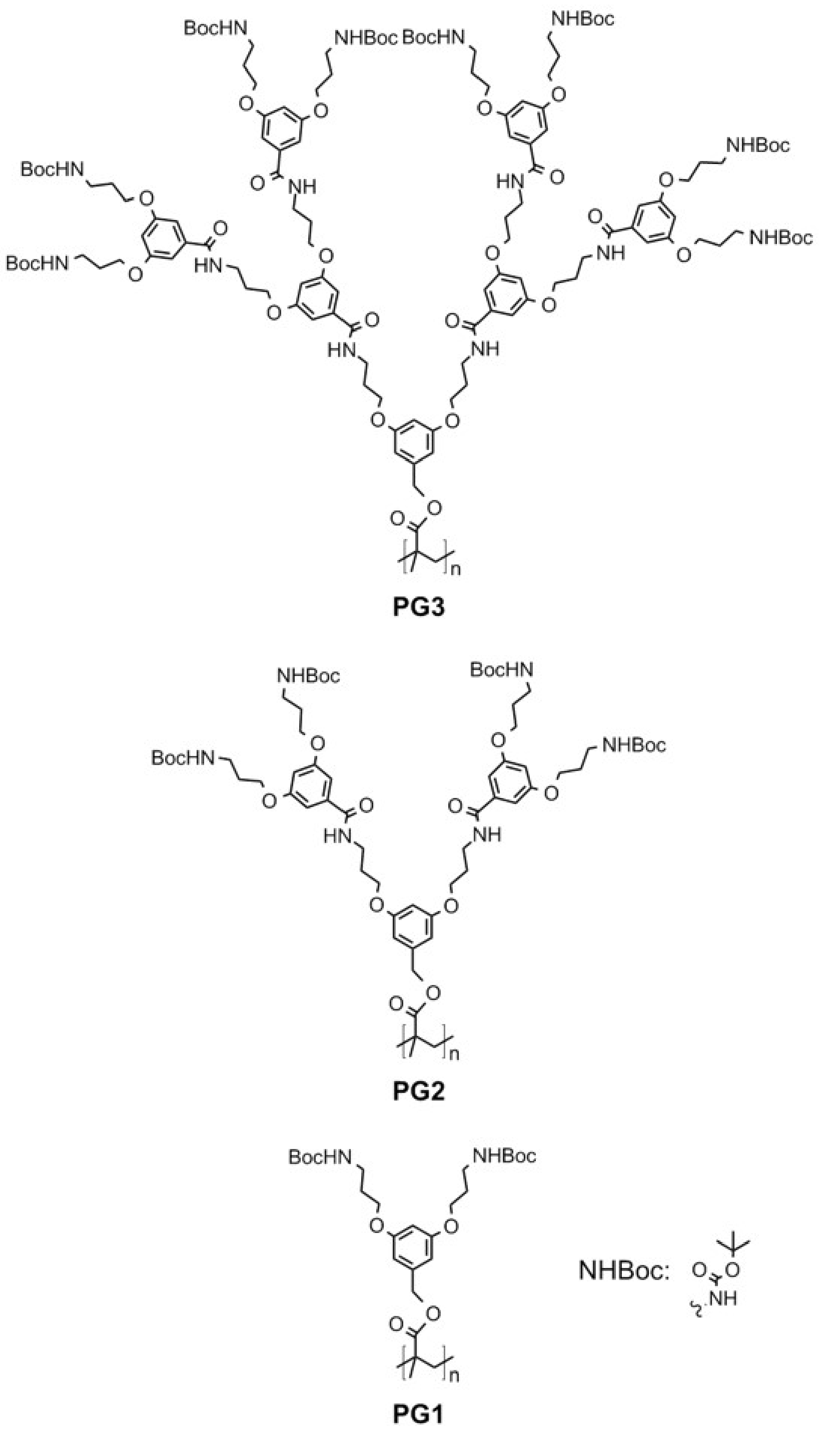

Figure 2.4: Illustration of the chemical structures of PG1, PG2 and PG3. Only the outermost generation is expected to exert intermolecular $\pi - \pi$ stacking and hydrogen bonding interactions.

		Polymerization[a]				GPC analysis[b]			
entry	sample	AIBN (mol%)	CDB (mol%)	time (h)	yield (%)	M_n (kDa)	M_w (kDa)	PDI	P_n
1	PG1-50	2	2	23	70	23	28	1.2	44
2	PG1-300	0.4	0.4	18	67	140	210	1.5	260
3	PG1-1000	0.2		13	81	520	900	1.7	1002
4	PG1-1500	0.2		14	62	760	1090	1.4	1448
5	PG1-2000	0.2		16	73	1030	1530	1.5	1975
6	PG1-3000	0.1		14	68	1600	2900	1.8	3060

		dendronization					
entry	sample	coverage[c] (%)	yeld (%)	M_n (kDa)	M_w (kDa)	PDI	P_n
7	PG2-50		72	54	58	1.1	44
8	PG2-300		71	310	500	1.6	255
9	PG2-1000		79	1150	1690	1.5	942
10	PG2-1500		76	1740	2100	1.2	1422
11	PG2-2000	99.8	64	2350	2790	1.2	1924
12	PG2-3000	99.9	82	3610	4000	1.1	2950
13	PG3-50		81	113	123	1.1	43
14	PG3-300		63	630	860	1.4	238
15	PG3-1000		45	2440	3140	1.3	930
16	PG3-1500		64	3570	4320	1.2	1359
17	PG3-2000	99.3	65	5000	6040	1.2	1910
18	PG3-3000	99.9	73	7560	13600	1.8	2880

Table 2.2: Conditions and results for the radical polymerization of MG1 Yielding PG1 polymers and PG2 and PG3 via dendronization. [a]Carried out with MG1 at a concentration of 1 g mL^{-1} in DMF at 65°C. [b]GPC in DMF at 45°C calibrated with poly(methylmethacrylate) standards. [c]Determined by UV-labeling with 1-fluoro-2,4-dinitrobenzene (Sanger's reagent). AIBN = Azobisisobutyronitrile; CDB = cumyl dithiobenzoate.

minor modifications to a previously reported procedure, followed by a divergent approach involving repeated deprotection/dendronization reactions to obtain a series of homologous DPs up to the third generation [86]. The chemical characteristics of the first-generation PG1 polymers and their respective second- and third-generation homologues PG2 and PG3 are listed in table 2.2. This mode of synthesis was chosen in order to have the least possible impact of the growth reaction on P_n and polydispersity, which allows for systematic and generation-dependent studies. For the two longest chain lengths in this study, the degrees of structural perfection were determined with labeling experiments4 [87, 88] to be close to 100% for each step, resulting in an overall perfection of >99% for PG3.

2.1.5 UPy-functionalized dendronized polymers

In order to study the effect of enhancement of supramolecular interactions on the rheology of dendronized polymers we decided to functionalize dendronized polymers with UPy. The synthetic approach towards DPs of generation numbers $g = 1 - 3$ bearing various fractions of UPy at the $g = 1$ level is outlined in Scheme 2.5. Reaction of the known macromonomer 1c16 with trifluoroacetic acid (TFA) afforded a statistical mixture of mono- and doubly-deprotected species along with unreacted starting material, from which the desired product was easily isolated by column chromatography owing to the vastly different polarities of the involved compounds. Thus, 2a was obtained on a multi-gram scale (50 – 60% yield from 1c). Subsequently, macromonomer 2b was quantitatively obtained from 2a in a coupling reaction with CDI-activated 6-methylisocytosine (3), which has been demonstrated in the literature to proceed smoothly with primary amines. The two synthesized monomers, i.e. 1c bearing two Boc-protected amines and 2b comprising one Boc and UPy motif each in the side chains, were subjected to radical polymerization as specified in Table 1 to give PG1-Pn-UPy(f).

Here, the terms P_n and (f) in PGg-P$_n$-UPy(f) denote the approximate degree of polymerization and the theoretical molar fraction of UPy in the copolymers. Two different polymer series were prepared, i.e. polymers featuring similar degrees of polymerization but varying UPy contents (Entries 1 – 6; Mn $\approx$ 21 kDa, $P_n \approx 40$ as determined by GPC in DMF) and polymers with larger degrees of polymerization but constant UPy loading (Entries 7 – 9; $P_n \approx 120, 710, 1200, 25$ mol% UPy). These backbone chain lengths were carefully chosen in order to obtain, on the one hand, short-chained samples lacking the ability for entanglements and, on the other hand, samples comprising longer backbone chain lengths in order to capture potential effects arising upon the transition from the oligomeric to the polymeric regime. Higher generation numbers ($g = 2, 3$; Entries 10 – 17) were synthesized in a g by g fashion, i.e. by applying the commercially available $g = 1$ dendronization reagent 1d in a two-step deprotection-coupling.

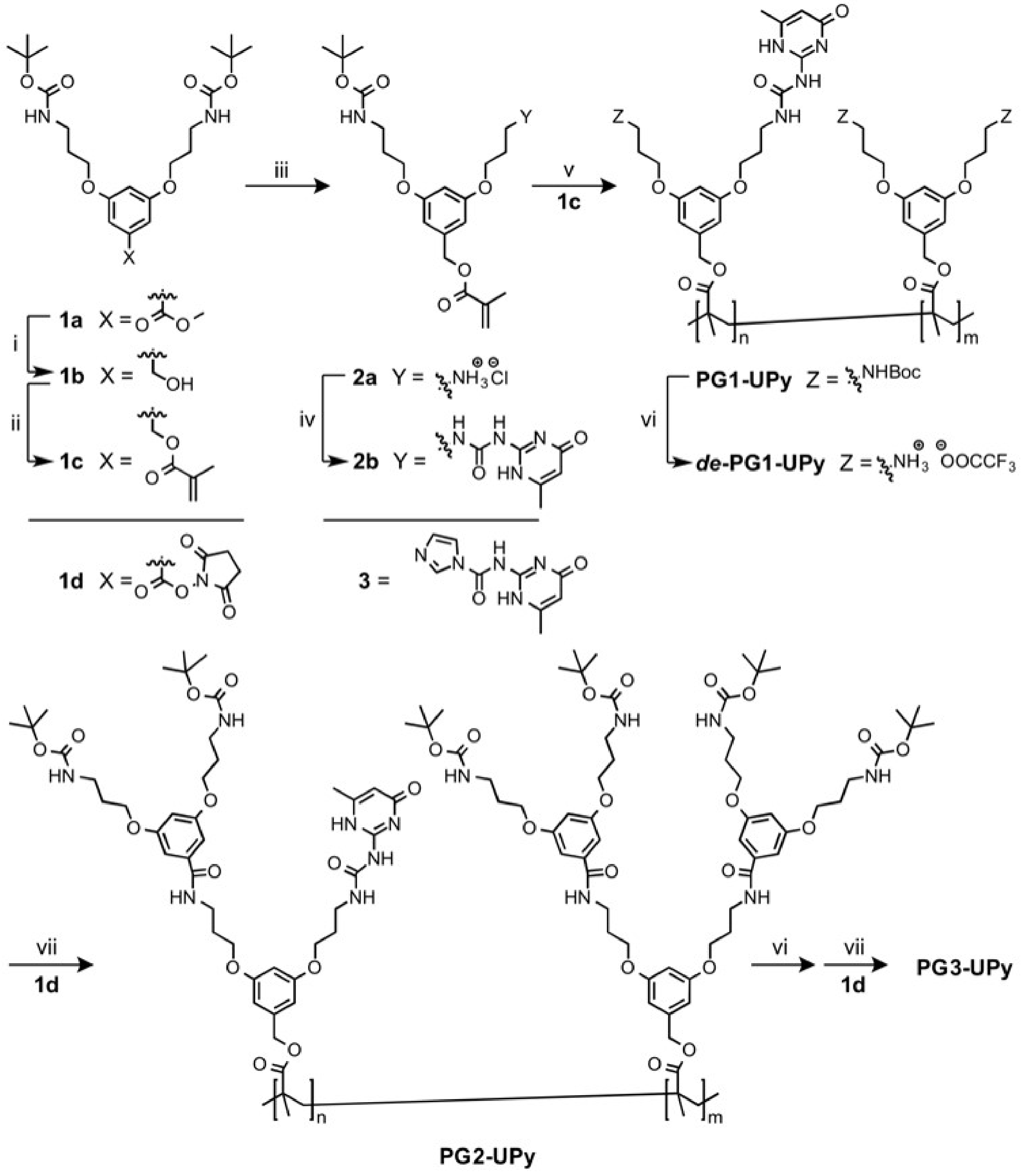

Figure 2.5: Synthesis of UPy-functionalized dendronized copolymers. (i) LAH, THF, -10°C; (ii) MAC, Et_3N, CH_2Cl_2, 0°C; (iii) TFA, CH_2Cl_2; (iv) 3, Et_3N, DMF; (v) AIBN, (CDB), DMF, 65°C; (vi) TFA, 0°C; (vii) Et_3N,DMAP, DMF.

		Polymerization[a]					GPC analysis[c]		
entry	sample	method	feed (**1c**:**2b**)	$f_{2b,th}$ (mol%)	$f^{b}_{2b,exp}$ (mol%)	yeld (%)	M_n (kDa)	PDI	P_n
1	PG1-40-UPy0	RAFT	1:0	0.0	0.0	83	21.4	1.1	41
2	PG1-40-UPy5	RAFT	9:1	5.0	5.5	88	19.3	1.2	37
3	PG1-40-UPy10	RAFT	4:1	10.0	10.1	82	23.2	1.2	43
4	PG1-40-UPy-25	RAFT	1:1	25.0	25.1	80	22.8	1.2	41
5	PG1-40-UPy33	RAFT	1:2	33.3	33.4	92	20.5	1.1	37
6	PG1-40-UPy50	RAFT	0:1	50.0	50.0	87	20.9	1.2	38
7	PG1-100-UPy25	FRT	1:1	25.0	25.2	97	71.5	2.1	130
8	PG1-700-UPy25	FRP	1:1	25.0	25.2	91	390.5	2.0	710
9	PG1-1200-UPy25	FRP	1:1	25.0	25.2	97	668.3	1.7	1200

		Dendronization[d]		GPC analysis[c]		
entry	sample	coverage[e] (%)	yeld (%)	M_n (kDa)	PDI	P_n
10	PG2-40-UPy0	99.8	72	50	1.1	41
11	PG2-40-UPy5	99.8	70	44	1.1	36
12	PG2-40-UPy25	99.7	69	44	1.2	40
13	PG2-40-UPy50	99.1	70	35	1.2	38
14	PG3-40-UPy0	99.8	81	105	1.1	40
15	PG3-40-UPy5	99.9	77	94	1.1	37
16	PG3-40-UPy25	99.2	85	86	1.2	41
17	PG3-40-UPy50	99.1	78	61	1.2	37

Table 2.3: Conditions and results for the RAFT polymerization of **1c** and **2b** (see figure 2.5) yielding PG1-UPy, PG2-UPy and PG3-UPy via Dendronization. [a]Carried out at a concentration of 1.0 g mL^{-1} (Entries 1-6), 0.25 g mL^{-1} (Entry 7), 0.39 g mL^{-1} (Entry 8), and 0.50 g mL^{-1} (Entry 9) in DMF at 65°C using azobisisobutyronitrile (AIBN) as an initiator and cumyl dithiobenzoate (CDB) as the chain transfer agent in RAFT. [b]Determined by ^{1}H NMR spectroscopy. [c]GPC in DMF at 45°C calibrated with poly(methyl methacrylate) standards.[d]Carried out at a concentration of 1.0 g mL^{-1} in DMF at room temperature.[e]Determined by UV-labeling with 1-fluoro-2,4-dinitrobenzene (Sanger's reagent).

The conversion of these postpolymerization dendronization reactions, i.e. the degree of DP structure perfection, was determined by labeling of possibly unreacted peripheral amines with 1-fluoro-2,4-dinitrobenzene (Sanger's reagent) and quantification of the resulting absorbance at 357 nm via UV-Vis spectrophotometry. Since the characteristic absorbance band of UPy is centered around 282 nm, 20 no interference between UPy and Sanger-labeled sites was assumed. This way, the calculated degrees of structure perfection exceeded 99% for all g. The rheological characterizations were performed on selected polymer samples only, which nevertheless allowed for a sufficiently comprehensive picture of the role of strong hydrogen bonding units in determining the mechanical properties of such systems. In the case of the series containing 50 mol%

UPy, unclarified foaming events prevented adequate rheological characterizations.

2.2 Methods

2.2.1 Vacuum compression molding

The polymer systems studied in the present work possess a glass transition temperature higher than room temperature. At room temperature, ring and linear PS, Cayley-tree and dendronized polymers have the appearance of fine powders. A first approach to shape the specimens for rheology is to load the polymer powders directly into the rheometers at high temperature and allow for melting. However, such a strategy leads to the formation of air bubbles and sample inhomogeneities which affect rheological measurements. For this reason, we used compression molding under vacuum in order to prepare proper specimens in a controlled fashion. Vacuum compression molding consists in pressing the powders above the glass transition temperature in vacuum atmosphere. The simultaneous application of high pressure and temperature promotes expulsion of the air contained in the powders and allows for creating homogeneous and well-shaped specimens. In order to apply vacuum compression molding, we designed and built a home-made mold. The schematic of such mold is depicted in figure 2.6. Vacuum is ensured by an outer chamber which is made of a container and a cap (grey). The outer chamber is connected to a vacuum pump through a tube of 6 mm diameter. The container and the cap are sealed together through a rubber airtight o-ring (dark red). The upper cap and the container are placed between the heated platens of a press. The inner mold is made of a lower plate (orange) and a drum (cyan), held together by a hollow cylindrical holder (green). The sample (pink) is loaded in the drum and then, an upper piston (yellow) is placed on top. The piston is pressed and heated directly through the cap of the outer chamber whereas the lower plate and drum are pressed and heated by the bottom part of the container. The pressing action of the piston is opposed by rubber rings (dark red) placed between the upper piston and the drum.

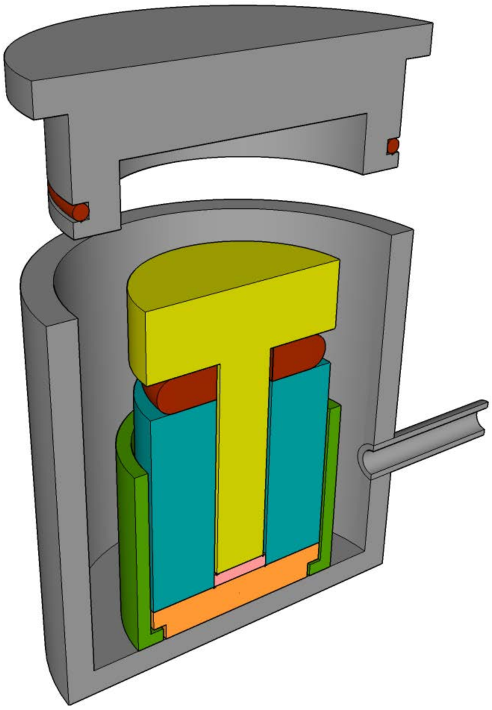

Figure 2.6: Schematic of the mold for compression molding in vacuum (dark grey, outer chamber; light green, inner piston; cyan, drum; orange, lower plate; dark green, drum-plate holder; pink, sample; red, rubbers).

The purpose of the rubber rings is to avoid excessive pressure on the sample so that penetration of the material between the drum and the plate is prevented. The mold is placed in a hydraulic press from Perkin-Elmer (USA) which allows for pressing up to 10 tons. Moreover, the mold can be heated from room temperature up to 150°C in about 10 min, with heated platens ATLAS$^{\mathrm{TM}}$ from SPECAC LTD (UK). After proper temperature has been reached, few minutes (from 5 to 15) are enough to obtain a well-shaped, bubble-free sample. The diameter of the inner drum and the piston can be varied in order to obtain specimens of different diameters. In this work we prepared specimens with diameters of 4, 6, 8 and 10 mm.

2.2.2 Filament stretching rheometer

The extensional stress measurements described in this thesis were performed at the Technical University of Denmark (DTU) with a filament stretching rheometer (FSR)

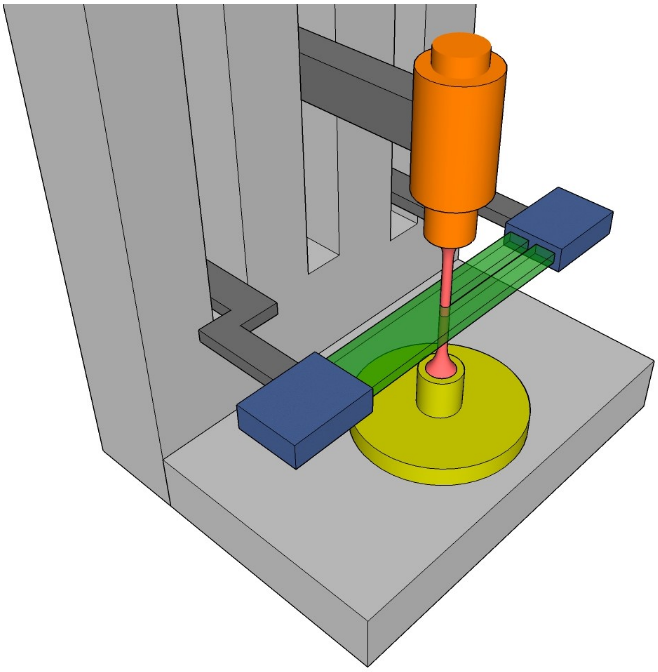

Figure 2.7: Schematic of the FSR (yellow, lower plate with force transducer; red, sample; blue, laser micrometer; green, laser beam; orange, moving plate [74, 76, 89].

[89] (figure 2.7). In such a rheometer, the sample (red) is placed between two plates. The lower static plate (yellow) is connected to a force transducer that measures the transient force $F = F(t)$ acting throughout the sample. The upper moving plate is driven by a feedback loop so that the stretching rate $\dot{\varepsilon}_H$ is kept constant in the middle of the filament. The transient diameter $2R(t)$ at the midfilament plane is monitored by a laser micrometer (blue). At small deformations during the start-up of elongational flow, part of the force comes from the radial variation due to the shear component of the deformation field. This effect may be compensated by a correction factor [90]. For large strains, the correction vanishes, and the radial variation of the stress in the symmetry plane becomes negligible [91]. The Hencky strain ε_H and the mean value of the stress difference over the midfilament plane are calculated from $R(t)$ and $F(t)$ as [92]:

$$\varepsilon_H(t) = -2\ln\frac{R(t)}{R_0} \tag{2.2}$$

and

$$\langle \sigma_{zz} - \sigma_{rr} \rangle = \frac{F(t) - m_f g/2}{\pi R^2(t)} \times \frac{1}{1 + [R(t)/R_0]^{10/3} \exp(-\Lambda_0^3)/(3\Lambda_0^2)} \tag{2.3}$$

where m_f is the weight of the filament, Λ_0 is the aspect ratio of the sample, R_0 its initial radius, and g is the gravitational acceleration. A recently updated control scheme [93] is employed in the FSR to ensure accurate constant stretch rate, $\dot{\varepsilon} = d\varepsilon_H/dt$. The extensional stress growth coefficient is defined as $\eta_{el}^+ = \langle \sigma_{zz} - \sigma_{rr} \rangle / \dot{\varepsilon}$. The geometries consist in stainless steel parallel plates whose diameter can be varied between 10 and 4 mm, according to the quantity of tested sample. Moreover, temperature control is provided by a convection oven and inert atmosphere by continuous N_2 flow.

2.2.3 ARES rheometer equipped with CPP geometry

All nonlinear shear measurements described in the next chapters were carried out on an ARES rheometer (TA Instruments, USA) equipped with a force rebalance transducer (2KFRTN1) and a CPP fixture. Most of samples were tested by using the configuration with a diameter of 6 mm for the inner partition. We built also an inner partition with a diameter of 10 mm. We used both 6 mm and 10 mm partitions to test two PS solutions in order to extract the first and second normal stress differences. The bottom geometry consists of a standard stainless steel cone with an angle of 0.1 *rad* and a truncation of 51 μm. The CPP geometry can fit into the ARES convection oven, so as to guarantee a temperature control of ±0.1°C. Inert atmosphere is provided through continuous N_2 flow. Since cone-partitioned-plate rheometry is a relevant part of this work, all details on the implementation, validation and performance of our homemade CPP are given in the next dedicated chapter.

2.2.4 Anton Paar rheometers

Some linear measurements in the present work were carried out on Physica benchtop, stress-controlled rheometers from Anton Paar (Germany). Particularly, we used the models MCR502 and MCR702. Temperature control was ensured by a Peltier hood for the first one and by a hybrid controller CTD180 (with water circulation and air convection) for the second. Inert atmosphere was ensured by continuous N_2 flow. Most samples were tested with stainless steel, parallel plate geometry (diameters, 8 and 4 mm). The MCR702 is equipped with two stress-controlled motors allowing for measurements in counter-rotating shear. The main advantage of stress controlled rheometers is the possibility to perform creep measurements. Conversely, the main disadvantage is the relatively long time to reach steady $\dot{\gamma}$ in transient shear experiments.

2.3 Supplemental information for linear and ring polymers

2.3.1 Shear measurements

Prior to rheological measurements, the polystyene samples were molded into discotic specimens with diameter of 8 mm and thickness ranging from 300 to 500 μm. To this end, we used the homemade compression vacuum mold described in section 2.2.1. Linear PS solutions were molded at 130°C while Linear PS melts and linear/ring blends at 150°C. Ring PS melts were molded at 140°C as they are more prone to degradation compared to the respective linear precursors. The pressure applied ranged between 0.2 and 0.4 tons. The annealing time was 15 min for melts, solutions and blends. This interval was sufficient to ensure complete relaxation of the polymer chains after molding. The temperature range for dynamic linear measurements was between 110 and 170°C. The temperatures for nonlinear measurements were chosen in such a way that in a frequency sweep from 0.1 to 100 rad/s we could observe both the terminal flow and the rubbery plateau region [94]. Linear viscoelastic (LVE) measurements were carried out both with standard 8 mm parallel plates and with the CPP geometry in order to have a comparison of different geometries. Nonlinear viscoelastic (NLVE) start-up tests at constant shear rate were performed by using the CPP geometry described in chapter 2. NLVE tests on linear PS133k, PS185k and Lin/Ring PS185k, were carried out at 160°C, NLVE tests on PS285k/2k-47 were performed at 140°C whereas PS285k72k-65, Linear PS84k, Ring PS84k and Lin/Ring PS84k were tested at 150°C in nonlinear regime. In order to ensure that shear transients were not influenced by edge fracture, we run frequency sweeps between successive start-up tests and compared them with the first result right after loading. Moreover, we randomly repeated start-up tests at high shear rates. Fresh samples were loaded when consistency and reproducibility were found to be beyond experimental error.

2.3.2 Extensional measurements

The protocol used for the preparation of the samples for uniaxial extension is different from that followed in shear. However, this does not affect the results because polystyrene samples do not undergo aging. Before measuring, all samples were dried in vacuum oven at 55°C for 24h and then molded into cylindrical test specimens with a fixed radius of either $R_0 = 2.7$ mm or $R_0 = 4.0$ mm. The initial length L_0 of the cylindrical test specimen was controlled by adding an appropriate mass of sample into the mold. The aspect ratio $\Lambda_0 = L_0/R_0$ ranged between 0.48 and 0.59. The samples were pressed at a temperature in the range of 140-155°C and annealed at the same temperature under vacuum until the polymer chains were completely relaxed. They were prestretched to a radius R_p ranging from 1.2 to 3 mm at elevated temperatures, 140-150°C fro PS solutions and 160°C for the PS melts, prior to the extensional experiments. After prestretching, the temperature was decreased to the desired measurement temperature T for the extensional stress measurements. Temperature was chosen so that $\dot{\varepsilon}\tau_R > 1$ when the stretch rate is suitable (typically $\dot{\varepsilon} < 1$ s^{-1} for the control scheme of the FSR [93]. We chose T = 110°C and T = 120°C for the two solutions PS285k/2k-47 and PS285k/2k-65, respectively, and T = 130°C for the two melts, PS133k and PS185k. Measurements were carried out in nitrogen atmosphere.

2.4 Supplemental information for Cayley-Tree Polymers

2.4.1 Sample preparation

Prior to molding, the samples were dried in a vacuum oven at 90°C for two to three days. The materials were then molded into cylindrical test specimens using homemade vacuum molds (typically, between two Teflon disks). The amount of sample for each specimen was about 20-40 mg. The materials were pressed at approximately 170°C (the mold was put in a hot press with applied load of 0.4 tons). This protocol ensured that the samples were properly annealed. Given the low quantity of samples, the specimens for both extensional and shear measurements were reused when necessary, after a rheological test was completed. The recovered sample from the rheometer was remolded by using the same protocol described above. Possible degradation was checked before new rheological measurements via reproducibility of LVE measurements and size exclusion chromatography.

2.4.2 Uniaxial extensional measurements

The extensional stress measurements were performed with a FSR [76, 89, 93]. The molded specimens had a fixed radius of R_0 = 2.7 mm. The initial length L_0 of the cylindrical test specimen was controlled by inserting an appropriate mass of sample into the mold. The aspect ratio $\Lambda_0 = L_0/R_0$ ranged between 0.41 and 0.56. The samples were prestretched to a radius R_p ranging from 1.2 to 2.4 mm at 180°C prior to the extensional experiments. After prestretching, the measurements were carried out in nitrogen atmosphere at the same temperature. The extensional stress decay coefficient is defined as $\eta_{el}^{-} = \langle \sigma_{zz} - \sigma_{rr} \rangle / \dot{\varepsilon}$, where $\dot{\varepsilon}$ is the strain rate in the start-up of the flow.

2.4.3 Simple shear measurements

Measurements were performed in a strain-controlled ARES rheometer (TA instruments, USA) equipped with a force rebalance transducer (2KFRTN1). Linear and nonlinear measurements were performed with the homemade CPP fixture described in chapter 3, in order to avoid experimental artifacts associated with edge fracture. Nitrogen flow reduced the risk of degradation. The lowest attainable shear rate with this geometry was 0.01 s^{-1}. Nonlinear start-up tests with sample G3 were carried out at 180°C. The measurements with the sample G4 at the two lowest shear rates (0.001 and 0.003 s^{-1}) were performed at 200°C and then shifted to 180°C by using the horizontal shift factor of the LVE data [50]; measurements at larger rates were performed at 180°C.

2.4.4 BoB modeling

In order to gain a deeper understanding of molecular relaxation mechanisms of Cayley-trees polymers, we used the BoB model [95–97] to describe rheological properties of such systems. The modeling of rheological data was carried out by dr. Chinmay Das at the University of Leeds (UK). Computational rheology [49, 96, 98] follows coupled relaxation in time of a numerical ensemble of molecules after a small, affine, step strain. For a Cayley-tree molecule, the relaxation starts by arm retraction [47, 99] of the outermost segments with one free end. The relaxed segments act like solvent for the yet to be relaxed segments [100], and thus coupling the relaxation of all the molecules considered in the calculation (hierarchical relaxation). The inner segments can only relax (by Rouse-like explorations as described below) once the outer segments have relaxed completely and their relaxation is slowed due to the localized friction at the branch points (which is accouted for). Hence, inner segments become gradually available for branch-point withdrawal. The time at which certain part (of inner segment) becomes available for relaxation is assigned as its stretch relaxation time. Relaxation of such compound segments that contain one or more localized friction points is described by a multidimensional first-passage problem and it is simplified by considering the portion of this compound arm that can move coherently with the chain end at a given time and assigning a dynamics to this effective pivot point of a compound segment [96]. Specifically, when the first two generations have relaxed, there are two localized friction points in the *compound* arm. We consider that the contour length fluctuations process in branch retraction is limited to the length available via the above mentioned Rouse process. In general, the final unrelaxed material behaves like a linear polymer and the terminal relaxation is via reptation. However, for the symmetric molecules considered here, reptation plays no role. We used a value for the dilution exponent of $\alpha = 1$ and branch point hopping parameter $\mathrm{p}^2 = 1/40$. Concerning the latter, we note that it is significantly smaller than the more commonly chosen value of $\mathrm{p}^2 = 1/12$ [101, 102], but this choice was found to simultaneously fit all rheological data of asymmetric star and other branched polymers [53, 96, 103–105]. Part of the reason for smaller value of the chosen parameter is because we consider that the friction from a relaxed side-arm is set by the tube diameter at the time-scale of the branch-point retraction. The exact numerical value probably is of no great significance. Rather this is a fit parameter that would have been different, we have made different choices for complete branch retraction. Note that the default choice in BoB model is to consider branch-point retraction only when the chain end visits the origin; in this work, we consider complete retraction when the chain end reaches 0.15 times the current effective tube diameter. This change was necessary in order to describe both systems with a single value of the entanglement molar mass. We have chosen this small value of effective entanglements as the criteria for complete branch-withdrawal to ensure that results for well entangle polymers remain unchanged.

For reasons still not fully resolved, small side-arms (of the order of one entanglement or even less than one entanglement) have been found to provide significantly larger friction compared to expectations from tube theory predictions based on long side-arms [104, 106]. Recent molecular dynamics results also suggest that entanglement constraints at the branch-points are stronger than those for linear polymers [105]. For this reason, we have decided not to have a cut-off function at order of one entanglement like in the hierarchical model [49, 97]. Having a zero (as in the original BoB model) or a small value (as in the present work) allows us to predict the rheology of branched polymers with segment lengths down to the order of one entanglemnt. To predict the nonlinear flow response, we resolve the linear relaxation as a set of pom-pom modes.

2.5 Supplemental information for dendronized polymers

2.5.1 Gel permeation chromatography

Gel permeation chromatography (GPC) was performed at ETH Zurich by dr. Thomas Schweizer and dr. Leon Serc. GPC measurements were conducted on a Malvern VISCOTEK GPCmax VE-2001 instrument equipped with two D5000 columns (300× 8.0 mm), refractive index (RI), viscometry (VI) and light scattering (LS; 15°and 90°angles) detectors. Column oven and detector temperatures were regulated to 45°C. DMF containing LiBr (c = 1 g L^{-1}) was used as the eluent at flow rate of 1mL min^{-1}, and the samples were filtered through syringe filters with 0.45 μm pore sizes prior to injection. Experimental molar masses (M_n, M_w) and polydispersity values(PDI) of the synthesized polymers were determined by light scattering using Malvern's OmniSEC software. Poly(methyl methacrylate) standards with peak molecular weights (M_p) of

0.10, 0.212, 0.66, 0.981, and 2.73 MDa (Polymer Laboratories Ltd., UK) were used for calibration. The molecular weight standard closest to the theoretical molecular weight of the respective polymer was used as reference. It is important to mention that PMMA is certainly not an appropriate standard because the hydrodynamic volume of each DP depends on the generation. With larger generation the volume increases. This is to some degree counteracted by the increase of mass per segment length with increasing generation. Universal calibration, if possible for such nonflexible polymers, might have improved on the accuracy of the results. In earlier work [107] an effort was made to properly calibrate GPC for DPs using light scattering and classical PG1 as reference. It was concluded that proper molar mass analysis on higher generation DPs is challenging largely due to the fact that it is so difficult to obtain molecularly dispersed solutions. A detailed light scattering investigation in dilute solutions is the subject of future work. Given these issues, we believe that the present GPC analysis, which is in line with earlier works on DPs (e.g., refs [87] and [108]), allows for reliable relative comparison of different molecular weights.

For the higher-generation, short-chained DPs (P_n =50, 300) the apparent experimental molecular weights determined by GPC agree well with the theoretically calculated ones, whereas the experimentally determined values for the longer backbone lengths are somewhat smaller by a factor of approximately 1.1. It is known that very large appendices, such as in dendronized polymers, can result in discrepancies between theoretical and experimental molecular weights. These may be explained by the opposing effects of (i) chain thickening, i.e., the polymers mass per repeat unit length being much larger than the calibration standards leading to an underestimation of molecular weights, and (ii) chain stiffening with increasing PG, leading to an overestimation of hydrodynamic volume and molecular weights, respectively. Notwithstanding, the performed UV-labeling experiments and the fact that GPC elution traces consistently shift toward shorter retention times with both increasing PG and P_n support the conclusion that the conversion obtained in the dendronization reactions is effectively 100%.

2.5.2 Thermal analysis

Differential scanning calorimetry (DSC) measurements were conducted on a DSC Q1000 from TA Instruments (USA) in a temperature range of -50 to +140°C with a heating rate of 10°C/ min^{-1}. Dried samples of a total weight ranging between 4 and 25 mg were weighed into aluminum pans, covered by a punched cap, and analyzed in a nitrogen atmosphere. The reported glass temperatures (T_g) were taken from the second heating run.

2.5.3 Rheology

At room temperature classic dendronized polymers have the form of a fine powder. In order to load the samples into the rheometer, we shaped them to 4 or 8 mm discoid specimens by compression molding in vacuum with the homemade mold described in section 2.2.1. The temperature applied was $T = T_g + 5°\text{C}$, and the pressure applied was 0.1 ton. The molding procedure was carried out for approximately 5 min, so that the molding time was negligible with respect to the equilibration time of the samples. Linear rheological tests were performed with Physica MCR-502 and Physica MCR-702 rheometers from Anton Paar (Austria). The instruments were equipped with different devices for temperature control. Particularly, we used an electric hood for MCR-502 and a hybrid temperature control (Peltier and convection oven) for the MCR-702 (CTD180 from Anton Paar). Inert atmosphere was ensured during all the tests with nitrogen flow in order to prevent sample degradation. The temperature calibration of the two instruments was checked by measuring the actual temperature values with an external thermocouple (type K). Slight differences were found among the used instruments. Small horizontal shifts were applied to the linear viscoelastic master curves in order to account for the different thermal calibration of the rheometers. Parallel plate geometries (stainless steel) of 4 and 8 mm diameter were utilized for the linear tests. Nonlinear shear measurements were performed with the CPP setup described in chapter 2, in order to prevent artifacts caused by flow instabilities, i.e., edge fracture. In order to investigate the linear rheological behavior of some of the samples in the low-frequency regime, we carried out creep experiments (on Physica 702) and converted the creep compliance, $J(t)$, into the dynamic moduli, $G'(\omega)$ and $G''(\omega)$. Creep experiments were performed at the highest experimentally accessible temperature for dynamic measurements. The $J(t)$ function was converted into $G'(\omega))$ and $G''(\omega)$ by means of NLReg software, based on a generalization of the Tikhonov regularization method [109]. This is a well-known ill-defined problem since the calculation of relaxation spectra is not unique, but with this method we obtain consistent and reliable results.

2.5.4 X-ray scattering

X-ray scattering measurements were performed at the Max Planck Institute in Mainz by prof. George Floudas, using Cu Kα radiation (Rigaku Micro Max 007 X-ray generator (Japan), Osmic Confocal Max-Flux curved multilayer optics). Oriented fibers of 1.0 mm diameter were prepared by a miniextruder. Despite the extrusion process, the diffraction patterns where nearly isotropic, suggesting correlations of short-range order. Wide-angle X-ray scattering (WAXS) measurements were made with a sample-to-detector distance of 35 cm using a Mar345 detector. Intensity distributions as a function of the modulus of the scattering vector, $q = (4\pi/\lambda)\sin(2\theta/2)$, where 2θ is the scattering angle, were obtained by radial averaging.

2.5.5 Simulations

Simulations on dendronized polymers were performed by prof. Martin Kröger at ETH, Zurich.

Coarse-grained melt packing model

To calculate inter- and intramolecular distance between hydrogen bonding donor-acceptor pairs, $\pi-\pi$ stacking benzene-benzene pair histograms, and the volume fraction profile of locally cylindrical PGs with respect to their backbones, a growth model was adopted and extended [110]. In brief, within this model all $n_g = 4 + 7\sum_{k=1}^{g} 2^k = 2(7 \times 2^g - 5)$ united atoms making the skeleton of each g-generation dendron (featuring $2^g - 1$ benzene rings) are modeled as hard spheres of diameter $d = 0.14$ nm. Each randomly (via Monte Carlo) generated configuration without overlap is equally likely. Temperature does not enter the model due to the hard sphere interactions; hence, there is no need for annealing by molecular dynamics or additional Monte Carlo. At start-up we set $W = 1$. This quantity will become the probability of the configuration to be generated. At each bond creation or *growth* attempt we considered a finite number of $k = 20$ orientations drawn from an isotropic distribution of unit (bond) vectors and identified the subset of $s \leq k$ growth moves without immediate overlap. From this subset we choose randomly and multiply the probability of the configuration by its Rosenbluth weight, $W \rightarrow W/s$. If $s = 0$, the whole configuration is discarded. Using $P_n = 50$, the root atoms of the DP side chains are placed equidistantly separated by a distance $\delta = 0.25$ nm along a straight line in x-direction, subject to periodic boundary conditions. All bonds between united atoms are of equal length ($b = 0.2$ nm) and oriented freely, subject to excluded volume interactions. All bonds are placed (i.e., effectively grafted) in successive, but random, orientational order (with respect to the backbone axis), taking into account a branching event following each seventh linear growth step. In any event, a new bond is formed at random orientation subject to excluded volume constraints. In this way, we grow a PG free of defects and overlaps (bond- and generation-wise). In marked contrast to the original model, we use a simulation box with hexagonal cross section of perimeter 6Δ in the yz-plane that contains the PG-g on its $P_n\delta$-long centerline. Interactions between a PG-g and its own periodic image in y- and z-directions are denoted as *intermolecular* interactions. The hexagonal arrangement serves to represent the situation encountered locally in a melt, and we choose the size Δ so that the overall volume fraction φ is a constant, independent of g. To be specific, $\Delta = 3(\pi d^3 n_g/\varphi\delta)^{1/2}$, with $\varphi = 0.13$. Averages are sampled from 10^7 independent configurations obtained in this way. Results are qualitatively unaffected by the precise choice of φ and d as long as (i) the size of a dendron exceeds δ by far, (ii) excluded volume interactions severely hinder the free growth, and (iii) the maximum generation is close to the known $g_{max} \approx 7$[58, 86, 88]. In light of Flory-theoretical calculations for dendronized polymers, the quantities δ, b, and φ are chosen to approximately reproduce the maximum, minimum, and random walk size of a g-generation strand of the simulated dendrimer, respectively. For $\Delta = \infty$, the original model is recovered [110]. Each dendron contains $2^{g+1} - 2$ hydrogen-bonding donors (NH groups) and $2^{g+2} - 2$ acceptors (O atoms). The volume fraction profiles are obtained from so-called unfolded coordinates that reveal the conformation of a single PG in the melt. Volume fraction profiles calculated using folded coordinates are flat (not shown) [86, 88].

Local orientational order in the melt

The molten PG sample consists of linear, thick dendronized polymers that can be characterized by their mean thickness D, persistence length l_p, and contour length L or length-to-width ratio $n = L/D$. The persistence length of the backbone is defined by the tangent-tangent correlation function at bond distance. The effective persistence length of the DP backbone had been mainly studied in theoretical works so far, and it probably depends on concentration and tends to decrease with increasing concentration. Direct determination of the persistence length requires single chain scattering or visualization of single DPs in the melt. To our knowledge both had not been achieved so far. The state-of-the-art concerning persistence length of neutral DPs in solution has been summarized by some of us in footnote 24 of ref [86] (for a third-generation DP, the theoretical value of the persistence length is about 50 nm). To study the effect of P_n on the local orientational order of the dendronized polymers, we investigate a classical model polymer melt made of semiflexible chains with N_a segments, each via a hybrid Monte Carlo/molecular dynamics scheme, [111] and calculate the bond-bond orientational order parameter as a function of the distance between bonds. To this end, we generate samples with 1000 semiflexible chains contained in a cubic simulation box with periodic boundary conditions for systems with varying bending stiffness $\mathcal{K} \in [1, 20]$ and $n = 3, 4, ..., 20$ under conventional melt conditions [112]. Results for (i) the bond-bond orientational order parameter for pairs of bonds separated by a given distance in space (cf. caption of Figure 6.10), (ii) persistence length from intramolecular bond-bond correlations (as expected, we find $l_p \approx \mathcal{K}D$), and (iii) bead-bead radial pair-correlation function $g(r)$ are obtained by averaging over 100 independent samples for each $(N_a, \mathcal{K})$ pair of parameters. We note that the used picture of semiflexible chains here is too simplistic, but this does not change the message from the simulation results.

2.6 Supplemental information for UPy-functionalized dendronized polymers

2.6.1 Gel Permeation Chromatography

Gel permeation chromatography measurements were carried out by dr. Leon F. Serc at ETH, Zurich. (GPC) using DMF containing LiBr (c = 1 g L^{-1}) as the eluent was performed on a VISCOTEK GPCmax VE-2001 instrument (Malvern, UK) equipped with D5000 columns (300×8.0 mm), refractive index (RI), viscometry (differential pressure) and light scattering (LS; 15°and 90°angles) detectors. Column oven and detector temperatures were regulated to 45°C. All samples were filtered through 0.45 μm PTFE syringe filters (Macherey-Nagel, Germany) prior to injection and the flow rate was 1 mL $\min^{-1}$. Poly(methyl methacrylate) standards with peak molecular weights (M_p) of 0.10, 0.212, 0.66, 0.981 and 2.73 MDa (Polymer Laboratories Ltd., UK) were used for calibration. Experimental molar masses (M_n, M_w) and polydispersity values (PDI) of the synthesized polymers were determined by light scattering using the commercially available OmniSEC software (Malvern, UK).

2.6.2 Thermal Analysis

thermal analysis measurements were carried out by dr. Leon F. Serc at ETH, Zurich. Differential scanning calorimetry (DSC) measurements were conducted on a DSC Q1000 (TA Instruments, USA) over a temperature range from -90 °C to 250 °C in a nitrogen atmosphere. Approximately 4 – 25 mg of dried sample was weighed into an aluminum DSC pan and covered with a punched cap. The samples were subjected to $\geq$2 heating/cooling cycles with a linear heating/cooling rate of 10 °C $\min^{-1}$. The glass transition temperatures (T_g) were determined from the second heating runs and analyzed using the commercially available Universal Analysis software (TA Instruments, USA).

2.6.3 Rheology

Annealing of the samples

In order to avoid ageing effects, we pre-annealed the samples in a vacuum oven at 100 °C for 8 days. After pre-annealing, the sample were cooled down and stored in vacuum at room temperature. Brittleness of the materials below glass temperature hindered vacuum compression molding at high temperature to shape the samples to disc specimens for rheological measurements. For this reason, the annealed powders were cold-pressed to disc-shaped capsules using vacuum molding at room temperature. The capsules were loaded into the rheometer and allowed for melting and homogenization at T_g+50°C for 20 minutes. Successively, the temperature was lowered to T_g+30°C and rheological measurements were started. Whenever possible, the leftovers coming from filament breaking in nonlinear extension or fracture in nonlinear shear, were recycled and cold-pressed to new specimens. Possible degradation was checked in simple shear before each nonlinear measurement by performing frequency sweeps in linear regime and checking overlap with previous data. For uniaxial extension, possible degradation was checked by verifying reproducibility of the transient measurements and consistency with data at different stretching rates.

Simple shear

Linear measurements were performed on a Physica MCR702 (Anton Paar, Germany), equipped with a hybrid temperature control (CTD180) and on an ARES rheometer (TA, USA) equipped with a convection oven. Linear measurements were carried out with 8 mm and 4 mm parallel plate geometries. The samples were cold pressed to disc-shaped specimens of the proper diameter and allowed for melting into the rheometer. Nonlinear shear measurements were performed with a homemade cone-partitioned plate geometry to prevent artefacts from edge fracture instability [92] (see chapter 2). The temperature for nonlinear shear was chosen as $T_g + 45$°C for all the samples apart from PG1-50.

Uniaxial extension

Extensional measurements were performed at DTU on a filament stretching rheometer (Rheofilament, USA), described in section 2.2.2. The specimens were formed to cylinders of 6mm diameter by means of cold-pressing. Nonlinear extensional measurements on the samples investigated were performed at $T_g + 29$°C. The aspect ratio of the samples ranged from 2.2 to 2.9.

Chapter 3

CONE-PARTITIONED PLATE RHEOMETRY

3.1 Introduction

One of the most interesting features of polymer systems undergoing nonlinear shear is their ability to develop normal stresses in orthogonal directions with respect to that of motion. As discussed in section 1.4, normal stresses induce a variety of flow instabilities which are relevant for polymer processing. Therefore, a complete characterization of the flow behavior of a specific polymer system should provide the dependence of all the viscometric functions, namely viscosity η, first and second normal stress differences, N_1 and N_2, upon shear rate $\dot{\gamma}$. As the rise of normal stresses in liquids undergoing shear is a second-order effect, normal stress differences are usually presented in terms of normal stress coefficients, $\Psi_1 = N_1/\dot{\gamma}^2$ and $\Psi_2 = N_2/\dot{\gamma}^2$. Such functions can be determined from transient start-up experiments in rotational shear rheometers. However, obtaining reliable data in strong rotational flows is not trivial because of the aforementioned instabilities. Above all, edge fracture is the most serious problem hindering correct measurements in shear because it is harder to control. The onset of fracture creates voids into the measurement volume and induces underestimation of viscosity and normal stresses. The larger the fracture, the larger is the error in evaluating η, N_1 and N_2. As pointed out in section 1.5, a good strategy to overcome this issue is to use a cone-partitioned plate (CPP) geometry. Such geometry restricts the measuring volume to the inner part of the sample so that edge phenomena do not affect the measurements. However, CPP geometry with single partition can provide reliable measurements only for viscosity. In modern rotational rheometers, N_1 can be direcly accessed by means of axial transducers. The value of N_1 read from rheometers equipped with CPP geometry is an apparent one (N_{app}) because of the contribution to the normal stress distribution coming from the outer non-measured sample. Such contribution causes an overestimation of N_1 that can exceed the true value by a factor larger than 2. As a further complication, N_2 measurements cannot be performed directly or in a straightforward manner. Different methods have been used to determine N_2. The second normal stress difference can be determined by measuring the free surface shape of fluids flowing down a semicircular channel [113], or with flow birefringence experiments [114]. Concerning rotational rheometry, the most effective methods are based on the evaluation of the normal stress distribution in cone-plate (CP) or parallel plate (PP) geometries, starting from the equations of motion for liquids [31, 115, 116]. Normal stresses distributions can be obtained with two types of different techniques. The first approach is to flush-mount transducers on the plate at different radii of the sample [117]. The second approach is to measure the total normal force acting on partitions of the plate with different radii [33]. Both methods involve the use of CP geometry rather than PP, as the shear rate $\dot{\gamma}$ in the former configuration, is constant throughout the gap. In this chapter we introduce the theory of the CP geometry and present the mathematical tools to evaluate N_1 and N_2 therein. Then, a short review of the development of the cone-partitioned plate geometry and the methods used to determine N_1 and N_2 is presented. Finally, we report on our homemade CPP setup for ARES rheometer. Moreover, we propose a simple method to evaluate N_1 and N_2 for polystyrene solutions at high temperatures by using our CPP setup.

3.2 Theory

3.2.1 Velocity profile in cone-plate geometry

In cone-plate geometry the velocity gradient, $\partial v/\partial h$ is constant throughout the gap [10] (with h being the distance between cone and plate). In order to demonstrate this, let us consider a cone and plate geometry with cone angle $d\theta$, as shown in figure 3.1. Let Ω be the angular velocity of the moving cone. The tangential velocity $v = v(r)$ of the cone at radius r is given by:

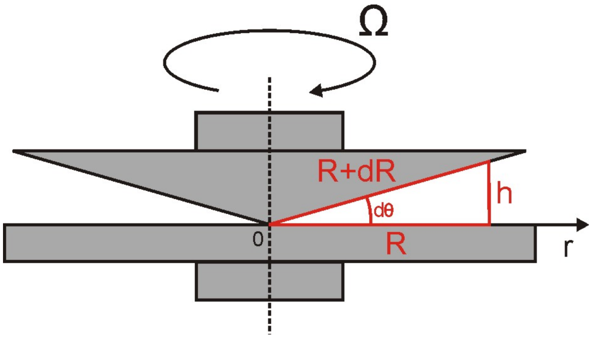

Figure 3.1: Cone-plate geometry.

$$v(r) = \Omega r \tag{3.1}$$

Considering no-slip boundary conditions, $v(r)$ is also the velocity of the first layer of fluid in contact with the cone at radius r. The gap $h(r)$ at radius r is given by:

$$h = (r + dr)\sin(d\theta) \tag{3.2}$$

by solving the equation of motion for simple shear in spherical coordinates, one obtains that the velocity profile is linear [8]. Therefore, the velocity gradient is:

$$\dot{\gamma} = \frac{\partial v}{\partial h} = \frac{v}{h} = \frac{\Omega r}{(r + dr)\sin(d\theta)} \tag{3.3}$$

In the limit case of very small angles we can approximate $\sin(d\theta)$ with θ. With an angle of 0.1 rad, such approximation yields an error smaller than 0.2%. Moreover, we note that $r = (r + dr)\cos(d\theta)$. With $d\theta$= 0.1 rad, the value of $\cos(d\theta)$=0.995, therefore the difference between $r + dr$ and r is negligible with an error of 0.5%. Considering such approximations we can write:

$$\dot{\gamma} = \frac{v}{h} = \frac{\Omega r}{(r + dr)\sin(d\theta)} \approx \frac{\Omega r}{r d\theta} = \frac{\Omega}{d\theta} \tag{3.4}$$

Equation (3.4) states that the velocity gradient in cone and plate geometry is independent of the radius. Moreover, when Ω is fixed, the velocity gradient $\dot{\gamma}$ is constant throughout the gap. Since the viscometric functions η, N_1 and N_2 depend on the velocity gradient, in cone and plate geometry such functions are independent on the radial position. This makes cone and plate geometry the best geometry for nonlinear measurements. A more rigorous mathematical demonstration of equation3.4 is possible through the equation of motion [10]. However, this is beyond the scope of this thesis.

3.2.2 Viscometric functions in cone-plate geometry

The cone-partitioned plate geometry is a very useful tool for rheological measurements insofar as it allows for measuring all the viscometric functions in a reliable fashion by means of rotational rheometry. While the viscosity at a single shear rate can be directly measured in a transient start-up shear experiment, the first and second normal stress differences can be obtained from multiple measurements with a single CPP or from a single start-up shear experiment with a CPP cell with two partitions [33]. Measurements of N_1 and N_2 are obtained based on the radial normal stress distribution calculated from the momentum equation. In order to derive the normal stress distribution let us consider the motion of fluid into CP geometry descibed in spherical coordinates (figure 1.10). From the radial component of the equation of motion in spherical coordinates, neglecting the centrifugal force term $-\rho v_\phi^2/r$ (where ρ is the density and v_ϕ the velocity in ϕ direction) we obtain:

$$0 \;=\; -\frac{\partial p}{\partial r} - \frac{1}{r^2}\frac{\partial}{\partial r}\left(r^2 \tau_{rr}\right) + \frac{\tau_{\theta\theta} + \tau_{\phi\phi}}{r} \tag{3.5}$$

Where p is the scalar isotropic pressure and $\tau_{\theta\theta}$ and $\tau_{\phi\phi}$ are normal stresses acting in θ and ϕ directions, respectively. Note that all the components of the stress tensor are constant with r because viscometric functions η, Ψ_1 and Ψ_2 depend only on $\dot{\gamma}$ which is constant over r in cone partitioned plate geometry (as shown in section 3.2.1). Therefore we have:

$$\frac{1}{r^2}\frac{\partial}{\partial r}\left(r^2 \tau_{rr}\right) \;=\; \frac{2\tau_{rr}}{r} \tag{3.6}$$

Inserting equation (3.6) in equation (3.5) we obtain the following:

$$r\frac{\partial p}{\partial r} = \tau_{\theta\theta} + \tau_{\phi\phi} - 2\tau_{rr} \tag{3.7}$$

which can be rewritten as:

$$\frac{\partial p}{\partial \ln(r)} = \tau_{\theta\theta} + \tau_{\phi\phi} - 2\tau_{rr} \tag{3.8}$$

The global stress tensor is equal to $\boldsymbol{\sigma} = p\boldsymbol{\delta} + \boldsymbol{\tau}$ where $\boldsymbol{\delta}$ is the unit tensor and $\boldsymbol{\tau}$ is the deviatoric component of the stress tensor. Therefore, $\sigma_{\theta\theta} = p + \tau_{\theta\theta}$. Since $\tau_{\theta\theta}$ is constant, we have:

$$\frac{\partial p}{\partial \ln(r)} = \frac{\partial \sigma_{\theta\theta}}{\partial \ln(r)} \tag{3.9}$$

The stress component $\sigma_{\theta\theta}$ can be measured on the plate ($\theta = \pi/2$). The stress at the edge of the plate $\sigma_{rr}(R)$ can be related to the atmospheric pressure p_a through a normal stress balance at the rim of the sample ($r = R$). Assuming that the rim of the sample is spherical, we have $\sigma_{rr}(R) = p_a$. Here, we consider the compression stresses to be positive, and we define the second normal stress coefficient as follows:

$$\Psi_2 = \Psi_2(R) = \left[\sigma_{rr}(R) - \sigma_{\theta\theta}(R)\right]/\dot{\gamma}^2 = \left[p_a - \sigma_{\theta\theta}(R)\right]/\dot{\gamma}^2 \tag{3.10}$$

Note that Ψ_2 defined in equation (3.10) has opposite sign with respect to the definition given in section 1.4 because of the different convention on the sign of tensile stresses. Ψ_2 is constant over r and equal to its value at $r = R$. From equation (3.10) we have the following:

$$\sigma_{\theta\theta}(R) = p_a - \Psi_2\dot{\gamma}^2 \tag{3.11}$$

Inserting equation (3.9) in (3.8) we have:

$$\frac{\partial\sigma_{\theta\theta}}{\partial\ln(r)} = \tau_{\theta\theta} + \tau_{\phi\phi} - 2\tau_{rr} \tag{3.12}$$

Consistently with the convention used for the definition of Ψ_2 in equation (3.11), we define the first normal stress difference as $\Psi_1 = \tau_{\theta\theta} - \tau_{\phi\phi}$. The second term of equation (3.11) can be reformulated as follows:

$$\begin{aligned}\tau_{\theta\theta} + \tau_{\phi\phi} - 2\tau_{rr} &= 2\tau_{\theta\theta} - \tau_{\theta\theta} + \tau_{\phi\phi} - 2\tau_{rr} = \\ = -(\tau_{\theta\theta} - \tau_{\phi\phi}) - 2(\tau_{rr} - \tau_{\theta\theta}) &= -(\Psi_1 + 2\Psi_2)\dot{\gamma}^2\end{aligned} \tag{3.13}$$

Inserting equation (3.13) in (3.12) we obtain the following:

$$\frac{\partial\sigma_{\theta\theta}}{\partial\ln r} = -(\Psi_1 + 2\Psi_2)\dot{\gamma}^2 \tag{3.14}$$

Equation (3.14) can be integrated directly between R and r and yield:

$$\sigma_{\theta\theta}(r) - \sigma_{\theta\theta}(R) \;=\; -(\Psi_1 + 2\Psi_2)\dot{\gamma}^2 \ln\left(\frac{r}{R}\right) \tag{3.15}$$

Inserting (3.10) in (3.16) we obtain:

$$\sigma_{\theta\theta}(r) \;=\; p_a - \Psi_2\dot{\gamma}^2 - (\Psi_1 + 2\Psi_2)\dot{\gamma}^2 \ln\left(\frac{r}{R}\right) \tag{3.16}$$

Equation (3.16) gives the pressure distribution on the plate of the cone-plate geometry. Such equation can be integrated between 0 and R to yield:

$$\Psi_1 = \frac{2F}{\pi R^2 \dot{\gamma}^2} \tag{3.17}$$

Where F is the total thrust on the plate without the contribution of the atmospheric pressure p_a. If we select a value of the radius internal to the volume of the sample, R_i such that $0 < R_i < R$, then the integration yields the following equation [31, 116]:

$$N_{app} = \frac{2F_i}{\pi R_i^2} \;=\; N_1 + 2(N_1 + 2N_2)\ln\left(\frac{R}{R_i}\right) \tag{3.18}$$

Where $N_1 = \Psi_1\dot{\gamma}^2$, $N_2 = \Psi_2\dot{\gamma}^2$ and F_i is the normal force exerted on the plate with radius R_i. Equation (3.18) provides the means to determine N_1 and N_2 (or correspondingly, Ψ_1 and Ψ_2) in rotational rheometers with cone and plate fixture. However, several assumptions have been made to derive it [10]: we have neglected the fluid inertia and viscous heating and assumed spherical surface at the edge. If now the apparent normal force as a function of the logarithm of R/R_i is known, one can obtain both the first and second normal stress differences, as shown in figure 3.2. The apparent normal force is a quantity which can be directly obtained experimentally as all modern rotational rheometers possess normal transducers. In order to determine N_{app} as function of $\ln(R/R_i)$, two different approaches can be followed. One can fix R_i by fixing the inner partition and vary the outer radius of the sample, R. This is an easy-to-implement approach as only one CPP setup with single measuring partition is needed. One can load samples of different masses so that different outer diameters will be reached after

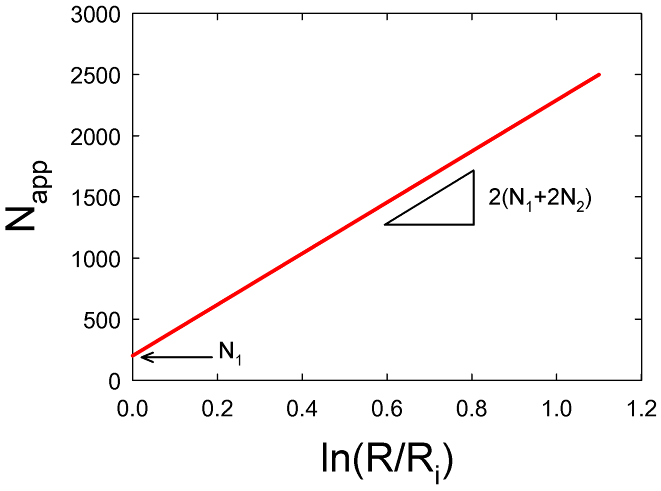

Figure 3.2: Graphical representation of the working equation of CPP geometry to detect N_1 and N_2.

loading, according to the following equation [116]:

$$R = \sqrt[3]{\frac{3m}{2\pi\rho\theta}} \tag{3.19}$$

where m is the mass of the sample, ρ is the density and θ is the cone angle. The second approach is to use the same R and detect the apparent normal force at different R_i (at least two values). This technique requires more sophisticated setups compared to the first approach. On the other hand, the first approach requires multiple measurements for each shear rate, mainly because of the error between the calculated value of R from equation (3.19) and the actual one. In the second procedure, such an error is minimized and N_1 and N_2 can be obtained with a single measurement by using a cell with two measuring partitions, [33] or with two measurements by using two CPP setups with one measuring partition having different inner radius (this work). In the following sections we discuss the advantages and disadvantages of both approaches and we present some experimental data obtained by using the second approach with two CPP setups.

3.3 Historical overview of CPP geometry

As already mentioned, first and second normal stress differences are difficult to measure in rotational rheometry because of edge fracture. Evidence of edge fracture instability in shear flows was first reported by the early work of Pollett [30, 118], Tanner and Keentok [29] and Keentok and Xue [26]. Tanner and Keentok established a correlation between the magnitude of N_2, the surface tension and the amplitude of the fracture. The first attempt to overcome the edge fracture issue in rotational rheometers was done by Meissner et al. in 1989 [31]. They modified a commercial RMS800 rotational rheometer and equipped it with a CPP fixture to measure the viscometric functions of LDPE samples. In order to extract N_2, Meissner used equation (3.18) with a fixed inner radius of 6 mm and varying the outer radius R. This procedure involves multiple measurements for each shear rate. The outer radius is estimated from the mass of the sample according to equation 3.19. The same method was used by Schweizer in 2002 [116], in order to measure the viscometric functions of a polystyrene melt (M_w=158k) [116]. Later, Schweizer used this approach to measure also a polystyrene melt with M_w=200k [119]. In this case, the inner radius was reduced to 4mm to avoid early overload of the axial transducer of the instrument. Apart from overloading issues, Schweizer also studied the problems related with the axial compliance of the instrument [120]. He found out that axial compliance induces delays in the axial force signal of rotational rheometers. Since axial compliance cannot be completely eliminated, delays affecting the N_1 signal are always present, therefore reliable data are restricted to the steady state values of normal force. In order to reduce axial compliance and increase the normal force maximum load, Schweizer and coworkers built up a homemade rheometer (MTR 25) with normal force capacity of 25kg and large axial stiffness of 10^7 N/m [121]. The MTR 25 had another important characteristic: by means of two axial transducers it detects normal force both on the inner and outer partition. This allows to determine N_1 and N_2 simultaneously in a single start-up experiment. Such strategy was first implemented by Pollett [30] and it has the main drawback that the part of the sample on the outer partition (and consequently the measurements) is affected by edge fracture. Moreover, MTR 25 requires large quantities of samples as the outer radius is around 10-15 mm. The design was improved and downsized with the CPP3 cell of Schweizer et al. [33]. Such a cell was designed to fit MCR502 rheometers and has three partitions (figure 3.3). Schweizer's CPP3 consists in an inner measuring partition with radius R_1, an outer measuring ring with diameter R_2 and an outer non-measuring partition to prevent edge fracture. The working principle is similar to that of MRT25: the outer radius is fixed and the distribution of normal stresses are integrated over two radii. The N_1 and N_2 signals are obtained by reiterating equation (3.18) on the two partition with fixed outer radius:

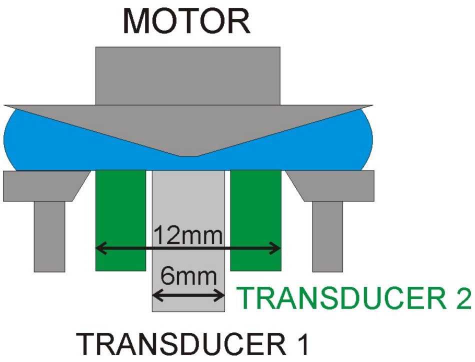

Figure 3.3: Schematic representation of Schweizer's CPP3 setup. The lower plate is made of an inner 6mm partition connected to transducer 1 (light grey), an outer ring connected to transducer 2 (green), and an outer nonmeasuring ring (grey).

$$N_{app,1} = \frac{2F_1}{\pi R_1^2} = N_1 + 2(N_1 + N_2)\ln\left(\frac{R}{R_1}\right) \tag{3.20}$$

$$N_{app,2} = \frac{2(F_1 + F_2)}{\pi R_2^2} = N_1 + 2(N_1 + N_2)\ln\left(\frac{R}{R_2}\right) \tag{3.21}$$

In equations (3.20)-(3.21) the geometrical parameters are known as well as $N_{app,1}$ and $N_{app,2}$ which are the apparent normal forces detected on partition 1 and 1+2, respectively. The only two unknowns are N_1 and N_2 which can be easily determined. One of the disadvantages of the CPP3 cell is the temperature control which is made by film heaters [33]. These devices can create large thermal gradients into the sample and cannot exceed 110°C. Moreover, the CPP3 requires multiple controllers for the different heaters and a post-processing of the data obtained from the cell transducers to reduce signal noise. Such limitations are not present in the simple CPP of Meissner. Snijkers et al. [94] came-up with a CPP setup on the ARES rheometer. The design is similar to that of Meissner but an extension of the convection oven of ARES rheometer is needed to achieve good thermal control. Such design is a good tool for obtaining reliable viscosity measurements but cannot determine all the viscometric functions. A similar setup was also used on ARES rheometer by Ravindranath and Wang [122]. The setup of Snijkers was improved with our CPP setup which represents the state-of-the-art for CPP rheometry with single measuring partition. It is worth mentioning that at the moment, two commercial version of CPP setups are available from TA instruments (USA) on ARES rheometer and from Anton Paar (Austria) on Physica MCR702.

Other techniques have also been adopted to determine N_1 and N_2 on rotational rheometers. One approach involves determining the normal stress distribution as a function of the radius with the use of small transducer mounted at different radii of the measuring plate [117, 123, 124]. Another approach is to use a combination of parallel plate and cone and plate experiments [125] or adopt optical method based on birefringence experiments [114]. The direct evaluation of the pressure distribution on the plate is a reliable method for determining N_2 but it requires larger quantities of samples compared to CPP3 cell as the flush-mounted transducers have to be spaced enough from each other and the radius of the sample has to be at least 10 mm. Moreover, such flush-mounted transducers cannot operate at very high temperatures.

3.4 Homemade CPP setup

Figure 3.4(a) shows a schematic of our homemade CPP setup. The bottom cone is attached to the motor of the ARES rheometer. For measuring polymer melts and solutions we used a standard cone with a diameter of 25mm and a cone angle $\theta = 0.1$ rad/s. Such a value of θ represents a good compromise between the necessity of reducing axial compliance [120] and that of preventing edge fracture [33]. Indeed, normal forces originating in strong start-up shear tend to push the tools apart, resulting in a squeeze flow which occurs over a characteristic time scale $t_a = (6\pi R\eta)/K_a\theta^3$ (with R being the radius of the sample, η the viscosity, K_a the axial stiffness) [120]. The squeeze-flow delays the normal force signal by a time which scales linearly with t_a.

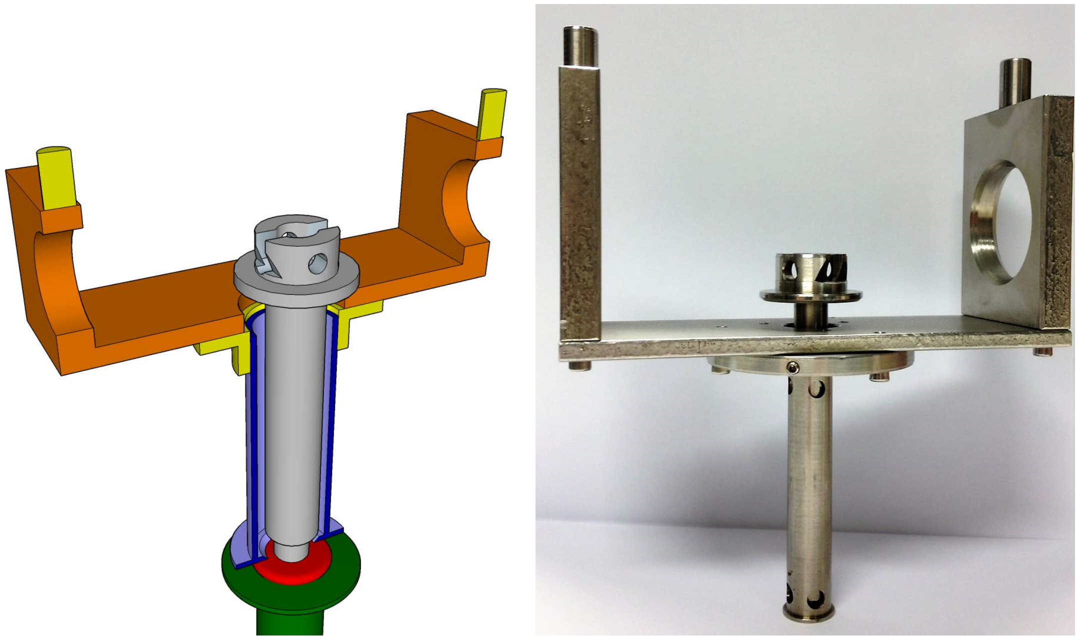
(a) (b)

Figure 3.4: a) Schematic of the CPP setup (green, bottom cone; red, sample; grey, inner shaft; blue, outer partition; orange, hollow bridge; yellow, translation stages). b) Photo of the homemade setup.

Therefore, the larger θ, the smaller is t_a, the smaller the delay of the normal force signal. On the other hand, larger cone implies larger gap at the edge of the sample.

Such a condition enhances edge fracture. The inner partition is a homemade stainless-steel parallel plate with a diameter of 6mm. The inner shaft is slender compared to standard tools for ARES rheometers. The reason for this choice is to provide enough space around the shaft to house the outer partition so that the geometry can fit into the ARES convection oven. The outer partition is a non-measuring ring with an inner diameter of 6.2 mm and an outer diameter of 15 mm. The outer partition is attached to a hollow bridge by means of a horizontal translation stage. The outer partition and the translation stage are fixed together with three screws. The translation stage is attached to the hollow bridge through three tap bolts. The holes into the translation stages are 0.5 mm larger than the diameter of the tap bolts. The tap bolts can be loosened so that the translation stage is free to translate on the plane parallel to the shaft direction. This serves to make the outer partition concentric with the shaft. After the outer partition is aligned concentrically with the shaft, the tap bolts are tightened to block translation. To help with the alignment process, the translation of the outer partition is guided by means of an outer corona with three screws that press around the stage (not shown in figure 3.4 for clarity). The hollow bridge possess two cylindrical attachments at the edge (yellow). These cylinders slide into the holes of the rheometer head and are fixed by means of through screws. In order to perform the alignment, we perform the following operations:

1. the inner shaft is mounted at the top while a parallel plate (with a diameter of 25-50 mm) is attached at the bottom.
2. the gap is zeroed.
3. the upper stage is raised to the top position and the bridge with the outer partition is inserted into the head.
4. the upper stage is brought back to the zero position and the hollow bridge is allowed for sliding down until it seats on the bottom plate together with the

inner shaft.

5. the hollow bridge is blocked into the upper stage.

6. the stage is raised and the translation stage on the hollow bridge is loosened and translated in order to achieve concentricity of the inner shaft and the outer partition. This operation is carried out with the help of a small mirror.

7. the translation stage is blocked and vertical alignment is re-checked by verifying the zero position of the whole geometry. If the zero is within 5 μm from the previous one, the alignment is accepted otherwise, the whole operation is repeated.

Once the geometry is mounted and aligned, the samples have to be centered on the bottom cone. Samples with a diameter $d = 8$ mm are generally prepared for an inner partition with $d = 6$ mm. Hence, there is the problem of properly centering a discotic specimen with $d = 8$ mm on a cone with $d = 25$ mm. This is done with the help of centering tools, as illustrated in figure 3.5.

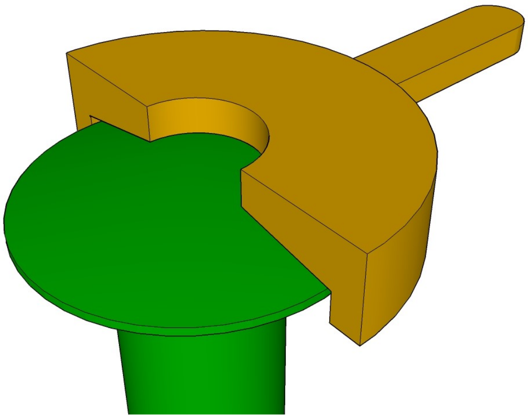

Figure 3.5: Schematic of centering tool for our CPP setup.

3.5 Validation of the homemade CPP

The homemade CPP setup described in section 3.4 was tested and compared with other geometries both in LVE and NLVE measurements. Figure 3.6 shows an example of such comparison.

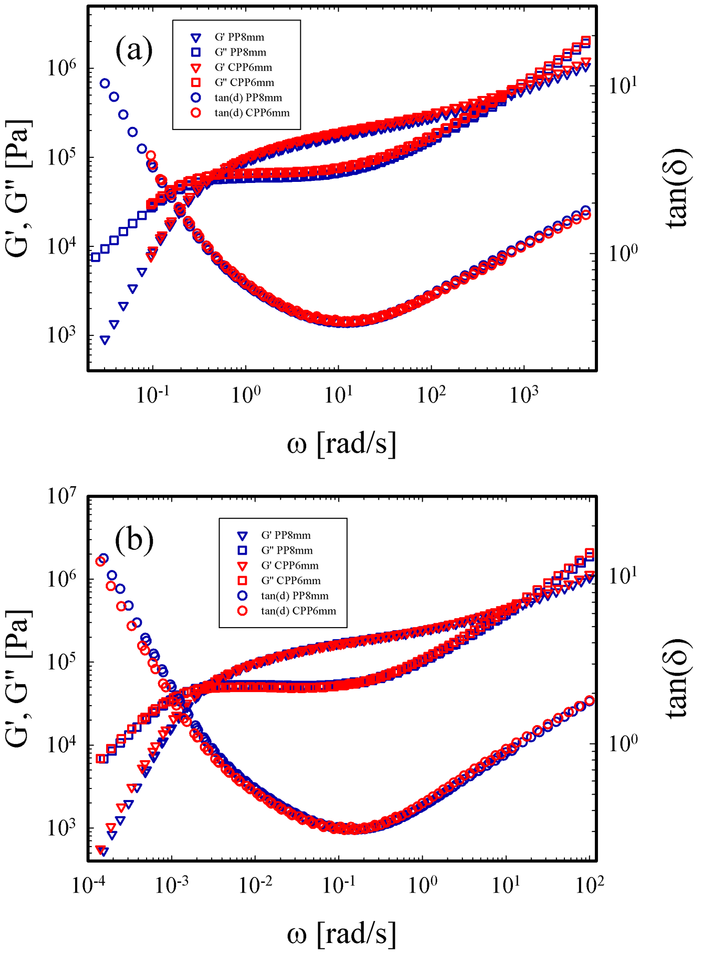

Figure 3.6: a) Mastercurves of PS133k at 150°C and b) Mastercurves of PS185k at 130°C

Figure 3.6.a shows the mastercurves of a polystyrene (PS) melt with M_w=133k at the reference temperature of 150°C while figure 3.6.b shows the mastercurves of a PS melt with M_w=185k at T_{ref}=130°C. In both cases, data displayed with blue symbols have been obtained with a standard parallel plate geometry with a diameter of 8mm (PP8) whereas the data displayed with red symbols have been collected by using our

homemade CPP geometry (CPP6). The excellent agreement between the datasets from the two geometries provides a convincing proof of the reliability of our CPP in the LVE regime. Small vertical discrepancies are due to slight overfilling of the CPP geometry: part of the sample unavoidably penetrates into the gap between the inner and the outer partition, creating extra friction which affects torque measurements. However, if the loading is performed correctly (by gradually squeezing the sample between the cone and plate, allowing it for relaxation while the proper gap value is attained), the amount of sample penetrating into the gap is minimal and its contribution to the torque negligible. In this respect, the loading should be discarded when linear data measured with the CPP are larger by 10% with respect to measurements with standard geometries. Minimal horizontal shifts can be attributed to slight differences in the thermal inertia of the two geometries. In order to prove the performance of our CPP in the NLVE regime, we tested it against the prototype of the commercial CPP from Anton Paar. Figure 3.7 shows the comparison between nonlinear measurements on PS71k obtained with our setup (grey symbols) and the CPP from Anton Paar (red symbols). Shear rates are indicated in the legend. The excellent agreement between NLVE data from two different setups mounted on two different rheometers confirms the reliability of our homemade setup in measuring viscosity in start-up shear. Discrepancies at early times are due to the fact that the Physica MCR702 is a stress controlled rheometer and requires more time to reach steady state of $\dot{\gamma}$ compared to ARES. In this regard, the use of the strain-controlled ARES rheometer constitutes an advantage because it allows to collect reliable data starting from shorter times with respect to the MCR702. Another disadvantage of the CPP for the MCR702, compared to our setup is the fact that the inner partition has a diameter of 8 mm, thus requiring larger quantities of sample. On the other hand, MCR702 has a maximum normal force load of 5 kg which, compared to the maximum load of the ARES (2 kg), allows for measuring larger normal stresses.

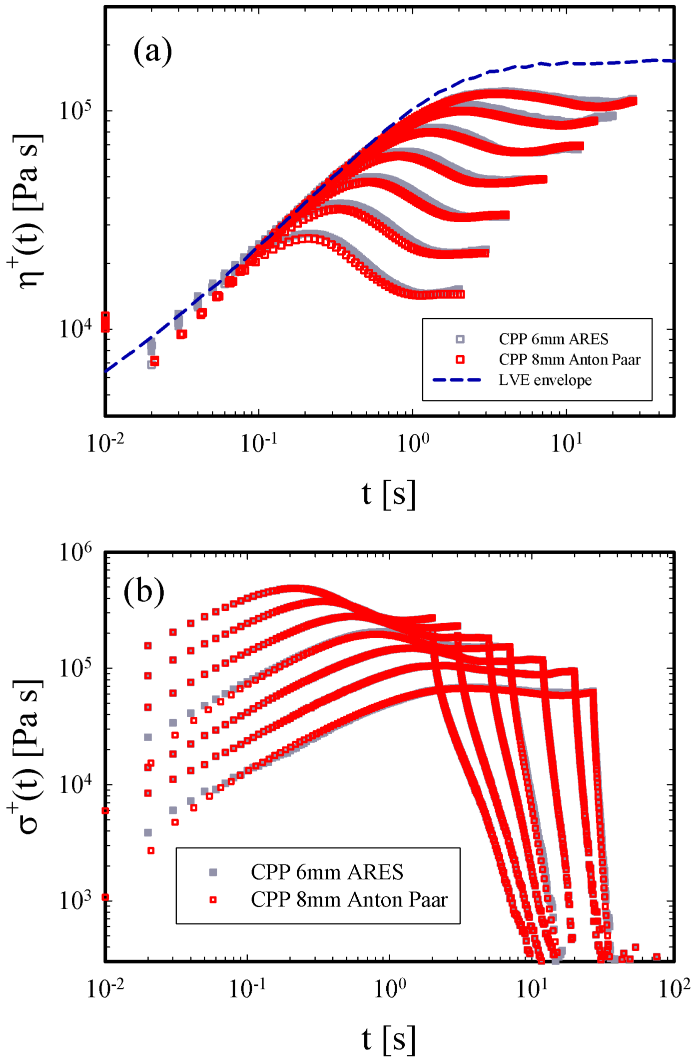

Figure 3.7: PS71k measured at 140°C; (a), transient viscosity; (b), transient stress (Shear rates from top to bottom $[s^{-1}] = 0.562, 1, 1.78, 3.16, 5.62, 10, 17.8$; grey symbols, homemade CPP; red symbols, commercial CPP from Anton Paar).

3.6 Measuring normal stress differences with two CPP partitions

Schweizer's CPP3 cell has limitations with temperature control. As mentioned before, the temperature cannot exceed 110°C and a long time is required for the equilibration of the whole cell (in the order of 3 hours at 80°C). Moreover, thermal gradients persist in the setup and in the sample even after the equilibration. On the other hand, such a cell has the advantage of direct measurement of normal stresses at two different radii of the sample in a single measurement. We did a modification of our homemade CPP setup in order to take advantage of the direct measurement of normal stresses at different radii while keeping good temperature control. Our CPP setup is modular: the inner shaft can be easily replaced as well as the outer partition (see photos in figure 3.8(bottom)). Therefore we made another inner shaft that has a 10 mm diameter and a corresponding outer partition with an inner diameter of 10.15 mm (CPP10). The outer partitions of CPP6 and CPP10 setups have the same outer diameter and they can be attached to the hollow bridge by means of the same translation stage. Such a setup is schematically depicted in figure 3.8(top). The setup with two partitions mimics the functioning principle of Schweizer's setup and it is based on the same equations (3.20-3.21). However, in order to get the two signals of $N_{app,1}$ and $N_{app,2}$ we need to run two measurements instead of one. The advantage is that the thermal control and stability is ensured from the convection oven of the ARES and measurements are accurate even at high temperatures. Disadvantages related to the particular instrument used (ARES) are the maximum normal force capacity (max. 2kg) and the noise of the signal of the normal force. This restricts detection of N_1 and N_2 to a narrow range of shear rates. The lower limit is set by shear rate values high enough to obtain clear signals of normal force. The upper limit is set by shear rates at which the apparent normal force reaches the peak of 2kg. In general, polymer systems with lower plateau

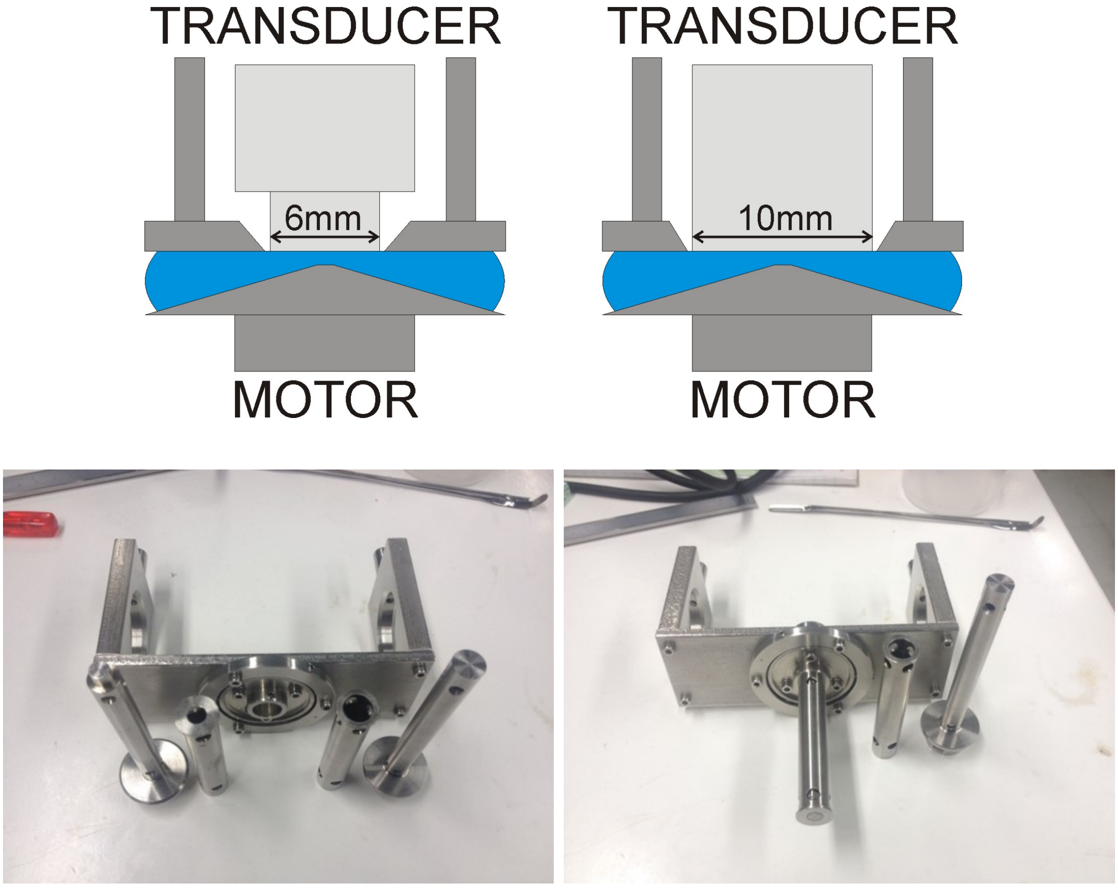

Figure 3.8: CPP with two partitions to measure N_1 and N_2.

of the elastic modulus, G_N^0 allow to reach higher shear rates before overloading the transducer. Therefore, we diluted high M_w polystyrene in oligostyrene in order to obtain two solutions with relatively low values of G_N^0. Nonlinear data on such systems are shown in the next section.

3.7 Normal stress differences of PS solutions

In order to test the performance of the CPP with two partitions in extracting viscometric function of polymers at high temperature, we prepared two polystyrene (PS) solutions by diluting high molecular weight PS in oligostyrene 2k (M_w=2 kDa). The first solution was prepared by diluting PS with M_w=200 kDa in oligostyrene 2k at 50% (w/w) therefore it is referred to as PS200k-2k-50. The second solution was prepared by diluting PS with M_w=545 kDa in oligostyrene at 30% (w/w). This solution is referred to as PS545k-2k-30. Details about the methods for the preparation of PS solutions are given in section 2.1.1 of the second chapter. Concentration values are such that a plateau modulus of 5×10^4 Pa for PS200k-2k-50 and 1×10^5 Pa for P545k-2k-30 is reached, according to theoretical predictions from tube model ($G_N^0(\varphi) = G_N^0(1)\varphi^{(1+\alpha)}$ where $G_N^0(\varphi)$ is the plateau modulus of the solution, $G_N^0(1)$ is the plateau modulus of the melt, and α is the dilution exponent, here assumed as equal to 1) [74, 75]. The choice of the values of $G_N^0(\varphi)$ is such that normal force overload should not be reached when $\dot{\gamma}$ approaches values corresponding to frequencies around the plateau region of G'. Figure 3.9 shows the LVE mastercurves of the two solutions at the reference temperature, $T_{ref} = 130$°C.

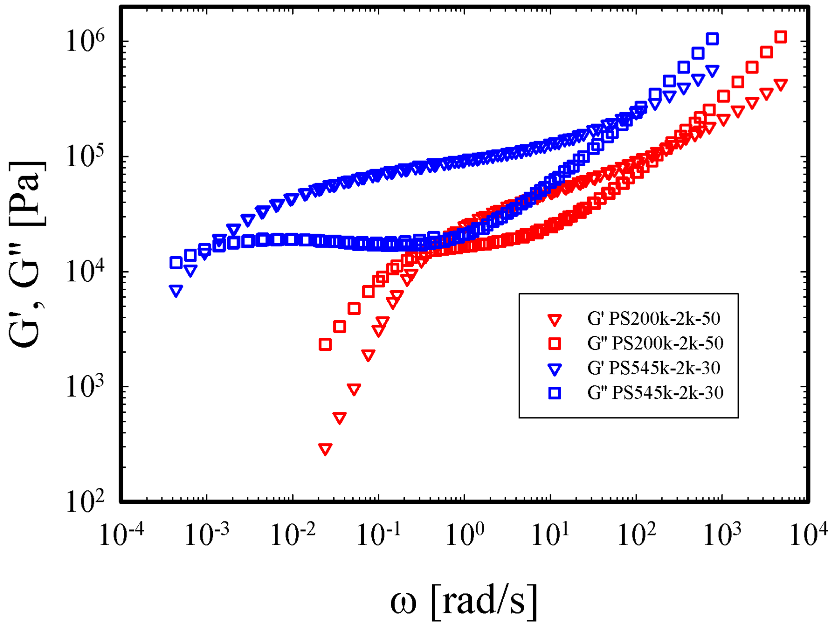

Figure 3.9: Mastercurves of PS200k-2k-50 and PS200k-2k-30 at T_{ref}=130°C.

The experimental plateau values of G' were similar to the expected ones within an error smaller than 10% (as mentioned before, this is the maximum accepted error for sample overfilling). Regarding nonlinear measurements, we prepared 10 samples for each solution by means of vacuum compression molding (details in chapter 3). The mass m of the samples was between 45mg and 47mg, so that the outer radius value R is equal to 6.04±0.05 mm , according to equation (3.19). After preparation we loaded the samples into the ARES rheometer equipped with the CPP and performed step rate tests at selected shear rates. Figure 3.10 shows start-up shear tests performed on the solution PS200k-2k-50 at different shear rates (indicated in the panels). Different samples were loaded for each shear rate and measurements were carried out with both CPP6 and CPP10.

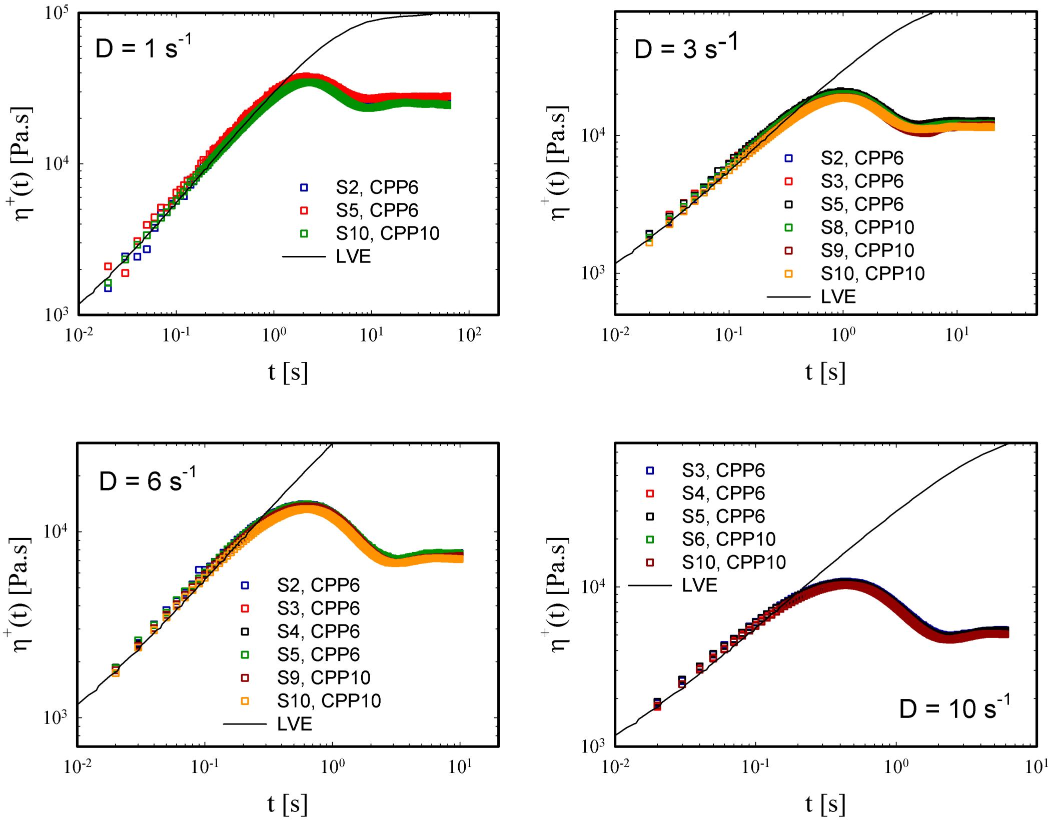

Figure 3.10: PS200k-2k-50 measured at 130°C. Shear rates as indicated in the panels.

From figure 3.10, we can observe the high reproducibility of the transient viscosity with the two different geometries. On the other hand the resulting apparent normal stress acting on the 6mm partition is different from that acting on the 10mm partition, as depicted in figure 3.11. Normal force signals in figure 3.11 are affected by noise and axial compliance. However, a neat separation between the steady state values of $N_{app,1}$

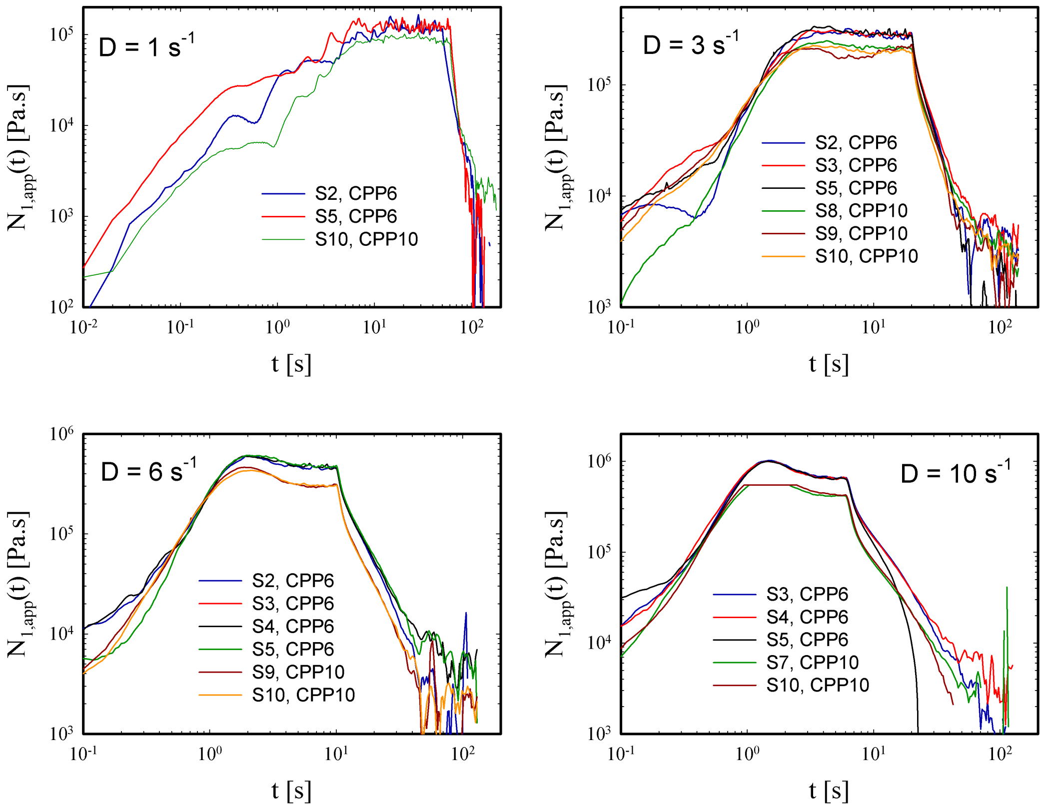

Figure 3.11: PS200k-2k-50 measured at 130°C. Shear rates as indicated in the panels.

with 6mm and $N_{app,2}$ with 10mm is clear. From the N_{app} signals we can therefore extract the steady state values of $N_{app,1}$ and $N_{app,2}$ and insert them in the equations (3.20)-(3.21), in order to obtain the steady state values of N_1 and N_2. From such values we can extract Ψ_1 and Ψ_2 dividing N_1 and N_2 by $\dot{\gamma}^2$, respectively. The viscometric functions η, Ψ_1 and Ψ_2 are reported for the two solutions in figure 3.12 along with the predictions for the transient viscosity and for Ψ_1.

The quantity $\eta(t)_{\mathrm{experimental}}$ was obtained by the complex viscosity from a combination of the Cox-Merz rule [22], $\eta(\dot{\gamma}) = \eta^*(\omega)|_{\omega=\dot{\gamma}}$ with the Gleissle rule [126], $\eta^+(t) = \eta(\dot{\gamma})|_{\dot{\gamma}=1/t}$. The quantities $\eta(t)_{RTS}$ and $\Psi_1(t)$ have been calculated from equations 2-3 of reference [33], namely:

$$\eta^0(t) = \sum_{i=1}^{n} \tau_i g_i \left(1 - \exp\left(-\frac{t}{\tau_i}\right)\right) \tag{3.22}$$

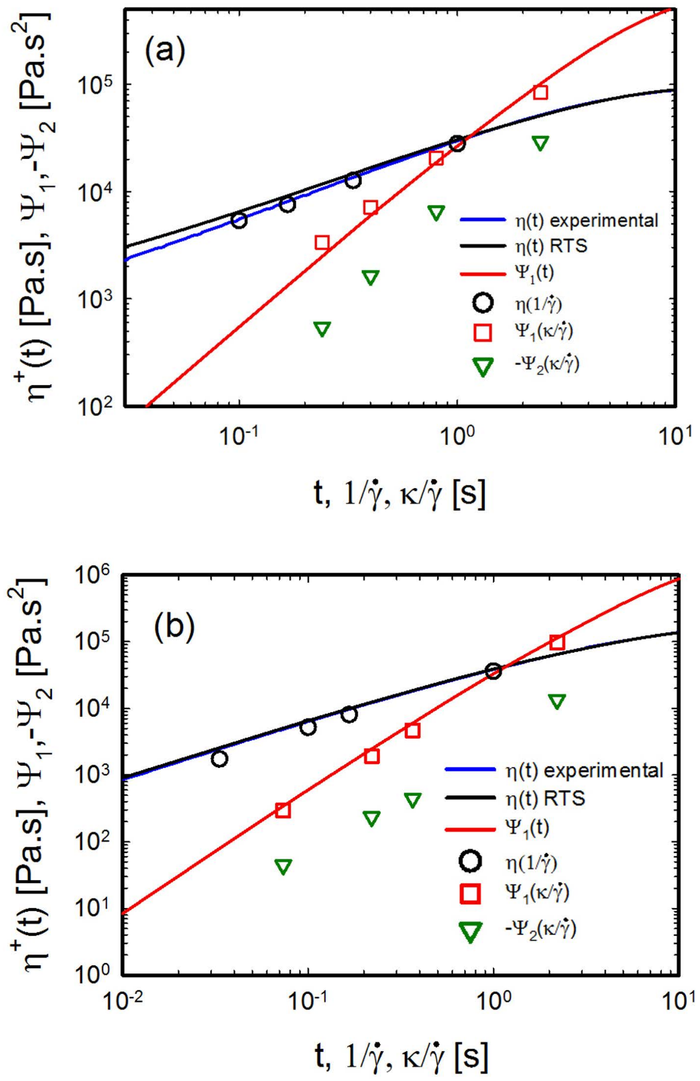

Figure 3.12: Viscometric steady-state functions for a) PS200k-2k-50 and b) PS545k-2k-30.

$$\Psi_1^0(t) = 2\sum_{i=1}^{n} \tau_i^2 g_i \left(1 - \left(1 + \frac{t}{\tau_i}\right) \exp\left(-\frac{t}{\tau_i}\right)\right) \tag{3.23}$$

The relaxation spectrum τ_i, G_i for such calculation was obtained by fitting the mastercurves with Maxwell modes through the software REPTATE. The results of the fit are reported in table 3.1. Figures 3.12(a) and 3.12(b) show a good agreement between the predicted values of Ψ_1 and the experimental ones. The predictions for N_2 are quite scattered but the value of the ratio $-N_2/N_1$ is comprised between 0.35 and 0.1 as reported from previous studies [124]. In order to demonstrate this, we report a super-

PS200k-2k-50		PS545k-2k-30	
τ_i [s]	G_i [Pa]	τ_i [s]	G_i [Pa]
3.20×10^1	3.43×10^2	5.97	2.39×10^4
3.64	2.17×10^4	6.91×10^{-1}	2.81×10^4
4.15×10^{-1}	2.29×10^4	7.99×10^{-2}	2.32×10^4
4.72×10^{-2}	2.81×10^4	9.25×10^{-3}	2.03×10^4
5.37×10^{-3}	7.98×10^4	1.07×10^{-3}	2.81×10^4
6.12×10^{-4}	1.39×10^5	1.24×10^{-4}	9.37×10^4
6.96×10^{-5}	3.67×10^6	1.43×10^{-5}	2.11×10^5
		1.66×10^{-6}	2.41×10^6
		1.92×10^{-7}	8.82×10^6

Table 3.1: Maxwell fit of the mastercurves in figure 3.9.

position of our data with those from reference [124] for polymer solutions of high M_w polystyrene (range of M_w between 200k and 2000k) in normal butylbenzene at fixed PS concentration of 0.45 (w/w) (figure 3.13). A fair agreement is found between our data with both solutions and those from Gao *et al.*

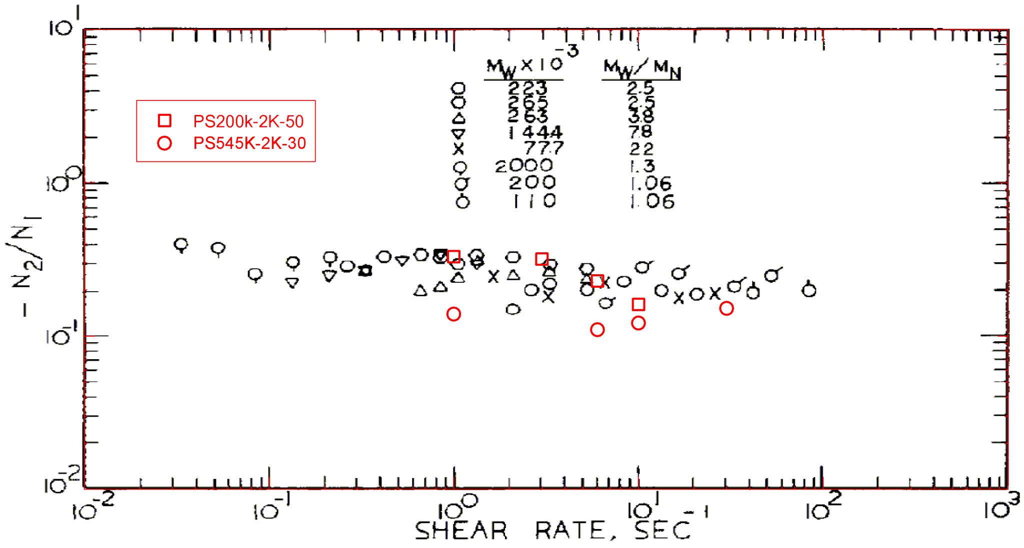

Figure 3.13: Comparison of the ratio $-N_2/N_1$ obtained with the two partitions with previous data from Gao et al. [124].

In general, the Doi-Edwards model predicts that the ratio $-N_2/N_1$ for concentrated polymer systems is equal to 2/7 in the zero-shear-rate limit whereas it decreases upon shear rate increase [127]. Several authors reported that $-N_2/N_1$ oscillates between

0.3 and 0.1 [117, 119, 124]. Particularly, Schweizer has reported shear thinning of $-N_2/N_1$ from 0.3 to 0.1 [119]. In general our data show good agreement with those from literature. Moreover, for the solution PS200k-2k-50, the shear thinning behavior is confirmed.

We also tried to measure the same sample reported by Schweizer [33], i.e., PDMS calibration fluid from TA Instruments (Order no. 700.01011), in the same range of shear rates. However, strong slip and overload of the ARES transducer hindered good measurements. Roughening the surfaces of our CPP would help to prevent slip, however the overload of the transducer cannot be avoided.

3.8 Concluding remarks

Rotational rheometry is an indispensable tool for measuring shear and normal stresses in polymeric systems. Indeed, from the equation of motion solved for CP geometry, one can extract the radial normal stress distribution from which it is possible to evaluate both N_1 and N_2. However, edge fracture instability in rotational shear flows is a serious issue hindering correct measurements of viscosity and normal stress differences. An effective method to overcome issues related to edge fracture is to use a CPP geometry. CPP geometry was pioneered by Pollet [30] and Meissner[31]. Since its first implementation, substantial progress has been made to carry out nonlinear shear tests in a reliable fashion. Moreover, Schweizer showed the possibility to extract N_1 and N_2 with CPP in a single measurement [33]. However, this setup is affected by experimental issues such as thermal stability. Building up on previous work on CPP rheometry, we implemented a new CPP setup for ARES rheometer to perform reliable viscosity measurements with small amount of samples and thermal stability at high temperatures. Moreover, within some limitations, Ψ_1 and Ψ_2 coefficients can be extracted both at room and high temperatures. Such a device allowed us to explore the nonlinear properties of a large variety of polymer systems. The results of this study are presented in the next chapters. The main outcome in using CPP geometry is reliable data on transient viscosity. In this regard, a single CPP would be sufficient. The possibility to detect N_1 and N_2 determines the difference between different CPP setups. The advantages and disadvantages of each setup in measuring normal stress differences are summarized in table 3.2.

Setup	Advantages	Disadvantages
Single CPP	• Good temperature control up to 230°C	• Multiple measurements to obtain N_1 and N_2 (more than 2 for each shear rate)
CPP3	• Possibility to detect η, N_1 and N_2 in a single measurement	• Not suitable for measurements above 110°C • Raw data require post-processing in order to remove signal noise
Two Single CPP with different radii	• Possibility to detect η, N_1 and N_2 in 2 measurements • Good temperature control up to 230°C	• More prone to error compared to a single measurement with CPP3

Table 3.2: Summary of the advantages and disadvantages of different CPP setups in measuring the viscometric functions N_1 and N_2.

Chapter 4

LINEAR AND RING POLYSTYRENE MELTS, SOLUTIONS AND BLENDS

4.1 Introduction

One of the most remarkable accomplishments in polymer physics has been the development of the tube model. Since its formulation (by Doi and Edwards [11]) the original model has been subjected to many refinements in order to provide realistic predictions of polymer dynamics. Concerning linear viscoelasticity of entangled linear polymers, in addition to reptation, other relaxation mechanisms were proposed in order to explain some distinctive features of their rheological behavior. For example, contour length fluctuations (CLF) explain the 3.4 (instead of 3) power-law dependence of the zero-shear viscosity on molecular weight[34], while thermal constraint release (CR) - or alternatively, dynamic dilution - explains the effects of polydispersity. [100, 128–130]. Finally, the contribution of longitudinal relaxation modes in the frequency region around the minimum of the loss modulus G'' can rationalize the 4/5 factor used in the plateau modulus expression $G_N^0 = (4/5)\rho RT/M_e$, where ρ is the density, R the gas constant, T the temperature, and M_e the entanglement molecular weight [131]. The great success of the tube model in predicting the linear viscoelasticity of entangled polymers (linear and branched) over a wide range of time-scales relies on the universal validity of the smoothed-out treatment of interchain interactions, which forces the chain to diffuse curvilinearly along an effective tube, as well as on the correct interpretation of chain-end dynamics. On the other hand, such model is not appropriate to predict the LVE of polymer systems with no chain ends, i.e. ring polymers. The lack of free-ends in ring polymers prohibits stress relaxation via CLF and reptation, even when M_w is large enough to form entanglements. For this reason additional models have been developed for rings, such as the lattice-animal and modified Rouse models [44, 45] in order to describe the key features of their rheological behavior. Stress relaxation in ring polymers is characterized by the absence of plateau of G' and a power-law decay at long times. Such decay has been attributed to threading of the ring chains by linear contaminants [41]. In this respect, the rheology of linear/ring blends is interesting insofar as their terminal relaxation time is in general longer than the pure linear and ring samples because of multiple linear/rings threading.

Nonlinear rheology of polymers is more challenging, both from theoretical and experimental standpoints. As far as linear polymers are concerned, the original Doi-Edwards model based primarily on segmental orientation in the flow direction, predicted excessive shear thinning leading to an unstable flow curve (shear stress vs shear rate). The problem was solved with the introduction of the concept of convective constraint release (CCR), which was shown to attenuate thinning [35]. In extensional flows, chain stretching is responsible for strain hardening, and finite chain extensibility must be accounted for [19]. These key advances, along with several other relevant improvements, have led to the development of constitutive models for the description of the flow of entangled polymeric liquids of any chemistry [37, 132]. The molecular parameters that control rheology of linear entangled polymers are the monomeric friction coefficient and the number of entanglements (Z), both affecting relaxation times. Hence, it is implied that solutions and melts of linear polymers will have the same rheology (in dimensionless coordinates) as long as they possess the same Z. However, recent experiments with linear polymer melts and solutions having the same Z have demonstrated that while these systems exhibit identical linear rheology, their nonlinear extensional behavior is drastically different [74–76]. In particular, PS melts subjected to fast extensional flows exhibit thinning behavior (i.e., the steady-state extensional viscosity decreases with increasing extensional rate), whereas in the same range of dimensionless extensional (stretch) rates (or Weissenberg numbers) the steady-state extensional viscosity curve of the PS solutions exhibits an upturn with increasing stretch rates. The tube model, properly modified with the introduction of chain stretch, correctly predicts the nonlinear extensional behavior of PS solutions but fails to describe that of PS melts [133, 134]. An important recent development that resolved the aboveobserved discrepancy is the concept of alignment-induced reduction of the (anisotropic) monomeric friction coefficient, which is particularly effective in melts [135–139]. For PS solutions in oligomeric solvents, the anisotropic friction leads to polymer-solvent nematic interactions [75, 76, 103]. However, the increased extensibility of a polymer chain upon dilution allows solutions to stretch to a larger extent compared to melts. Very recently, it was shown experimentally that in order to have the same linear and nonlinear extensional rheological behavior, two different polymeric systems should have the same number of entanglements Z, the same finite extensibility λ_{max}, and the same monomeric friction reduction ζ/ζ_0 where ζ is the actual value of the monomeric friction coefficient during flow and ζ_0 is the monomeric friction reduction at equilibrium [140]. An obvious question stemming from the above is whether the observed difference between polymer melts and solutions in extensional flow also occurs in shear flow. The vorticity component of the shear strain tensor is in fact expected to reduce chain orientation and stretch compared to the extensional flow case. Hence, monomer alignment is expected to be less effective, and the monomeric friction reduction reduced or even absent, as in fact shown by recent Brownian dynamics simulations [136]. On the other hand, the possible effects of vorticity have not been decoded. Additional recent molecular dynamics simulations [38, 141] have revealed that entangled molecules also experience tumbling in fast shear flows, similarly to what experimentally observed in single DNA through video fluorescence microscopy [142]. Therefore, it appears highly desirable to perform a systematic comparative study of nonlinear shear and extensional rheology of entangled polymers with the same Z, and this is one of the goals of the present chapter. In addition, other important questions stemming from the discussion above, are:(i) how does nonlinear rheology of ring polymers compare to their linear counterparts? (ii) What are the main characteristics of nonlinear rheological behavior of entropic polymer blends? We shall attempt at answering both questions restricting our investigation to nonlinear transient shear. Regarding the first question, ring polymers are less prone to deformation compared to linear ones therefore they should exhibit weaker dependence of viscosity upon shear rate also in the entangled regime. Nonlinear shear measurements on such systems have been hindered by the very small quantities available from synthesis.

Rheological measurements of fast shear flows of entangled polymers are extremely challenging because of the occurrence of flow instabilities at large values of the imposed shear rate $\dot{\gamma}$ (expressed in dimensionless form through the Weissenberg number $Wi = \dot{\gamma}\tau$ where τ is a characteristic relaxation time of the polymer). Such instabilities include wall slip, shear banding, and edge fracture. The latter phenomenon has been widely documented in the literature since the early work of Tanner and Keentok [29]. The most efficient method to reduce the effects of edge fracture in rheological shear measurements is the use of cone-partitioned-plate (CPP) geometry (described in chapter 2). We have made several improvements to the original design that allow us to perform better-controlled shear measurements and therefore reach larger values of Wi with very small quantities of material. The use of CPP also postpones the occurrence of wall slip due to the large normal force exerted on the sample. However, occurrence of wall slip and/or of shear banding cannot be completely excluded (as discussed below). In this work, we provide a unique combined extensional and shear rheological data set on two pairs of entangled polymeric systems, each made up of a PS melt and of a PS solution with the same number of entanglements (a pair with $Z \approx 10$ and another pair with $Z \approx 14$). Moreover, we present the main features of nonlinear shear rheology of two PS ring melts and two linear/ring blends of same molar mass. Details on the preparation of PS solutions as well as the synthesis of ring PS are given in the sections 2.1.1 and 2.1.2, respectively. Concerning linear PS, we show that unlike uniaxial extensional flows, the difference between melts and solutions at large values of Wi ($Wi \geq 10$, based on the Rouse relaxation time τ_R) is not detectable in shear flows. The experimental data collapse into master curves, and we extract the respective scaling laws. Concerning ring PS we show that pure ring melts are characterized by a weaker shear thinning behavior(i.e., steady-state viscosity, normalized peak-viscosity). On the other hand, we demonstrate that linear/ring blends possess the rheological characteristics of linear entangled systems. Limited to entangled linear PS melts and solutions, we rationalize the experimental findings by using a tube-based model with two main ingredients: tumbling (which is important for shear) and alignment-induced friction reduction (which is important for extension). Modeling of the nonlinear rheology of rings is beyond the scope of the present thesis.

4.2 Experimental results on linear PS melts and solutions

4.2.1 Linear viscoelasticity

The LVE master curves of the samples were first fitted with the empirical Baumgaertel-Schausberger-Winter (BSW) relaxation model [74, 143]. The BSW model divides the relaxation spectrum into a viscoelastic part and a glassy part and has three parameters: G_N^0, τ_c and τ_m. The parameter τ_m has a value approximately equal to the terminal relaxation time of the system, while τ_c has a value approximately equal to the relaxation time of the subchain between consecutive entanglements. The difference in both cases is by a factor of order unity. The parameter G_N^0 is the entanglement (rubbery) plateau modulus of the system. The parameters obtained from the model are listed in table4.1

samples	T [°C]	n_e	n_g	G_N^0 [Pa]
PS133k	160	0.23	0.7	2.79×10^5
PS185k	160	0.23	0.7	2.58×10^5
PS285k/2k-47	140	0.23	0.7	0.58×10^5
PS285k/2k-65	150	0.23	0.7	1.035×10^5
	τ_c [s]	τ_m [s]	τ_R [s]	η_0 [Pa·s]
PS133k	1.24×10^{-3}	1.66	0.124	0.89×10^5
PS185k	1.4×10^{-3}	5.10	0.271	2.48×10^5
PS285k/2k-47	3.42×10^{-3}	4.51	0.342	0.50×10^5
PS285k/2k-65	1.65×10^{-3}	5.32	0.319	1.04×10^5

Table 4.1: material properties of the samples obtained from the BSW fitting

Figure 4.1 depicts the LVE master curves of the samples together with the BSW model predictions. The master curves of the solutions have been shifted vertically (each by a factor of 10, see caption for clarity). As already demonstrated in previous works [76, 140]. having the same Z is a sufficient condition for exhibiting identical LVE response (in dimensionless coordinates). Hence, when the dynamic moduli are normalized by the entanglement plateau modulus, and the frequency by a characteristic time (here τ_c), the master curves of polymer melts and solutions with the same Z should collapse, as indeed confirmed in figure 4.2. The excellent agreement also constitutes a strong indirect proof of the quality of the data and of the prepared specimens.

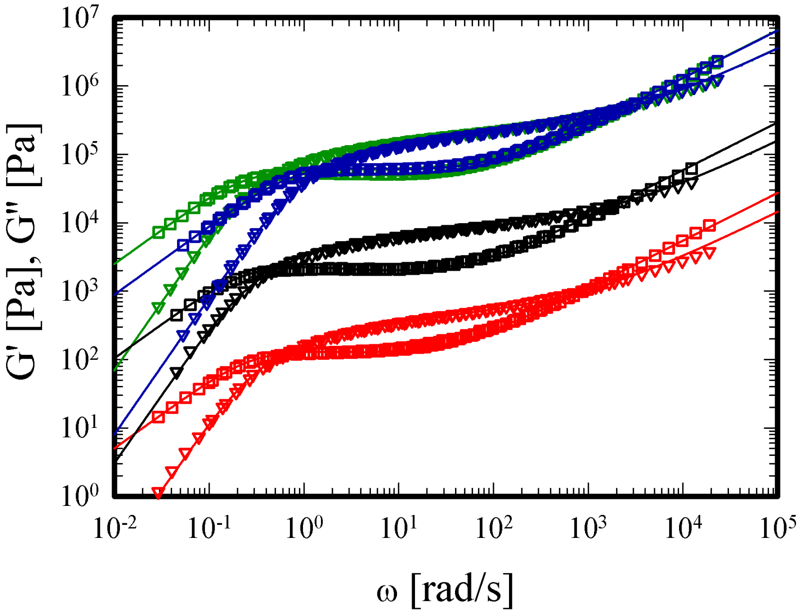

Figure 4.1: Linear viscoelastic mastercurves of PS melts and solutions along with the BSW predictions (lines). For all the sampels, G' ∇, G'' □ . PS185k at 160°C, green; PS133k at160°C, blue; PS285k/2k-65 at 150°C, black (moduli multiplied by 10^{-1}); PS285k/2k-47 at 140°C, red (moduli multiplied by 10^{-2}).

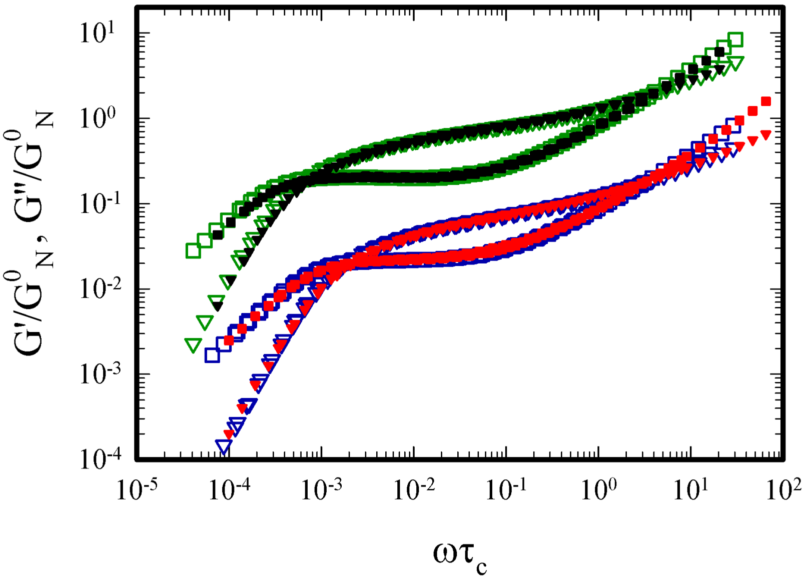

Figure 4.2: Normalized mastercurves of polystyrene melts ans solutions. PS185k, green: ∇, G'; □, G''. PS133k, blue (data shifted for clarity: ∇, $G' \times 10^{-1}$; □, $G'' \times 10^{-1}$. PS285k/2k-65, black: ▼, G'; ■, G''. PS285k/2k-47, red (data are shifted for clarity): ▼, $G' \times 10^{-1}$; ■, $G'' \times 10^{-1}$.

4.2.2 Uniaxial extension

Extensional measurements were carried out by Dr. Huang at the Technical University of Denmark (DTU) We carried out nonlinear extensional measurements with both linear PS melts and the corresponding solutions with the same number of entanglements and compared the respective results. Figure 4.3 shows an example of nonlinear transient viscosity measurements with the PS melt of $M_w = 133$k and the PS solution PS285k-2k-47. By focusing on the quasi-steady values of elongational viscosity, we observe the characteristic extensional thinning behavior of the melt, i.e. the steady-state extensional viscosity decreases as the extensional strain rate, $\dot{\varepsilon}$ increases. Conversely, the PS solution exhibits opposite behavior, i.e. the steady state values of extensional viscosity increase with $\dot{\varepsilon}$. Figure 4.4 depicts the normalized steady state extensional viscosity as a function of the Rouse-Weissenberg number ($Wi_R = \dot{\gamma}\tau_R$) for PS133k and PS185k and for the corresponding solutions.

When Wi_R exceeds unity, there is a clear separation between the extensional viscosity of solutions and melts with the same Z. This trend is attributed to Kuhn segment orientation due to significant chain stretch in extensional flow, which is not observed in shear flows.

4.2.3 Simple shear

The samples investigated in uniaxial extension were comparatively tested in nonlinear shear. With the use of the CPP geometry described in chapter 2 we were able to obtain reliable shear flow data for both PS melts and solutions at relatively high shear rates. Figure 4.5 depicts an example of shear startup data for the PS133k melt and the PS285k/2k-47 solution. Remarkably, at very high rates, the viscosity overshoot is followed by an unambiguous undershoot and eventually steady state. This feature is more evident in the solution than in the melt. We note that undershoots have been

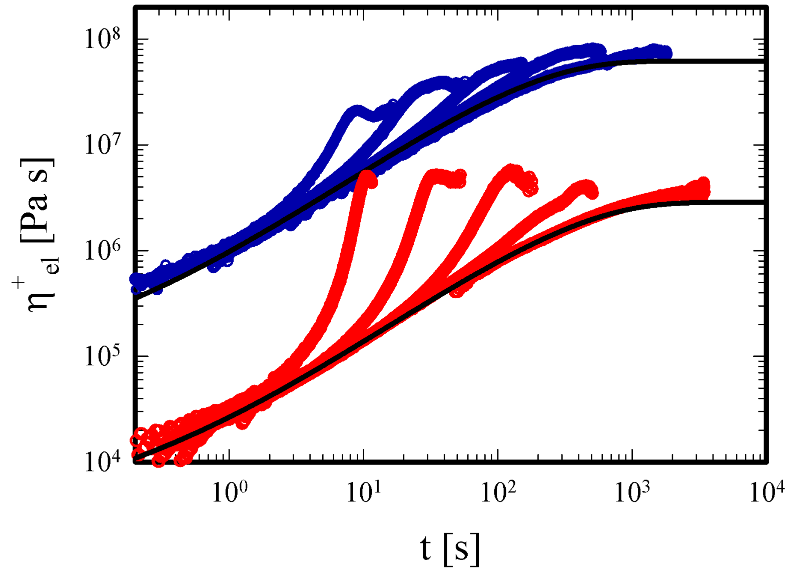

Figure 4.3: Extensional stress growth coefficient as a function of time at different stretch rates for PS133k (blue symbols; stretch rates: 0.3, 0.1, 0.03, 0.01 and 0.003 s^{-1} from left to right) and PS285k/2k-47 (red symbols; stretch rates: 0.3, 0.1, 0.03, 0.01 and 0.001 s^{-1} from left to right). Black lines are the LVE envelopes from the BSW spectrum. For clarity, the extensional data of the solution have been downshifted by one decade.

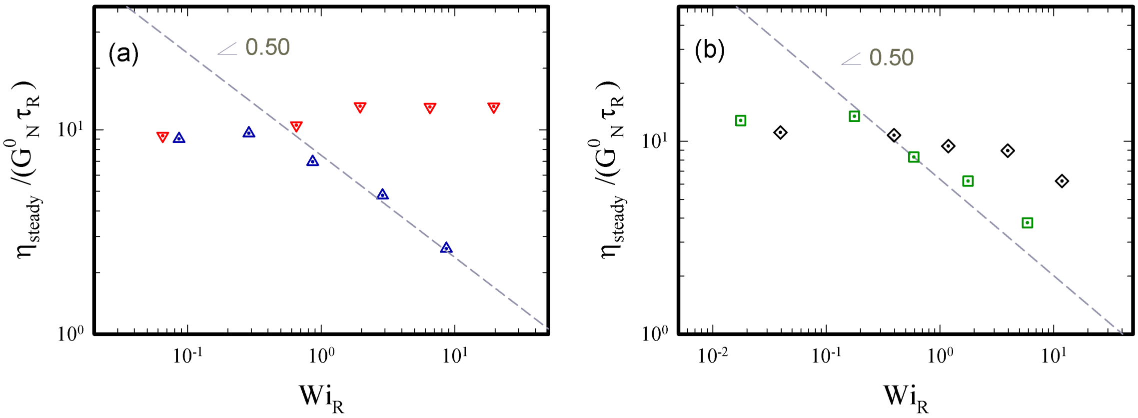

Figure 4.4: Comparison of the normalized steady state extensional viscosities as a function of the Rouse-Weissenberg number for (a) PS133k (blue) and PS285k/2k-47 (red) and for (b) PS185k (green) and PS285k/2k-65 (black). The slopes of the dashed lines are -0.5.

observed before with both linear[144] and branched[145] but the explanation of their physical origin remains elusive. The data in figure 4.5, as well as the data for the other two samples, are compared with model predictions in the modeling section.

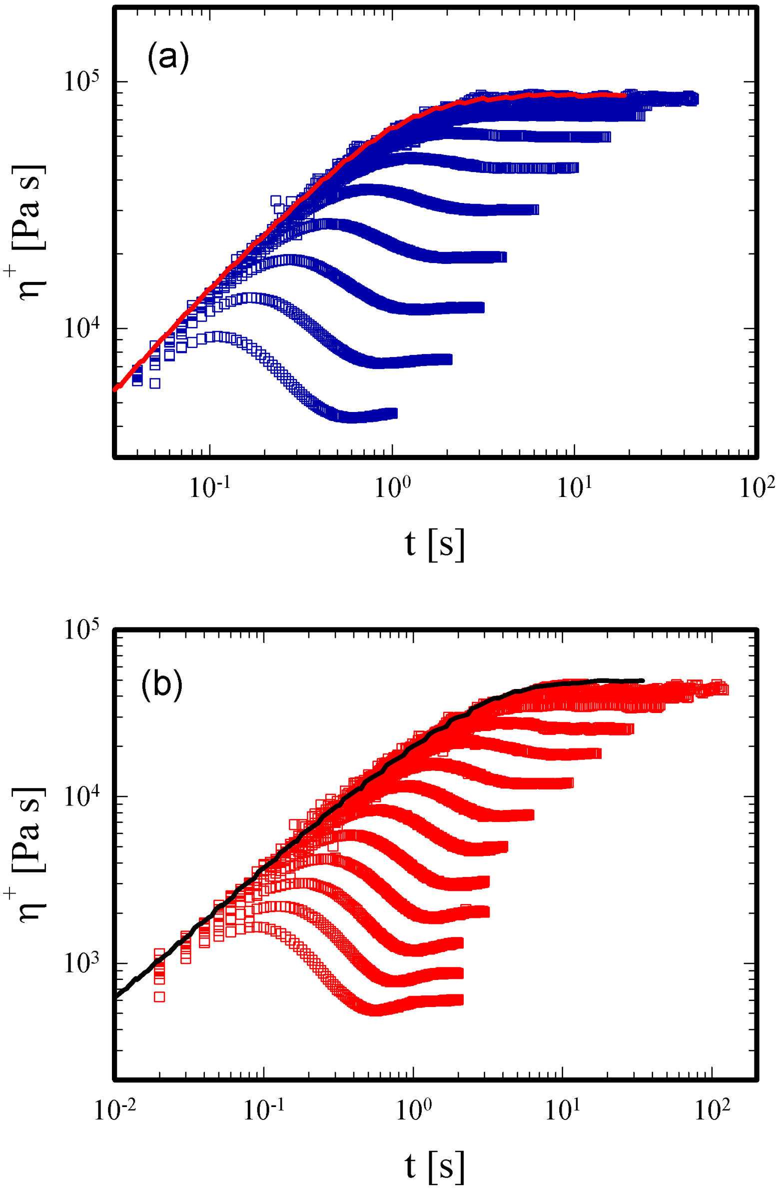

Figure 4.5: Transient shear viscosity at different shear rates for PS133k (panel a, blue symbols; shear rates are 0.1, 0.178, 0.316, 0.562, 1, 1.78, 3.16, 5.62, 10, 17.8 and 31.6 s^{-1} from top to bottom) and PS285k/2k-47 (panel b, red symbols; shear rates: 0.1, 0.178, 0.316, 0.562, 1, 1.78, 3.16, 5.62, 17.8, 31.6, 56.2, and 100 s^{-1} from top to bottom). Red and black lines are the LVE elvelopes obtained from Cox-Merz [22] and Gleissle [126] rules (see chapters 1 and 3).

Figure 4.6 shows data from figure 4.5 in dimensionless form in order to compare melt and solution behavior in simple shear flow at the same value of $Z = 10$. Given the fact that the experimental Weissenberg numbers are not strictly identical, and also considering experimental uncertainties, we can safely conclude that in shear flows there is no appreciable difference between melts and solutions with the same Z.

The steady-state shear viscosities, normalized with respect to the dynamic zero-shear viscosity, i.e., the product $G_N^0 \tau_m$ (see table 4.1 for the values of τ_m), exhibit a universal dependence on $Wi_m = \dot{\gamma}\tau_m$, as shown in 4.7. This should be expected since the viscosity is controlled by the long-time viscoelastic behavior, characterized in the BSW model by the terminal relaxation time τ_m. The slope of the high-shear-rate power law is -0.82, consistent with earlier reports on shear thinning polymers.[33, 91, 119] The strain γ_{max} at the viscosity peak of the start-up curves for all systems is plotted against Wi_R in figure 4.8. We observe that for $Wi_R < 1$ the value of γ_{max} is virtually constant (≈ 2.3), consistent with the Doi-Edwards prediction of tube orientation, in the absence

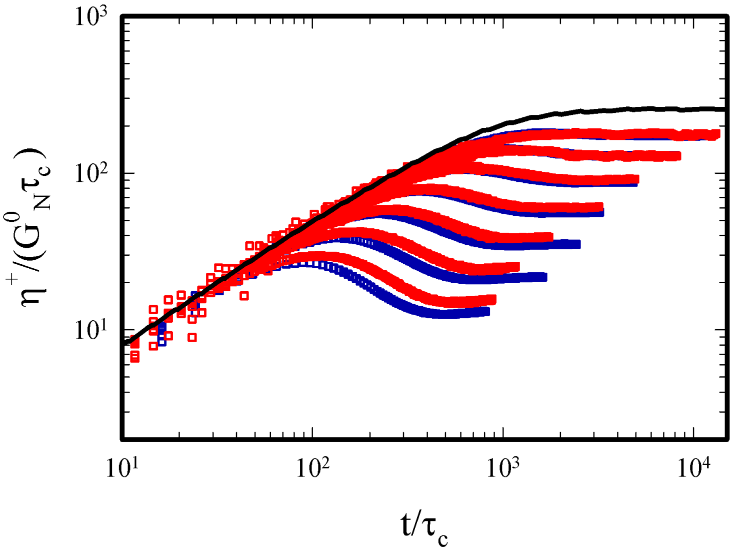

Figure 4.6: Normalized transient shear viscosity of PS133k and PS285k/2k-47 for several Rouse-Weissenberg numbers, Wi_R. PS133k, blue symbols: $Wi_R = 0.124$, 0.220, 0.391, 0.694, 1.24, 2.20, and 3.91 from top to bottom; PS285k/2k-47, red symbols: $Wi_R = 0.108$, 0.192, 0.342, 0.609, 1.08, 1.92, and 3.42 from top to bottom. Black line is the LVE envelope.

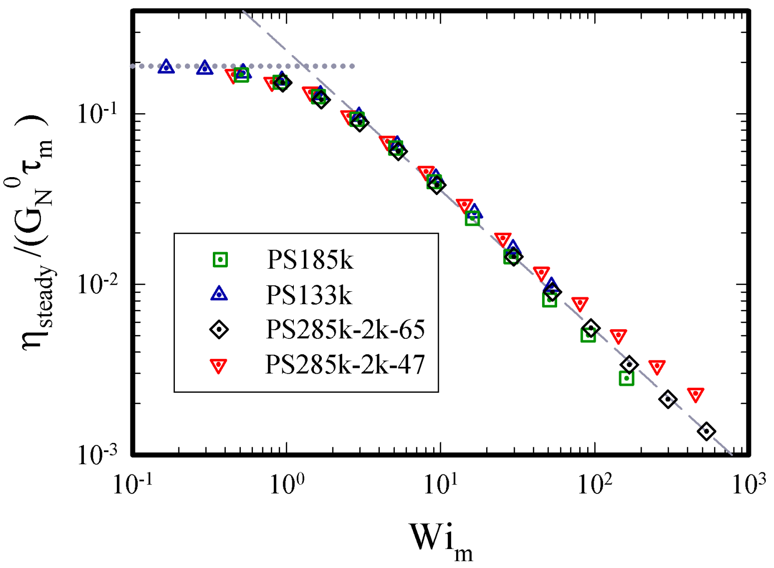

Figure 4.7: Comparison of the normalized steady-state viscosities as a function of the Weissenberg number based on terminal time, $Wi_m = \dot{\gamma}\tau_m$, for PS133k (blue), PS285k/2k-47 (red), PS185k (green), and PS285k/2k-65 (black). The dotted horizontal line marks the zero shear viscosity. The slope of the dashed line is -0.82.

of chain stretch[11]. For faster flows, i.e. for $Wi_R > 1$, γ_{max} increases because of chain stretch. For both melts and solutions the scaling law exhibits an exponent of 0.33. The latter value is consistent with the observation from a group of linear polymers [33, 119] but still lower than the slope of 1 predicted by the GLaMM theory [37]. Recently, Schweizer predicted a slope of 0.33 for entangled polymers at $Wi_R > 1$ by invoking that chain retraction requires a minimum internal force to happen and correlates with the overshoot strain [146].

The recovery after the overshoot can be highlighted by plotting in figure 4.9 the ratio of the peak viscosity η_{max} to the steady-state viscosity η_{steady} as a function of the Rouse-Weissenberg number. Such a ratio is essentially the same for all four systems and is seen to increase with increasing Wi_R, but only slightly, namely with a weak power law of 0.20. Figure 4.10 shows an example of stress relaxation data upon shear flow cessation for the PS133k melt. Stress relaxation data for all systems are reported in the modeling section for comparison with model predictions. For completeness, we depict

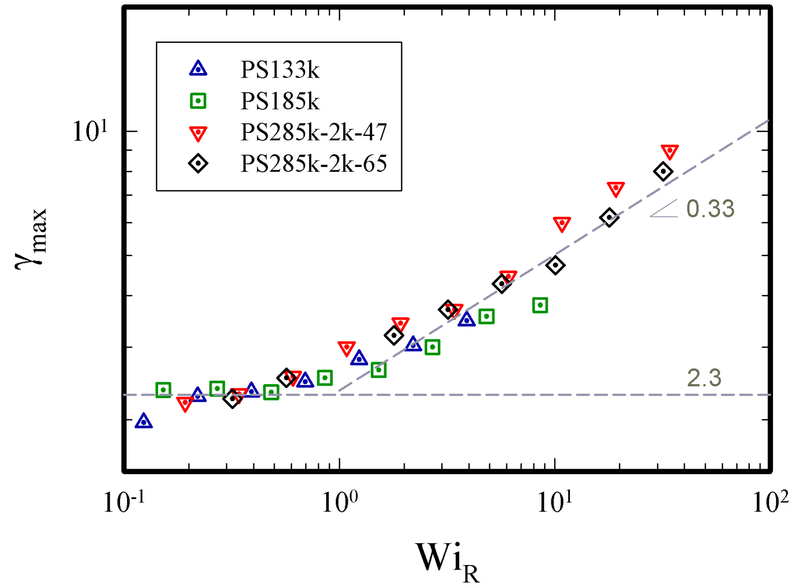

Figure 4.8: values of the strain at the viscosity peak as functions of the Rouse-Weissenberg number for PS185k (green), PS285k/2k-65 (black), PS133k (blue), and PS285k/2k-47 (red). Dashed lines are drawn to guide the eye.

in figure 4.11 typical data of the transient apparent first normal stress idfference $N_{1,app}$, for one of the PS solutions. We could obtain clear $N_{1,app}$ data only for the two solutions and only at thigh shear rates due to limitations of the normal force transducer. The apparent normal force $N_{1,app}$, results from a linear combination of the true first and second normal stress differences, N_1 and N_2, respectively, according to [31]

$$N_{1,app} = \frac{2F_i}{\pi R_i^2} = N_1 + 2(N_1 + 2N_2)\ln\left(\frac{R}{R_i}\right) \tag{4.1}$$

In our experiments, the ratio between the outer radius of the samples (R) and the radius of the inner partition ($R_i = 6$ mm) does not exceed the value of 1.5. This observation along with the assumption that N_2 is usually very small compared to N_1 [19], leads to a vertical error which can be up to a factor of 2. Hence, the measured $N_{1,app}$ values are larger than the true N_1. However, the qualitative behavior of normal stress is correct. Regarding the horizontal error, due to axial compliance effects, the

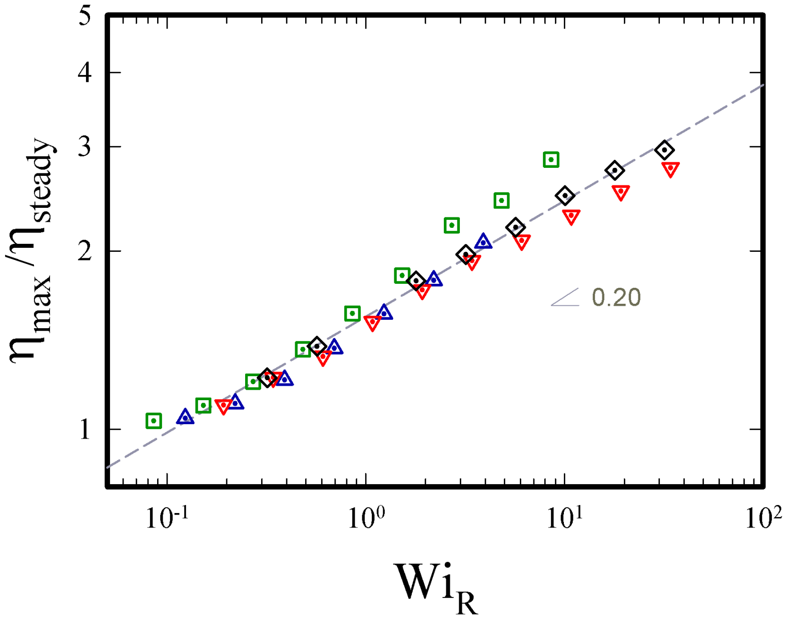

Figure 4.9: Values of the peak viscosity normalized to the steady shear viscosity as a function of the Weissenberg number based on Rouse time for PS133k (blue), PS285k/2k-47 (red), PS185k (green), and PS285k/ 2k-65 (black). The slope of the dashed line is 0.20.

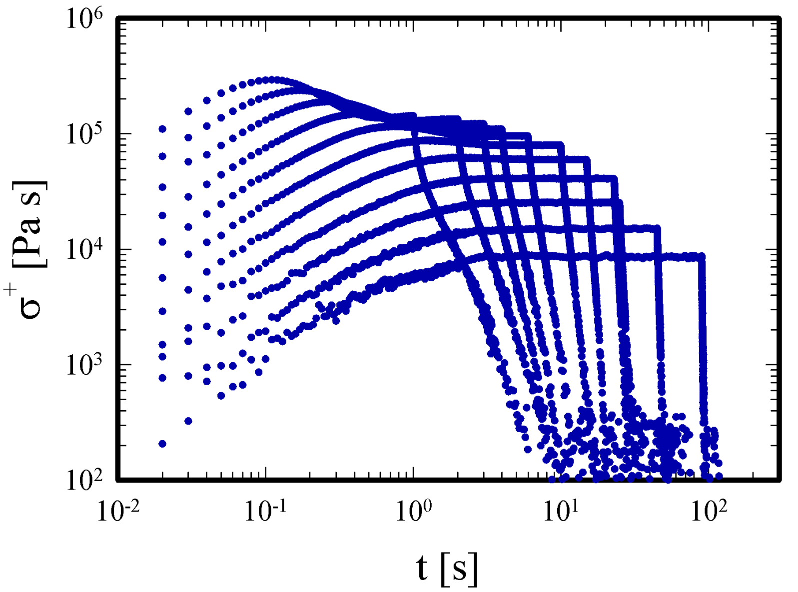

Figure 4.10: Stress relaxation upon cessation of simple shear flow for the PS133k melt. Shear rates during startup are 0.1, 0.178, 0.316, 0.562, 1, 1.78, 3.16, 5.62, 10, 17.8, and 31.6 s^{-1} from bottom to top.

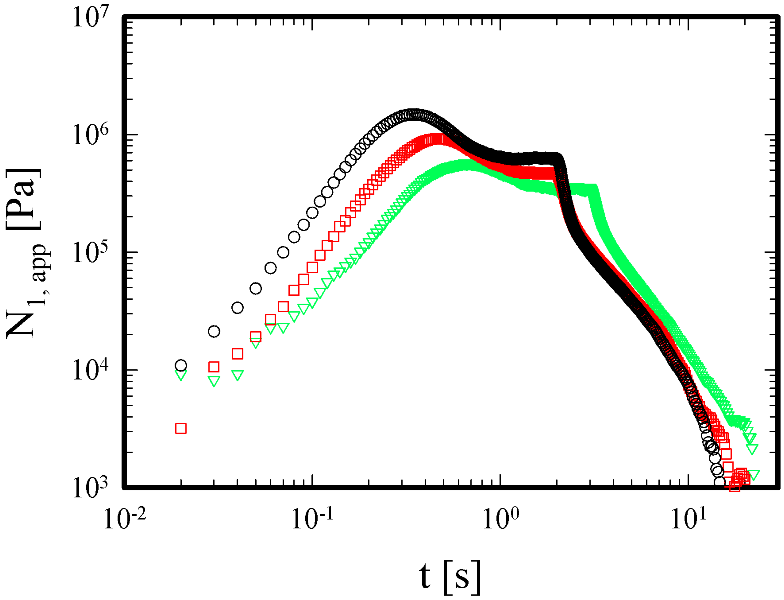

Figure 4.11: Transient apparent first normal stress difference as a function of time for PS285k/2k-47 (shea rates in s^{-1} are 17.8 (green), 31.6 (red), and 56.2 (black)).

$N_{1,app}$ curves are delayed with respect to the transient shear viscosity data.

4.3 Experimental results on ring PS melts and their blends with linear PS

In this section we present experimental results on nonlinear rheology of ring polymers. The master curves of the dynamic moduli as a function of shifted frequency for the PS ring polymers, their linear precursors, and their blends with linear chains are shown in Figure 4.12 at the reference temperature of T_{ref} = 150°C. The linear PS185k and PS84k exhibit a clear entanglement plateau. On the other hand, the ring polymers with same M_w exhibit power-law dynamics and a shorter relaxation time. We note also that the terminal slopes are virtually reached for PS84k, while this is not observed for PS185k and rings of high molar mass in general [41, 43, 147]. This complies with the suggestion that the slow mode in ring relaxation is primarily attributed to unlinked linear contaminants and ring-ring interpenetration (not resolved by LCCC), whose fraction is even less significant at lower molar mass (due to higher linking probability in the reaction process) [147]. These features are consistent with the previous findings [41, 43]. The rheological master curve of the mixtures ring/linear PS84k with ϕ_L =85% (ϕ_L being the fraction of linear component) and PS185k with ϕ_L =75%, virtually overlap with the respective linear counterparts at frequencies higher than the terminal $G' - G''$ crossover, ω_c. On the other hand, below ω_c, the mixture exhibits a broadening of the terminal region and hence a higher viscosity. This reflects the threading of the rings by the linear chains, widely reported in experimental and simulation works in the literature [148–151].

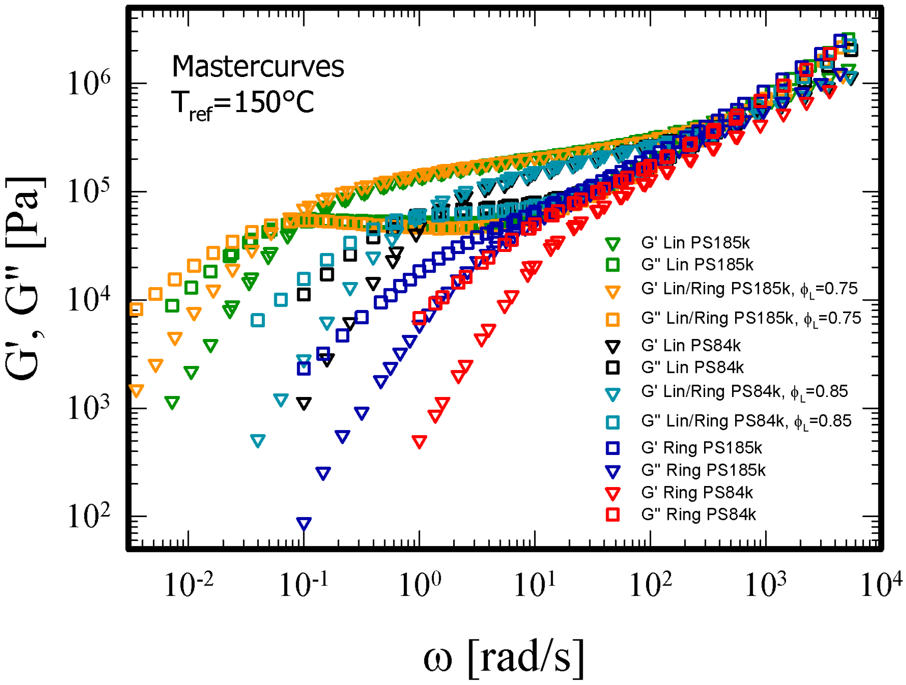

Figure 4.12: LVE mastercurves of ring polystyrenes along with the linear precursors and solutions.

The transient shear viscosity η^+ as a function of time t for different imposed shear rates $\dot{\gamma}$ (indicated with symbol D in the legends) at 150°C is depicted in Figure 4.13 for ring PS-185k and the respective mixture ring/linear with ϕ_L =0.75. Similar data have been collected for ring PS84k and its mixture with linear and are shown in reference [46]. The linear viscoelastic (LVE) envelope lines are shown as well (red lines) to confirm data consistency. The respective lines are calculated by direct transformation of the dynamic mastercurves according to the empirical Cox-Merz rule [22] in conjunction with the Gleissle rule [126] (see chapters 1 and 3). Beyond the start-up time of the motor, the nonlinear data collapse on the LVE envelope at low times or strains. A deviation of transient viscosity from LVE envelope was observed with increasing shear rate and time. After an overshoot, the transient viscosity reaches its steady-state value. Visual comparison of Figures 4.13.a and 4.13.b, in particular at the highest shear rates which are comparable, indicates the linear PS has more prominent overshoot than the ring PS. Since the overshoot reflects the maximum flow-induced deformation of the polymer, this qualitative observation already implies that the rings experience less deformation than its linear precursors in simple shear flows. This is consistent with the recent experimental observations of Schroeder and co-workers on single DNA ring extension, which is reduced compared to linear DNA [152]. However, we note that this analogy is only offered on a qualitative basis in order to emphasize the smaller deformation of rings compared to their linear analogues; it is important to keep in mind that the single DNA of ref [152] is a very different problem from the present melt of PS rings. On the other hand, the ring-linear blends exhibit a transient shear response which is quantitatively very similar to that of linear polystyrenes. Given the fact that even small fractions of linear chains alter the viscoelastic nature of the ring via formation of an effective network [41, 151] this result is not surprising.

Several nonlinear rheological parameters, extracted from the nonlinear data on ring polymers and mixtures with linear, can be used in order to further analyze the data. The normalized steady-state shear viscosities (to the zero-shear value) η_{steady}/η_0, the relative peak (maximum) viscosities with respect to the steady state value η_{max}/η_{steady}, and the strains at the peak viscosities, γ_{max}, represent measures of chain deformation in shear flow and are plotted in figures 4.14, 4.15 and 4.16 against the normalized shear rate (Weissenberg number), respectively. The Weissenberg number is defined as

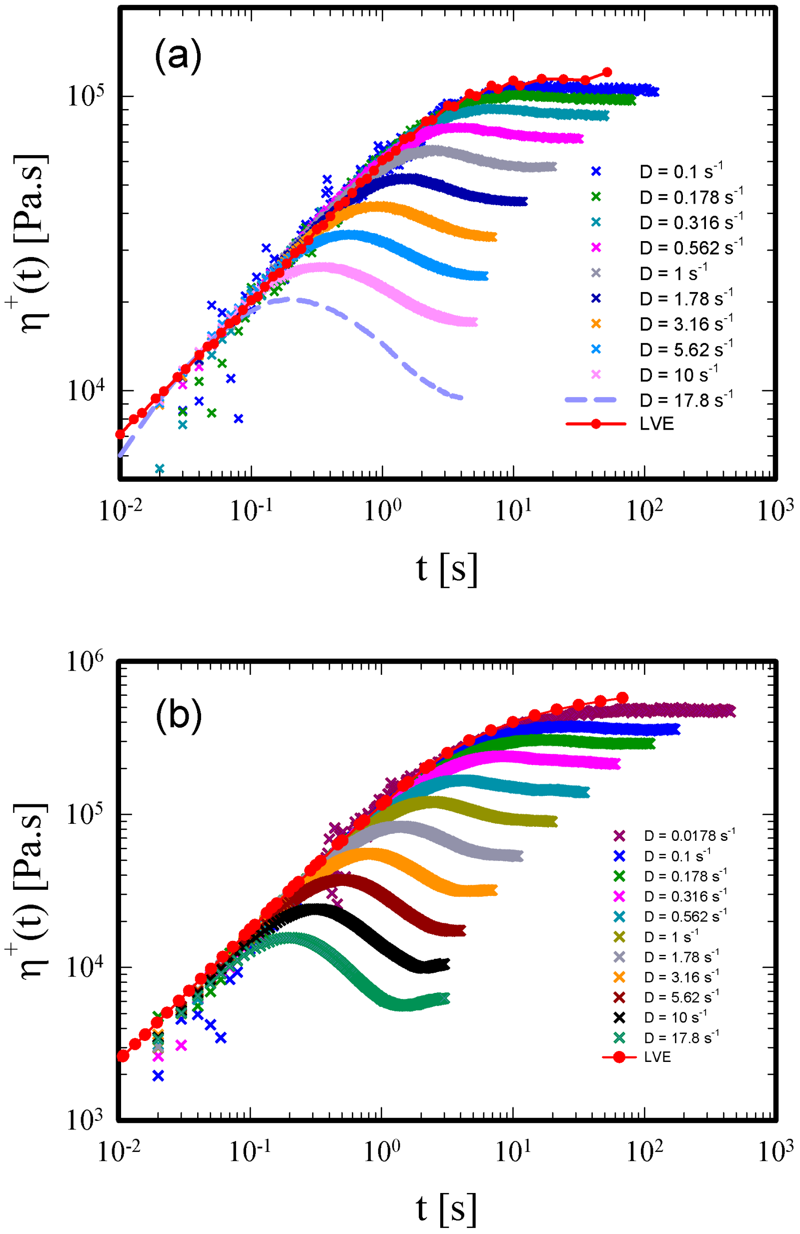

Figure 4.13: Nonlinear start up shear on ring PS185k (panel a) and ring/linear PS185k blend at $\phi_L = 0.75$ (panel b). Shear rates are indicated in the respective legends.

$Wi = \dot{\gamma}\tau_D$, with τ_D being the terminal relaxation time, determined by the inverse of the intersection of the extrapolation of the limiting power laws of $G' \propto \omega^2$ and $G'' \propto \omega$ [1]. Note that the determination of τ_D is the main source of the horizontal errors in determining Wi_D for ring polymers. In figure 4.14 LVE envelopes transformed from the linear oscillatory data as a function of the respective Deborah number $De_0 = \omega\tau_D$ are plotted.

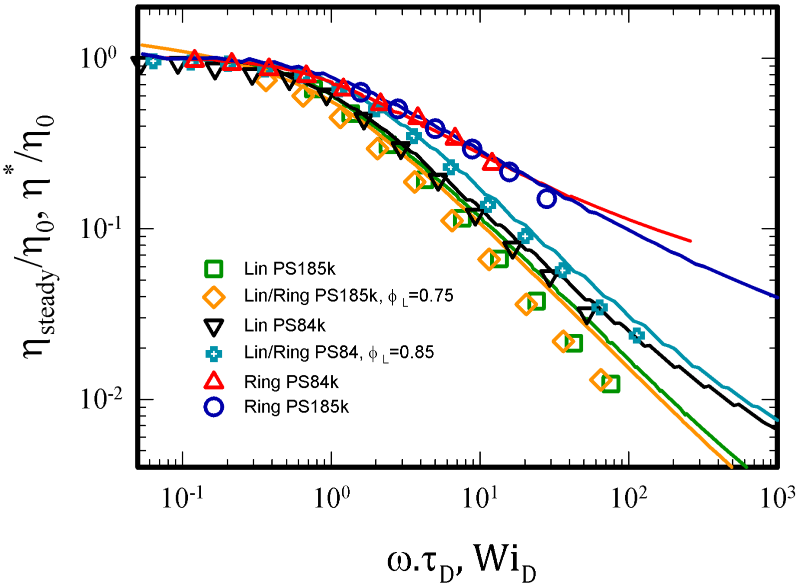

Figure 4.14: Cox-Merz rule for ring polymers.

The nonlinear data overlap with the LVE envelope line very well at $Wi_D < 30$ within experimental error, which confirms the validity of the Cox-Merz rule [22] for both linear and ring polymers. At higher shear rates, the nonlinear data are slightly lower than the linear envelope. The same observation has been reported for linear [94] and comb polymers [54]. This deviation may reflect a failure of this empirical rule or could be tentatively attributed to onset of weak wall slip or edge fracture propagating up to the gap between partition and cone of the CPP (although this is not supported by the long-time steady viscosity data in Figure 4.13). These possibilities have been discussed in detail recently [54, 94]. Nevertheless, it is reasonable to conclude that the empirical Cox-Merz rule is valid for ring polymers. We also note that the η_{steady} data for entangled linear PS (Z=5 and Z=11, for linear PS84k and PS185k respectively) overlap within error over the whole Wi_D range and share the shear thinning slope of -0.86 ± 0.03. The η_{steady}/η_0 data of the ring polymer overlap with those of the linear at low Wi_D in the linear (Newtonian) regime and deviate at higher values Wi_D. The weaker shear-thinning slope (-0.43±0.03) resembles behavior akin to unentangled chains with finite extensibility [153–155]. The data of the ring-linear mixtures are very close to those of entangled linear polymers, but not identical, especially for the slightly weaker shear thinning slope (-0.79 ± 0.01). That implies the addition of small percentages of rings can efficiently influence the nonlinear shear thinning behavior of linear matrix. Figure 4.15 depicts the relative viscosities η_{max}/η_{steady} as functions of Wi_D.

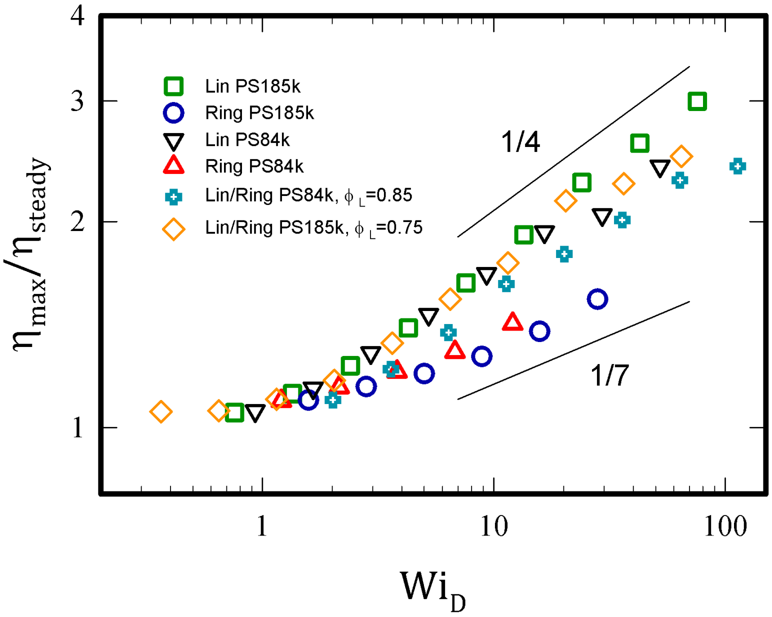

Figure 4.15: Ratio of the peak over the steady state viscosity values, η_{max}/η_{steady} vs Wi_D for ring polymers and linear/ring blends along with the linear precursors.

Experimental errors are associated with torque resolution at low shear rates and start-up of the motor at high shear rates. The transient viscosity reduction after its peak toward steady state reflects chain retraction (manifested as partial disentanglement) and the parameter η_{max}/η_{steady} is the measure of the effective chain deformation at steady state. The data show its progressive increase with increasing Wi_D. In fact, for $Wi_D < 1$, i.e. in the linear regime where practically no viscosity peak occurs, η_{max}/η_{steady} of linear and ring polymers are rate-independent and assume a value of 1. Indeed, in this regime linear and ring chains are not expected to be deformed. For $Wi > 1$, the data of entangled linear PS collapse and follow a power-law with a scaling slope of 1/4, which is also observed in other linear polymers in our previous works [94]. On the other hand, the ring data deviate from the linear data and exhibit weaker shear rate dependence with a slope about 1/7. This observation implies that the effective deformation of rings is smaller compared to linear chains, again in agreement with literature on single rings [152]. The data of the ring/linear mixtures are in-between again with a slope of 1/5, pointing to the role of rings in altering linear chain nonlinear dynamics. In steady shear flow, at sufficiently high rates, linear coils deform (and partly disentangle [156] much more efficiently than rings. Figure 4.16 depicts the strain at the peak viscosities, γ_{max} as function of the Weissenberg number, Wi_D. The errors on γ_{max} are related to the uncertainties in determining the time at the peak of viscosity due to data scattering around the peak region. All three data sets overlap within experimental error. We note that γ_{max} denotes the maximum instantaneous deformation whereas η_{max}/η_{steady} is proportional to the maximum deformation at steady state; hence, they differ in their sensitivity to molecular structure. The peak strain γ_{max} is between 2.0 and 2.3 at $Wi_D < 10$, consistent with observations in the literature [94, 144] and the Doi-Edwards model [11] for linear monodisperse polymers, which predicts that γ_{max} is due to orientation of the tube and attains a shear rate-independent value of 2.3. At higher Wi_D, the combination of both chain stretch and orientation governs the overshoot; hence, γ_{max} is expected to increase with Wi_D. The peak strain γ_{max} increases gradually with shear rate, and the high-Wi_D scaling slope is 1/3, consistent with the

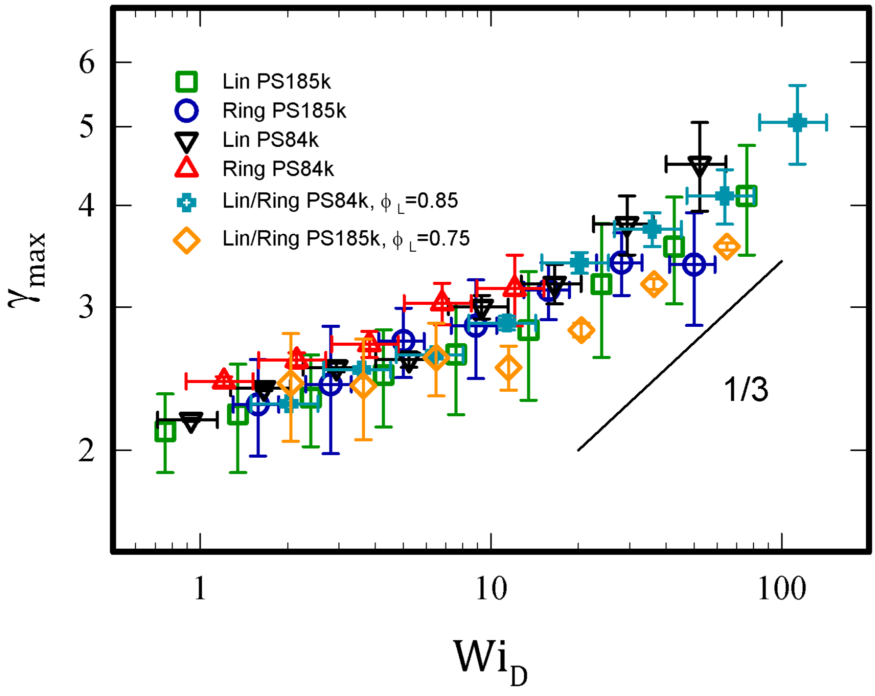

Figure 4.16: strain corresponding to the maximum viscosity, γ_{max} vs Wi_D for ring polymers, linear/ring blends and the respective linear precursors.

observation from a group of linear polymers [94] but still lower than the steeper slope (= 1) predicted by the GLaMM theory [37]. For linear polymers, the idea of convective constraint release (CCR) has proven to be an effective molecular mechanism to describe the nonlinear start-up shear flow behavior with good accuracy. For branched polymers like combs, a nonlinear hierarchical deformation scenario, including a short time branch withdrawn and a long time backbone orientation and stretch, drawn from the pom-pom model, was found to provide a reasonable description of nonlinear shear response. On the other hand, a molecular understanding of the nonlinear deformation of ring chains is still absent. One can advocate the double-folded ring conformation as a prime reason for their weak deformability. In other words, compared to their linear precursors, ring polymers have less freedom to change their conformation under shear flow because of their more compact structure. Additionally, the cooperative motion of ring segments under shear flow appears to be different from that of linear chains. Ring-specific dynamic mechanisms, such as cooperative orientation of parallel segments or the tumbling of segments, may account for the weak chain deformation under flow. In fact, recent simulations for small isolated rings (with number of Kuhn segments N = 60, 80, and 120, i.e., the latter being almost identical to PS-84k with $N \approx 117$) in solution indicate different tumbling behavior compared to linear polymers [157] More importantly, they show that finite extensibility is important for shear thinning with slope of -0.40, which is very close to the present value of -0.43. Whereas the present experimental system is different from simulations (marginal melt in the entanglement transition) and therefore this agreement should be taken as a full explanation, nevertheless this suggests that finite extensibility is at work here and rings indeed exhibit a weaker response to shear flow. Of course, one would qualitatively anticipate this result based on the power-law behavior of the moduli in the intermediate frequency region (figure 4.12).

4.4 Modeling of the Nonlinear Rheology of Linear PS

Modeling of the rheological data was carried out by prof. Giovanni Ianniruberto and prof. Giuseppe Marrucci at the University of Naples, Federico II. In the proposed model the stress tensor $\boldsymbol{\sigma}$ is written as a sum $\sum$ over modes. In the LVE limit, the shear stress becomes

$$\sigma_{xy}(t) \;=\; \int_{-\infty}^{t} dt' \gamma(t,t') \sum \frac{G_i}{\tau_{i0}} \exp\left(-\frac{t\,-\,t'}{\tau_{i0}}\right) \tag{4.2}$$

where $\gamma(t,t')$ is the shear deformation between past time t' and current time t and $\{G_{i0}, \tau_{i0}\}$ is the discrete set of LVE moduli and relaxation times. Indeed, we have replaced the BSW spectrum with a discrete Maxwell-like one in the model. Relaxation times in equation (4.2) are indicated with the index 0 (referring to equilibrium) because in fast flows they can be modified, and become time-dependent due to alignment-induced reduction of the monomeric friction coefficient ζ [135–137]. Normalized values of the moduli and relaxation times for $Z = 10$ and $Z = 13.9$, obtained by fitting the normalized frequency response data in figure 4.2 by means of the open source software Reptate, are reported in table 4.2. Obviously, time ratios like τ_i/τ_c are independent of flow-induced changes of the friction coefficient ζ. For each of the four systems, the values of $\{G_i, \tau_{i0}\}$ are obtained by multiplying the ratios in table 4.2 to G_N^0 and to the equilibrium value of τ_c (reported in table 4.1), respectively. The nonlinear constitutive equation for the stress tensor $\boldsymbol{\sigma}$ is written by decoupling the set of mode orientations $\mathbf{S}_i$ from the average subchain stretch ratio λ:

$Z = 10$		$Z = 14$	
G_i/G_N^0	τ_i/τ_c	G_i/G_N^0	τ_i/τ_c
1.14×10^2	2.16×10^{-3}	6.02×10^1	4.39×10^{-3}
2.52	5.9×10^{-2}	1.96	9.73×10^{-2}
8.8×10^{-1}	3.33×10^{-1}	6.90×10^{-1}	6.02×10^{-1}
3.81×10^{-1}	1.53	2.74×10^{-1}	3.28
2.07×10^{-1}	6.87	1.69×10^{-1}	1.67×10^1
1.70×10^{-1}	2.90×10^1	1.64×10^{-1}	7.28×10^1
1.76×10^{-1}	1.11×10^2	1.92×10^{-1}	3.06×10^2
1.37×10^{-1}	3.63×10^2	1.86×10^{-1}	1.30×10^3
2.03×10^{-1}	8.92×10^2	1.29×10^{-1}	2.88×10^3

Table 4.2: dimensionless discrete relaxation spectra for the two Z values of the four PS systems

$$\begin{aligned} \boldsymbol{\sigma} &= C_Q \lambda^2(t) \frac{f(\lambda)}{f_0} \sum G_i \mathbf{S}_i, \\ \mathbf{S}_i &= \int_{-\infty}^{0} \frac{dt'}{\tau_i(t')} \exp\left(- \int_{t'}^{t} \frac{dt''}{\tau_i(t'')} \right) \mathbf{Q}\left[\boldsymbol{E}(t,t') \right] \end{aligned} \tag{4.3}$$

In equation (4.3) the integral defining the ith mode orientation tensor $\mathbf{S}_i$ is written by accounting for the flow induced time dependence of the relaxation spectrum, tensor $\mathbf{E}$ is the deformation gradient between past time t' and current time t, and $\mathbf{Q}$ is the

Doi-Edwards tensor, here replaced (for simplicity) by the following unit-trace Seth-type measure [158, 159]

$$\mathbf{Q} = \frac{\mathbf{B}^{1/2}}{tr\,\mathbf{B}^{1/2}} \tag{4.4}$$

based on the Finger tensor $\mathbf{B} = \mathbf{E^T} \cdot \mathbf{E}$. In the stress expression, C_Q is a $\mathbf{Q}$-dependent scalar coefficient ($C_Q = 6$ for our choice of $\mathbf{Q}$) [134], and $f(\lambda)$ is the force factor that accounts for the non-Gaussian behavior of subchains:

$$f(\lambda) = \frac{\mathcal{L}^{-1}(\lambda/\lambda max)}{3\lambda/\lambda_{max}}, \qquad \lambda_{max} = a/b \tag{4.5}$$

In equation (4.5), $\mathcal{L}^{-1}$ is the inverse Langevin fuction, $b = 18$ Åis PS Kuhn length, [1] and a is the tube diameter, changing with dilution according to $a(\phi) = a(1)\phi^{-a/2}$ (see equation 2.1, where the PS melt tube diameter is given (in Å) by $a(1) = 85(3f_0/C_Q)^{1/2}$ [1, 134, 160]. Finally, in equation (4.3), f_0 is the equilibrium value of f. Indeed, because in PS melts a is not much larger than b, even for $\lambda = 1$, i.e., at equilibrium, f_0 comes out slightly larger than unity.

There remains to define how λ varies with time. In line with similar suggestions [39, 161] we will assume that the stretch ratio obeys the differential equation

$$\frac{d\lambda}{dt} = \mathbf{k} : \overline{\mathbf{S}}\lambda - \frac{f\lambda - f_0}{\tau_R(t)},$$

$$\overline{\mathbf{S}} = \int_{-\infty}^{t} \frac{dt'}{\tau_d(t')} \exp\left(-\int_{t'}^{t} \frac{dt''}{\tau_d(t'')}\right) \mathbf{Q}\left[\mathbf{E}(t,t')\right] \tag{4.6}$$

with the initial equilibrium condition $\lambda = 1$ for start-up flows. In equation (4.6), τ_R is the Rouse time (the equilibrium value of which is reported in table 4.1), $\mathbf{k}$ is the velocity gradient tensor, and $\overline{\mathbf{S}}$ is an average subchain orientation based on the disengagement time τ_d, defined as [146, 162]

$$\tau_d(t) = \frac{\sum_i G_i \tau_i^2(t)}{\sum_i G_i \tau_i(t)} \tag{4.7}$$

Concerning friction reduction and in particular the dependence of the monomeric friction coefficient ζ on the order parameter S, we have used the simple recipe (with $S_c = 0.14$) suggested by Ianniruberto [103]:

$$\frac{\zeta}{\zeta_0} = 1 \qquad \text{for } S \le S_c$$

$$\frac{\zeta}{\zeta_0} = \left(\frac{S}{S_c}\right)^{-1.4} \qquad \text{for } S > S_c \tag{4.8}$$

where, because of the somewhat different stress constitutive equation used here, the exponent of the power law has been slightly changed (-1.4 instead of -1.25). For S larger than the critical order parameter S_c (marking the onset of friction reduction effects), all relaxation times are reduced proportionally to the ratio ζ/ζ_0.

In the case of uniaxial elongational flows, the order parameter S_p of the polymer is calculated through the following equation [136]:

$$S_p(t) = \frac{\lambda^2(t)}{\lambda_{max}^2}\left(\overline{S}_{zz} - \overline{S}_{rr}\right) = \frac{\lambda^2(t)}{\lambda_{max}^2}\int_{-\infty}^{t} \frac{dt'}{\tau_d(t')} Q\left[\epsilon_H(t,t')\right] \times \exp\left(-\int_{t'}^{t} \frac{dt''}{\tau_d(t'')}\right) \tag{4.9}$$

where, we recall, z is the elongation direction and r is orthogonal to it. The second equality in equation (4.9) is obtained by using equation (4.6) for $\overline{\mathbf{S}}$ with $Q = Q_{zz} - Q_{rr}$ and $\epsilon_H(t,t')$ the Hencky strain between t' and t. For the case of solutions, from the order parameter of the polymer we calculate that of the solution through the formula [103]:

$$S = \left[\phi + (1-\phi)\varepsilon\right] S_p \tag{4.10}$$

where ε is the nematic interaction parameter of the oligomeric solvent.

For the start-up of uniaxial elongational flows, figure (4.17) shows the comparison between predictions of equations (4.3)-(4.10) and data for all four systems. Panels a and b in figure 4.17 refer to melts, and comparison between the solid and dotted lines highlights the importance of friction reduction. In panels c and d, referring to solutions, all curves account for friction reduction, and the difference between the solid (obtained with $\varepsilon = 0.3$) and dotted lines ($\varepsilon = 0$) marks the significance of the nematic interactions between the ligomeric solvent and the polymer. The best fit value of the nematic interaction parameter, $\varepsilon = 0.3$, for the 2k oligomeric solvent used here appears consistent with the value $\epsilon = 0.5$ found in the case of 4k oligomers [103].

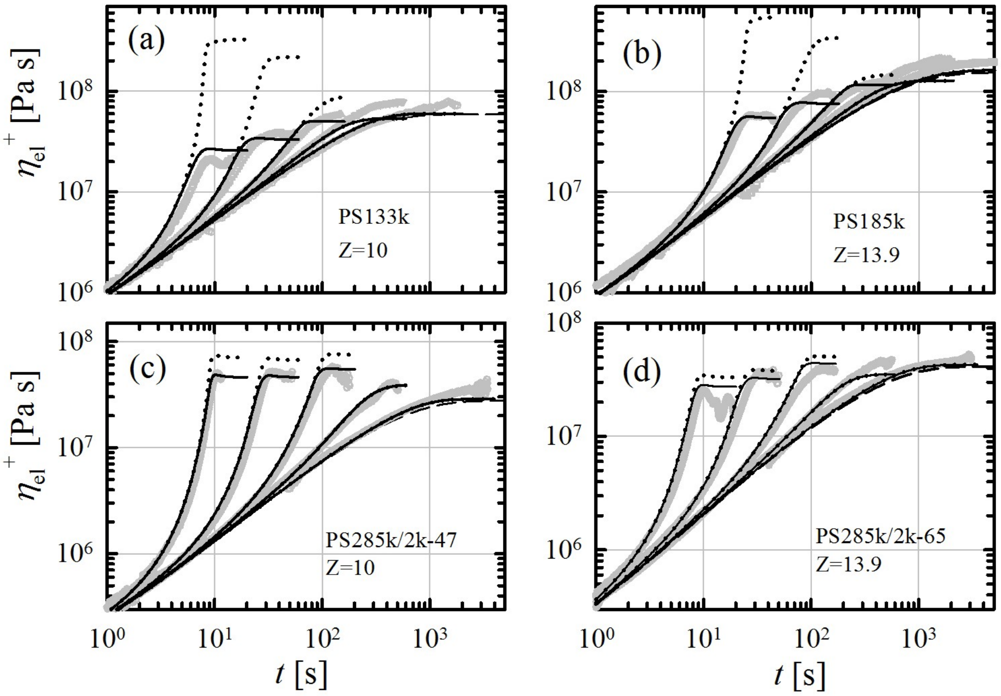

Figure 4.17: Extensional stress growth coefficient as a function of time for several stretch rates: comparison of predictions (black lines) to data (gray symbols). Dotted lines in panels a and b for melts were obtained by ignoring friction reduction effects. In panels c and d for solutions, friction reduction is always present, and dotted lines were obtained by ignoring nematic interactions ($\varepsilon = 0$). Stretch rates [s^{-1}] are from left to right: (a) 0.3, 0.1, 0.03, 0.01, 0.003; (b) 0.1, 0.03, 0.01, 0.003, 0.0003; (c, d) 0.3, 0.1, 0.03, 0.01, 0.001. In all panels, dashed lines represent the LVE response.

Figure 4.18 compares predictions to data in figure 4.4 for the steady state elongational viscosity (steady state was assumed at a Hencky strain of 5). The cusps in the curves of figure 4.18 are due to the abrupt transition from a constant friction coefficient to the power law (see equation 4.8). Those cusps would disappear by smoothing such a transition.

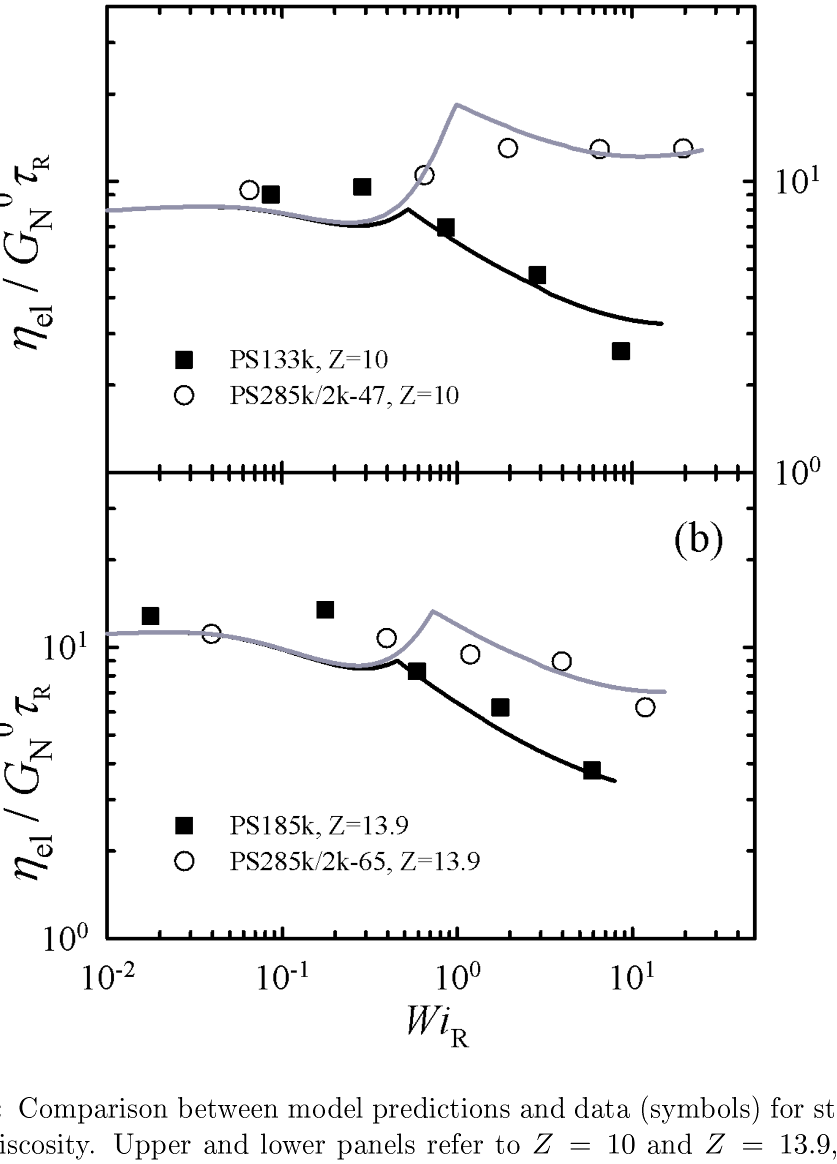

Figure 4.18: Comparison between model predictions and data (symbols) for steady uniaxial extensional viscosity. Upper and lower panels refer to $Z = 10$ and $Z = 13.9$, respectively. Black and gray lines refer to melts and solutions, respectively.

Moving on to the model predictions for shear flows, equation (4.3) for the stress is in fact simplified because friction reduction effects are expected to be absent and therefore relaxation times remain fixed at their equilibrium values. Figure 4.19 shows results for the $Z = 10$ systems (both melt and solution).

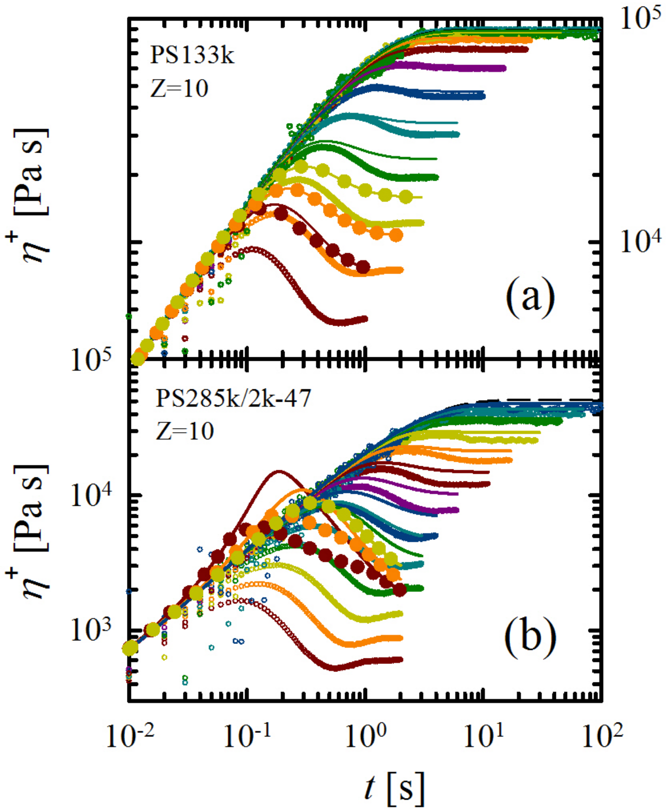

Figure 4.19: Predictions for the transient shear viscosity of the $Z = 10$ samples without accounting for tumbling. Data (symbols) and predictions (lines) with the same color refer to the same shear rate. PS133k melt (upper panel); PS285k/2k-47 solution (lower panel). Shear rates are as in figure 4.5. The highest viscosity curves coincide with the linear viscoelastic response (barely distinguished dashed black lines). Filled circles correspond to the predictions for the three highest rates, accounting for friction reduction without tumbling (see text).

Dramatic discrepancies between predictions and data emerge, especially at high shear rates, and similarly unsatisfactory results are found for $Z = 13.9$. Such large discrepancies remain even if convective constraint release (CCR), which has been ignored so far, is accounted for. Actually, for a multimode relaxation spectrum CCR is only a minor correction [132, 134]. One possible source for the discrepancy is the fact that in fast shear flows entangled molecules experience tumbling, as recently demonstrated by molecular dynamics simulations [38], a feature not accounted for. Consequently, the model is modified by inserting into equation (4.5) for the rate of change of λ the *tumbling* function $\varphi(t)$ given by

$$\varphi(t) \;=\; \cos(2\pi\omega t)\exp(-\beta t) \tag{4.11}$$

Equation (4.11) actually mimics equation 1 of Sefiddashti *et al.* [38], who considered the autocorrelation function of the end-to-end vector of the molecules. The cosine function describes a regular tumbling of a molecule with frequency ω, and the negative exponential accounts for a gradual loss of coherence among tumbling events, $1/\beta$ being the corresponding decorrelation (relaxation) time. For the shear case, equation (4.6) then becomes

$$\begin{aligned} \frac{d\lambda}{dt} \;&=\; \dot{\gamma}\overline{S}_{xy}\varphi\lambda \;-\; \frac{f\lambda - f_0}{\tau_R}, \\ \overline{S}_{xy} \;&=\; \int_{-\infty}^{t} \frac{dt'}{\tau_d}\exp\left(-\frac{t-t'}{\tau_d}\right) Q_{xy}\left[\gamma(t,t')\right] \end{aligned} \tag{4.12}$$

where $\dot{\gamma}$ is the shear rate, and it is understood that τ_R and τ_d remain at their equilibrium values.

Figure 4.20 reports the results for all the four systems examined, obtained by using the following values for the tumbling parameters ω and β:

$$\omega \;=\; \frac{\mathrm{Wi}_R^{-0.2}}{8\pi}\dot{\gamma}, \qquad \beta \;=\; \frac{\mathrm{Wi}_R^{-0.2}}{8}\dot{\gamma} \tag{4.13}$$

Note that equation (4.13) assumes that both the tumbling and the decorrelation frequencies, ω and β, respectively, are proportional to $\dot{\gamma}^{0.8}$, consistent with the NEMD simulation results (figures 10 and 11 of Sefiddashti et al. [38]). The dependence of the specific system appears through the Rouse time and it is embodied in the weak

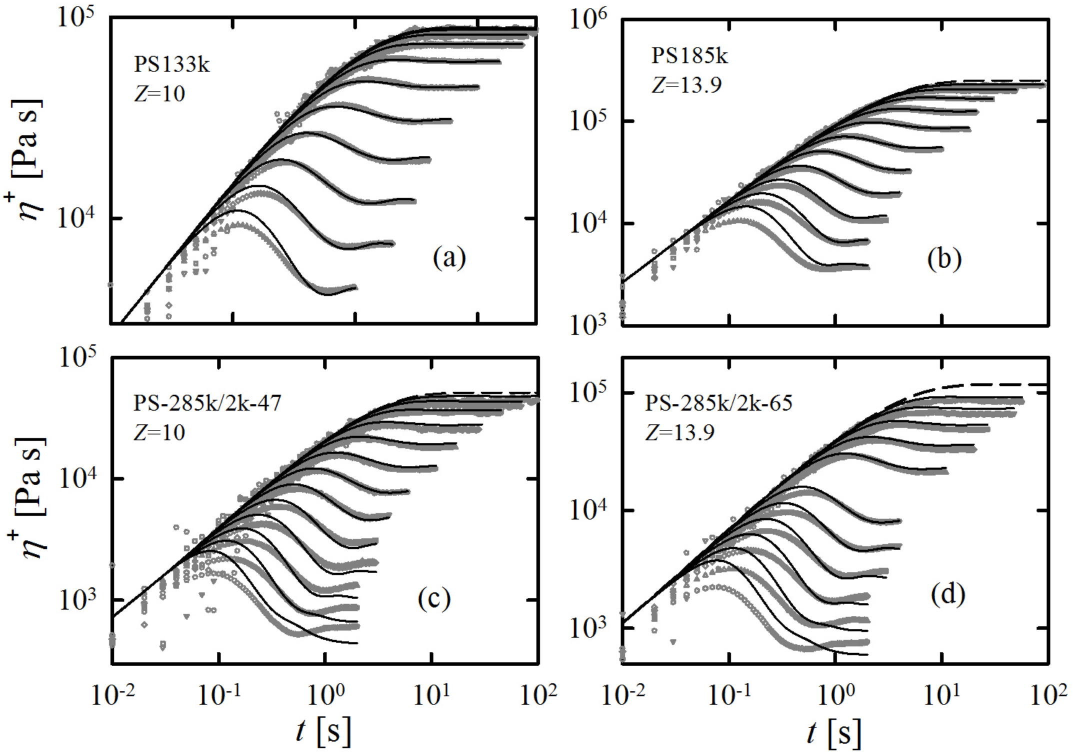

Figure 4.20: Comparison between predictions accounting for tumbling (solid lines) and data (symbols) in shear startup tests. Dashed black lines are LVE response. (top left). PS133k at shear rates as in Figure 4.5; (top right) PS185k at shear rates 0.1, 0.178, 0.316, 0.562, 1, 1.78, 3.16, 5.62, 10, 17.8, 31.6, and 56.2 s^{-1} from top to bottom; (bottom left) PS285k/ 2k-47 at shear rates as in figure 4.5; (bottom right) PS285k/2k-65 at shear rates 0.1, 0.178, 0.316, 0.562, 1, 1.78, 5.62, 10, 17.8, 31.6, 56.2, and 100 s^{-1} from top to bottom.

power law of Wi_R. Although the predictions of figure 4.20 are reasonably consistent with the data for the four systems considered, it should be emphasized that equations (4.11)-(4.13) are essentially phenomenological, as no molecular theory for tumbling in entangled systems has been proposed so far. On the positive side, figure 4.20 shows that the proposed model naturally predicts the possible appearance of undershoots (arising from the cosine function). We consider this as an important result since it provides a physical explanation for the origin of stress undershoot, i.e., tumbling. It is worth noting that modification and generalization of the model introduced through equations (4.11)-(4.13) require that it can be extended to an arbitrary flow, with the obvious requirement that the tumbling correction disappears in extensional flows. We also emphasize that to predict the transient response and undershoot in stress, the tumbling function in equation (4.11) is really necessary. Indeed, we have performed additional calculations without tumbling, but accounting only for friction reduction. The result is reported in figure 4.19. It is apparent that friction reduction without tumbling does not solve the problem. Going back to the predictions of figure 4.19 without tumbling, the predicted shear-hardening merits a quick comment: recent experiments with highly branched polymers reported such an effect [163]. Our experimental results do not show any hardening in shear. Given our analysis, the present data are dominated by tumbling. We postulate that at higher shear rates (not reached experimentally) the tumbling contribution may be weaker and hardening may indeed occur. By the same token, in complex architectures such as that of ref [163], it is possible that tumbling is reduced and stronger shear deformation may lead to hardening. Interestingly, recent multichain slip-link simulations results do confirm the existence of the undershoot (see Figure 13 of ref [136]), suggesting that they automatically account for tumbling. However, in that case the undershoot was very weak because the shear rates in the simulations were not sufficiently high and the respective highest Wi_R was about 3.

Figure 4.21 reports the steady-state viscosity curves obtained from the model, which compare favorably with the data previously reported in figure 4.7 It should be noted that in view of the negative exponential in equation 4.11 for the tumbling function $\varphi(t)$, at steady state the stretch ration λ is predicted from equation 4.12 to reduce to the equilibrium value $\lambda, = 1$. The comparison in figure 4.21 appears to confirm such a prediction, at least for the shear stress component.

Figure 4.22 compares predictions of stress relaxation upon shear flow cessation with the corresponding data for all four samples, and a very good agreement is generally

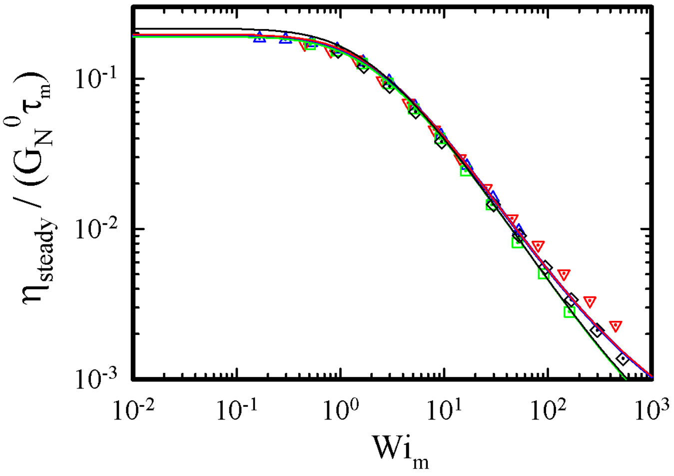

Figure 4.21: Comparison between predictions (lines) and data (symbols)for the steady-state shear viscosity. Colors as in figure 4.7.

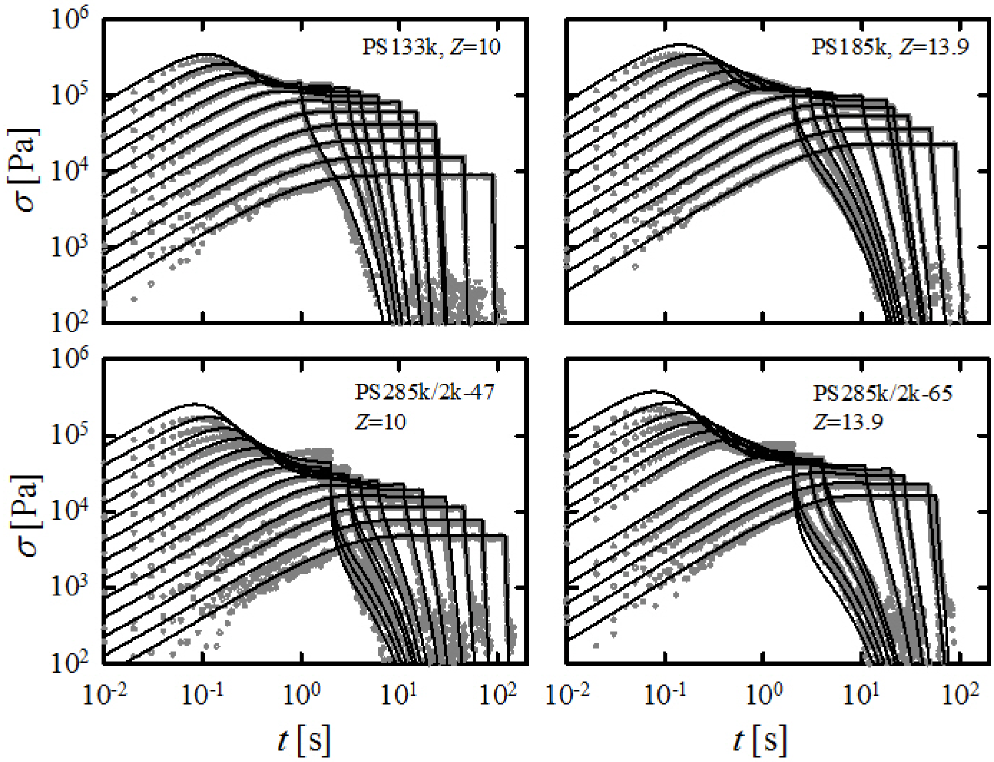

Figure 4.22: Comparison between predictions (lines) and data (symbols) in shear startup followed by relaxation upon flow cessation. Shear rates are the same as in Figure 4.20. (top left) PS133k, (top right) PS185k, (bottom left) PS285k/2k-47, and (bottom right) PS285k/2k-65.

found.

One should note that at high shear rates the relaxation essentially occurs in two steps: a fast relaxation followed by a significantly slower one. Since relaxation starts from the steady state where, as shown above, the stretch contribution is essentially absent, the fast process is interpreted as due to the relaxation of the fast modes of the orientation spectrum, which at high shear rates contribute significantly to the steady state value of the shear stress. To appreciate the relaxation, in particular the early times, and the success of the model, we show in Figure 4.23 the data and model prediction only for stress relaxation upon flow cessation.

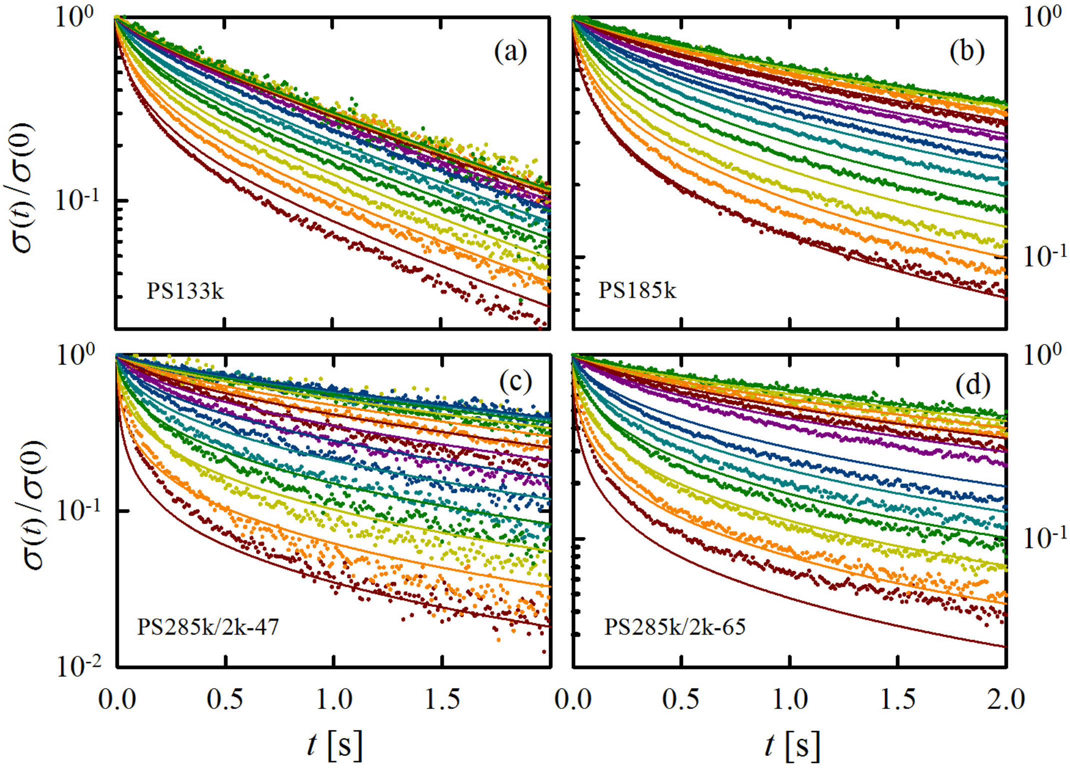

Figure 4.23: Comparison between predictions (lines) and data (symbols) for the relaxation upon flow cessation. Shear rates as in Figure 4.20.

Finally, Figure 4.24 shows predictions and data for the first normal stress difference N_1 for the PS285k/2k-47 solution. It is evident that the model fails to fit the data,

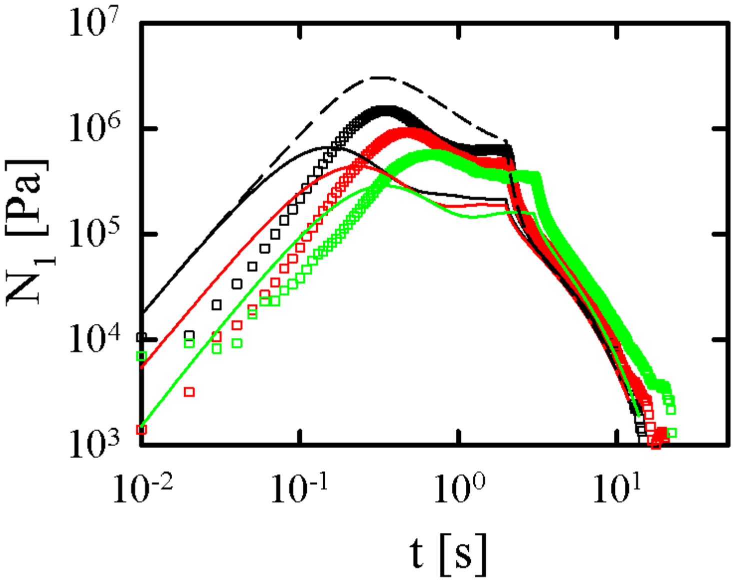

Figure 4.24: Comparison between N_1 predictions and data (apparent) in shear startup and subsequent relaxation upon flow cessation for the PS285k/2k-47 solution. Color codes for shear rates as in Figure 11. Solid lines are predictions with tumbling. The dashed line (for the highest rate) is obtained without tumbling.

both with and without the tumbling correction. A similar mismatch is found also for the other solution. We should point out that we did not attempt to provide data for the effective N_1 and N_2 in shear as the main purpose of this work is to underline differences between rheological behavior of PS melts and solutions in shear and extensional flow in the high Wi_R range.

4.5 Discussion and concluding remarks

Concerning linear polymer melts and solutions, we have presented a systematic investigation of the nonlinear shear and extensional properties of polystyrene melts and solutions having the same number of entanglements (10 and about 14) by means of state-of-the-art experiments and modeling. As expected, the LVE response of PS melts and solutions having the same Z exactly coincides to within a vertical and a horizontal shift (in log scales) that define the respective moduli and characteristic times. In the nonlinear regime we have demonstrated that the differences between melts and solutions observed in uniaxial extensional flows are not detectable in shear flows over the same range of Rouse-based Weissenberg numbers ($0.01 < Wi_R < 40$), with the highest values corresponding to significant chain stretching. This fact confirms that in strong aligning flows (uniaxial extension) friction reduction differentiates melts from solutions, the latter reaching a smaller value of the average order parameter because of the reduced orientation of the solvent molecules. It should be also noted, however, that the oligomeric solvent molecules are not fully random because of nematic interaction with the polymer molecules. Conversely, in shear flows, because of vorticity, the order parameter of the Kuhn segments always remains sufficiently low so that the monomeric friction coefficient essentially remains at its equilibrium value. Concerning fast shear flows, a specific phenomenon due to the rotational component of flow appears to play a significant role, namely tumbling of entangled molecules, which has been recently demonstrated by the molecular dynamics simulations of Sefiddashti *et al.* [38]. These authors also emphasize that tumbling is associated with a significant loss of entanglements. Indeed, a few lines after their Figure 6 (where molecular configurations in melts and dilute solutions are compared at $Wi = 10600$), they write *"These snapshots serve to reinforce the evidence of the lack of entanglements in the melt at high shear rates, since the observed configurations are very similar to those of the dilute solution."* Sefiddashti *et al.* [38] also directly measured the flowinduced loss of entanglements in their Figure 15 and again stressed that tumbling is directly linked to disentanglement in their Conclusions section.

The model proposed here accounts for tumbling (and implicitly for disentanglement) in a very simplistic way, with this effect only modifying the stretch ratio λ. Since λ is a scalar quantity, affecting in equal ways all components of the stress tensor, the tumbling-induced λ reduction through the function φ of equation 4.11 modifies the shear stress σ and the first normal stress difference N_1 in the same way. Now, the real picture emerging from NEMD simulations (see Figure 6a of Sefiddashti et al. [38] is one where the highly oriented and stretched polymer molecule goes from a positive xy component of the conformation tensor to a negative one during the tumbling cycle (thus effectively reducing the xy component of the stress, i.e., shear stress), while at the same time remaining on average significantly stretched along the shear direction x (hence maintaining a permanently positive value of the normal stress, $N_1 = \sigma_{xx} - \sigma_{yy}$). The simple scalar tumbling model proposed here cannot capture this latter aspect, which explains the failure in fitting the $N_{1,app}$ data in figure 4.24. An equally important factor explaining the data-model mismatch is the experimental difficulties in measuring the normal stress because of the axial compliance of the rheometer. We note further, however, that figure 4.23 shows that tumbling plays some role also in somewhat reducing N_1 because in fact $N_{1,app}$ data fall in-between predictions with and without tumbling. This is again in agreement with the NEMD simulations which show that although the $xx - yy$ component of the conformation tensor is positive throughout the tumbling cycle, the average stretch gets significantly reduced during part of it (Figure 6a of Sefiddashti et al. [38]). Clearly, a model fully accounting for tumbling cannot make use of the classical approximation of decoupling stretch (the scalar λ) from the orientation tensor. However, such a more faithful model including the tumbling phenomenon is yet to be developed. An important feature of the tumbling model proposed here is the prediction of a transient undershoot following the stress (or viscosity) overshoot at high shear rates, also seen in the data (see figure 4.20). Such a feature is absent without the tumbling correction (see figure 4.19), as is true for all integral constitutive equations of the Doi-Edwards type, which only predict the overshoot. It is also worth noting that the multimode relaxation revealed by the LVE response has important consequences in the nonlinear range. On the one hand, it appears to make the role played by CCR relatively marginal, as previously observed by Likhtman and Graham [132]. Multimode relaxation also appears to inhibit banding instabilities in shear flows. Indeed, for steady shear flows, the power law exponent (-0.82) of the experimental viscosity curve in figure 4.7 clearly indicates absence of steady shear banding, which is also excluded by the predictions of the model (see figure 4.21). For startup of shear flows, work is in progress to show that multimode relaxation can inhibit the transient shear banding predicted for the unstretched single mode case by Moorcroft and Fielding [164]. Moreover, they have also shown that chain stretching essentially cancels the transient *elastic* instability even for the single mode relaxation. Finally, in the range of shear rates examined, there has been no evidence of wall slip.

Concerning ring polymers, we have presented linear and nonlinear rheological data of two experimentally pure ring polymers and two respective ring/linear mixtures. The linear viscoelasticity of rings exhibits the established power-law stress relaxation, however with an exponent larger than 0.4, predicted by the lattice-animal model. For moderately entangled rings ($Z = 5 - 10$), terminal flow behavior is approached whereas a slower mode is apparent in the relaxation of ring PS185k. The overshoot in transient viscosity of the rings at high Weissenberg numbers, is less prominent compared to their linear precursors, suggesting that the nonlinear deformation of rings is weaker compared to their linear counterparts. This is also reflected in their weaker shear thinning behavior. Data obtained with ring-linear blends exhibit a nonlinear shear behavior closer to that of entangled linear chains and confirm the emerging picture. Available fragmental information from single DNA ring extensional deformation and molecular simulations of sheared single ring in solution provide further evidence for the weaker ring deformation and the importance of finite extensibility, especially for small molecular weights. The present data set should motivate further shear and extensional experiments with larger molecular weights and mixtures as well as theoretical developments in this exciting field of research.

Chapter 5

STRESS START-UP AND RELAXATION IN CAYLEY TREE POLYMERS

5.1 Introduction

The use of model polymers of well-defined architecture is important in probing molecular rheology [85, 165–167]. Indeed, substantial progress has been made in decoding the linear viscoelasticity (LVE) of model branched polymers (such as combs or pom-pom-like macromolecules), and more recently their nonlinear response in shear and extension. The rheological properties of model polymers provide profound implications in finessing molecular models and improving material performance in technological applications [51–53, 95, 163, 168–173]. Focusing on the nonlinear rheology of comb polymers, one important consequence of the recent progress in experimental extensional and shear rheology is the quantitative assessment of the role of dynamic dilution in transient strain hardening and stress overshoot, respectively. Moreover, it has been demonstrated that, still using the comb paradigm, introducing long-chain branching induces strain hardening in start-up shear [163]. It is therefore evident that whereas branching is crucially important in processing, the exact role of number, size, and distribution of branches is not fully quantified. We note that Nielsen *et al.* measured the transient response of model pom-pom polystyrenes [169] (which are the limiting case of combs with only two branch points at the ends of the backbone) and reported strong extension hardening, even at low deformation rates, due to the stretching of the backbone between the two branch points. The extensional viscosity reached steady state with values scaling with the extensional rate with a power-law exponent of about -0.5, in agreement with modeling predictions [140, 169]. The latter were based on the concept of internal chain pressure which counterbalances the contraction due to applied deformation, [174, 175] coupled with backbone tube dilation due to the earlier relaxation of the branches. These ideas were also implemented into the time marching algorithm by van Ruymbeke *et al.* [50, 176] in order to predict the extension hardening of Cayley-tree poly (methyl methacrylates) (PMMA) of different generations. However, in the latter case, despite the very good predictions of transient stress growth coefficient, the experimental measurements were limited to a maximum Hencky strain of 4, and in some cases steady state was not reached. Moreover, Marrucci and Ianniruberto suggested that the tube pressure is not a universal concept and proposed instead the idea of anisotropic monomeric friction as the main mechanism to account for the response of polymer melts and solutions in uniaxial extension [103, 136, 137]. An important element of the pom-pom model is the branch withdrawal at rates larger than the effective Rouse rate of the polymer. This worked out for the case of multiple branches along the backbone, and a modified pom-pom model for combs captured the transient extensional data remarkably well [173]. In parallel, whereas experiments with well-defined branched polymers (such as combs) are in general necessary in order to elucidate the role of the molecular parameters (number, size, and distribution of the branches, distances between branch points) in the rheological response, the state-of-the-art branch-on-branch (BoB) model, developed for randomly branched polymers [96], can be adopted to well-defined branching in a straightforward way. In some specific situations, the complex transient response of combs can be described with simple models accounting for branch withdrawal and convective constraint release, but a universal constitutive model is far from reach. In addition, it is important to emphasize that nonlinear rheological experiments with polymer melts are far from trivial. Challenges of particular significance are the potential achievement of steady state in extension and associated ability to reach sufficiently high Hencky strains on the one hand, and the occurrence of wall slip and edge fracture instabilities in shear on the other hand. Moreover, stress relaxation has emerged as an important experimental indicator of material performance baring information on the role of molecular structure on macroscopic response [177, 178]. Hence, outstanding challenges remain in the field, on both experimental and modeling sides.

Recent advances in instrumentation have opened the route for obtaining high quality experimental data, especially in nonlinear transient conditions. More specifically, the development of the filament stretching rheometer (FSR) allows for the measurement of true stress in a well-controlled uniaxial extension at large Hencky strains and that of stress relaxation upon cessation of extension [89, 177]. At the same time, the implementation of cone-partitioned plate (CPP) in rotational strain-controlled rheometry offers the ability to reliably measure transient shear stress over the large possible range of shear rates [33, 92, 94]. It is therefore essential to combine novel macromolecular structures of relevance in processing and state-of-the-art experimental tools in order to provide useful, reliable experimental information in different flow histories, toward a better understanding of the behavior of complex polymers and a critical assessment of predictive models and their eventual improvement.

In this chapter, we address this challenge and present a combined set of accurate experimental data with a well-defined dendritically branched macromolecule of third and fourth generation subjected to both nonlinear shear and uniaxial extensional deformation, during both start-up and relaxation upon flow cessation. We compare these data against model predictions using BoB. The choice of the particular Cayley-tree type of structure is motivated by the fact that it is an excellent model for investigating the hierarchical role of the branches (with and without free ends, with varying number and molar mass) in rheology, and represents a next step in complexity from combs [50, 179]. One well-known, albeit intriguing aspect of such macromolecules is their rather low zero-shear viscosity and larger level of extension hardening due to the fact that their very large total molar mass is split into multiple segments (hyperbranched), each having a small molar mass. Here, we present new data with Cayley-tree poly(methylmethacrylates) of generations 3 and 4, whose LVE and strain hardening were investigated before. We show, in particular, the transient extensional data with steady state values at the large Hencky strains, respective transient shear data, the Cox-Merz representation, and the relaxation of extensional and shear stresses, along with the BoB predictions.

5.2 Results and discussion

5.2.1 Linear Viscoelasticity

Details on the molecular architecture of the specific PMMA-based Cayley-tree polymers of generation 3 (coded as G3) and 4 (coded as G4) are reported in section 2.1.3. Supplemental information on the preparation of the samples for rheology and rheological measurements are reported in section 2.4. As reference, we present first the LVE data of the two samples in figure 5.1. The mastercurves are taken from van Ruymbeke *et al.* [50, 176] and shifted to the reference temperature T_{ref} = 180°C and are shown in separate plots in order to better appreciate the BoB predictions. The shift factors are discussed in [50]. In fact, we have remeasured the frequency-dependent dynamic moduli at 180°C and our results were identical to those of van Ruymbeke *et al.* [50, 176], hence confirming that the samples were not degraded. We remind here the main outcome from the linear data (shown in the separate plots of figure 5.1): time-temperature superposition works remarkably well, high-frequency data collapse for G3 and G4 having the same glass temperature (of about 100°C), the plateau G'

(corresponding to about 10^2 rad/s) is identical for the two samples and typical of that of linear atactic PMMA. Continuous decrease of G' with decreasing frequency reflects the dynamic dilution due to relaxation of branches of different generations from outer proceeding inward [50, 99]. Finally, the terminal relaxation of G4 is slower than that of G3. In particular, the respective terminal moduli crossover frequencies are 0.005 and 0.03 rad/s. Regarding the nonlinear rheology that follows, the imposed shear and extensional rates cover a range from 3×10^{-1} to 10^{-3} s^{-1}. This is a rather wide range given the experimental limitations, and at the same time very useful as it encompasses the transition from rubbery (deformed polymers) to terminal response, respectively. For Bob modeling, we chose $M_e = 5000$ g/mol (slightly higher than that reported in [50] and $\tau_e = 2.5$ ms (consistent with [50] when the experimental temperature of 180°C is considered). The plateau modulus is indepentently set at 0.98 MPa. Though the *bare* molar masses of all segments of the molecules are greater than two entanglements, the *diluted* lengths of the inner generation segments are significantly smaller than one entanglement. However, the relaxation of the inner segments remain dominated by branch-point friction and constraint release Rouse processes, and a description based on the relaxation of entangled polymers provides reasonable agreement for the stress relaxation of the current Cayley-trees. The LVE responses (lines in figure 5.1 for both G3 and G4) are predicted satisfactorily. The predicted high frequency regime before the onset of entanglements substantially deviates from the data, but this is a typical problem and attributed to both tube-modeling (that does not apply there) and experiments (segmental dynamics region approached) [102, 181]. Relaxation of each generation introduces separate features in the linear relaxation (most easily seen in the phase angle). The predicted features are sharper than the experimental observations. This may be explained by the inevitable presence of slight polydispersity in molecular structure, which is not uncommon in complex model polymers [85, 166]. The experimental elastic modulus for G4 fails to reach the terminal slope at the lowest frequency

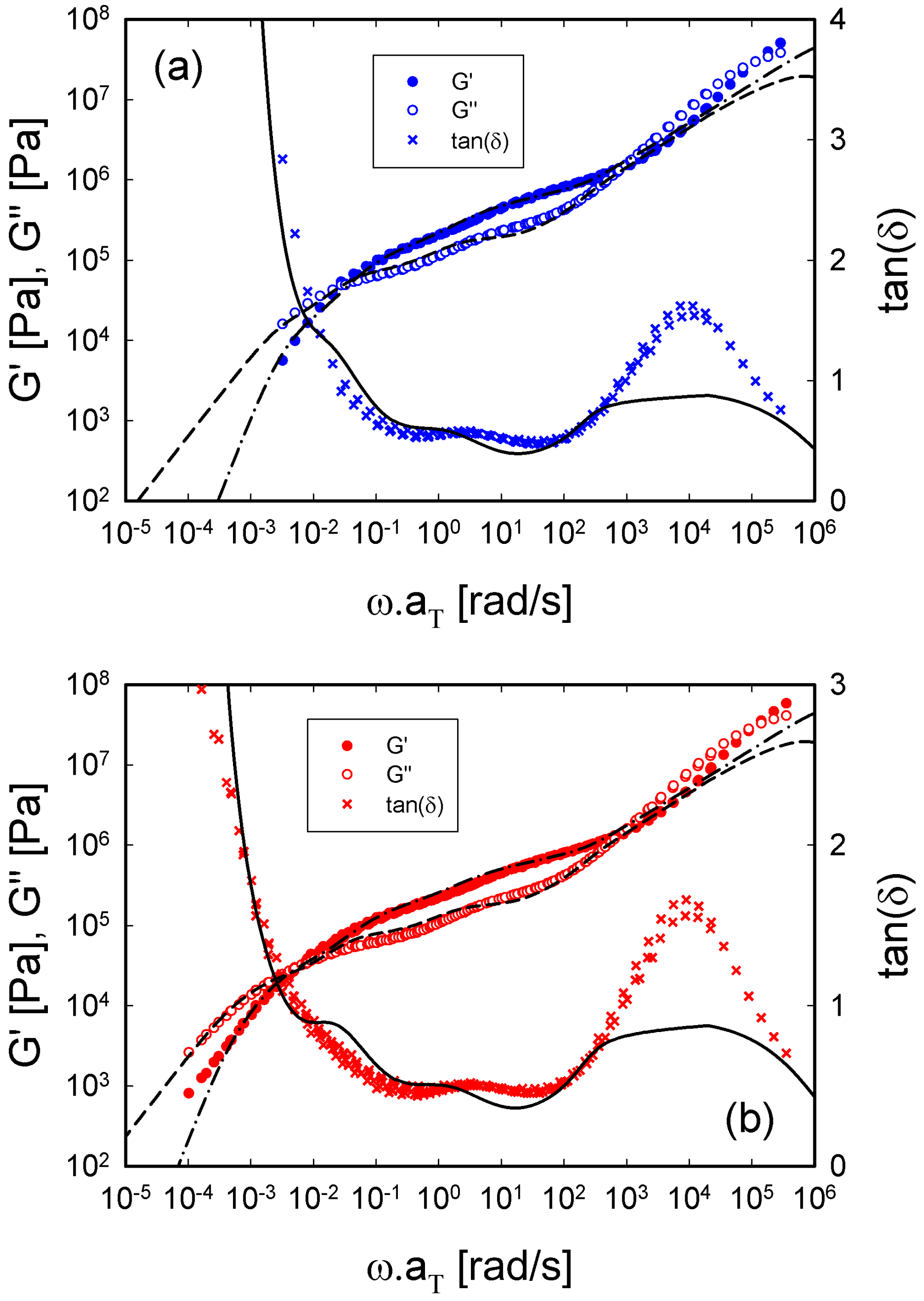

Figure 5.1: LVE mastercurves from van Ruymbeke *et al.* [50], depicting G' (closed circles), G'' (open circles), and tan(δ) (crosses) versus shifted frequency ($\omega \cdot a_T$) at a reference temperature T_{ref} = 180°C for G3 (a) and G4 (b). For both graphs, black lines are predictions from BoB model (G', dashed-dotted line; G'', dashed line; and tan(δ), solid line) [180].

probed. This likely reflects the presence of small fraction of side-products [50, 80, 84], as already discussed previously. An important remark concerns the actual relaxation which, based on BoB, occurs well after the moduli crossover (due to relaxation of diluted inner segments), as seen clearly in fig 5.1. In fact, the predicted longest relaxation times are about 419 s and 1677 s for G3 and G4, respectively. These values differ sharply from the inverse G'-G'' crossover to the terminal region (33.3 s and 200 s). Given the lack of experimental data at low enough frequencies, we shall use below the terminal crossover as a measure of characteristic terminal time for extracting the Weissenberg number.

5.2.2 Transient uniaxial extension and shear

Data modeling

Data modeling was carried out by dr. Chinmay Das at the University of Leeds. Details about the parameters used for the Bob model are given in section 2.4. In figure 5.2, the transient data for G3 are depicted. The stress growth coefficient in figure 5.2(a) exhibits strain hardening even at rates as low as 3×10^{-3} s^{-1}. This remarkable finding confirms the earlier results of van Ruymbeke *et al.* [50]. It is interesting to note that this lowest rate is below the terminal rate for G3 (around 2×10^{-2} rad/s, see figure 5.1, and of course also below the estimated bare Rouse rates of the dendritic polymer (about 0.28 s^{-1}) or the outer branch (about 20 s^{-1}) [50]. In the former case, the bare Rouse time was considered as the time for the molecule to diffuse its own size with the friction given by monomer friction, and estimated as $\tau_R = rZ_{tot}^2\tau_e = 3.6$s, with Z_{tot} being the total molar mass divided by the entanglement molar mass and r is the radius of gyration/contraction factor [80]. Note that the expected stretch relaxation time is much longer than this bare Rouse time, because the important stretch relaxation process is determined not from monomer friction, but from the friction of branch-point hopping. The calculation to obtain this longer stretch relaxation time is like a *Rouse*

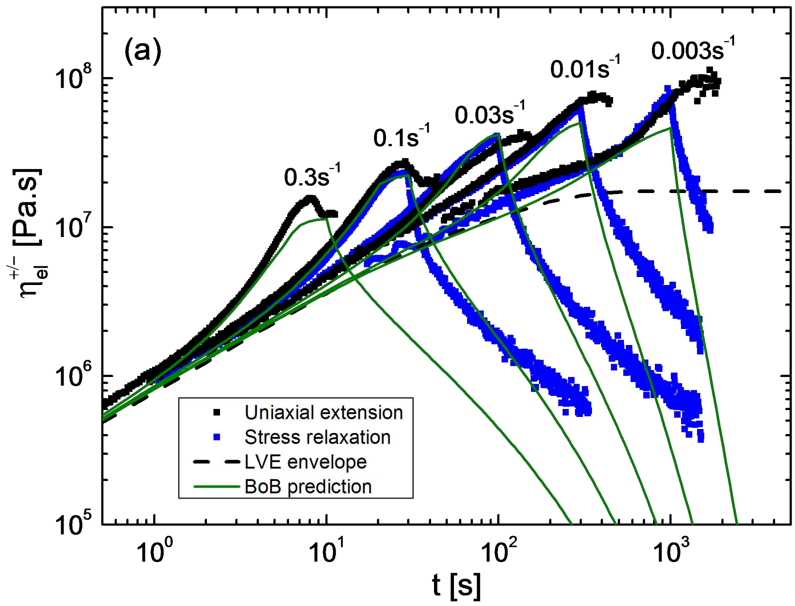

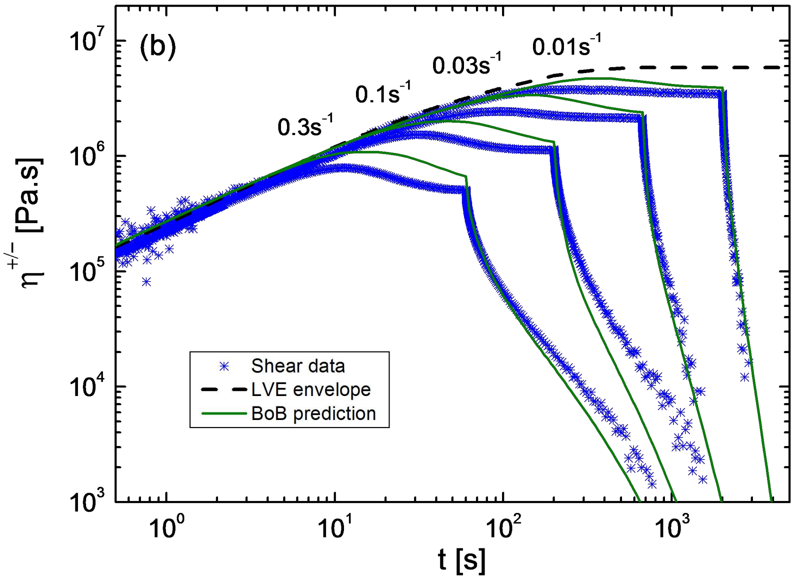

Figure 5.2: (a) Stress growth coefficient of G3 at different elongational rates (indicated in the plot) and its relaxation, at 180°C. The black points are data from experiments performed up to steady state in uniaxial extension. The blue data show data of stress growth up to a certain value (before steady state) and subsequent relaxation. The black dashed line is the LVE envelope (from figure 5.1).(b) Respective start-up data in shear, indicating the time evolution of the transient viscosity (blue). The black dashed line depicts the LVE envelope. The viscosity relaxation data are recorded after steady state is attained and flow is subsequently stopped (see text). Green solid lines are predictions from BoB model [180].

calculation, in which the monomer friction is replaced by branch point friction (and this is the route taken in BoB to calculate the stretch relaxation time). For the sake of clarity, in order to avoid confusing the two different Rouse times, we refer always to the Rouse time based on monomer friction as the bare Rouse time (shown in figure 5.8), whilst the longer relaxation time is called the *stretch relaxation time*. Viewed this way, the latter time is actually the Rouse time of molecule and the dilution is not considered. Concerning the outermost segments, their Rouse (or stretch) relaxation time is (star-like) $\tau_s = 4Z_{seg}^2\tau_e = 0.05$ s, with Z_{seg} being the effective number of entanglements per segment. Further and more importantly, we can clearly observe in figure 5.2(a) that the steady state is reached at long enough times, hence Hencky strains. The unique relaxation data in this figure were collected after stopping the extensional deformation at the same Hencky strain ($\varepsilon_H = 3$) for all strain rates investigated, before, however, the steady state is attained. The respective shear data are depicted in figure 5.2(b). The transient shear viscosity exhibits well-known features of polymers [92]. In particular, it greatly depends on the imposed shear rate. At early times, the data collapse into the LVE envelope. With increasing shear rate, a viscosity overshoot appears before reaching a steady state value. The steady state value of viscosity decreases upon increasing shear rate. The available data do not show any evidence of undershoot before steady state. Moreover, there is no evidence of strain hardening in shear. The latter was reported for an entangled solution of multiply branched comb-like polystyrene, having long branches with about ten entanglements each in the bulk, at Weissenberg numbers (based on terminal time) of $O(10^4)$, which were achieved by measuring at different temperatures [163]. The relaxation data (obtained by stopping the shear flow once the accumulated strain reached a value of about 20) suggest that viscosity relaxes faster in shear compared to uniaxial extension (figure 5.2(a)). Same remarks hold for the compiled elongational and shear data of figure 5.3 for G4 (with the lowest imposed rate being 10^{-3} s^{-1}, and the accumulated strain being about 20 for the two lowest and

25 for the two highest shear rates). Here, the bare Rouse time is estimated to be about 10.6 s. We note further that the absolute values of stress growth coefficient are larger compared to G3, and this is expected since the structure of the latter consists of a small number of segments between branches. In order to predict the nonlinear flow behavior, we aim to assign equivalent pom-pom modes [51] that describe the linear relaxation of the molecules and contain stretch and orientation relaxation times of the molecules (which are relevant to nonlinear flow properties). A pom-pom molecule is characterized by a modulus (g), the maximum stretch that the backbone can support before branch points start withdrawing in the backbone tube (q is the number of side arms in each side of the backbone for a symmetric pom-pom molecule), the stretch relaxation time (τ_s), and the orientation relaxation time (τ_0). In the differential version of the pom-pom model, the preaveraged stretch λ satisfies the following equation [52, 99]:

$$\frac{d\lambda}{dt} = \lambda\, \boldsymbol{K} : \boldsymbol{S}^{\boldsymbol{T}} - \frac{(\lambda - 1)}{\tau_s} \exp\left[\frac{2}{q-1}(\lambda - 1)\right] \tag{5.1}$$

Here, $\boldsymbol{K}$ and $\boldsymbol{S}$ are the deformation rate and the preaveraged backbone orientation tensor, respectively. The evolution of the orientation tensor is conveniently described by the auxiliary tensor $\boldsymbol{A}$ with $S \equiv (\boldsymbol{A}/tr(\boldsymbol{A}))$ and satisfying the following equation:

$$\frac{d\boldsymbol{A}}{dt} = \boldsymbol{K}.\boldsymbol{A} + \boldsymbol{A}.\boldsymbol{K}^{\boldsymbol{T}} - \frac{1}{\tau_0}(\boldsymbol{A} - \mathbf{1}) \tag{5.2}$$

The stress evolution is given by the following equation:

$$\boldsymbol{\sigma} = 3\, g\, \lambda^2(t)\boldsymbol{S}(t) \tag{5.3}$$

The advantage of using the set of evolution equations (5.1)-(5.3) is that, for both uniaxial and shear start-up, the evolution of $\boldsymbol{A}$ and hence the orientation tensor $\boldsymbol{S}$ can be solved analytically. On the other hand, the evolution of the stretch is solved nu-

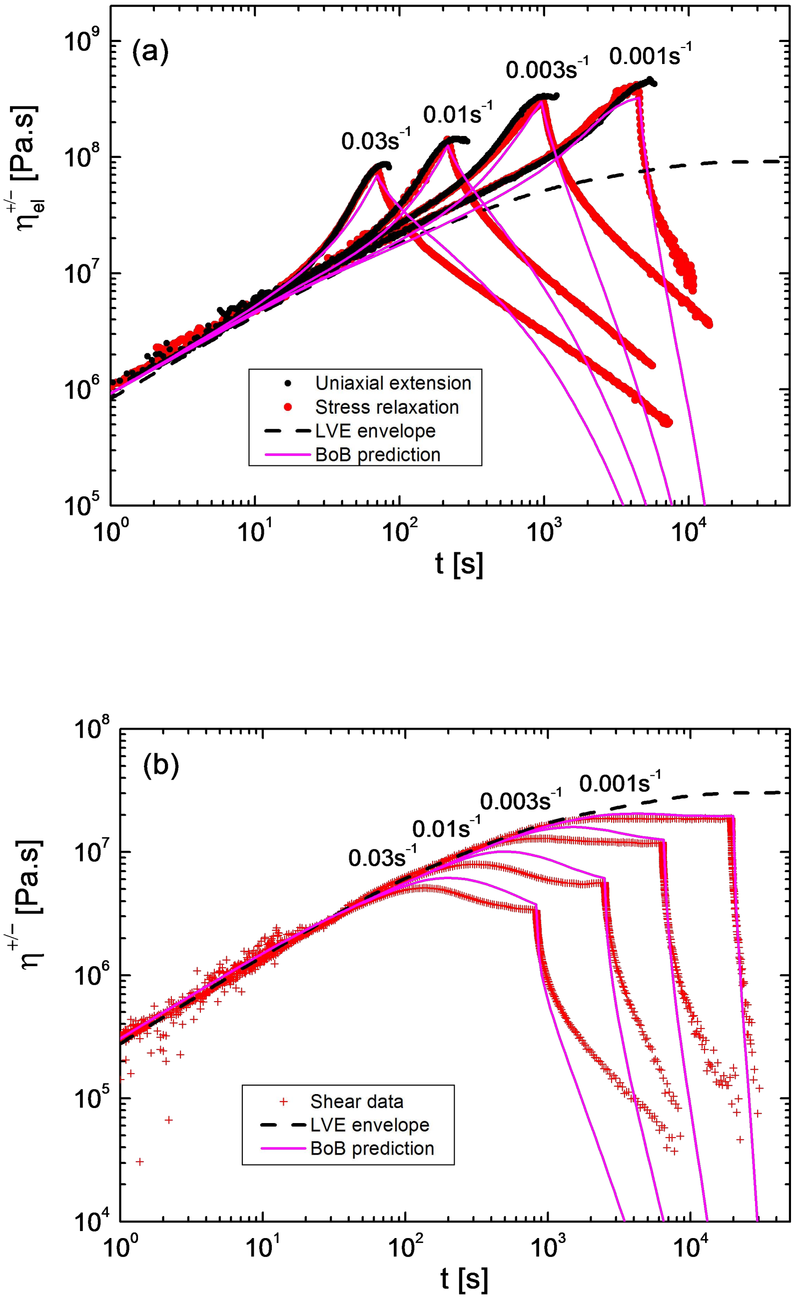

Figure 5.3: Respective data of figure 5.2 for the transient response of G4 in uniaxial extension (a) and simple shear (b). The same temperature of 180°C, rates and symbols are used, but different colors (growth depicted in red). Solid pink lines are predictions from BoB model [180].

merically. In a multimode pom-pom description, a set of such pom-pom molecules is considered, and the stress is calculated by a simple sum over stress from each of the pom-pom modes. The numerical calculation for the linear rheology prediction offers a natural choice to resolve the molecules in terms of multiple *independent* pom-pom modes [95, 97]. The parts of the molecules relaxing at a certain time t_c have orientation and relaxation time $\tau_0 = t_c$; the time at which these parts (segments) can move coherently with the chain ends define the stretch relaxation time τ_s. In addition, the branching topology from the currently relaxing segments define the maximum stretch of q as the priority variables [182], and the modulus relaxed in this time interval sets the modulus of the pom-pom mode. Based on the pom-pom model [51], equating the maximum tension with the tension along the backbone gives a maximum stretch of q. In the present case of Cayley-trees, we consider any molecular segment between two branch points being equivalent to an effective backbone in a pom-pom molecule. At each time interval, separate pom-pom modes are used to describe the relaxation due to chain escape from the confining tube and due to the constraint release of the chains still confined in the tube potential at this time. When the flow rate is much slower than the stretch relaxation time, the geometric criteria for assigning the maximum stretch lead to an over-prediction of the extensional hardening for randomly branched polymers, hence flow-dependent modifications of the priority variables are required in order to describe the experimental data [95, 97]. However, the available approximation for this flow modification requires vastly different relaxation times (as in industrial randomly branched low density polyethylene) and is not valid for symmetric model polymers. Fortunately, at the flow rates considered, the bare priority is found to describe the amount of extension hardening reasonably well for the two dendritically branched polymers considered here. When the flow is stopped, the stress evolution from equation (5.3) is asymptotically equivalent to

$$\frac{d\boldsymbol{S}}{dt} = -\frac{1}{B\tau_0}\left(\boldsymbol{S} - \frac{\boldsymbol{1}}{3}\right) \tag{5.4}$$

with $B = tr(\boldsymbol{A})$ [183, 184]. The trace of the auxiliary tensor has no physical significance and can become arbitrarily large. We chose to work with the tensor $\boldsymbol{A}$ during the start-up flow and construct the orientation tensor $\boldsymbol{S}$ at the beginning of the flow cessation. Subsequent relaxation in the absence of flow is calculated from equation (5.4) with the choice $B = 1$. Another commonly used variant of the stress evolution equations considers $B = \lambda^2$ [183] that couples the orientation and the stretch evolution together and requires both of these to be solved simultaneously numerically. The origin of such a coupling can be rationalized by considering the increase in the reptation time of the pom-pom backbone in the stretched backbone tube in the absence of constraint release. Since our pom-pom modes describe relaxation of different parts of a dendritic molecule, if such orientation-stretch coupling is important, its form should be different from $B = \lambda^2$. Here, the choice of $B = \lambda^2$ does not affect the approach to steady state and predicts only marginally higher steady state values of the stress. The stress decay, especially at high rates, is delayed significantly compared to the experiments (and compared to the $B = 1$ choice used here).

The solid lines in figures 5.2 and 5.3 depict the predicted uniaxial stress growth/decay coefficients for G3 and G4, respectively. Except for the lowest flow rate for G3, the stress growth coefficient for uniaxial extension is described reasonably well. But eventually, in all cases, the experimental relaxation becomes much slower than predicted. The experimental long-time relaxation is approximately power-law decay (linear in log-log plot). Such a nonexponential behavior may reflect coupling between different modes (see also discussion on the parameter B above): The stretches in different segments of the dendritic macromolecule are coupled, hence describing them as relaxing independently is not completely correct [99, 173]. Once stretched, the stretch of inner segments can only relax after that the stretches in the outer segments had already relaxed. This sets a formidable challenge for future work. We further note that the start-up shear predictions (in figures 5.2(b) and 5.3(b)) show significant overshoots absent in the experimental data. The physical origin of such overshoot in the pom-pom model is due to stretching of the tubes as they start orienting along the flow. We conjecture that the short segments in the experimental system prohibit such stretch and stress overshoot. The steady state shear stress is described reasonably well. The stress relaxation after shear cessation is described well except for the high rates for G4, but as already mentioned, there is a possibility of structural polydispersity in the dendritic polymers, which can affect flow properties in different ways.

5.2.3 Compilation of data and scaling

A phenomenological analysis of the evolution of material functions in uniaxial extension and shear is presented in figure 5.4. A measure of the level of strain hardening achieved can be obtained by the strain hardening factor SHF, which is defined as the ratio of the stress growth coefficient $\eta_{el}^{+}(t,\dot{\varepsilon})$ to the respective LVE value, $SHF = \eta_{el}^{+}(t,\dot{\varepsilon})/\eta_{LVE}^{+}(t)$ and is plotted in figure 5.4(a) for the different values of strain rates used for G3 and G4. The onset of strain hardening is marked by the departure of SHF from 1. The stronger hardening of G4 compared to G3 at the same stretch rate is evident. On the other hand, focusing on the G3 data, there is an unambiguous nonmonotonic dependence of SHF and in particular its peak value on stretch rate. First, we note that at rates $\dot{\varepsilon} \geq 0.03$ s^{-1}, i.e., above the terminal moduli crossover where segments are not fully relaxed (figure 5.1), the SHF is expectedly enhanced with increasing rate. On the other hand, as the stretch rate decreases below its terminal value, an increase of SHF is observed. The latter is a consequence of the definition of SHF and the shape of the LVE envelope. Eventually, at lower rates SHF will drop to 1, at the linear

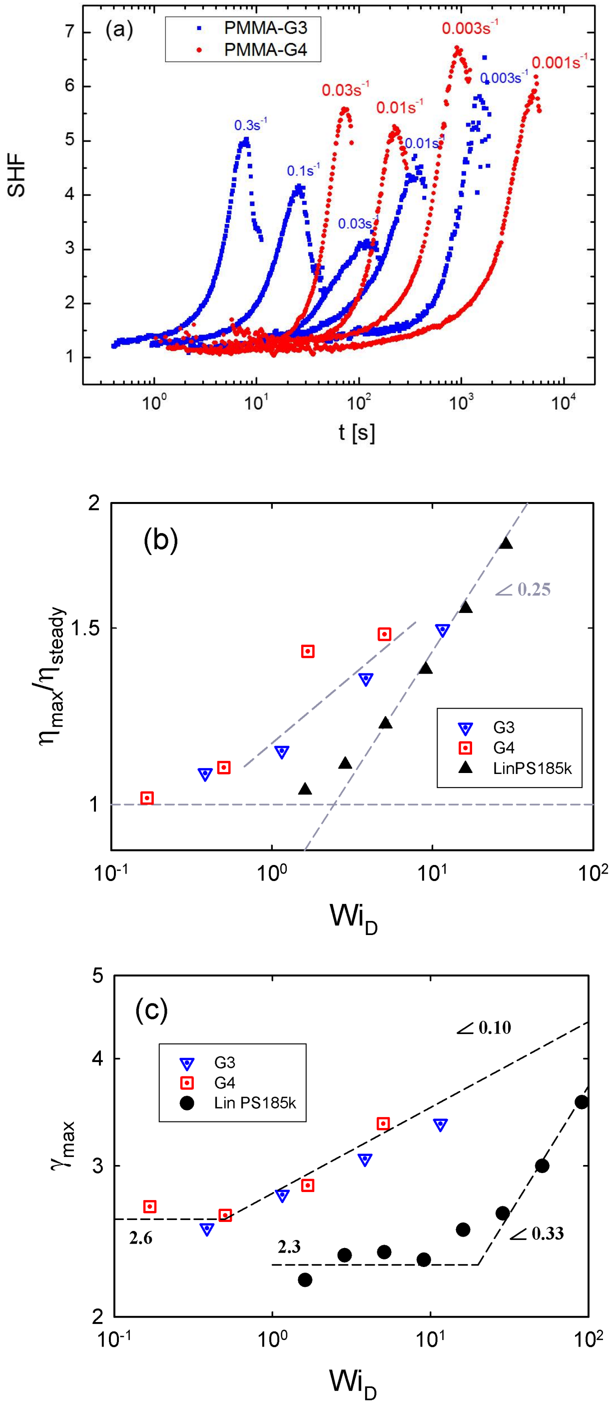

Figure 5.4: (a) Strain Hardening Factor (SHF), namely the ratio of the stress growth coefficient to the respective LVE value at different stretch rate for G3 (blue) and G4 (red).(b) Normalized peak viscosity and (c) peak strain at the maximum viscosity as functions of the Weissenberg number based on the inverse terminal G'-G'' crossover (see text). In (b) and (c), we show for comparison data with linear polystyrene LinPS185k, whereas the lines are drawn to guide the eye (see text) [180].

envelope. The (fewer) data with G4 are consistent with this picture. The important message is that these dendritically branched polymers strain harden significantly even when stretched at rates below their terminal rate, in sharp contrast to linear or star polymers [185]. Furthermore, in figure 5.4(b) we plot the fractional overshoot in shear viscosity $\eta^+(t,\dot{\gamma})_{max}/\eta^+(\dot{\gamma})_{steady}$ against Wi_D, for G3 and G4. Wi_D is the Weissenberg number based on a characteristic time τ_D, extracted from the inverse moduli crossover frequency as discussed above, $Wi_D = \dot{\gamma}\tau_D$. The viscosity overshoot is a measure of maximum shear deformation of the dendritic polymers at steady state. For comparison, we include in this figure data from the literature [92] with linear polystyrene of molar mass 185k (about 14 entanglements, see chapter 4). First, we note that at low rates (up to about $Wi_D = 1$) there is no overshoot. We further observe that the data for both G3 and G4 are very close, almost collapse (given the experimental uncertainties) and exhibit a different (stronger) dependence on Wi_D compared to entangled linear polymers (which exhibit a power-law with exponent 0.25). However, the available dendritic data are not enough in order to extract a reliable power-law exponent. The value of shear strain at the viscosity overshoot is plotted against Wi_D for G3, G4 and the linear polystyrene in fig5.4(c). First, at low Wi_D the data are constant, indicating a saturation of peak strain (which is the maximum instantaneous shear deformation). For linear polymers this value is 2.3 and known to reflect segmental orientation as predicted by the tube model. For comb polymers, this value is also about 2.3 as reported by Snijkers *et al.* [54]. For the dendritic Cayley trees here, the available experimental data suggest a value of 2.6 [figure 5.4(c)]. Furthermore, with increasing Wi_D the peak strain increases, reflecting stronger deformation (stretching). It follows power-law with exponent of 0.33 for linear polymers and much smaller (0.1) for both dendritics. This result reflects the molecular structure which makes it more difficult to deform a Cayley-tree (more) compact structure compared to a linear flexible polymer. Since the issue of steady state is one of the challenges, we elucidate this further in figure

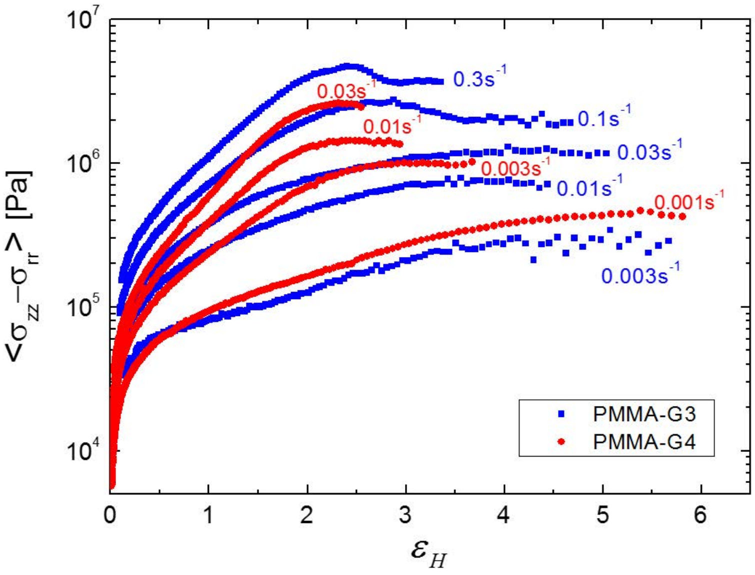

Figure 5.5: Net tensile stress for G3 (blue) and G4 (red) versus Hencky strain for different values of the imposed Hencky strain rate, at 180°C [180].

5.5, where the tensile stress for both G3 and G4 is plotted against the Hencky strain for the different values of Hencky strain rate tested (in figures 5.2 and 5.3). Indeed, this figure demonstrates the attendance of steady state for both polymers. Steady state is reached at lower values of Hencky strain for larger Hencky strain rates. Moreover, for the two larger rates of G3, one may note the appearance of a broad overshoot. Such overshoot has been reported for branched polymers [50] but here the limited data do not allow further discussion. Understanding the extensional overshoot remains a challenge in the field; however, the present polymers are not amenable to the currently available experimental window. The steady state extensional and shear viscosities are plotted together versus the respective Hencky strain and shear rates in figure 5.6, along with the dynamic viscosity data (versus oscillatory frequency). The latter are multiplied by 3 (Trouton ratio). It is noted that the empirical Cox–Merz rule validated for this class of hyperbranched polymers. This is not expected to a first sight since branching contributes to deviations from this rule [186]; however, we note that the

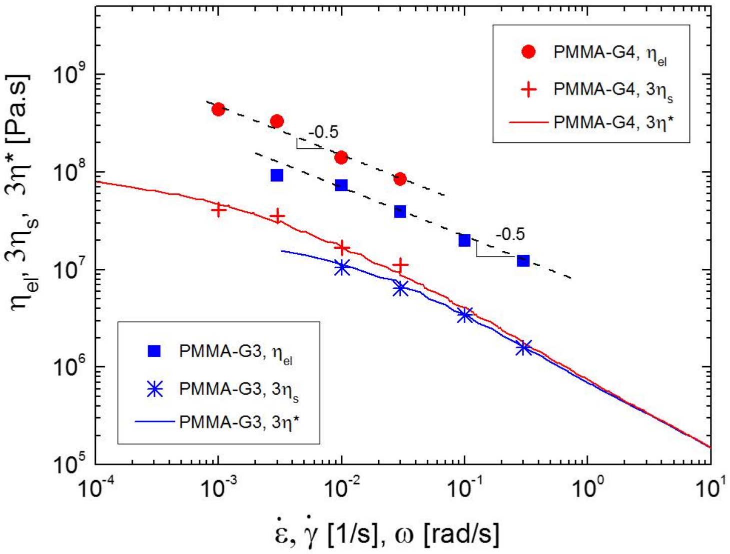

Figure 5.6: Steady-state data on extensional viscosity (open symbols), shear viscosity (crosses and stars) and dynamic complex viscosity (solid lines, multiplied by the Trouton ratio 3) plotted against Hencky strain rate, shear rate and oscillatory frequency, respectively, on the same axis. Data are shown for G3 (blue) and G4 (red). The dashed lines through the extensional data have a slope of -0.5 [180].

branches are barely entangled and this may be at the origin of the good agreement of dynamic and steady shear data. Moreover, both shear/dynamic and extensional data exhibit thinning with increased rates. In the former case, the shear data follow a scaling law with thinning slope of -0.7 for both generations, which is smaller than the usual slope of about -0.82 which has been reported for entangled linear polymers [92, 140]. On the other hand, the extensional data exhibit a thinning slope of -0.5, again for both G3 and G4, with the latter having higher values (see also fig5.2 and 5.3). This complies with the BoB predictions and further confirms earlier findings with linear or pom-pom polymers [169] and is explained in the context of tube modeling [187]. Finally, the shear/dynamic data are always below the respective extensional data, due to strain hardening in this range of rates (see figures 5.2(a) and 5.4(a)). Futhermore, we remark that the extensional data do not show a tendency to overlap the dynamic and shear data at low rates, as is normally expected. However, it is reported that for branched polymers the steady viscosity in uniaxial extension is constant at low stretch rate (it overlaps with $3\eta^*$), then it exhibits extension thickening and after an overshoot it thins at higher rates [188, 189], as illustrated in figure 5.7.

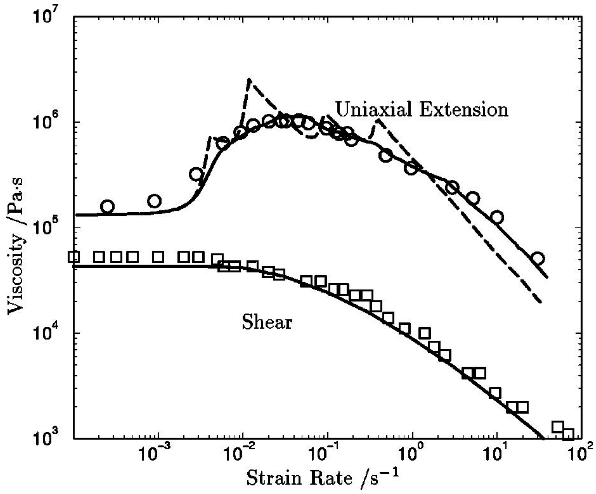

Figure 5.7: Shear and extensional steady state viscosities of branched IUPAC A LDPE from reference [188] (symbols, experimental data; lines, model predictions).

Based on this, we conjecture that the data of figure 5.6 are in the thinning regime past but close to the peak, and they are above the level of the zero-rate viscosity (not reached) which is expected to coincide with the zero-shear dynamic and shear viscosities, accounting for the Trouton ratio.

5.2.4 Stress relaxation upon flow cessation

Figure 5.8 reports the stress relaxation data upon cessation of shear or extensional flow, for the two dendritic PMMAs, G3 (a) and G4 (b). In the latter case, stress relaxation was recorded after cessation of steady shear flow. In the former case, the extensional flow was arrested before (albeit close to) the steady state and at nearly the same deformation in terms of Hencky strain (values reported in the caption). In the same figure, we plot the relaxation modulus $G(t)$ extracted from the LVE data of figure 5.1. Finally, four dashed vertical lines are plotted, representing the characteristic Rouse time of an effective outer branch/arm ($\tau_{R_{Arm}}$) and the whole dendrimer ($\tau_{R_{Bare}}$), as well as the characteristic terminal times extracted from the low-frequency crossover ($\tau_{D_{CO}}$) and from BoB modeling ($\tau_{D_{BoB}}$). We observe that the nonlinear stress relaxations in shear and extension are very different from the linear relaxation. In shear, for a wide range of times, up to about 1 s, the stress is almost constant (this is more evident in figure 5.9 due to different scale). Subsequently, relaxation becomes more pronounced, and beyond $\tau_{D_{BoB}}$ the stress for both G3 and G4 becomes essentially independent of the rate (i.e., the material loses its memory) and relaxes by linear mechanism as $G(t)$. Indeed, one expects that after nonlinear deformation polymer reorganizes and relaxes thermally according to its $G(t)$ in the end. The situation is different for the extensional data. Similar to the shear case, the net tensile stress relaxation data remain distinct for different stretch rates at short times, suggesting that the nonlinear induced state of the material has not relaxed during the experiment, whereas they virtually collapse (especially for G3) at longer times above $\tau_{D_{BoB}}$. Remarkably, even if at these times the polymeric response is linear, it is evident from both figures 5.8(a) and 5.8(b) that complete relaxation of this stress is slower than $G(t)$. This suggests the strong effects of initial extensional deformation, even at very low stretch rates. Note, in particular, that the two lowest rates used with G4 (10^{-3} and 3×10^{-3} s^{-1}) are below the Rouse rate of the outer segment, yet strong strain hardening is observed (figure 5.3) and strong nonlinear effects dominate the subsequent relaxation. It is evident that the extensional relaxation is much broader than the respective linear and nonlinear shear, and as a consequence, the extensional stress will relax well after complete relaxation of $G(t)$. As already noted above in conjunction with the description of the data of figures 5.2 and 5.3, this interesting effect should reflect the coupling of stretch in different parts (generations) of the dendritic macromolecule, and is of course much more significant in extensional deformation, in the examined parameter range. As a result of this coupling, the stress relaxation upon cessation of uniaxial extensional flow is expected to be substantially delayed. For completeness, we note that a similar behavior was

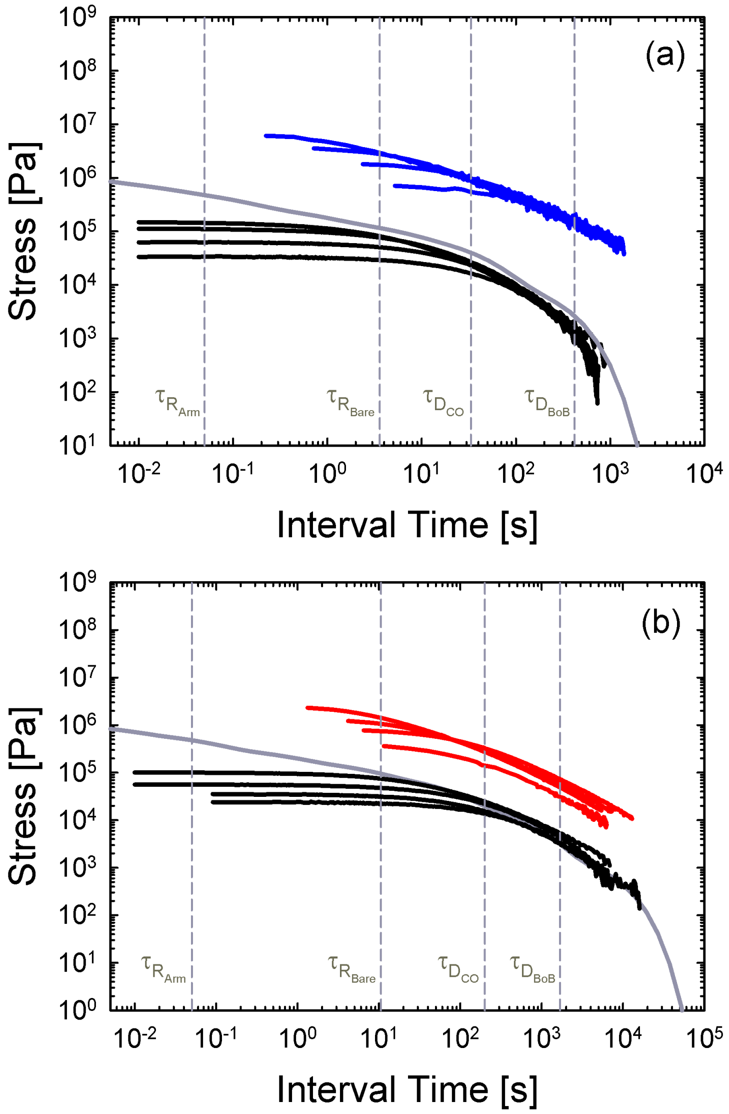

Figure 5.8: Stress relaxation of G3 (a) and G4 (b) as a function of time. Interval time is the difference between the absolute time and the time when relaxation starts. Blue curves are for the relaxation of G3 (a) and red curves for G4 (b) after extension. Black curves show the relaxation after shear in both cases. The applied rates and accumulated strain at cessation of flow are: (a) for shear, from top to bottom 0.3, 0.1, 0.03 and 0.01 s^{-1} (20 strain units for each shear rate); for extension, from top to bottom: 0.1, 0.03, 0.01, and 0.003 s^{-1} (3 strain units for each extension rate). (b) For shear, from top to bottom at short times 0.03, 0.01, 0.003, and 0.001 s^{-1} (25 strain units for each shear rate); for extension, from top to bottom 0.03, 0.01, 0.003, and 0.001 s^{-1} (corresponding strain units: 2.1, 2.2, 3, and 4.5, respectively). The relaxation modulus curve of the respective dendritic polymer is reported in both figures as a reference (gray line). The characteristic Rouse times of the outer branch ($\tau_{R_{Arm}}$) and the whole molecule ($\tau_{R_{Bare}}$), as well as the characteristic terminal times from the low-frequency crossover ($\tau_{D_{CO}}$) and from BoB modeling ($\tau_{D_{BoB}}$) are reported as reference (see text) [180].

reported recently for bidisperse blends of long and short linear polystyrenes undergoing relaxation after uniaxial extension was stopped [178]. In particular, for a blend of 50% short (seven entanglements) - 50% long (41 entanglements) linear polystyrene chains, the elongational stress relaxation exhibited power-law with an exponent of about -1 and appeared slower than that of either components. This was attributed to the remaining, persistent flow induced orientation of initially retracted long chains in a sea of relaxed short chains. The analogy with the present work is that the induced orientation can be considered as coupling of stretch in different chains. Concerning the present data, given the small range of times, we refrain from considering power-laws. Unfortunately, we do not have independent information of the flow-induced stretching in different generations and respective relaxation upon flow cessation (in fact, very limited data exist in general [168, 171, 190]), since this requires deuterated samples which are not currently available. To further elucidate the different relaxation after shear and extensional flow, we represent the data of figure 5.8 in normalized form in figure 5.9. In particular, the decreasing transient stresses $\sigma_{el}^{-}(t)$ for extension or $\sigma^{-}(t)$ for shear are normalized by the corresponding values of extensional stress growth coefficient when extensional flow was stopped (at almost the same value of Hencky strain $\varepsilon_H = 3$ for G3 and steady stress for G4) or shear stress at steady state (albeit at constant shear strain of 20). The broader and slower relaxation of extensional stress compared to shear stress is unambiguous for both G3 (a) and G4 (b). We note further that elongational flow (with zero vorticity tensor) deforms the polymer more severely than shear, despite the lower strain. Concomitantly, the viscosity is much higher in the former case due to hardening (figure 5.6). Concerning G4 (figure 5.9(b)), the relaxation is slower compared to G3 (figure 5.9(a)) and again broader relaxation in extension as opposed to shear is evident. Although the data can be agreed in this context, for quantitative analysis further work will be required in the future, especially accounting for the coupling of stretches as mentioned above.

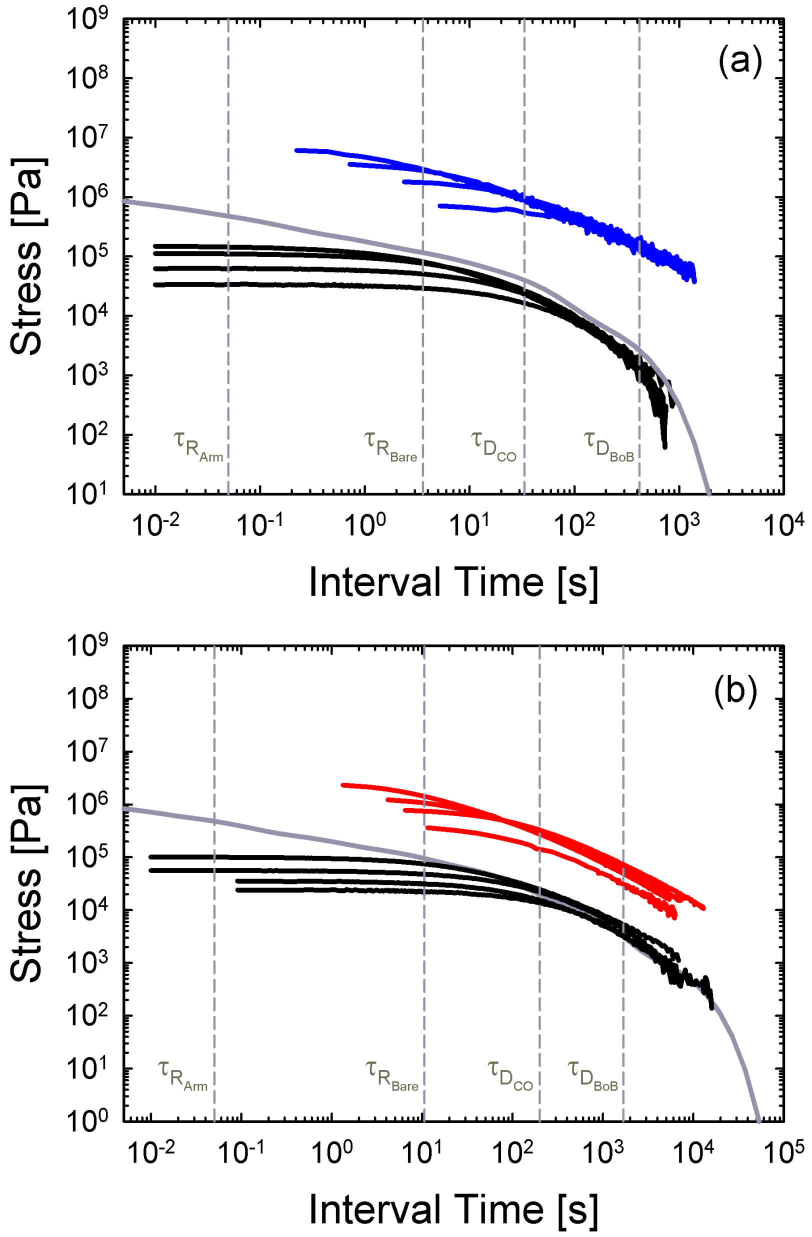

Figure 5.9: Data of figure 5.8 normalized by the respective values of shear stress or stress growth coefficient when shear or extensional flow was stopped (see text). Characteristic times are reported for reference as in figure 5.8 [180].

5.3 Concluding remarks

We have investigated the growth, steady state and subsequent relaxation of viscosity during uniaxial extensional and shear deformation of model, well-characterized Cayley-tree PMMA structures of third and fourth generation, having short, equal branches (about 2.4 entanglements each). The experimental data were obtained with the state-of-the-art instrumentation (FSR and CPP). The extension and shear rates cover a range extending from LVE terminal relaxation to rubbery regime. Despite the small values of the imposed rates, significant strain hardening was observed. At the same time, viscosity overshoots signaled the deformation of these polymers in shear as well. Extensional relaxation is broader and slower than in shear. The latter is different from that of the linear stress (or relaxation modulus $G(t)$) but at long times it appears to approach it. The unusual relaxation of viscosity upon cessation of uniaxial extensional is consistent with a stronger deformation in extension and the related strain hardening. The BoB framework based on independent pom-pom modes describes the experimental data in linear and nonlinear shear (growth and relaxation) and extension (growth and initial relaxation) reasonably well and without fit parameters. This is remarkable considering the fact that a segment between two branches in these molecules is less than three entanglements long. The slow relaxation upon cessation of extensional flow may reflect coupling of the stretches in different generations. To describe it, the pom-pom modes cannot be considered as independent, hence a modified model should be considered. Whereas this calls for further investigations, it shows a way to use strong flows for tailoring properties of polymeric materials and effectively enhancing their elastic memory. Furthermore, there is unambiguous evidence of steady state in extension. The small molar mass of branches appears to be responsible for the validation of the empirical Cox–Merz rule. At the same time, the high-rate regime in extension follows a thinning slope of -0.5 in accordance with predictions and findings with linear and branched polymers. This power-law is virtually followed by the shear data as well. In general, at first sight it is a surprise that BoB does such a good job in predicting the linear and non-LVE of such a polymer with barely entangled branches. We attribute this to the difference in the strength of the entanglement constraints at the branch point as opposed to the respective linear entangled polymers. This ensures that the dynamics of the inner segments remain dominated by the branch-point friction instead of the monomer friction and a framework based on the well-entangled polymers continues to capture the relaxation of unentangled (in the dilated tube) inner segments. In fact, the present case may be thought of as the limit of validity of the BoB model. The present work should motivate further investigation with similar systems, both in experiments and theory, in order to test the stretch coupling conjecture and predict viscosity relaxation consistently in shear and extension and eventually advancing constitutive modeling. At the same time, measurements of polymer conformation *in situ* or *ex situ* (by quenching deuterated samples below glass temperature during flow and analyzing them via Small Angle Neutron Scattering) and attempts to probe nonlinear material functions (including normal stresses) at higher rates will further advance the field.

Chapter 6

ASSOCIATIONS AND TOPOLOGY IN DENDRONIZED POLYMERS

6.1 Introduction

Dendronized polymers [57, 87, 191, 192] (DPs) combine the concepts of polymers and dendrimers and can be considered as promising candidates for applications in emerging fields of technology involving nanocarriers [193], bioconjugates [194, 195] or catalysis [196]. The ability to tailor a polymer's effective thickness and functionality in a controlled and well-defined manner sets DPs apart from conventional polymers but makes them somewhat similar, albeit not identical, to bottlebrush polymers [56, 197–199]. It turns out that thickness affects liquid crystalline transitions in semi-flexible polymers [200]. This is an inherent molecular parameter in DPs which possess a modular structure. An efficient strategy for the preparation of DPs with a minimum of synthetic steps relies on the use of bi-, tri-, or multifurcated dendritic building blocks in a stepwise, repetitive reaction sequence. The grafted structure on each repeat unit, which represents the effective thickness between the polymer backbone and the periphery, is referred to as the dendron generation, g. Hence, the representatives of such a homologous series allow for systematic, generation-dependent studies of structure-property relationships. To be consistent with earlier studies, we call this series PG (polymer generation) and identify them by their respective g and degree of polymerization, P_n. Note that in DPs, besides P_n and g, there is the functionality of junctions (i.e., molecular structure of dendrons) as an additional parameter that does not exist in bottlebrushes (see figure 6.1 for the different structures).

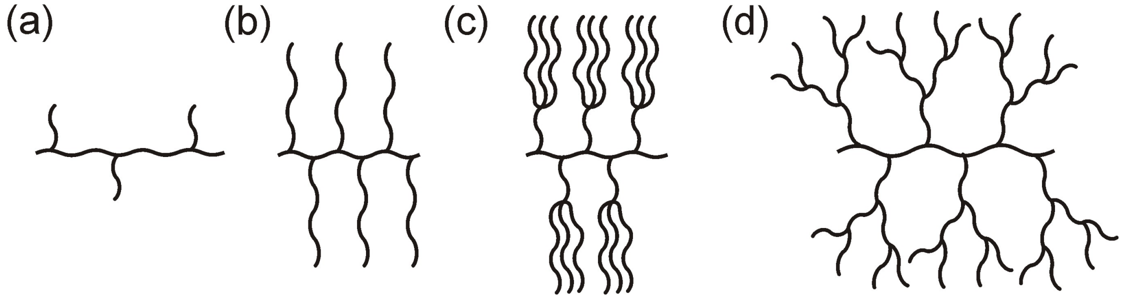

Figure 6.1: Cartoon illustration of (a) comb, (b) bottlebrush, (c) wedge and (d) dendronized polymers.

DPs are more compact than bottlebrushes because dendrons induce larger steric crowding around the backbone compared to linear chains; hence their width is better defined. There is also the possibility to insert functional groups at different grafting points of the inner part of the molecules by suppressing the growth of one side of the dendritic branches. Moreover, unlike bottlebrushes, where the volume of the side branches increases linearly with length, in DPs the dendritic branches experience a 2^g increase of mass and hence of their volume. As a result, the increase of the degree of local packing (and persistence length) upon increase of the length of the side branches is much more dramatic. Therefore, DPs are more tunable than bottlebrushes. It has been proposed that the rheology of DPs is dominated by the strong intermolecular interactions, which are enhanced with increasing generation, at the expense of intramolecular ones [108]. These interactions arise from hydrogen bonding and $\pi - \pi$ stacking of different groups [108, 201]. Variation of g and P_n appears to be a promising strategy for investigating the interplay of the interactions in DPs and tailoring their rheological response. So far, only the effect of g on linear viscoelasticity of DPs with constant P_n has been examined. It was found that increasing g strongly enhances the viscoelastic moduli and reduces their frequency dependence over an extended frequency

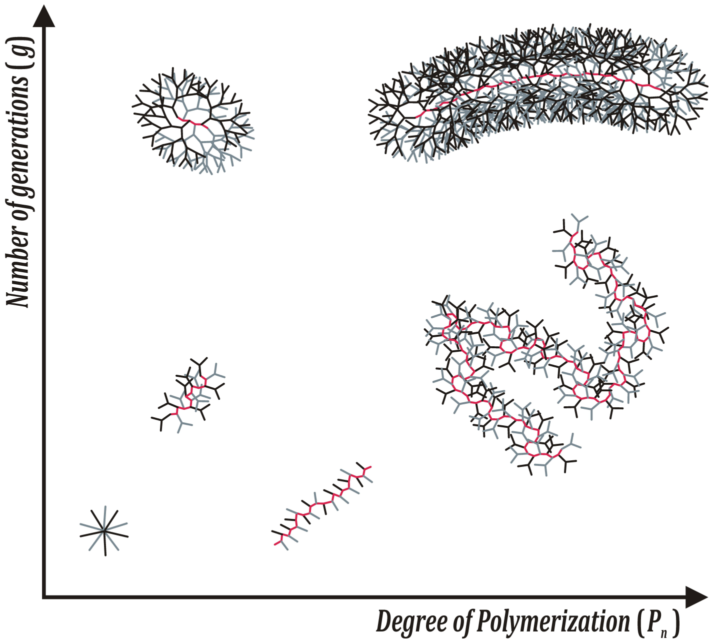

Figure 6.2: Schematic illustration of possible structures of dendronized polymers as a function of the key structural parameters, namely, the degree of polymerization of the backbone, P_n and the generation number of the dendrons, g. When branches are linear chains, the condition $g = 1$, $P_n = 1$ correspond to star polymers and the conditions $g = 1$, $P_n > 1$ correspond to comb or bottlebrush polymers. In general, the length of the effective side chain is proportional to g [202].

range [108]. By systematic variation of both g and P_n it is possible to map the properties of macromolecules into the diagram shown in figure 6.2 and, in principle, tailor their properties only with these two parameters. Here, we restrict the present discussion to the bulk behavior in the melt. We illustrate here the changing macromolecular conformation which allows spanning the range from branched oligomeric structures (low g, low P_n), to flexible polymers akin to shortchain branched systems (low g, large P_n), to colloidal molecules with shape slightly and gradually departing from spherical (large g, low P_n), and to semi-flexible wormlike moecules(large g, large P_n). One may already appreciate the functional character of DPs and ability to selectively span the gap between polymeric and colloidal behavior. In this regard, the sequential mode of DP synthesis enables access to potentially monodisperse side chains and much more sterically encumbered structures, which sets them apart from bottlebrush polymers, for which only the low-g region of figure 6.2 is relevant. The main challenge is to link this qualitative plot with properties so as to obtain the needed information for designing complex macromolecules with desired response. In this chapter we address this challenge and investigate systematically the role of combined variation of g and P_n on the structural and rheological properties of DPs. The synthesis and characterization of the chosen series of DPs is presented in section 2.1.4. Here, we present detailed experimental work involving rheology and X-ray scattering, and interpret the results with the support of simulations. Supplemental information about experimental procedures (i.e., differential scanning calorimetry, gel permeation chromatography, X-ray scattering and rheology) and simulations are given in section 2.5.

6.2 Results and discussion

6.2.1 Differential scanning calorimetry

All DPs in this study (Table 2.2) are amorphous materials featuring clearly visible enthalpy steps at the glass temperature. At room temperature, the DPs are in a glassy state. Figure 6.3 illustrates their compiled T_g values, which are obtained from the second DSC heating runs.

The steps in the DSC traces (i.e., PGs with $P_n = 1500$ in figure 6.4) reflect changes of enthalpy with increasing generation, consistently, suggesting that lower specific heat and smaller heat flow are involved in the liquid-to-glass temperature of higher generations. In addition, the width of the glass temperatures appears to increase with generation, which may be better seen in the differentiated DSC traces and is in accordance with respective data obtained for similar systems [203]. Previous MD simulations [108] suggested that in the present DPs the radial distribution of the terminal (end) Boc groups around the backbone exhibits a maximum, which clearly shifts toward the periphery with increasing polymer generation. Consequently, it can be argued that the prevailing fraction of terminal Boc groups resides near the outer surface (periphery)

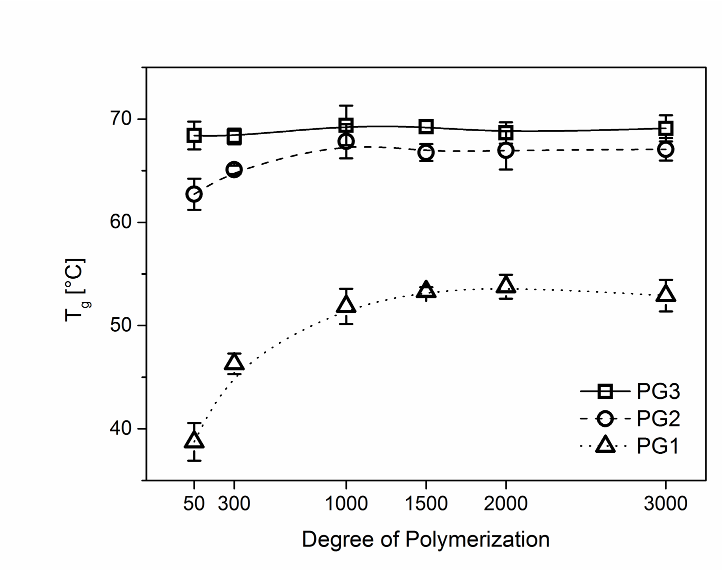

Figure 6.3: Glass temperatures of DPs as a function of P_n and g. The lines are drawn to guide the eye [202].

of the DPs. This can be rationalized especially at higher generations by the enhanced crowding that makes back-folding less probable. In light of the above, attributing the variation of the T_g values to the corresponding changes of the molecular structure, as is the case for conventional branched [204] or hyperbranched polymers,[203–205] seems tempting. Hence, we provide a rationalization of the results here, without accounting however for the fact that the segments between branching points in the present DPs are very short and the peripheral end groups in particular are involved in intra- and intermolecular bonding interactions. For linear amorphous polymers, the glass temperature originates from short-scale cooperative segmental motions and reflects the rigidity of the backbone. In DPs, however, the glass temperature may be affected by various parameters, such as the nature and number density of the branching points and the compactness of the structure, the number and chemical properties of the peripheral end groups, and the strength of bonding interactions [112]. Here, both the number of branching points and the number of end groups increase with generations. From a dynamic point of view, end groups and branching sites affect the glass temperature in opposite directions: Increased branching reduces the local segmental mobility due

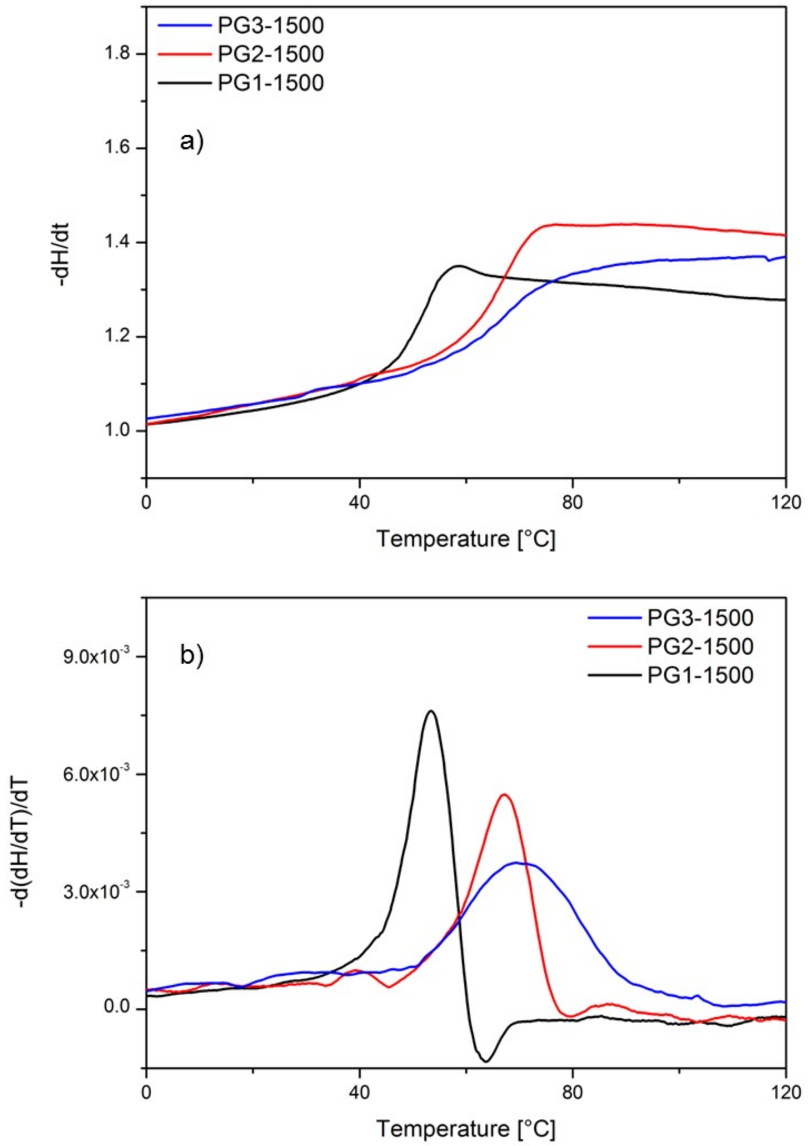

Figure 6.4: DSC traces for the samples PGs with $P_n = 1500$.

to denser packing and, hence, contributes to an increase of T_g. On the other hand, a larger number of dangling end groups enhances local fluctuations, and therefore the glass temperature decreases [203, 206, 207]. In the present PG1, PG2, and PG3 series, T_g increases with generation and eventually levels off, which is in line with existing reports showing that T_g increases with g approaching a final value, and no significant changes are found after approximately the fourth generation [108, 204, 207]. The saturation of T_g reflects increasing backbone rigidity due to the bulky pendant side groups in these DPs and can be considered analogous to the respective saturation with molar mass in linear polymers and dendrimers [208–210]. In addition, the presence of peripheral Boc and phenyl groups that engage in intra- and intermolecular bonding is arguably responsible for the increase of T_g with generation. In fact, WAXS data (discussed below) indicate the presence of very broad short-range correlations (typically at scale of about 0.35 nm), which provide indirect support to this argument. Moreover, various studies on the thermal behavior of dendrimers [206, 207] and other branched polymers [211–213] have shown that the nature of the chain ends significantly affects the T_g of dendritic macromolecules, with increases in chain-end polarities generally causing an increase in T_g values. Hence, dense branching and bonding groups reduce local mobility. As a consequence, the distribution of the local relaxation times and concomitantly the glass temperature are affected, as also supported by MD simulations [214]. In addition to the role of dendron generation and peripheral end groups, an influence of the backbone chain length on the effective glass temperature is also observed. This holds unambiguously true for the PG1 series, whereby the samples comprising the smallest degrees of polymerization (nominal $P_n = 50$ and 300) are characterized by lower T_g values by approximately 10 and 5°C, respectively. We note that the reduced T_g in samples with lower P_n is a well-known feature of linear polymers and attributed to the enhanced backbone mobility due to the presence of main-chain ends. In this respect, PG1 series bear similarities to linear polymers. However, in PG2 and especially in PG3 series, this feature is absent; i.e., T_g becomes independent of chain length. This is a consequence of the increased backbone rigidity even in the samples with the lowest degrees of polymerization. The backbone rigidity is expected to affect the degree of chains packing and will be discussed with respect to the X-ray results below. One important advantage of our present polymers is that the degree of polymerization in each homologous series remains almost constant, which allows for systematic investigation of properties as a function of generation (figure 6.2). Combined with the range of backbone lengths of the synthesized polymers, a separation of the effects resulting from variation of generation and degree of polymerization is in fact possible, and the results of figure 6.3 demonstrate that thermal properties can be tailored via generation growth and backbone length of the DPs.

6.2.2 Equilibration kinetics

One intriguing aspect of the molecular dynamics of dendronized polymers is their very long equilibration time [201]. As already mentioned, their synthesis is carried out in a dilute environment where the probability that the polymers form supramolecular bonds is very small. After the synthesis, the solvent is removed through a freeze-drying process which does not imply any increase of concentration of the reaction medium and thus does not allow molecules to interact with each other to a large extent. Therefore, DPs are far from equilibrium, and undergo physical aging. Above T_g, the molecules have enhanced mobility, tend to reduce local density gradients due to their monomer density profile (via partial interpenetration of the dendrons), and form supramolecular bonds as well [108]. Note that. as shown by simulations in accord with literature [108], the density profile indicated a gradient in monomer density which yields interpenetration in the melt. While the radial density profile is flat (plateau) at small distances, it decays within decreasing distance to the outer surface. Because of interpenetration, the total density is basically constant (in the melt). There is a

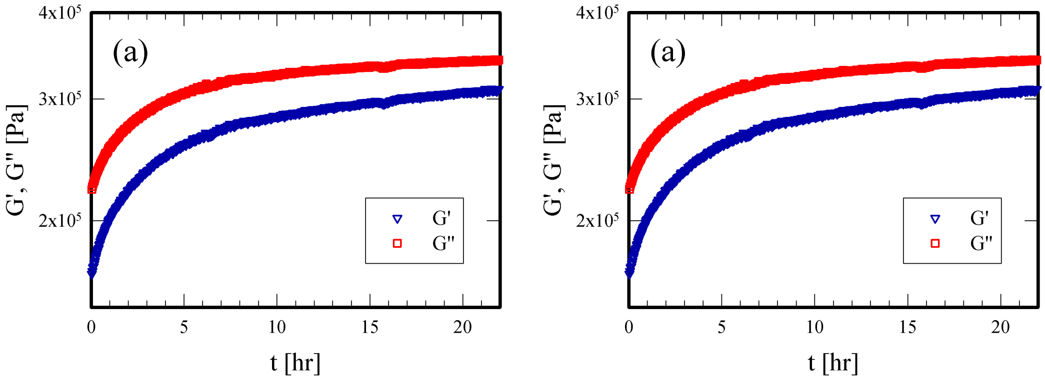

Figure 6.5: Results of equilibration kinetics dynamic time sweep tests of sample (a) PG2-2000 at $T = 100$°C, angular frequency $\omega = 1$ rad/s, and strain $\gamma_0 = 1\%$ (here, $G' < G''$) and (b) PG2-3000 at $T = 100$°C, $\omega = 1$ rad/s, and $\gamma_0 = 1\%$ (here, $G' > G''$) [202].

clear distinction between radial density profile and density. The equilibration process was monitored by measuring the temporal evolution of the dynamic moduli in the linear regime. In order to fully equilibrate the samples in the rheometer, we annealed them for a very short time. Moreover, loading of the samples into the rheometer was performed as fast as possible: each sample was loaded and squeezed between the measuring plates, and then after 20 min of thermal equilibration in the instrument, we performed a strain sweep test to assess the linearity range. Subsequently, we carried out a time sweep test in order to follow the equilibration process. Typical equilibration curves are shown in figure 6.5. We attribute the observed unusually long equilibration times to the above-mentioned weak interpenetration of the dendrons (at the level of the outer generation). Given the structure of the dendrons, this is a complex, cooperative process involving multisegmental local motion/rotation. To reach equilibrium, spatial rearrangement at large length scales (comparable with the length of a dendron) is necessary. For this reason, the time required for a complete equilibration is of the order of 20 hours at 30°C above the glass transition temperature. However, for PGs, the presence of bonding provides a directionality and, at the same time, limits the area of the cooperative interpenetration process since the local motion of dendrons is more restricted given the barrier from the bonding (see figure 6.10). This should result in a

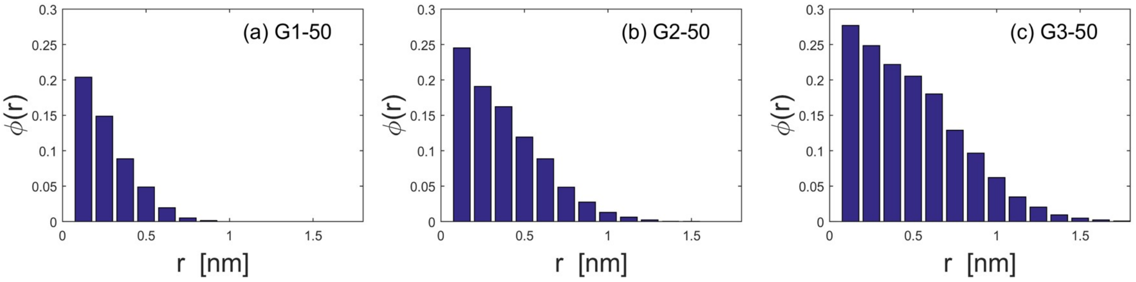

Figure 6.6: Simulated radial volume fraction profiles for the homologous series PG1-50 (a), PG2-50 (b), and PG3-50 (c) [202].

faster equilibration compared to unfunctionalized dendronized polymers [215].

6.2.3 Molecular interactions from simulations

Simulations of DPs were carried out by dr. Martin Kröger at ETH, Zurich. As explained in section 2.5, all simulations were performed for the $P_n = 50$ homologous series; hence we discuss here the effect of g. Figure 6.6 depicts the monomer density profiles for $g = 1$, 2, and 3. It is evident that DPs exhibit a g-tunable polymeric brush behavior, becoming more *compact* objects (toward molecular colloids) as the generation increases. Moreover, the decrease of (intramolecular) monomer density toward the periphery of the DPs explains the interpenetration in the melt, necessitated by the need to reduce local density fluctuations [108, 201]. In addition, here intermolecular interactions (discussed below) take place. It should be noted that the sum of intra- and intermolecular densities leads to a uniform density profile. The volume fractions are unrealistic, as we are considering a system of hard spheres. Actually, the melt density of the hard sphere system was chosen so that the probability for not discarding a whole configuration by the above procedure was below 1%. We varied this criterion, and all results were found to be insensitive to the precise value, as long as it does not exceed 1%. Larger values correspond to the situation encountered in dilute solution. The emerging picture is further elaborated in the snapshots of figure 6.7 where single DPs of different generations are shown (top) and the respective compactness of PG3-50 (more colloid-like) compared to PG1-50 (polymer-like) can be appreciated. Further, when such DPs are in the melt, they indeed interact at the periphery as seen in the cross-sectional view of figure 6.7 (bottom), leading to a uniform bulk density. We simulate a single DP in a simulation box with hexagonal cross section and periodic boundaries by the procedure discussed in section 2.5. To visualize this system, we

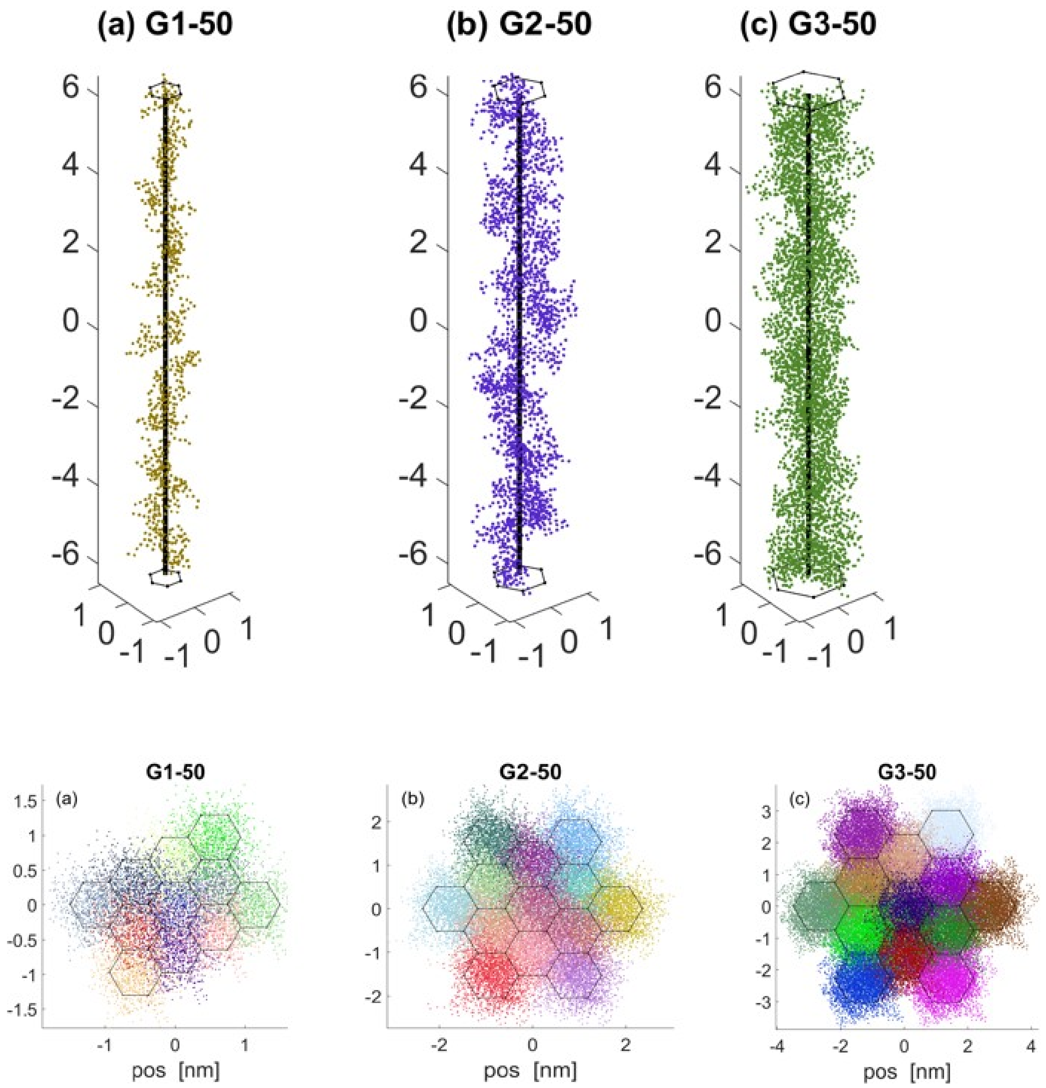

Figure 6.7: Top: snapshots of single DPs from the homologous series PG1-50 (a), PG2-50 (b), and PG3-50 (c). Bottom: respective cross-sectional view in the melt with constant bulk density. Positions (pos) are in nm. Note that we plot the unfolded DP for all shown boxes successively on top of each other to be able to still see the unwrapped molecule. The melt density is fixed by the volume of the central simulation cell and the number of hard spheres it contains (see text) [202].

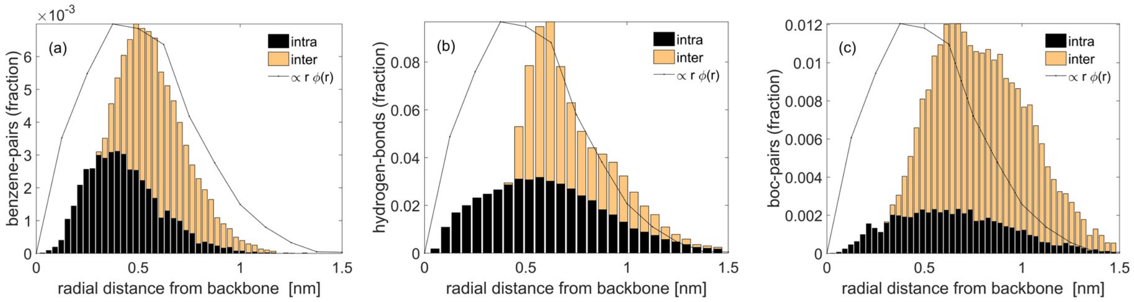

Figure 6.8: Indicative pair-distance distribution for PG2-50 potentially interacting pairs (a) benzene-benzene ($\pi - \pi$ stacks), (b) donor-acceptor (hydrogen bonds), and (c) Boc-Boc. Both intra- and intermolecular interactions are determined. The radial distance is calculated from the backbone toward the periphery of the DP. The lines represent the product of distance and radial volume fraction profile, that is, the unscaled radial volume fraction, to be able to rate the location of the maxima relative to the location where most of the material resides [202].

show in figure 6.7 the periodic images in addition with the central simulation cell. All hexagons have identical volume fractions. This is not visible, as we plot one unfolded box after the other on top of each other, to be able to see the unfolded DP. The intra- and intermolecular associations in the melt can now be determined accurately.

Figure 6.8 depicts indicative results for PG2-50 in terms of fractions of the total groups of the macromolecules that participate in different types of bonds (benzene, i.e., $\pi - \pi$ stacking or hydrogen bonding or Boc, in the dendron ends). Note that for these calculations a critical threshold distance below which two neighboring groups are considered a pair was used (note that because this model has hard sphere interactions only, there is no interaction energy upon bonding). The main information is thus in the shape of the curves and relative numbers, while the absolute fraction will depend on the choice of the *is a pair* criterion; hence we call them *potential interacting pairs*. Further, in this figure one may appreciate the distribution of associations of different origins and in particular the interplay of intramolecular (which dominate the inner part of the DP) and intermolecular (mainly in the outer part) bonding. The predominance of intermolecular bonding in the periphery corroborates the suggestion (based on the molecular structure) that interpenetration among DP does not proceed very deeply into the dendrons (complying with the findings of ref [108]); it appears rather limited to the outer segments (not necessarily terminal groups only). This is particularly evident in the bonding due to the external Boc groups (c). It is important to note that the fraction of the benzene $\pi-\pi$ bonds is extremely small (there is a factor 10^{-3} on the vertical axis in plot (a)). This small fraction is anticipated, given the particular orientation needed to stacking interactions [201], which is unfavorable in these DPs, and moreover it explains why there is no relevant signal in the X-ray scattering data (see below). The maximum fractions for benzene bonds are about 0.6%, for hydrogen bonds about 7%, and for Boc about 1.2%. These relatively small numbers and predominance in intermolecular bonding in the outer part of the DPs are in qualitative agreement with experiments and support the Velcro type of picture proposed (see figures 6.10 and 6.22). Figure 6.9 depicts typical results from the analysis of local order in the melt.

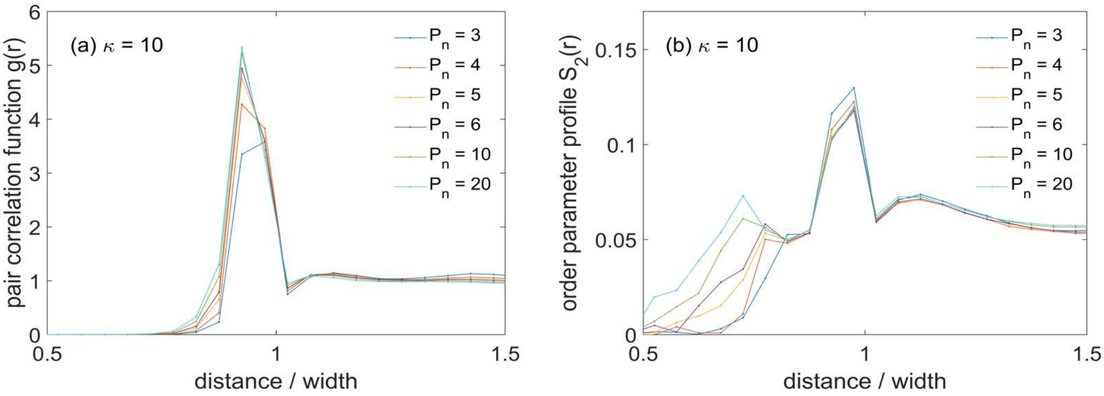

Figure 6.9: (a) Pair correlation function $g(r)$, calculated from the full polygons defining the backbone of diameter D, as a function of reduced center-to-center distance r/D, for polymers of given stiffness ($\mathcal{K} = 10$, $l_p/D = 9.1517$), at different number of repeat units P_n. (b) Respective orientational order parameter $S_2(r)$ [202].

Note that these results were obtained by a model of semi-flexible chains with excluded volume in a dense melt. Pair correlation functions for polymers of a given stiffness and varying degree of polymerization are shown in figure 6.9(a). Evidently, correlations increase with chain length. They are also enhanced with stiffness. In figure 6.9(b), we plot the respective orientational order parameter $S_2(r)$, i.e., the mean second Legendre polynomial, $S_2 = (3/2)\,\langle P_2(\boldsymbol{u}_1, \boldsymbol{u}_2)\rangle$ of the scalar product of two segment unit vectors $\boldsymbol{u}_1$ and $\boldsymbol{u}_2$ at their center-to-center distance r. For perfectly parallel segments we have $S_2 = 1$, whereas for randomly oriented segments $S_2 = 0$. We observed that the orientational order is more pronounced for longer backbones and varies with stiffness especially at short distances. These results support the findings of X-ray scattering concerning local orientational order and rheology concerning Velcro-type effects of P_n on viscoelasticity (see also relevant discussion below). Here we show indicative results for one pair of $(\mathcal{K}, l_p)$ values. Note that while theoretical works exist that discuss the dynamics, length scales, and sizes of polyelectrolyte chains in dilute solution [216], we are not aware of a simple model that could represent the neutral, thick DP and produces a tangent-tangent correlation function unlike that of a semi-flexible chain. Because the stiffness of the dendron-free backbone is irrelevant, we expect a single length scale (the persistence length), as discussed in related works [86, 217, 218]. Hence, the adopted simplistic consideration of semi-flexible chains with excluded volume can be thought as a good first attempt to model DPs. In Figure 6.10 we provide a schematic illustration of the proposed interactions of two neighboring DPs based on simulation results. Such a situation is consistent with the Velcro-type effect.

6.2.4 Spatial organization of DPs from SAXS and WAXS

X-ray scattering measurements were performed by prof. Floudas at the Max Planck Institute (Mainz). They were carried out with both fresh and *aged* (i.e., long annealed) PGs samples and showed practically no difference. Figure 6.11 compares the diffraction patterns from PG1 and PG2 generations with the same degree of polymerization. The peaks at small and wide angles reflect backbone-backbone correlations and van der Waals distances, respectively. Backbone-to-backbone correlations increase with increasing generation whereas van der Waals correlations remain unchanged. In addition, the narrower small-angle peak for the higher generation reveals increased lateral correlations with a possible liquid crystalline underlying order. The correlation distances

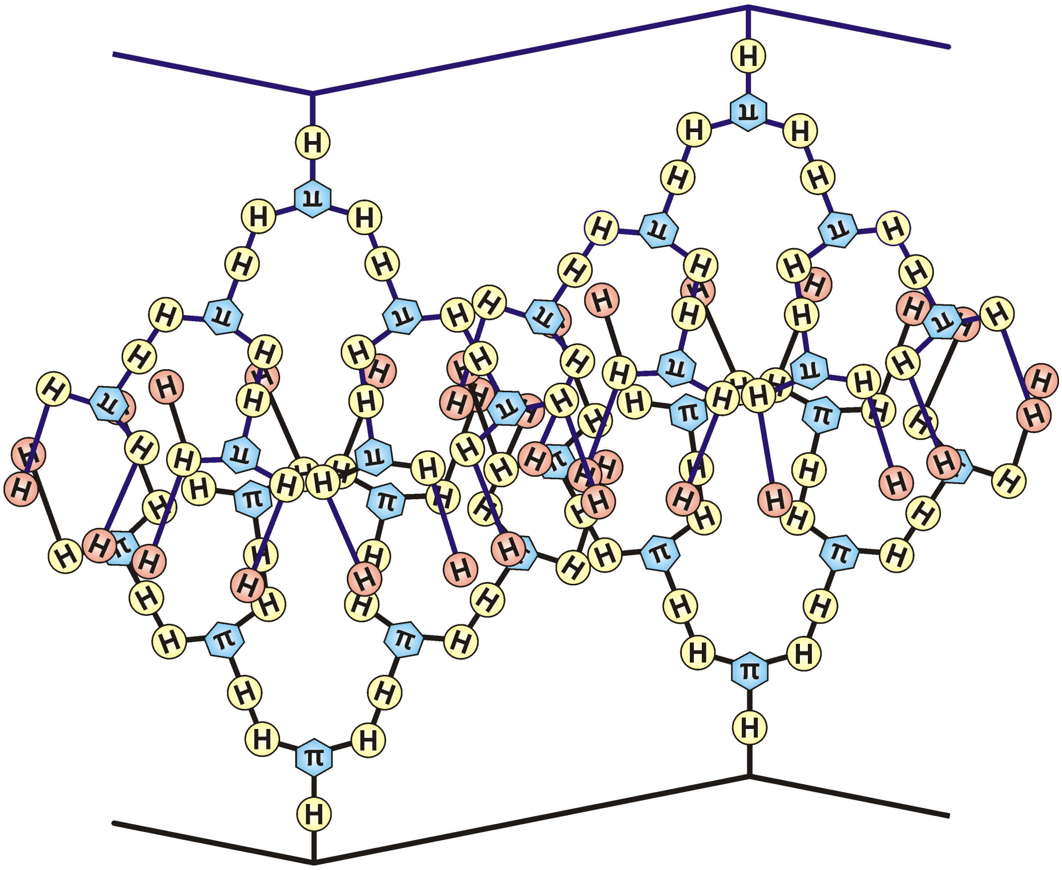

Figure 6.10: Schematic illustration of intra- and intermolecular DP associations and the Velcro effect between neighboring dendrons (PG3). Hydrogen bonding (H) is promoted via carbonyl and amide groups (in yellow), particularly on the outermost branches where Boc groups are present (red). In addition, $\pi-\pi$ interactions are in principle also possible via aromatic rings (in blue). Top and bottom lines represent the backbones of the interacting DPs. Note that most interactions appear roughly in the middle of the backbone-backbone distance, in the region of the outer peripheries of the weakly interpenetrating DPs [202].

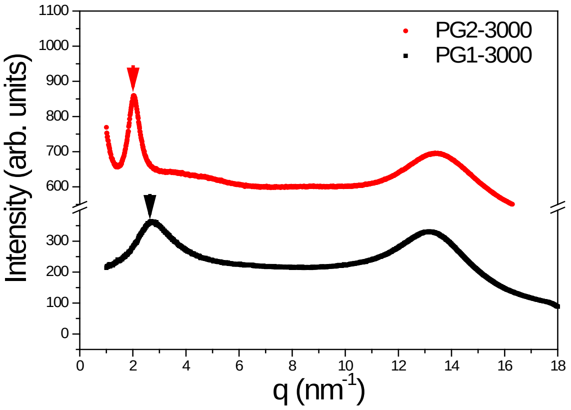

Figure 6.11: Wide-angle X-ray scattering intensity distribution of two DPs as a function of the scattering vector at 303 K. Arrows indicate the low-q scattering peaks (see text) [202].

corresponding to the small-angle peak (i.e., backbone-to-backbone correlations) as a function of the degree of polymerization for the three generations are shown in Figure 6.12(a). Correlation distances are obtained as $d = 1.23 \times 2\pi/q$, where the factor 1.23 accounts for nearest neighbor correlations only [219]. Correlation distances corresponding to backbones as a function of the molecular mass of the polymer repeat unit are shown in Figure 6.12(b).

Lines with slopes of 1 and 1/2 are indicated that correspond to a layered (1-D) or columnar (2-D) arrangement of backbones [219–221]. The data for the three generations suggest the latter arrangement. Hence, the emerging picture of molecular packing is of backbones with a columnar arrangement and with improved backbone-to-backbone correlations with increasing P_n. As mentioned, this picture is further supported by the simulations. We note that in WAXS we do not see specific local interactions such as $\pi - \pi$ stacking. Indeed the WAXS patterns for all the samples were nearly isotropic (see example of figure 6.13. We attribute this to the small fraction (and related scattering intensity) of the pairs of bonded groups.

On the other hand, as mentioned, X-ray scattering reveals well-defined backbone-to-backbone interactions and only short-ranged and broad local interactions, providing

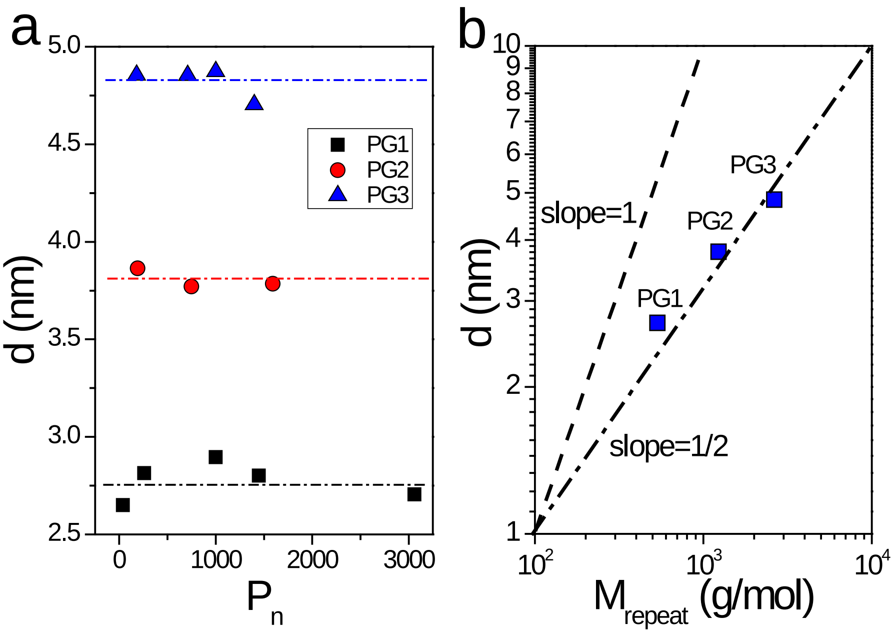

Figure 6.12: (a) Correlation distances corresponding to the small-angle peak (i.e., backbone-to-backbone correlations) as a function of the degree of polymerization for the three generations. (b) Respective correlation distances corresponding to backbones as a function of the molar mass of the polymer repeat unit, M_{repeat}. Lines with slopes of 1 and 1/2 are indicated that correspond to a layered (1-D) or columnar (2-D) arrangement of backbones (see text) [202].

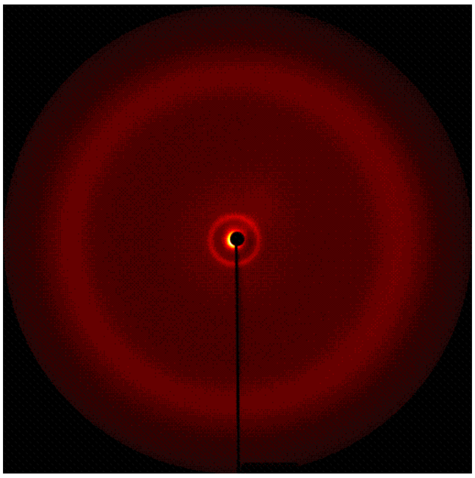

Figure 6.13: Example of isotropic WAXS pattern (sample PG2-3000 at 303°K).

further support to the emerging picture. For completeness, we note that we did not check for longer-range correlations. However, the present data (notice that the lower q value is 1 nm^{-1}, and hence the length scales captured are longer than in usual WAXS measurements from the literature) exclude correlations of up to 7 nm, meaning that if such correlations exist they need to be longer than 7-8 nm.

6.2.5 Linear viscoelasticity

Figure 6.14 shows the linear viscoelastic response of the *aged* (i.e., quasi-equilibrated, according to the equilibration protocol described in section 6.2.2) DPs. The master curves of the same series are presented at the same distance from the glass temperature, T_g. Moreover, for clarity of presentation, the plots are vertically shifted as indicated in the corresponding figures. The linear rheological behavior of the DPs from generation 1 to 3 reflects the role of the two key structural parameters, namely, the degree of polymerization of the backbone P_n, and the number of generation of the dendrons, g. Given a fixed value of g, an increase of the degree of polymerization translates into longer molecules and directly enhances the ability to form entanglements and, more importantly here, the number of intermolecular bonds. Moreover, as shown by simulations on DPs with $P_n = 50$ and confirmed by the X-ray study, the competition between intra- and inter-molecular interactions turns into favor of the latter as P_n increases with improved backbone-to-backbone correlations. Hence, an increase of the degree of polymerization acts in the direction of effective reinforcement by means of enhanced intermolecular corrections akin to a Velcro effect (see figure 6.22). We note for completeness that the high-frequency data with $g = 1$ and $P_n = 1500$, in figure 6.14(a), suffer from transducer compliance effects and could not be improved due to the low amount of available sample, but this does not affect the overall response and comparison with other DPs that follows. At fixed P_n, an increase of g has contrasting effects. On one side, by increasing the generation, the persistence length of the molecule

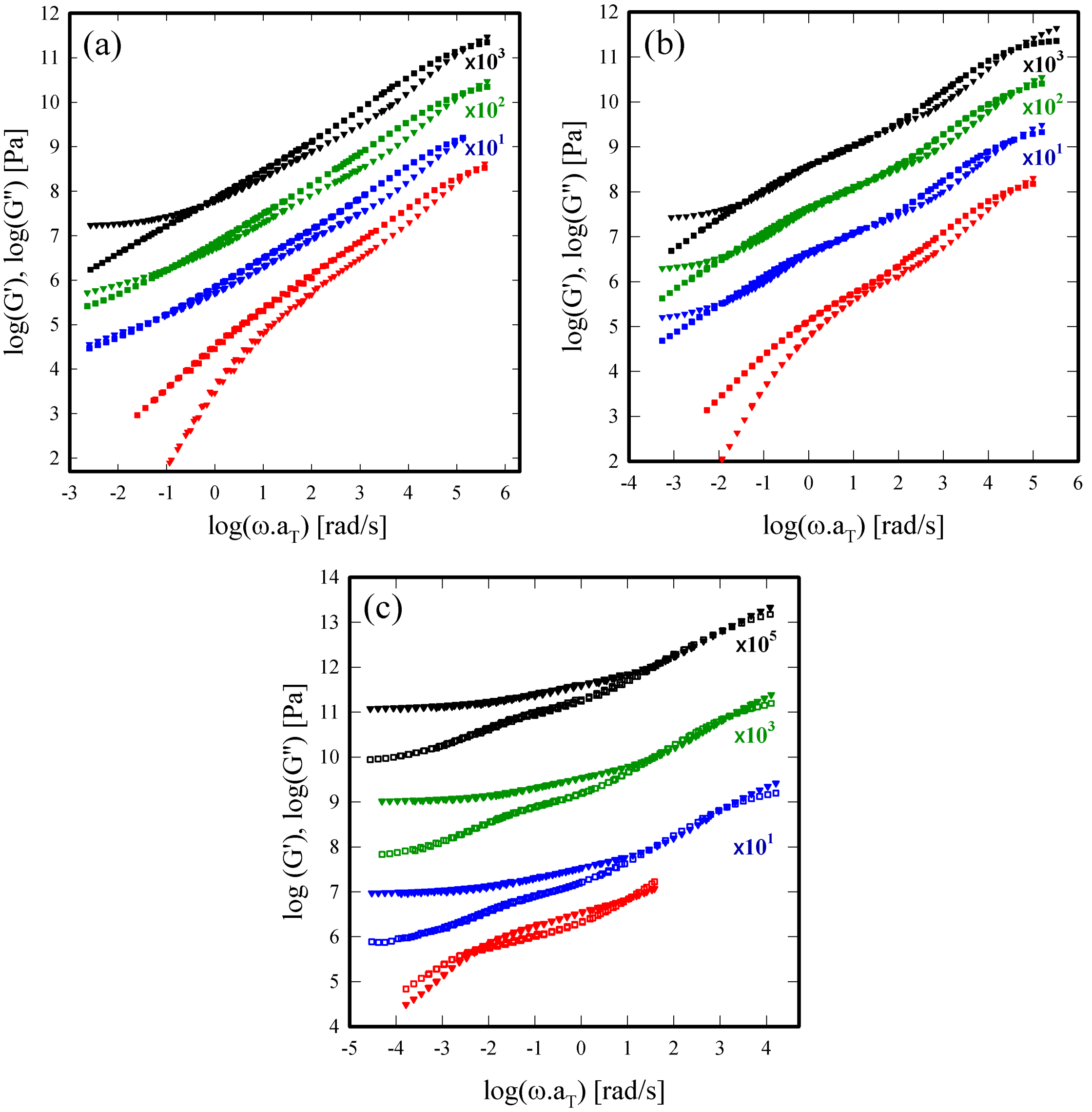

Figure 6.14: Linear viscoelastic master curves of the dendronized polymers at the same distance from glass temperature: generation $g = 1$ (a), generation $g = 2$ (b), and generation $g = 3$ (c) (degree of polymerization: red, $P_n = 50$; blue, $P_n = 1500$; green, $P_n = 2000$; black, $P_n = 3000$; G' open triangles, G'' open squares). The master curves have been vertically shifted for clarity (shift factors are indicated in the panels) [202].

is increased [58] as also suggested by the X-ray data. This results in fact in larger entanglement molecular weight and concomitantly smaller number of entanglements for the same macromolecule. This concept relates to the macromolecular thickness and is consistent with the packing length analysis of Fetters and co-workers (for Gaussian chains) [14]. It is worth mentioning here that if we ignore the intermolecular correlations and bonding interactions, application of the Kavassalis-Noolandi analysis [70, 71] and packing length considerations (as done recently for dense bottlebrushes [56]) to the present DPs suggests that the entanglement degree of polymerization P_e is between 1500 and 3000;

Concerning the Kavassalis-Noolandi analysis, we attempt at a simple analysis of the entanglement molar mass of DPs by ignoring correlations and bonding interactions. Evidently, this analysis is idealized and does not apply to the experimental system at hand, but it is aimed at assessing the role of thickness on the ability of such systems to entangle topologically in the absence of other interactions. The Kavassalis-Noolandi theory for entanglements in polymer systems states that the number of Kuhn segments between entanglements, N_e is not constant but it increases with the molecular weight of the polymer, approaching a constant value in the limit of infinitely long chains. In such a case, the asymptotic value of N_e is given by the following equation:

$$\lim_{N\to\infty} N_e = \left[6\left(\tilde{N}+1\right)/\pi\Phi\right]^2 \tag{6.1}$$

where Φ is the volume fraction of the polymer and $\tilde{N}$ is the coordination number, a geometrical parameter which accounts for lateral constraints to the motion of a polymer chain in the entanglement volume. In other words, the parameter $\tilde{N}$ can be regarded as the number of segments of length N_e included in the sphere spaced by an entanglements strand. Here we consider dendronized polymers in the melt state and then we assume $\Phi = 1$. Provided that dendronized polymers are thick molecules we expect a lower value of $\tilde{N}$ compared to conventional linear polymers (usually 20). For this reason, a typical value of $\tilde{N}$ for DPs could be 2 and from equation (6.1) we obtain:

$$\lim_{N\to\infty} N_e = [6(2+1)/\pi]^2 \approx 30 \tag{6.2}$$

Given a persistence length of the order of 10 nm for PG1-3, we obtain a contour length between entanglements, $l_e = 30 \times 10 = 300$ nm. The length of the repeating unit of the DPs coincides with the length of the repeating unit of PMMA, which is approximately 0.25 nm. At $P_n = 1500$ this gives a contour length of the molecules of 375 nm. Then scenario based on the Kavassalis-Noolandi analysis, is compatible with the onset of entanglements between $P_n = 1500$ and 3000.

Moreover, considering the plot of figure 1.16, the packing length p of DPs is beyond 10 Å, yielding a value of M_e of the order of 10^6 g/mol. This would imply a value of $Z = 2 - 3$ entanglements for $P_n = 3000$.

Therefore, we do not have topological entanglements in the classic sense here.

DPs of generations 1 and 2 are relatively flexible polymers exhibiting similarities with structurally similar systems such as bottlebrush and wedge polymers. For these polymers with no interacting groups, an elastic plateau is observed at low frequencies and is much lower than that of the backbone (because of the large values of the persistence length and entanglement molecular weight), yielding supersoft and superelastic melt properties [56, 199]. Here, however, bonding interactions (dependent on g and P_n) are primarily responsible for the values of viscoelastic moduli. The intermediate frequency region of the viscoelastic spectrum of these systems describes the behavior of the side branches which undergo self-similar dynamics between Rouse and Zimm (the slope of the curves is between 0.5 and 0.7 in the intermediate frequency range). This type of dynamics is not unusual in hyperbranched polymers [222] and attributed to their fractal nature (due to branching). A weak elastic plateau G_p is instead observed in the low frequency range which, based on the classic entanglement picture (i.e., in the absence of interactions other than entropic), reflects a large entanglement molar mass ($M_e \sim G_p^{-1}$ and the fact that eventual macromolecular mobility occurs at even lower frequencies. An interesting feature of DPs of generations 1 and 2 is the systematic increase of the low frequency elastic plateau as the degree of polymerization increases. Therefore, the dependence of G_p on P_n is a consequence of the addition of bonding interactions. In particular, hydrogen bonding and $\pi - \pi$ stacking will increase the plateau modulus via an enhanced number density of physical bonds n [223]:

$$G_p \sim \rho RTM_e^{-1} + nk_BT \tag{6.3}$$

The number density n should be of order 10^{24} for PGs. As already mentioned, these interactions take place largely at the periphery of the DPs; hence they depend on P_n. The net result is a plateau modulus that depends on molar mass. In light of the above discussion, the viscoelastic response of DPs in figure 6.14 is attributed to the enhanced correlations with increasing P_n. Within the range of P_n investigated, a clear rheological transition from weakly correlated, unentangled-like ($P_n = 50$) to strongly correlated regime akin to network-forming ($P_n =$ 1500-3000) is observed. By analogy, linear polymers exhibit a transition from unentangled to entangled behavior, characterized by a broadening of the elastic plateau region and a clear separation of the moduli beyond the crossover corresponding to the equilibration time of an entanglement strand.

From the above it is evident that the combined information from rheology, X-ray scattering, and simulations suggests that the moduli enhancement with P_n reflects increased intermolecular interactions. We note further that increasing g from 1 to 2 affects the values of the moduli in the intermediate frequency region. In fact, PG1 is a viscoelastic liquid with $G' > G''$, while for PG2 $G' \approx G''$, indicating a more elastic behavior compared to PG1 in the same frequency range. This may reflect a larger density of supramolecular bonds in PG2. The effect of g becomes even more apparent in the case of generation 3. For $P_n = 50$, the increased density of bonds leads to an elastic plateau modulus (figure 6.14(c)), in contrast to what is observed for the first and second generations. When the degree of polymerization is increased to 1500 and beyond, the enhanced density of intermolecular bonds results in strong correlations and a further increased value of G', which is here comparable to the entanglement plateau modulus of PMMA, i.e., the linear backbone of the DPs (this is simply an observation)[108]. Hence G_p increases substantially with P_n (as it does with g [108]). Concomitantly, the X-ray results above call for a liquid crystalline type of organization of the DPs, where their virtually parallel arrangement will promote intermolecular interactions with more exposed active area as P_n increases, hence the Velcro effect (figure 6.22).

Given the fact that DPs are considered as cylindrical objects with a *molecular thickness*, it is possible to define a cylindrical lateral surface which is in fact the exposed area. Intermolecular bonding capacity is enhanced when larger portions of the lateral surfaces of the polymers are in contact with each other. The contact area increases when the molecules are practically aligned parallel to each other. In such a case, given that with increasing g the intermolecular interactions are strictly reduced to the periphery of the DPs (due to their density profiles, as also supported by simulation results), the number density of DP-DP bonds responsible for the plateau modulus is almost independent of P_n (since the intermolecular bonding at the periphery is proportional to P_n). This explains the nearly constant value of plateau modulus in the Pn range 1500-3000 in figure 6.14(c). Indeed, the elasticity of PG3 should result exclusively from supramolecular interactions because the persistence length of generation 3 is large (and so is the entanglement molar mass M_e) [87]. Interestingly, in this class of polymers M_e depends on g but should not depend on P_n. Note further that the rubbery plateau modulus of the backbone (PMMA) is about 3×10^5 Pa [14].

In order to further elucidate the plateau region, we have extended the rheological master curves by means of creep measurements for one DP series, PG2. In particular, we run creep measurements on the aged PG2 samples and converted the creep compliance, $J(t)$ into dynamic moduli. The results of the conversions are reported in figure 6.15 which depicts the respective complete master curves (without the vertical shift of Figure 6.14(b)). The data superimpose fairly well in the high- and intermediate-frequency regions. At lower frequencies, a small albeit unambiguous increase of the elastic plateau modulus with increasing P_n is evident. From the trend of the resulting moduli one can infer that at long times, the flow behavior will be eventually approached. By extrapolating the low-frequency data, we find that the moduli crossover frequencies are approximately 10^{-7}, 5×10^{-8}, and 10^{-8} rad/s for P_n = 1500, 2000, and 3000, respectively. Hence the corresponding average terminal times τ_{terminal} are about 10^7, 2×10^7 and 10^8 s. These numbers conform to $\tau_{\text{terminal}} \sim P_n^3$ which comply with the pre-

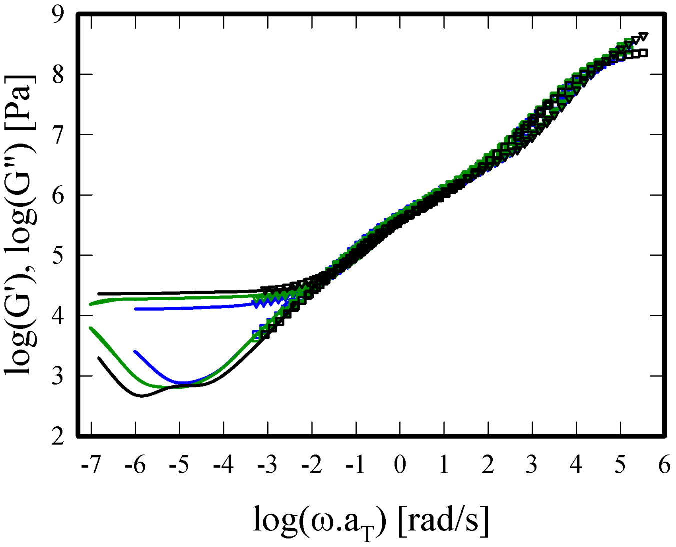

Figure 6.15: Linear viscoelastic master curves of the PG2 series along with the conversion of creep compliance measurements into dynamic moduli (lines). Color code (same as Figure 6.14(b)): degree of polymerization: blue, $P_n = 1500$; green, $P_n = 2000$; and black, $P_n = 3000$. The unusual shape of the black curve with two minima is due to conversion issues (which do not affect the main message however) and is not discussed further [202].

diction of the sticky reptation model $\tau_{\text{terminal}} \sim P_n^3 N_s^{-2}$ with N_s the number of average number of monomers along the chain between stickers) [223]. However, given the fact that P_n varies only by a factor of 2 and the analysis is rather crude, we do not suggest any scaling here but only offer this as an observation. This time should be associated with the average lifetime of bonds. Nevertheless, an unambiguous experimental finding is the following: DPs exhibit a plateau modulus which becomes more extended as P_n increases (and which increases in value with P_n and g). Hence, intermolecular bonding interactions, rather than chain entanglements, are at the origin of the plateau. Molecular organization promotes these interactions and indirectly affects the plateau modulus. These polymers also exhibit very long relaxation times, presumably linked to the lifetime and number of intermolecular bonds and eventual molecular reorientation, as in sticky Rouse [223], where the relaxation time, τ_{Rouse} of unentangled associating polymer chains is given by:

$$\tau_{Rouse} = \tau(Sp)^2 \tag{6.4}$$

with τ being the lifetime of a bond, S the number of stickers per chain and p the fraction of interchain associated stickers, or as sticky reptation models [69] where the terminal relaxation time τ_D is given by:

$$\tau_D = \left(\frac{N}{N_e}\right)^{1.5} \frac{2S^2\tau}{1 - 9/p + 12/p^2} \tag{6.5}$$

with N being the degree of polymerization of polymer chains and N_e being the number of monomers between entanglements. In fact, the terminal time depends on both the fraction of active bonds and the association/dissociation time of the bonds. These factors play a role in determining the exponent of the observed scaling relation.

Figure 6.16 reports the shift factors used to build the master curves of figure 6.14 at the same distance from the glass temperature. From Figure 6.3 it is clear that a plateau in the glass transition temperature is observed at $P_n > 50$. Hence, at $P_n > 50$

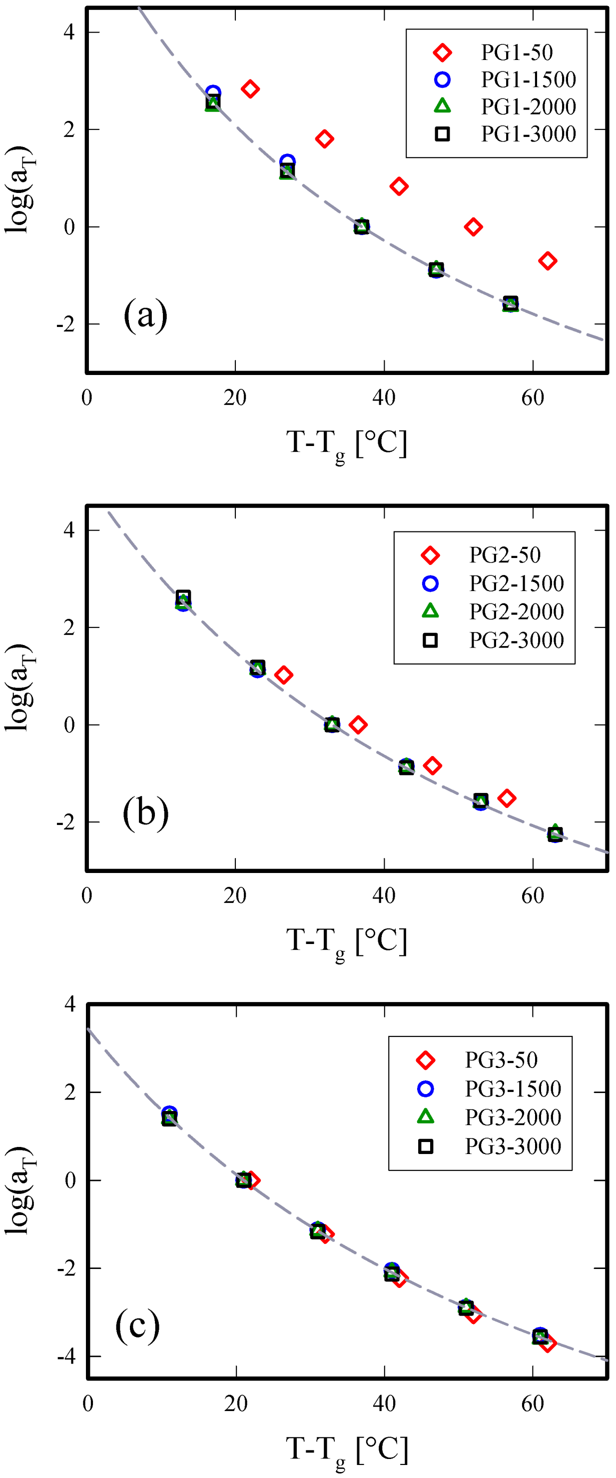

Figure 6.16: Horizontal shift factors of PG1 (a, $T_{ref} = 90$°C), PG2 (b, $T_{ref} = 100$°C), and PG3 (c, $T_{ref} = 90$°C). At fixed generation, the samples with $1500 \leq P_n \leq 3000$ have the same glass temperature and subsequently the same value of $T_{ref} - T_g$. For each generation, the sample at $P_n = 50$ is reported at the same value of $T_{ref} - T_g$ as the other samples of the series [202].

the same distance from T_g corresponds to the same reference temperature. A very good agreement between the shift factors of the same series at different degrees of polymerization is observed. Along with the shift factors, a WLF fit is also reported, according to the following equation:

$$\log(a_T) = -\frac{c_1(T - T_{ref})}{c_2 + (T - T_{ref})} \tag{6.6}$$

Where c_1 and c_2 are the two fitting parameters. The c_1 and c_2 constants were obtained from the arithmetic average of the WLF fit constants at different P_n. The constants are consistent with previous data [198], and with those of other amorphous polymers [146, 224]. The good agreement between the WLF fit and the experimental shift factors, along with the (more sensitive) van Gurp-Palmen (VGP) plots of the master curves (figure 6.17), confirms the validity of the TTS principle for this kind of systems.

The applicability of the WLF fit does not exclude the possibility of supramolecular bonds; hence further analysis of the local dynamics and fragility is not attempted. A comparison of the WLF lines and the relevant fit parameters for the three DP series and a simple analysis of fractional free volume reveal the clear differences among them, and in particular the distinct behavior of PG3, attributed to intermolecular bonding.

6.2.6 Response to nonlinear shear

In order to probe the unentangled character of DPs with small P_n we decided to test PG1-50 and PG2-50 in nonlinear shear. In this section we report on their nonlinear rheological response. These samples were such that the terminal regime was experimentally accessible (figure 6.14), and a characteristic disengagement time τ_d was extracted. Subsequently, the Weissenberg number has been calculated as the product of the shear rate $\dot{\gamma}$ and the disengagement time, $Wi_D = \dot{\gamma}\tau_d$.

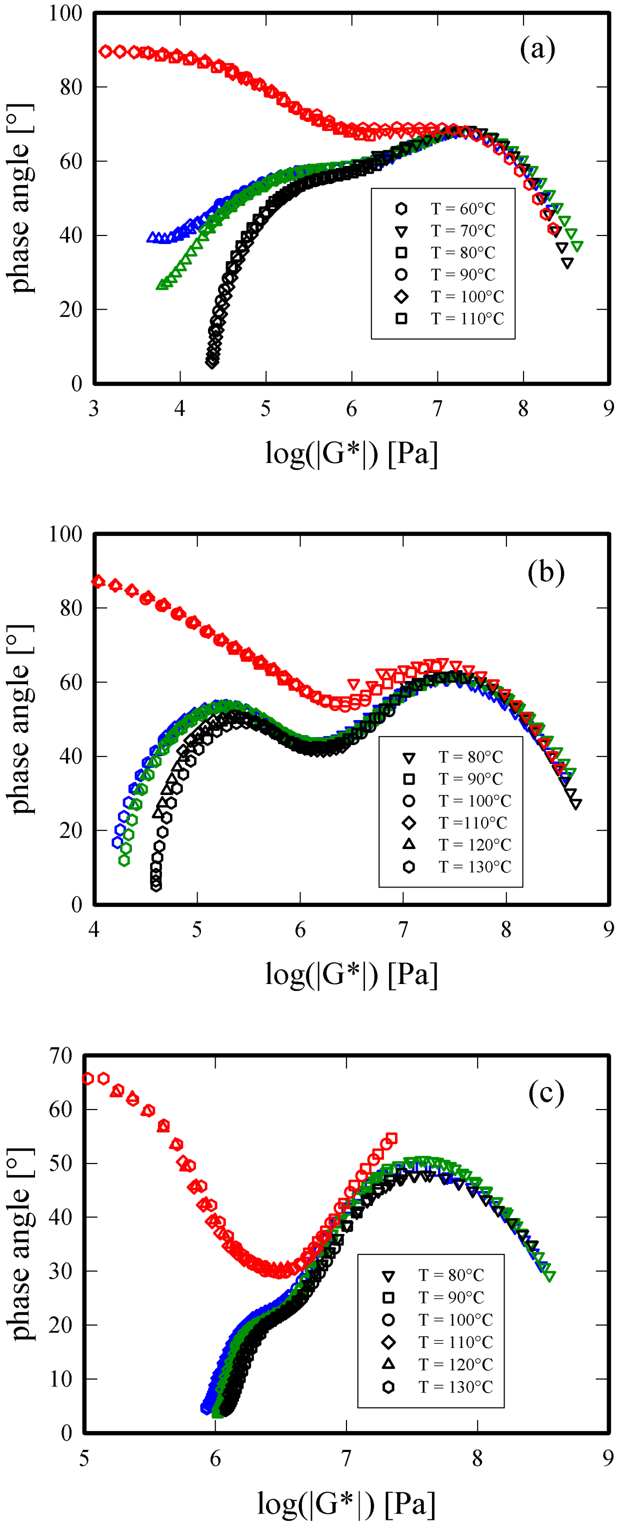

Figure 6.17: van Gurp-Palmen plots of (a) PG1, (b) PG2 and (c) PG3 series (red, $P_n = 50$; blue, $P_n = 1500$; green, $P_n = 2000$; black, $P_n = 3000$; temperatures as reported in the legends [202].

Figure 6.18 depicts the results of transient viscosity (step-rate) experiments with $PG2-50$ at $T = 100°\mathrm{C}$.

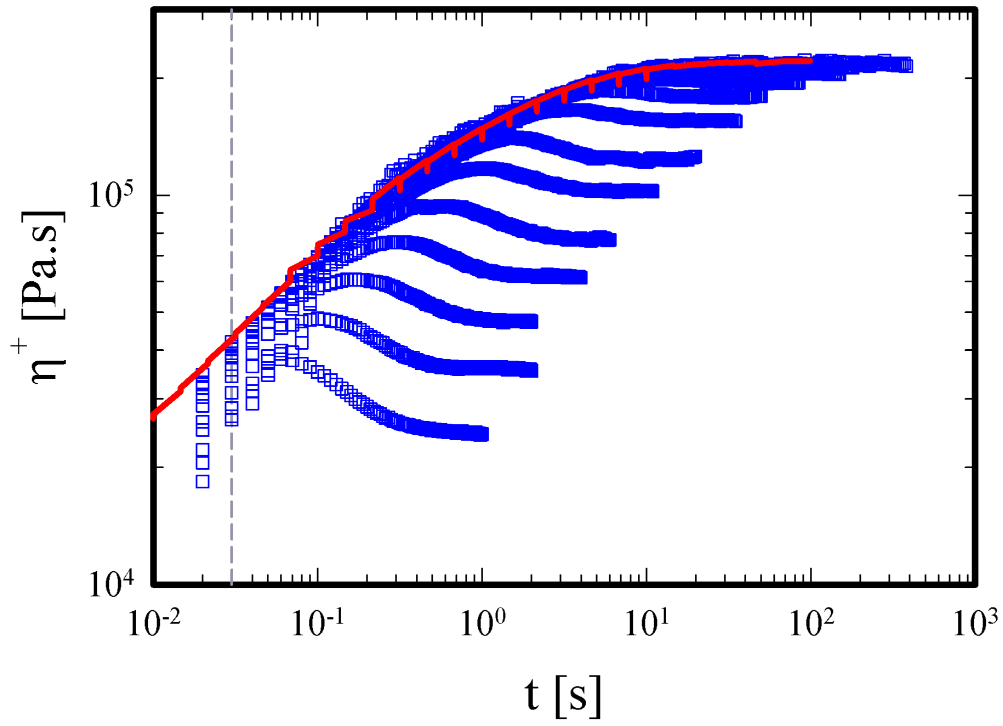

Figure 6.18: Nonlinear step-rate experiments depicting the transient viscosities of sample PG2-50 at $T = 100°\mathrm{C}$ (shear rates from highest to lowest curves, $\dot{\gamma} = 0.0316$, 0.0562, 0.1, 0.178, 0.316, 0.562, 1, 1.78, 3.16, 5.62, 10, 17.8, and 31.6 s^{-1}). The grey dashed line indicates the time resolution limit of the instrument [202].

Strain and viscosity response from nonlinear shear has been analyzed and compared with data from the literature on linear entangled systems [92, 94]. The data conform to the behavior of unentangled FENE-type of response with a weak stress/ viscosity overshoot, weak shear thinning (weaker than entangled polymers, see Figure 6.19), and no evidence of induced deformation (segmental orientation or stretching). The latter comes from the observation that the experimentally probed maximum instantaneous deformation saturates at the lowest imposed shear rate (figure 6.20) and remains independent of shear rate. Moreover, a very weak dependence of the ratio $\eta_{max}/\eta_{\text{steady}}$ is observed upon Wi number (Figure 6.21).

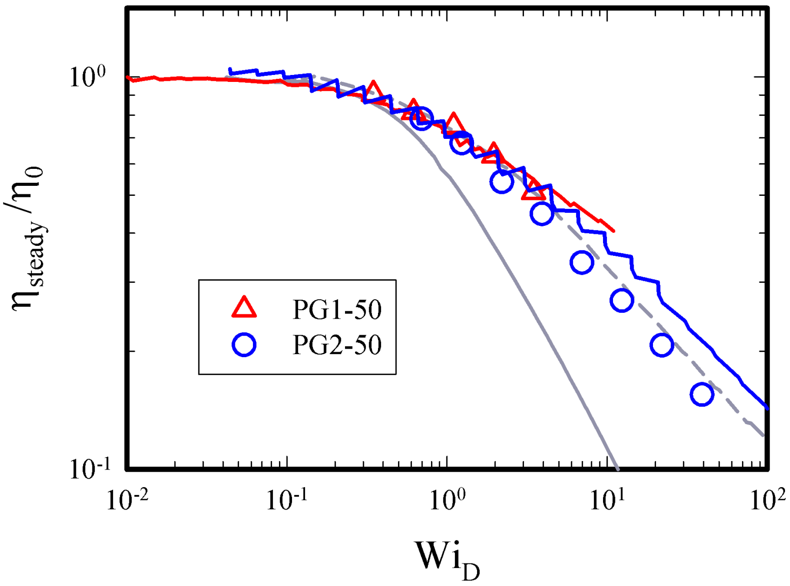

Figure 6.19: Cox-Merz rule applied to dendronized polymers (dashed line, polystyrene ring 84k; solid line, entangled PS182k. PG1-50 red triangles, PG2-50 blue circles; red line, LVE envelope of PG1-50; blue line, LVE envelope of PG2-50

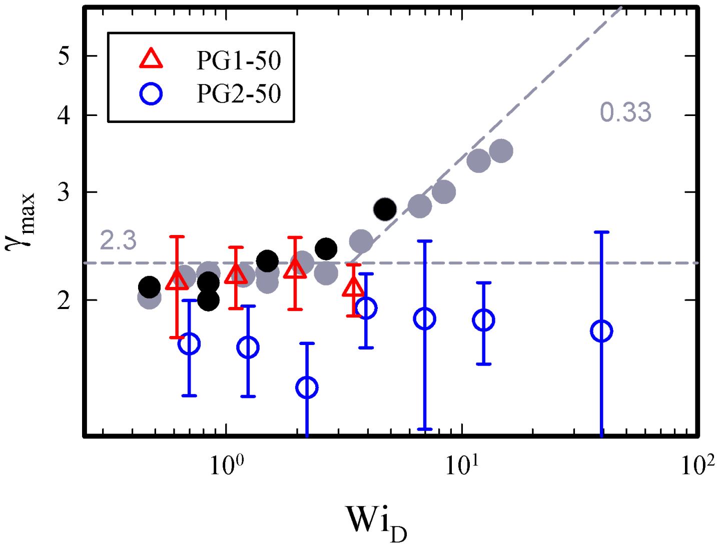

Figure 6.20: Strain corresponding to the peak viscosity (from figure 6.18) as a function of the Weissenberg number for PG1-50 and PG2-50. Data of entangled PI are reported as a reference [94].

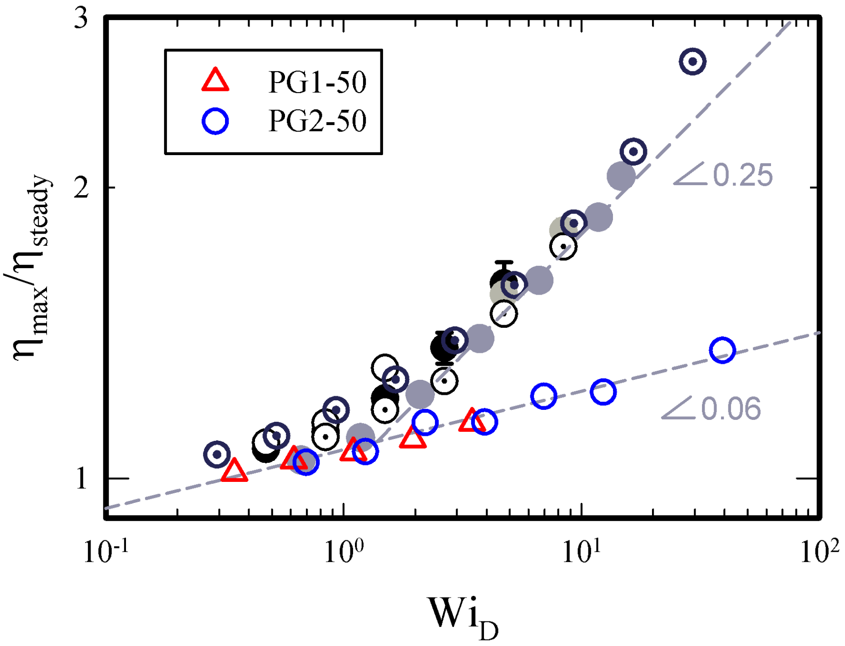

Figure 6.21: Normalized peak viscosity (from Figure 6.18) as a function of the Weissenberg number for PG1-50 and PG2-50. Data of entangled PS (open black symbols) and PI (closed black and gray symbols) are reported as a reference [94].

This is consistent with the X-ray scattering results of figure 6.12 which suggest columnar arrangement of the backbones. The emerging scenario is further supported by the simulation results of figures 6.6-6.8. In such a situation no further deformation is expected, especially at rather modest shear rates such as those used here. The induced deformation relates to the effect of molecular friction of interpenetrated outer segments of dendrons, complying to the proposed Velcro effect (figure 6.22). Finally, we did not succeed in extracting any good normal force signal from nonlinear shear measurements on PG1-50 and PG2-50. The reason is that, as the quality of the axial force signal improves upon shear rate increase, overload of the transducer is achieved. Indeed, despite the unentangled behavior of such systems, the normal forces involved in transient shear are very large. This is attributed to the Velchro-like interaction of the side-dendrons whose segments between branches are significantly stretched even at relatively low shear rates.

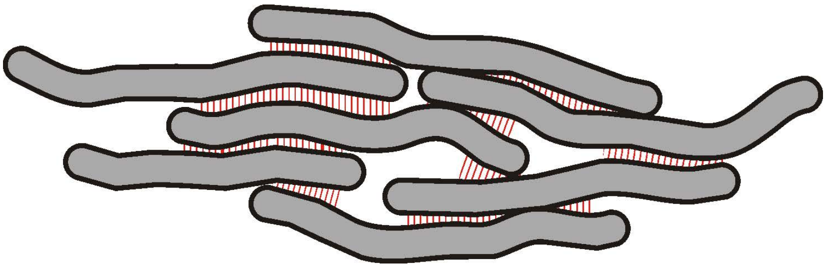

Figure 6.22: Schematic illustration of sheared DPs with Velcro-like interactions. The red dashed areas depict these intermolecular interactions between neighboring molecules. The DPs are oriented in flow (the long axis is at 45° with respect to the shear velocity).

6.3 Concluding remarks

Dendronized polymers are a relatively new class of polymers, characterized by a cross-sectional thickness length-scale depending on the branching generation. Whereas they exhibit similarities with bottlebrushes (thickness, leading to large entanglement molar mass), they are also distinct: their thickness can be accurately controlled and continuously increased with the degree of branching, their monomer density distribution decays less gradually (as we know from independent simulation studies [225]), they have an enhanced ability for intra- and intermolecular interactions, and they offer a significantly larger density of end groups per backbone unit length. Furthermore, the possibility to chemically modify these end groups in a wide range renders them more functional and tunable. Results from X-ray scattering, corroborated by simulations, revealed increased lateral backbone-backbone correlations with a 2D arrangement of backbones and a liquid crystalline underlying order. These structural features have direct effects on their viscoelastic properties. We have presented a systematic investigation of the linear and nonlinear rheology of well-characterized first-, second-, and third-generation DPs with degrees of polymerization varying from 50 to 3000. PGs were found to exhibit very long equilibration times due to their tendency to reduce gradients in monomer density. Aged PGs exhibit complex viscoelastic response dominated by the intermolecular bonding interactions, since entanglement interactions are at best weak (for $P_n > 2000$). The linear viscoelastic data indicate the occurrence of a plateau modulus for DPs, which can be lower than or comparable in value to that of the acrylic backbone (depending on generation g and degree of polymerization P_n). The intermolecular bonds and related molecular organization of DPs (liquid crystalline-like) are responsible for this modulus, whose extent in the frequency scale and actual value depends on both P_n and g. Eventually, the crossover of moduli marks the terminal relaxation and the very long relaxation times reflect the lifetime of the bonds. Their nonlinear response is akin to FENE chains without appreciable deformation and with weak shear thinning. The instantaneous maximum deformation is saturated from the lowest shear rates. Overall, a Velcro-type analogy is invoked to describe their behavior. DPs interpenetrate, however this does not constitute entanglement effects but rather enhanced molecular friction which appears to dominate viscoelasticity for small P_n and large P_n at the measured times. The Velcro analogy is directly related to the lateral surface of DPs with their exposed areas being in contact with each other, yielding an eventual highly cooperative motion. It is evident that the combination of bonding interactions and topology controls the linear and nonlinear viscoelastic response of DPs and at the same time offers the means to tailor these properties at will. Hence, we can tune the mechanical behavior by modifying the key structural parameters or the interacting groups, with implications to materials performance. Moreover, dendronized polymers, along with bottlebrush and wedge systems, provide a remarkable contribution to the understanding of topological interactions between thick molecules, based on the proposed picture of Fetters and coworkers.

Chapter 7

AGING CONTROL AND DUCTILE-TO-BRITTLE TRANSITION IN UPY-FUNCTIONALIZED DENDRONIZED POLYMERS

7.1 Introduction

In the previous chapter we have discussed the high degree of tunability of the molecular structure of classic dendronized polymers [108, 202]. Thereby, we have found that a variety of rheological behaviors could be attained by varying the degree of polymerization of the backbone P_n and the generation number of the dendrons, g. An additional degree of freedom in determining the rheology of dendronized polymers is the possibility to insert supramolecular groups in the inner and outer parts of the molecules. The outer molecular surface of dendronized polymers is made of a large number of side branches. In principle, each branch can be functionalized with a supramolecular group. Most of dendronized polymers synthesized to date possess terz-buthoxycarbonyl groups (Boc) on the side branches therefore they can form hydrogen bonds [108, 191]. This possibility is directly reflected in their mechanical properties [108, 202]. However, Boc groups are relatively weak hydrogen bonding groups. They can give rise to a stiff network only when the degree of polymerization of the backbone is large enough to provide enhanced correlation between neighboring molecules. In such a situation an increase of the bonding density occurs. As a consequence, the value of the low frequency plateau of the elastic modulus increases [202].

Recent developments in synthetic chemistry allowed for the functionalization of complex molecules with strong hydrogen bonding units in order to form supramolecular aggregates [62, 226]. Among the variety of hydrogen bonding groups, ureido-pyrimidinone (UPy) is one of the strongest units used in supramolecular chemistry [65]. This group can form an array of four hydrogen bonds with an exceptionally strong dimerization constant in Chloroform. Functionalization with UPy has been already proven to be a good strategy to form strong transient supramolecular networks starting from rather simple unentangled molecules [68]. On the other hand, incorporation of UPy groups in structurally complex systems such as dendronized polymers is a virtually unexplored field. An open question is how the presence of UPy affects the role of the key structural parameters in determining the rheological properties of DPs. Moreover, the effect of strong hydrogen bonding groups on the equilibration kinetics is yet to be decoded. Indeed, it is expected that UPy groups can lock the local motion of side dendrons by acting as strong molecular anchors, thus influencing both velocity of structural equilibration and final state.

In this work we provide an effective method to incorporate UPy on the surface of dendronized polymers at different degree of coverage (see section 2.1.5) and we investigate the mechanical properties of these novel systems. We start from relatively small molecules ($P_n = 40$, $g = 1$) with degree of substitution (f) of Boc groups with UPy ranging from 0 to 25%. A specific annealing protocol is followed in order to achieve consistency between measurements on the different samples. Moreover, we provide an effective way to screen stron intermolecular interactions by growing 1 and 2 classic generations on the UPy-DPs of first generation (see figure 7.1). In order to demonstrate the screening effect, we study the linear rheological behavior of PG2-40 and PG3-40 samples functionalized with UPy at $f = [0\%, 5\%, 25\%]$.

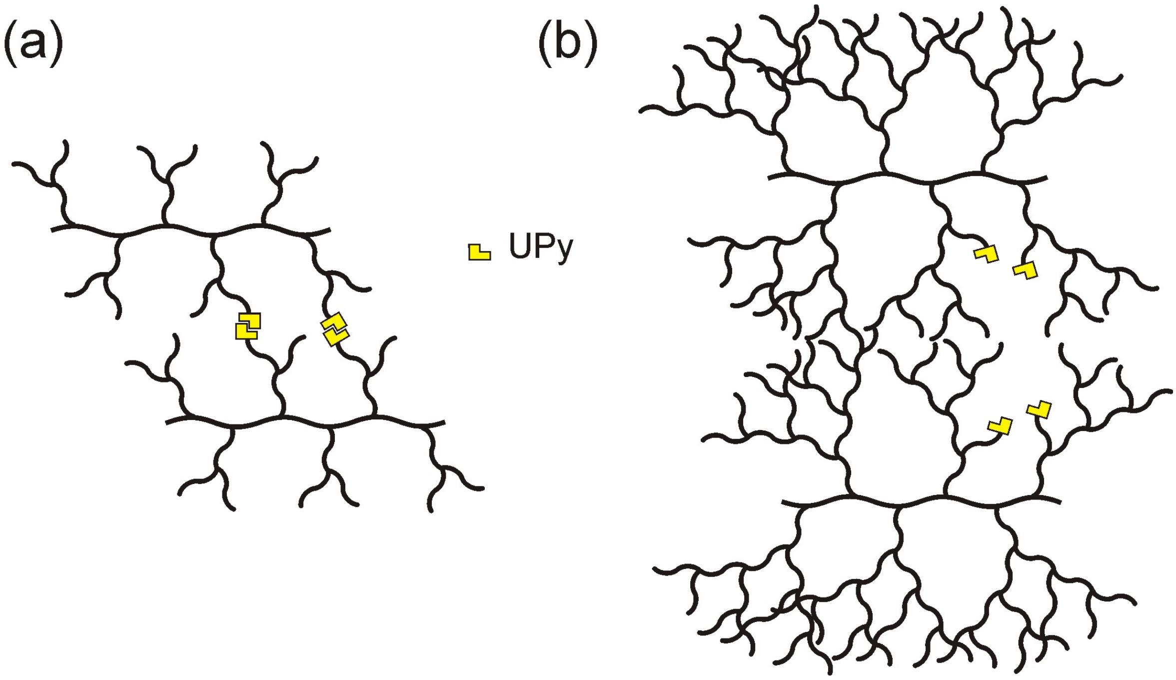

Figure 7.1: Cartoon illustration of interactions in UPy-DPs. (a) UPy-PG1, UPy groups are at proper distance to form intermolecular bonding. (b) UPy-PG3, UPy groups are immersed in the inner part of the molecule and cannot form intermolecular bonding.

7.2 Results

7.2.1 Differential scanning calorimetry

DSC measurements were performed by dr. Scherz at ETH, Zurich. The thermal transition of the synthesized DPs reflects the reduced segmental mobility originating from the enhanced steric hindrance around the polymeric backbone and the approach to the actual glass, respectively, as well as the effect of hydrogen bonding. Hence, we assign the *glass temperature* (T_g) as the characteristic temperature for this overall transition (only a single transition could be detected in DSC runs, albeit broad). Thereby, the presence of only one T_g for the copolymers suggests that the copolymerization of the

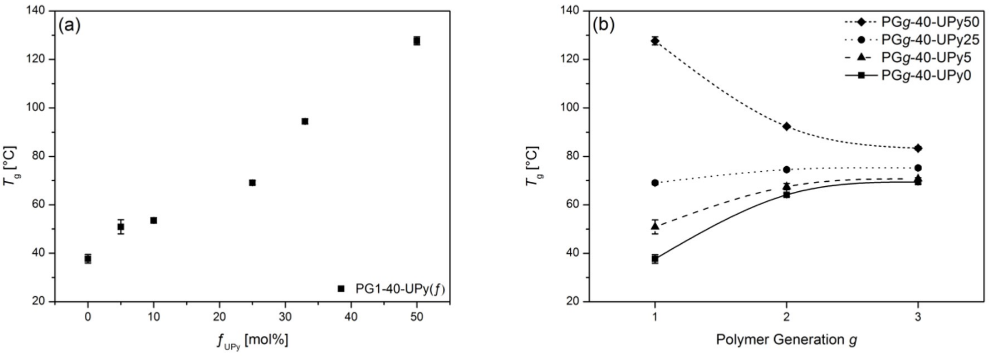

Figure 7.2: (a) Linear relation between T_g and the UPy content in PG1-UPy; $P_n \approx 40$. (b) T_g as a function of g for PGg featuring 0, 5, 25 and 50 mol% UPy monomer; $Pn \approx 40$ The results were obtained by DSC measured from -50 to 150 °C, with a heating rate of 10 °C min^{-1} in N_2 and the lines are drawn to guide the eye.

two macromonomers 1c and 2b proceeded in a random fashion. Figure 7.2.a depicts the compiled T_g values of the PG1-40-UPy copolymers as a function of UPy content. As shown previously in the literature for other random UPy-functionalized copolymers [68, 227, 228], the T_g values of the PG1-40-UPy samples increase in a linear fashion with the number of hydrogen bonding side groups (from ≈38 °C in PG1-40-UPy0 to ≈ 127°C in PG1-40-UPy50). At virtually identical backbone chain lengths ($P_n \approx 40$), the enthalpy steps involved in the glass transition of these copolymers decrease with increasing UPy content, consistently, as inferred from the relative DSC heat flow traces normalized by the sample weight (see figure 7.3). Here, the concomitant broadening of the transition becomes particularly apparent from the respective differentiated DSC traces. The observed results can be rationalized by the formation of a supramolecular network involving the strongly hydrogen bonding UPy groups, which act as temporary cross-links. By increasing the number of UPy groups in the copolymers, the network mesh size is reduced and, hence, chain dynamics are slowed down and the available free volume is decreased. By comparison, the interpretation of the results obtained for the higher-generation DPs in this study appears more complex, as the segmental mobility of these DPs becomes additionally related to the generation number [206].

Both the number of dangling end-groups and the number density of the branching points, i.e. the compactness of the structure, increase with increasing dendron generation. However, end-groups and branching sites affect the glass transition in opposite directions: On the one hand, increased branching entails a denser packing and, hence, reduces the local segmental mobility, which ultimately leads to an increase of T_g. On the other hand, a larger number of peripheral end groups enhances local fluctuation and effects a decrease of T_g. Figure 7.2.b illustrates the compiled T_g values of the DPs containing 5, 25 and 50 mol% UPy as a function of generation, along with the data on the respective DPs without UPy-groups. In the case of PG1-40-UPy0, PG1-40-UPy5 and PG1-40-UPy25, the T_g values saturate with increasing polymer generation, which is in line with existing reports showing that the glass temperature increases with g before approaching a final value, i.e. no significant changes are found after approximately the fourth generation [108, 202, 204, 207]. The observed saturation of T_g is owed to the bulky pendant side groups of these DPs and reflects their enhanced backbone rigidity with increasing dendron generation. In this regard, it can also be considered analogous to the respective saturation with molar mass in linear polymers and dendrimers. Even though, qualitatively, the T_g values of the UPy-functionalized and UPy-unfunctionalized DPs converge to intermediate temperatures with increasing DP generation, larger UPy contents translate into higher T_g values throughout the studied generations, consistently. With the exemption of the series containing 50 mol% UPy, the difference in T_g values between the first- and third generation DPs of each series narrows down with increasing UPy content. Based on the virtually identical T_g values of PG3-40-UPy5 and PG3-40-UPy0, it can be reasoned that the UPy moieties in PG3-40-UPy5 are completely immersed in the interior of the DP. Hence, the possibility for intermolecular, specific hydrogen bonding interactions by the UPy moieties is effectively inhibited due to the steric shielding by the surrounding dendrons. In addition, the random incorporation of the UPy-bearing monomer 2b into

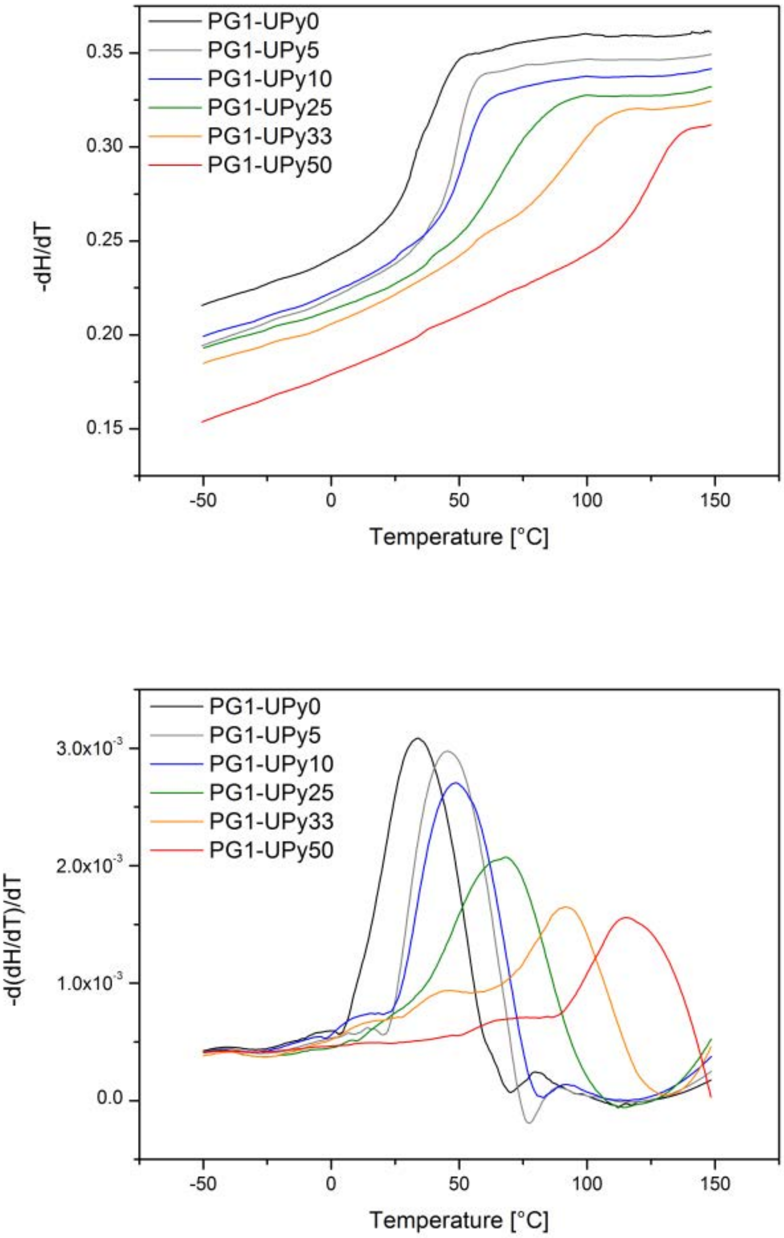

Figure 7.3: (a) Second heating DSC thermograms for the first-generation DPs comprising 0-50 mol% UPy normalized by the sample weight. In (b), the differentiated traces are shown to better visualize the shift and broadening of the glass transition.

the polymer combined with the large excess of unfunctionalized monomer 1c (1c:2b = 9:1) renders intramolecular UPy-UPy-dimerization unlikely, as substantiated by the results obtained from 1H NMR spectroscopy. On the other hand, the dendronization of PG1-40-UPy50 results in a greatly reduced T_g value of PG2-40-UPy50, despite the 50% lower grafting density compared to the UPy-unfunctionalized DPs. Evidently, already one dendron generation suffices to significantly reduce the amount of intermolecular UPy-UPy dimerization. In the following, the decrease in the T_g upon dendronization of PG2-40-UPy50 to PG3-40-UPy50 is marked albeit much smaller. Due to the close proximity of UPy moieties in the homopolymer of 2b, a shift from inter- to intramolecular UPy dimerization takes place, as already evidenced by the recorded 1H NMR spectra of the samples containing 25% UPy. It is important to note that one distinct advantage of our present polymers is that the degree of polymerization in each homologous series remains virtually constant, which allows for systematic investigation of properties as a function of generation. The results indicate that the thermal properties of the present DPs are predominantly governed by the number and location of UPy groups in the polymers. Hence, the T_g values of DPs can be tuned via both generation growth and the degree of UPy-functionalization.

7.2.2 Linear viscoelasticity

Aging protocol and reproducibility of the measurements

In the previous chapter, we have reported that dendronized polymers undergo aging due to the tendency of dendrons to mutually interpenetrate in order to minimize intermolecular density gradients. Because of steric hindrance and cooperative rearrangement of dendrons, the ageing process is rather slow, the required time depending on the initial state of the particular sample. Furthermore, the final interdigitated state depends on the particular path followed for equilibration.

For classic DPs we have used a consistent protocol to achieve an equilibrated state (see section 6.2.2): after cold-pressing, we loaded each sample in the rheometer, waited a short time for thermal stabilization and then monitored the equilibration at the same distance from T_g by following the temporal evolution of the dynamic moduli. Such protocol provides consistent data for classic DPs of different series and yields a typical equilibration time for PGs of order of 20 hours.

The incorporation of UPy groups onto the side dendrons induces a reduction of their local mobility. UPy groups act as molecular anchors locking segments of the branches. The reduced mobility of the dendrons should speed-up the equilibration kinetics because they have to find the most stable configuration among a relatively limited range of possibilities compared to classic DPs. Such a conjecture is demonstrated in figure 7.4 where the equilibration of the samples PG1-40 at different UPy concentration is reported. The samples of figure 7.4 have been equilibrated according to the protocol followed for the classic DPs. From the equilibration curves of the samples at different UPy contents, it is apparent that the equilibration is faster as the molecular concentration of UPy increases.

Concerning dendronized polymers of first generation functionalized with UPy, we also used a different annealing strategy compared to previous protocol, in order to facilitate nonlinear rheological measurements. Indeed, using the previous protocol for nonlinear shear measurements is virtually impossible, as a new equilibration procedure would be required at each shear rate. On the other hand, it is not possible to monitor the temporal evolution of the moduli in extensional rheometers. Another issue associated with the first protocol is the fact that nonlinear measurements imply sample recycling due to small amounts available. Therefore, we tried to stabilize the samples through long-time thermal annealing. As described in section 2.6, the samples were annealed in vacuum for 8 days at the highest possible temperature (100°C) compatibly with their chemical stability. After the annealing protocol used here, the samples were found

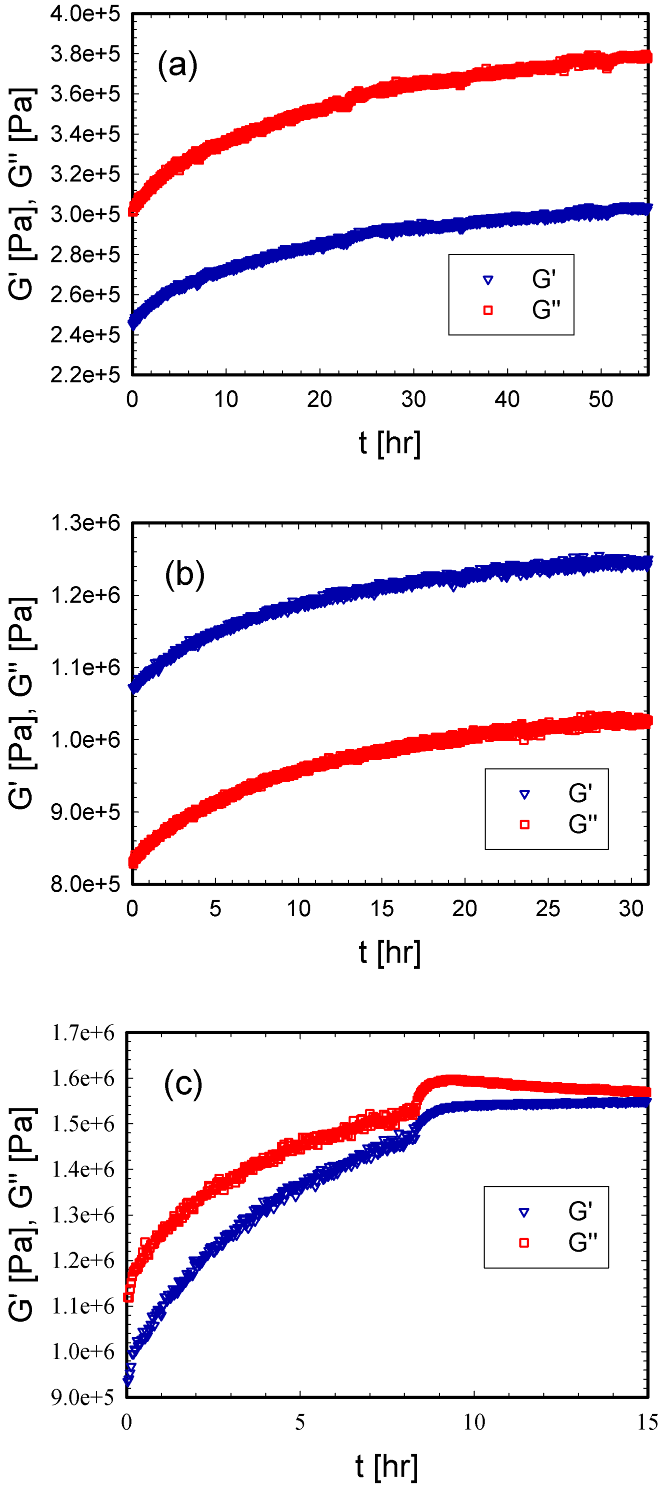

Figure 7.4: Equilibration curves of UPy samples of first generation. (a) PG1-40-UPy5 at $T = T_g + 29$°C; (b) PG1-40-UPy10 at $T = T_g + 28$°C; (c) PG1-40-UPy25 at $T = T_g + 29$ °C.

to reach a stable state that did not change upon further annealing and rheological measurements were reproducible before and after recycling, as depicted in figure 7.5. However, horizontal shifts were found between the mastercurves of the sample PG1-40 annealed with previous protocol and those of the same sample thermally annealed. This indicates that the two protocols are not equivalent.

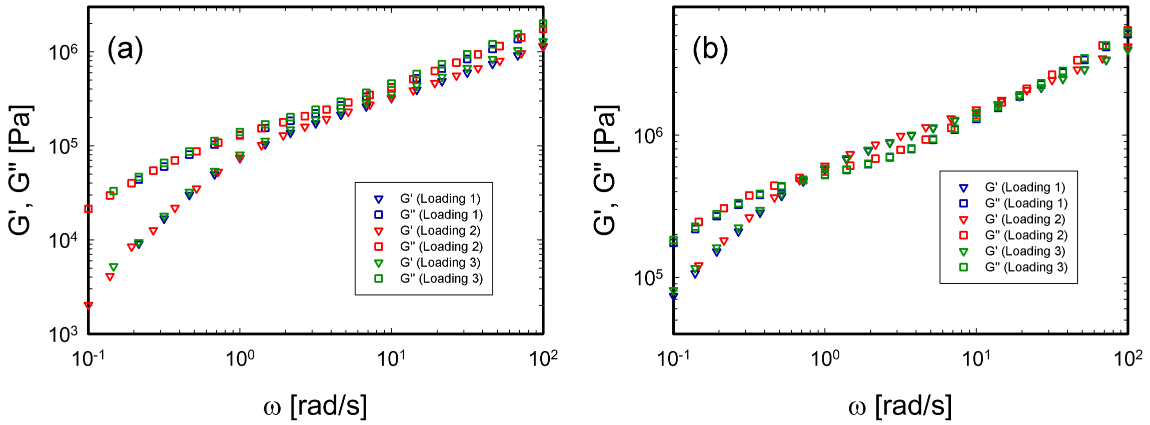

Figure 7.5: a) Frequency sweep tests performed on different specimens of the Sample PG1-40-UPy5 before nonlinear shear (T = 96°C). Specimen 1 was made from polymer after annealing in vacuum. Specimens 2 and 3 were obtained from polymer recycled from previous nonlinear measurements both in shear and extension. b) Frequency sweep tests performed on different specimens of the Sample PG1-40-UPy10 before nonlinear shear (T = 96°C). Specimen 1 was made from polymer after annealing in vacuum. Specimens 2 and 3 were obtained from polymer recycled from previous nonlinear measurements.

Effect of the coverage of the outer molecular surface with UPy groups

As mentioned above, Boc groups on the terminal part of the outermost branches can be replaced by UPy groups. The substitution of the outer branches can occur at different number fractions, f. Figure 7.6 reports the linear mastercurves of the samples PG1-40-UPy at different degrees of substitution of the outer branches, from 0 to 25%. The mastercurves are reported at the same distance from the glass temperature ($T_{ref} = T_g + 45$°C with T_{ref} being the reference temperature of the mastercurves). A Time-Temperature Superposition (TTS) algorithm based on two-dimensional minimization

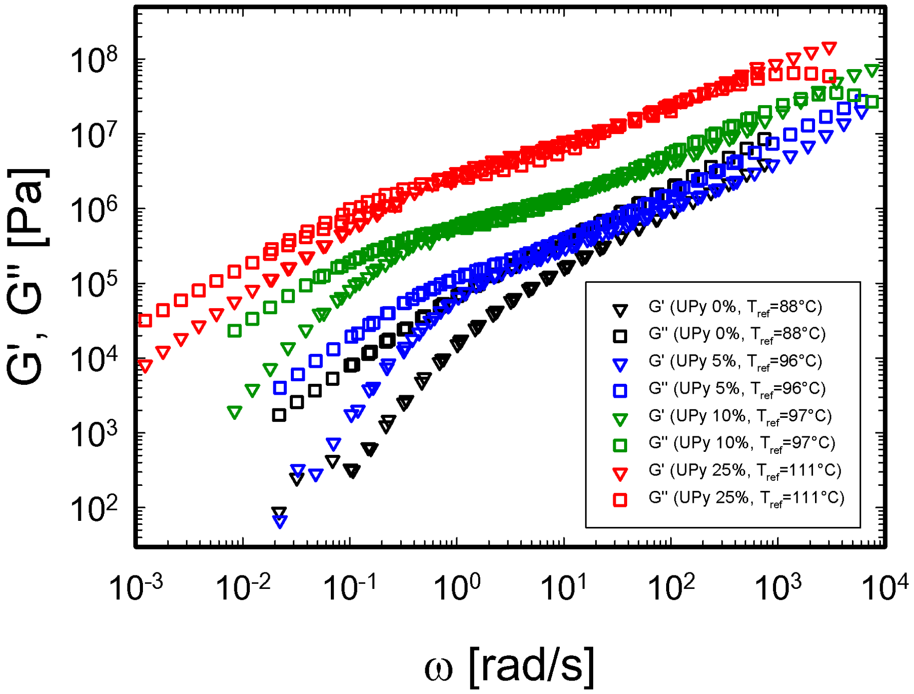

Figure 7.6: linear viscoelastic mastercurves of the samples PG1-40 with different degree of UPy coverage (from 0 to 25%) reported at the same distance from the glass temperature ($T_{ref} = T_g + 45°\text{C}$).

of errors was used in order to build all the mastercurves. The frequency sweep tests performed at ($T_{ref} = Tg + 45°\text{C}$) were used as TTS references in order to avoid artifacts induced by data shift. As expected, an increase of the concentration of UPy, induces an enhancement of the viscoelastic properties. The sample PG1-40-UPy0 has a liquid like behavior with $G'' > G'$ over the whole frequency range. At high frequencies, the moduli are parallel with a slope of 0.65 indicating Zimm-like dynamics in analogy with other branched systems [222]. At lower frequencies a clear transition from Zimm to terminal behavior is observed. In the high frequency range, the sample PG1-40-UPy5 has similar behavior as PG1-40-UPy0. However, the transition from high frequency behavior to terminal regime is characterized by the tendency of the elastic modulus to form a plateau. The plateau of G' becomes apparent as the UPy content is increased to 10%. For this sample G' is larger than G'' in the intermediate frequency range.

As the UPy content reaches 25%, the plateau increases by one decade compared to PG1-40-UPy10. Moreover, the slopes of the moduli at low frequencies are different from 1 and 2 for G' and G'', respectively. For all the samples, a terminal time τ can be evaluated as follows

$$\tau = \lim_{\omega \to 0} \eta_0 J_e = \lim_{\omega \to 0} \frac{G'}{\omega G''} \tag{7.1}$$

where ω is the angular frequency, η_0 the zero shear viscosity and J_e the steady state recoverable compliance. The extracted values of terminal time show that dynamics slow down as UPy content increases.

Shielding intermolecular interactions by immersing the UPy groups inside the macromolecule

UPy moieties can be immersed in the inner part of the DP molecule by growing classic generations on top of the first one. As intermolecular bonding mainly occurs between the outermost branches of different molecules [202], growing classic generations on top of the branches functionalized with UPy should screen strong intermolecular interactions. Figure 7.7 shows the mastercurves of UPy functionalized samples with second (fig. 7.7.a) and third (fig. 7.7.b) weakly interacting generations.

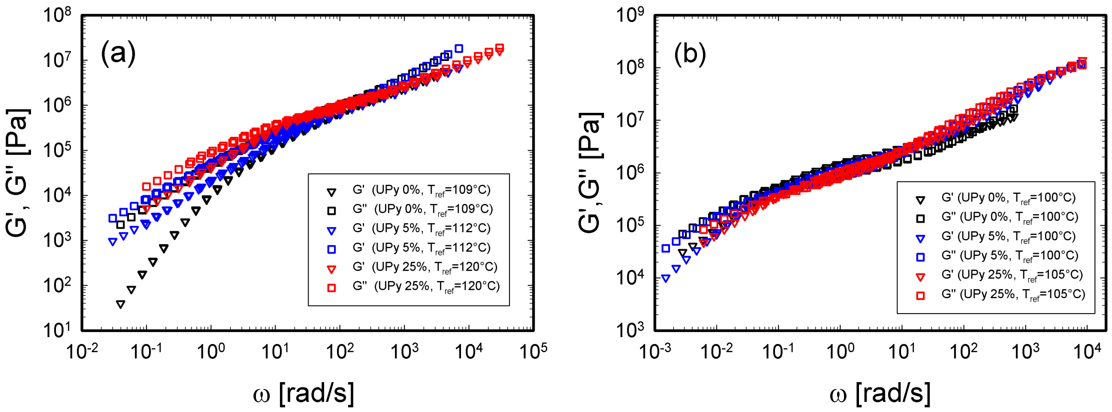

Figure 7.7: a) linear viscoelastic mastercurves of the samples PG2-40 with UPy ($T_{ref} = T_g +$ 45°C); b) linear viscoelastic mastercurves of the samples PG3-40 with UPy ($T_{ref} = T_g$+30°C).

Since measurements were restricted to linear viscoelasticity, the samples were annealed according to the protocol [202] used for the classic DPs. In both cases, an increase of UPy content from 0 to 25% in the inner part of the molecule, does not bring any significant contribution to the plateau modulus. This is more apparent for generation 3 where the screening of UPy groups is much more effective.

7.2.3 Nonlinear rheology

Uniaxial extension

PG1-40-UPy samples were tested in uniaxial extension at the same distance from the glass temperature. Results of transient uniaxial extensional measurements are shown in figure 7.8. For the unfunctionalized sample PG1-40-UPy0 the distance from T_g was slightly larger compared to the functionalized samples (34°C instead of 29°C). In the range of strain rates explored, PG1-40-UPy0 exhibited weak strain hardening, which can be barely discerned due to experimental noise (figure 7.8(a)). The noise is attributed to stress values at low rates which are close to the sensitivity of the transducer. Strain hardening becomes evident for PG1-40-UPy5 (figure 7.8(b)). For this sample, the departure of the transient extensional viscosity from the LVE envelope is unambiguous. Moreover, the stress growth coefficient reaches steady state for the three lowest rates. For the two highest rates, the elongational viscosity η_{el} shows an overshoot before steady state. We attribute such feature to the significant amount of stretch of the side dendrons at large values of extensional rates. Both PG1-40-UPy0 and PG1-40-UPy5 exhibit ductile behavior in uniaxial extension namely, they are able to deform in thin filaments without breaking under tensile stress. The samples could be stretched up to the maximum achievable strain with the instrument without failure. Note that the characteristic terminal relaxation time of PG1-40-UPy5, is τ_D=67±4 s at 80°C ($\omega_c = 0.015 \pm 0.01$ rad/s), and ductile behavior was observed even when the

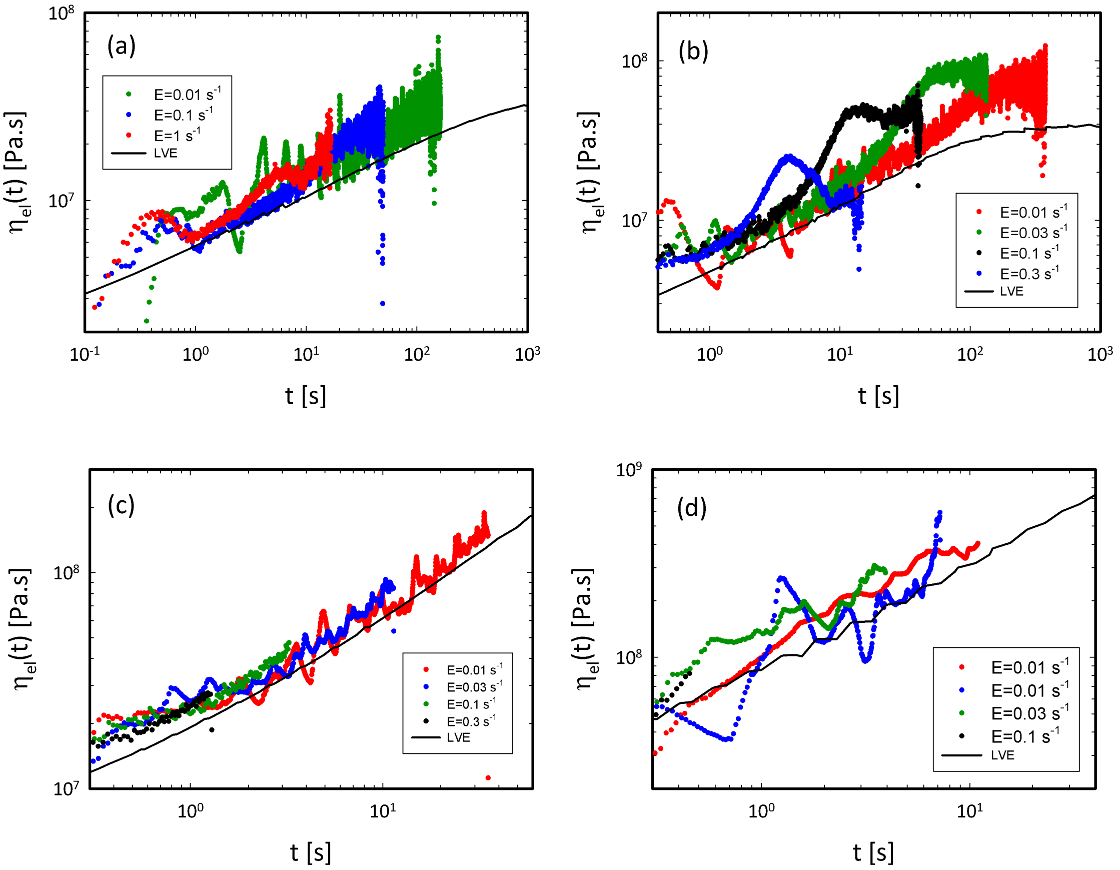

Figure 7.8: Uniaxial extension measurements on UPy samples at the same distance from T_g ($T_{ref} = T_g + 30$°C). (a) PG1-40-UPy0 at 72°C, (b) PG1-40-UPy5 at 80°C, (c) PG1-40-UPy10 at 81°C, (d) PG1-40-UPy25 at T=95°C. Strain rates are reported in the respective legends (symbol E).

strain rate exceeded the inverse of the characteristic time of the material. Some of the thin filaments originated from extension of such samples are displayed in figure 7.9 (1-4). Concerning samples with larger UPy fraction, it was not possible to detect strain hardening because brittle failure occurred as soon as extensional viscosity departed from the LVE envelope, i.e., no significant deformation was observed before breakage (figures 7.8(c) and 7.8(d)). The data for PG1-40-UPy25 are affected by relevant noise because the amount of deformation before breakage was very small and the rheometer could not properly resolve the stress signal in such conditions.

Typical images of catastrophic failure with samples PG1-40-UPy10 and PG1-40-

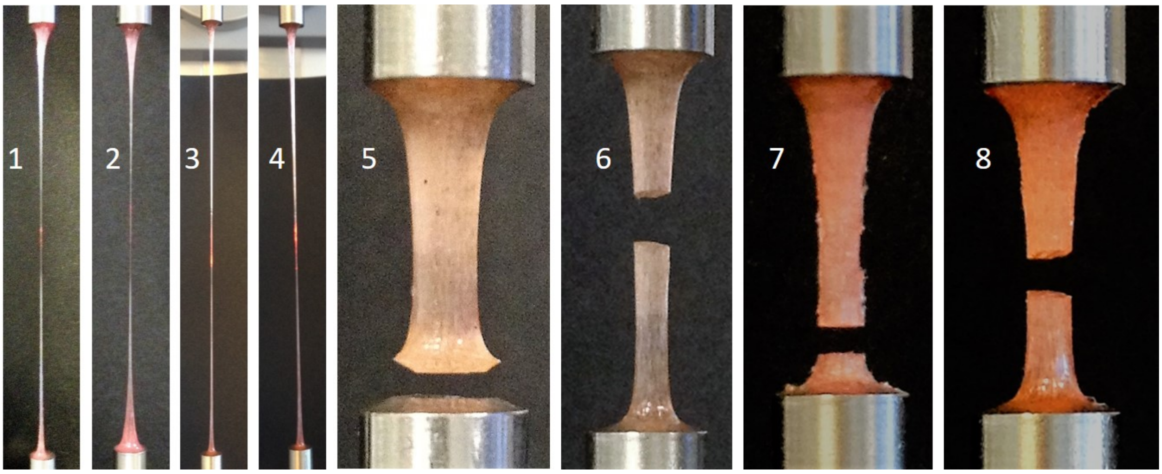

Figure 7.9: Ductile to brittle transition of UPy-DPs: 1. PG1-40-UPy0 ($\dot{\varepsilon} = 0.01$) 2; PG1-40-UPy0 ($\dot{\varepsilon} = 0.03$); 3. PG1-40-Upy5 ($\dot{\varepsilon} = 0.01$); 4. PG1-40-Upy5 ($\dot{\varepsilon} = 0.03$); 5. PG1-40-UPy10 ($\dot{\varepsilon} = 0.1$); 6. PG1-40-UPy10 ($\dot{\varepsilon} = 0.3$); 7. PG1-40-UPy25 ($\dot{\varepsilon} = 0.01$); 8.PG1-40-UPy25 ($\dot{\varepsilon} = 0.03$).

UPy25 are shown in 7.9 (5-8). It is interesting that brittle behavior was observed even at strain rates lower than the inverse of the terminal relaxation time (the latter being about 77 s at 81 °C). Similar behavior was observed for PG1-40-Upy25 (with terminal time of about 40 s at 95°C). The transition from ductile to brittle behavior upon increase of the UPy molecular content can be explained tentatively from a microscopic perspective by considering the evolution of the particular structure of UPy functionalized dendronized polymers in uniaxial extensional flow. The configuration of such polymers in the molten state is that of short bulky objects preferably oriented parallel to each other along the flow direction, with the side dendrons of one DP locked at the edge to the side dendrons of neighboring DPs via strong hydrogen bonds due to UPy groups. Upon application of uniaxial extensional deformation, molecules tend to orient in the direction of flow and possibly become stretched. The orientation/stretching process cause local motion and stretching of the dendrons locked by hydrogen bonding via UPy groups. The response of these side-dendrons is responsible for substantial resistance to extensional flow and strain hardening of the UPy-functionalized samples. If the fraction of UPy groups is below 5%, the modulus of the DPs is relatively low and they can deform elastically, giving rise to ductile response. With such a low fraction, bond breaking is not accompanied by easy recombination (which becomes less probable), hence this may lead to local dissipation of the elastic energy. If the bonding density is increased beyond 10%, the Velcro picture is relevant with bond breaking and reformation taking place in a cooperative fashion. At a certain stretch rate, the global breaking of bonds leads to material failure (brittle fracture) without possibility for immediate reformation. Typical examples are shown in figure 7.9 (5-8).

Simple shear

Nonlinear shear experiments on the unfunctionalized sample PG1-40-UPy0 (figure 7.10(a)), revealed a shear thinning behavior with reduced deformability [202]. The transient viscosity at the highest rate is affected by edge fracture after reaching steady state (data affected by fracture are indicated by red arrows in figure 7.10). Incorporation of strongly hydrogen-bonding units to DPs causes a remarkable transition from shear thinning to shear hardening transient behavior (figure 7.10). Strain hardening under shear has been already observed for aqueous solutions of associating polymers [229–231] and attributed to substantial stretch of the chains before bond breakage [232]. Here, we report on strain hardening in shear of dendronized polymer melts and ascribe it to stretch of locked segments of side-dendrons. At UPy concentration of 5%, as the shear rate is increased beyond 1 s^{-1}, the transient viscosity increases beyond the LVE prediction (figure 7.10(b)). The strain hardening is more apparent as the shear rate increases. A similar behavior is observed with 10% of UPy (figure 7.10(c)), even though fracture is observed as the shear thinning regime is entered. When the molecular content of UPy increases up to 25% the sample fractures around the peak viscosity region at the onset of strain hardening (figure 7.10(d)). In analogy to the extensional behavior, strain hardening in shear is attributed to stretching of the side dendrons before bond-breakage occurs. In particular, the transition from ductile to

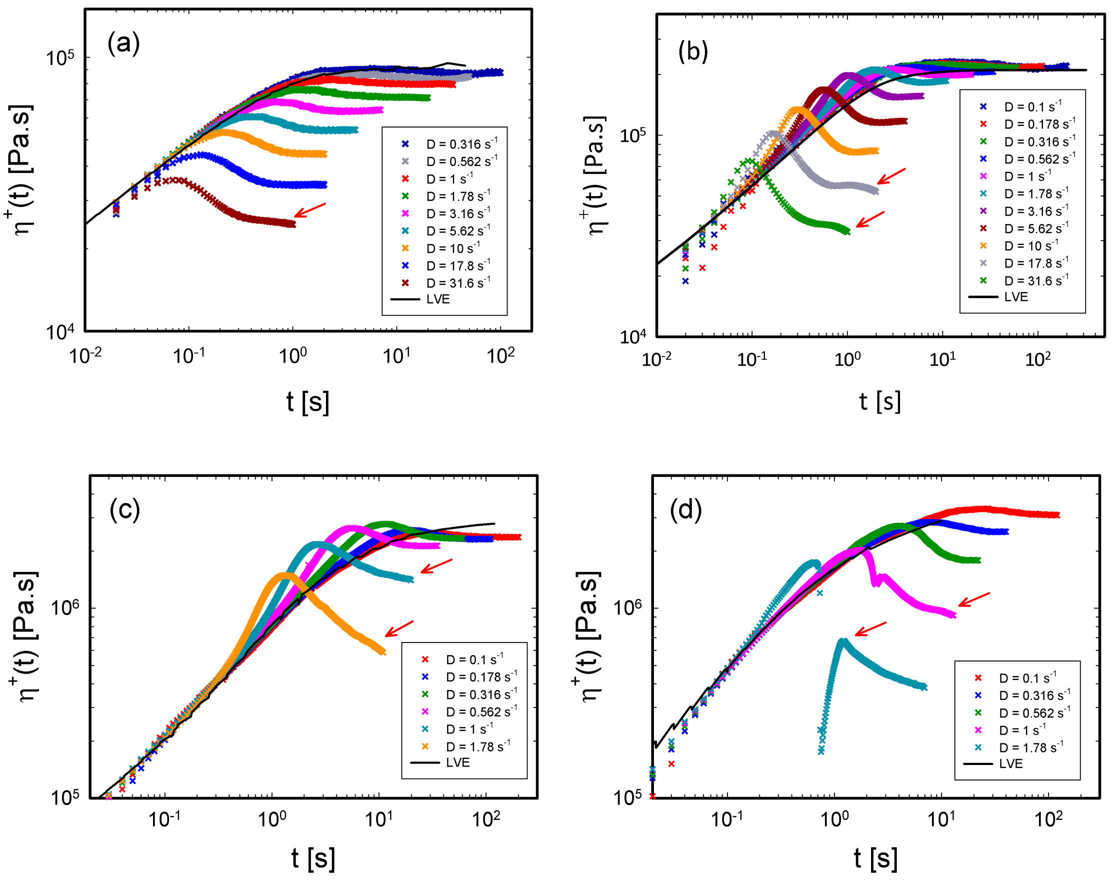

Figure 7.10: Nonlinear shear rheology of UPy-DPs. (a) PG1-40-UPy0 at T=88°C, (b) PG1-40-UPy5 at T=96°C, (c) PG1-40-UPy10 at T=97°C and (d) PG1-40-UPy25 at T=120°C. Shear rates (symbol, D) are indicated in the respective panels. Red arrows indicate shear fracture.

brittle behavior in extension can be related to the capacity of UPy-DPs to undergo shear thinning in simple shear.

Figure 7.11 reports the applicability of Cox-Merz rule [22] to UPy-DPs. The applicability of such rule to the unfunctionalized sample is confirmed. However, the introduction of small amounts of UPy to the molecules implies the failing of Cox-Merz. In particular, the steady state viscosity of the sample PG1-40-UPy5 tends to shear thinning at larger values of shear rate compared to the linear prediction, however when shear thinning occurs, the power-law decay of viscosity has a larger exponent than the LVE prediction (faster decay of viscosity upon shear rate). Both ductile samples have the ability to

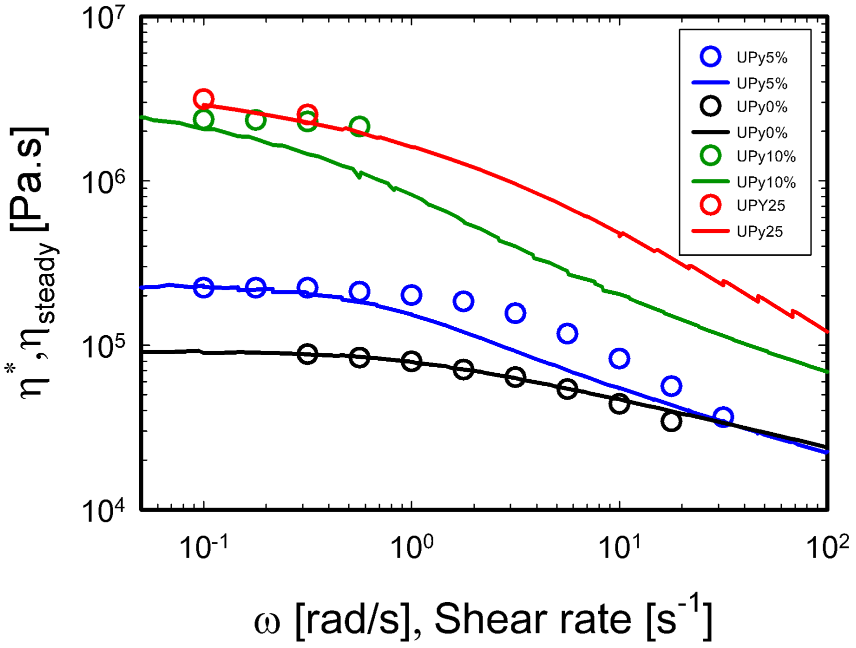

Figure 7.11: Application of the Cox-Merz rule to UPy-functionalized dendronized polymers.

shear thin in nonlinear shear. The strain hardening in shear has the same origin as in extension, i.e. stretching of the dendrons before hydrogen bonds are broken. However, when UPy fraction is less than 5%, molecule can easily uncorrelate from each other and diffuse, hence they display shear thinning in shear and ductility in extension. On the other hand, the samples PG1-40-UPy10 and PG1-40-UPy25 are virtually not allowed for shear thinning, as it can be observed in figure 7.11. Indeed, sample PG1-40-UPy-10 exhibit failure of Cox-Merz rule as for PG1-UPy-5%. Moreover, catastrophic failure occurs before shear thinning is observed. Strong shear fracture hinders the possibility to detect steady state viscosity in the shear thinning regime. A similar behavior is observed also for PG1-40-UPy25%. Figure 7.12 depicts the strain hardening factor of PG1-40-UPy5 and PG1-40-UPy-10, i.e., the transient nonlinear shear viscosity normalized by the viscosity evolution in linear regime. A larger capacity of strain hardening of PG1-40-UPy10 compared to PG1-40-UPy5 is apparent. Such capacity is attributed to the larger amount of stretch of the dendrons before molecules become

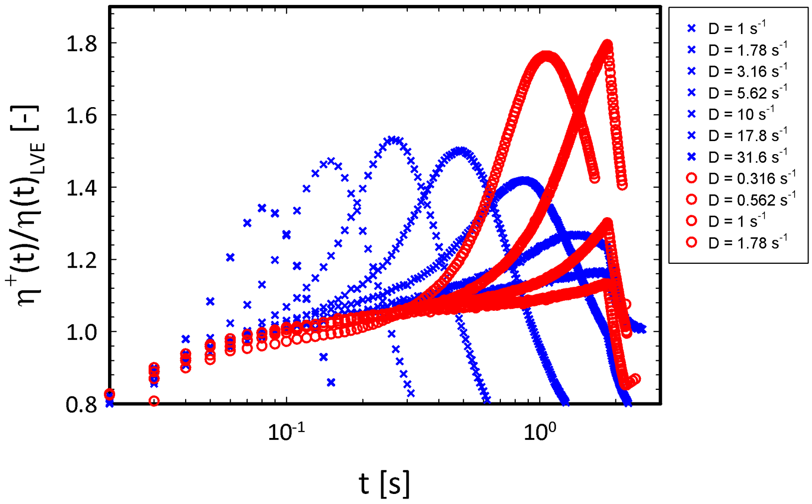

Figure 7.12: Strain hardening factor for PG1-40-UPy5 (blue crosses) and PG1-40-UPy10 (red circles). Shear rates are reported in the legend.

uncorrelated owing to the disruption of the hydrogen bonds. Figure 7.13 shows that the transient viscosity overshoot at high shear rates scales with the strain, whose value ($\gamma_{max} = 3.1 \pm 0.2$) is larger compared to that of unfunctionalized samples (PG1-40-UPy0, $\gamma_{max} = 2.3 \pm 0.2$). This means that the dendrons locked by UPy are effectively stretched compared to the unfunctionalized samples.

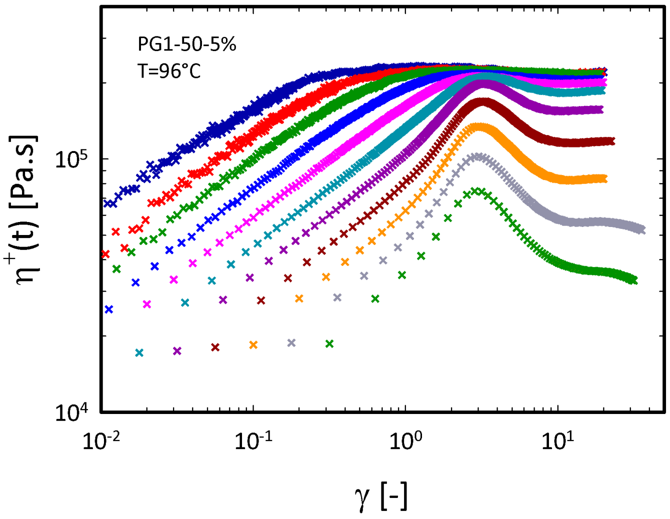

Figure 7.13: shear viscosity as a function of strain for PG1-40-UPy5.

7.2.4 Foaming of samples with UPy = 50%

In section 2.5 we have reported that we could not measure the rheological properties of dendronized polymers with UPy concentration larger than 25% because of unexpected foaming events. Figure 7.14 shows foaming of the sample PG1-40-UPy50 both in ARES and Physica MCR702 rheometers.

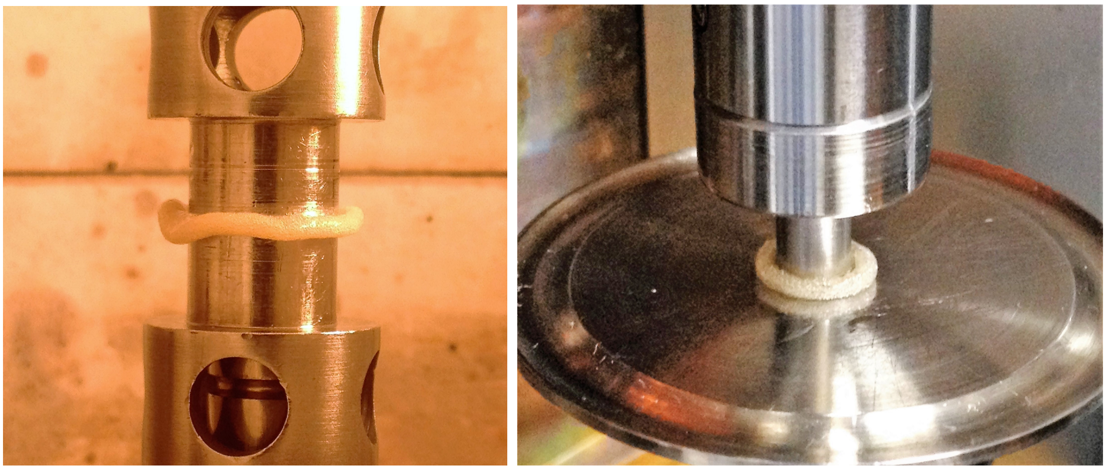

Figure 7.14: Foaming of the sample PG1-40-UPy50 in (a) ARES rheometer at 140°C and (b) Physica MCR702 rheometer at 140°C.

We observed foaming also for the samples PG2-40-UPy50 and PG3-40-UPy50 at temperatures above 130°C. Nitrogen atmosphere was provided in both cases presented in figure 7.14, with flow rates as indicated in the respective manuals of the rheometers. Therefore, the origin of foaming remains elusive, to date. Possibly, partial degradation of UPy groups occurs at temperatures larger than 130°C even with the presence of tiny amounts of oxygen.

7.3 Concluding remarks

We investigated the linear and nonlinear rheological properties of a series of short dendronized polymers of first generation with increase molecular content of strong hydrogen bonding groups, from 0 to 25%. Different annealing protocols revealed an unusual dependency of the characteristic times on the thermal history of the samples. This is attributed to the correlation between the thermal history and the degree of interdigitation of the samples. Linear measurements revealed enhanced viscoelastic properties upon increase of the molecular content of UPy. Nonlinear uniaxial extension experiments show a transition from ductile to brittle transition at the same distance from the glass temperature. This is attributed to the reduced availability of free ends for dissipating elastic energy as the UPy concentration increases. The incorporation of UPy groups inside PG1-40 DPs causes onset of strain hardening in nonlinear shear. Such a remarkable behavior is attributed to strong intermolecular forces arising from the interaction of the locked brushes under shear (akin to Velcro picture).

Regarding the $g = 2$ and $g = 3$ DP samples with UPy groups in the interior (at $g = 1$ level) we find that already one dendron generation beyond g=1 suffices to effectively block off intermolecular UPy interactions as proven by the virtually identical mechanical response of both DPs. This is in stark contrast to shielding experiments with structurally closely related DPs which instead of UPy carry solvatochromic probes at the $g = 1$ level. Solvent still can swell the corresponding DPs up to the $g = 4$ level, while the similarly sized UPy groups obviously cannot mutually interpenetrate beyond $g = 2$. The very fact that UPy groups are part of a macromolecule and not as independent as solvent molecules seems to have a bearing on this unexpected finding. The absence of intermolecular dimerization was used to create a situation in which the UPy groups could not dimerize at all, a case which because of the high binding constant had never been observed. In PG3-40-UPy5 the UPy groups are so spaced out along the main chain that they cannot find each other anymore resulting in the absence of the so typical UPy dimer signals in NMR spectroscopy. The high degree of tunability of both linear and nonlinear properties and the unique nonlinear behavior in shear and extension makes these novel polymers with only 40 RUs promising candidates for the design of new functional materials.

Chapter 8

CONCLUSIONS AND PERSPECTIVES

The need for fast processing of polymers has posed new challenges for rheologists. When polymeric materials are pumped, extruded or mixed at high strain rates they undergo strong nonlinear flow conditions. The rheological beavior of polymers in nonlinear flows is remarkably different compared to their linear viscoelastic response. For example, in strong nonlinear shear flows, normal stresses develop and can be responsible in part for flow instabilities, as pointed out in chapter 1. Such instabilities affect the processing and quality of the final products. Therefore, it is essential to understand material properties of polymers subjected to nonlinear flows both from microscopic and macroscopic perspective, in order to develop models at different scales and provide the ingredients for tailoring the mechanical properties according to particular needs. Measuring viscometric functions in nonlinear conditions is a non-trivial task because instabilities occur in lab-scale experiments as well as in industrial-scale units.

A relevant issue of significance is edge fracture in shear flows. The fracture of the sample at the edge in rotational rheometry affects both viscosity and normal force measurements and prohibits collecting reliable data on the viscometric functions of polymer melts and solutions in strong shear. An effective tool to overcome edge fracture instability is the CPP fixture.

In chapter 3, we presented our improvements to the state-of-the-art CPP rheometry. We designed and built a new CPP tool for the ARES rheometer with several advantages compared to previous designs. Our CPP is relatively easy to align both horizontally and vertically. It has large mechanical stability as it is attached to a balanced bridge. Thermal stability is ensured by the convection oven of the ARES. Moreover, the small inner diameter allows measuring very small quantities of sample (20 mg). We validated such CPP geometry and demonstrated that we can obtain reliable viscosity/stress measurements in transient shear. Moreover, by modifying our setup with a second modular partition of different inner diameter, we showed that N_1 and N_2 of polymer solutions can be determined with good accuracy by means of two experiments for each shear rate. The same protocol is applicable also to melts but we were limited by the maximum normal force of the ARES rheometer. Moreover, reliable data were limited to steady-state because of axial compliance effects. Future work should focus on adapting our tool and protocol to rheometers with larger normal force capacity. Furthermore, edge fracture is delayed but not avoided with CPP geometry. An efficient way of postponing edge fracture would be testing samples surrounded by other liquids, instead of air. This would change the surface tension at the interface without affecting the boundary conditions. Such procedure is yet to be investigated.
After developing and testing the CPP geometry, we proceeded with the investigation of nonlinear flows of different polymer architectures. The aim was to determine the interplay of topological constraints and supramolecular interactions with respect to both the linear and nonlinear rheology of polymer systems. For each of the systems investigated, nonlinear rheology has been a very effective tool to address specific open questions regarding nonlinear flow properties.

Starting from the simple picture of linear polymer melts and solutions, we presented in chapter 4 a systematic investigation of the nonlinear shear and extensional properties of polystyrene melts and solutions with the same number of entanglements and we rationalized the results in the framework of the tube-based model. In the nonlinear regime we demonstrated that the differences between melts and solutions observed in uniaxial extensional flows are not detectable in shear flows over the same range of Rouse-based Weissenberg numbers. This fact confirms that in strong aligning flows (uniaxial extension) friction reduction differentiates melts from solutions, the latter reaching a smaller value of the average order parameter because of the reduced orientation of the solvent molecules. Concerning fast shear flows, a specific phenomenon due to the rotational component of flow appears to play a significant role, namely tumbling. The latter was recently demonstrated by means of molecular dynamics simulations of Sefiddashti *et al.* [38]. The proposed model, accounting for friction reduction in uniaxial extension and tumbling in shear, was in good agreement with transient viscosity/stress data in both flow conditions. However, the model failed to provide reliable predictions of transient normal force in shear, apparently because data of transient normal force were affected by axial compliance. Future work should focus on further improving reliable transient normal force measurements in order to determine both the effective N_1 and N_2 for melts and solutions with larger number of entanglements. Modeling should relate tumbling to the characteristics of N_1 and N_2. In addition, molecular tumbling should be studied by quenching deuterated samples in the rheometer and measuring them by means of Small Angle Neutron Scattering (SANS). Moreover, it is worth to investigate how the nonlinear extensional rheology of unentangled molecules compares to nonlinear shear.

The linear and nonlinear rheological data of two experimentally pure ring polymers and two respective ring/linear mixtures were also discussed in chapter 4. Linear rheology revealed typical features of ring polymers, i.e. absence of G' plateau and power-law relaxation (with an exponent of about 0.4). For moderately entangled rings ($Z = 5-10$), terminal flow behavior involved an extra slower mode attributed to traces of unlinked linear and ring-ring penetration. The overshoot in transient viscosity of the rings at high Weissenberg numbers, was less prominent compared to their linear precursors, suggesting that the nonlinear deformation of rings is weaker compared to their linear counterparts. This is also reflected in their weaker shear thinning behavior. Data obtained with ring-linear blends exhibited a nonlinear shear behavior closer to that of entangled linear chains. The present data set should motivate further shear and extensional experiments with larger molecular weights and ring-linear, as well as ring-ring mixtures.

In order to decode the complex nonlinear extensional and shear rheology of branched polymers, we investigated in chapter 5 the growth, steady state and subsequent relaxation of viscosity during uniaxial extensional and shear deformation of model, marginally entangled Caley-tree structures. We used FSR for extensional and CPP for shear measurements. The extensional and shear rates covered a range extending from LVE terminal relaxation to rubbery regime. Despite the small values of the imposed rates, significant strain hardening was observed. At the same time, viscosity overshoots signaled the deformation of these polymers in shear as well. Extensional relaxation was broader and slower than in shear. The latter differed from that of the linear stress relaxation modulus initially, but at long times became nearly identical. The unusual relaxation of viscosity upon cessation of uniaxial extensional was consistent with a stronger deformation in extension and the related strain hardening. The BoB framework based on independent pom-pom modes described the experimental data in linear and nonlinear shear (growth and relaxation) and extension (growth and initial relaxation) reasonably well, without fit parameters. This is remarkable considering the fact that a segment between two branches in these molecules was less than three entanglements long. The slow relaxation upon cessation of extensional flow was suggested to reflect coupling of the stretches in different generations. To describe it, a modified model should be considered. Whereas this calls for further investigations, it already shows a way to use strong flows for tailoring properties of polymeric materials and effectively enhancing their elastic memory. Furthermore, there is unambiguous evidence of steady state in extension. The high-rate regime in extension followed a thinning slope of -0.5 in accordance with predictions and findings with other linear and branched polymers. This power-law is virtually followed by the shear data as well. In general, at first sight it is a surprise that BoB does such a good job in predicting both the linear and nonlinear rheology of such a polymer with barely entangled branches. We attributed this to the difference in the strength of the entanglement constraints at the branch point as opposed to the respective linear entangled polymers. This ensured that the dynamics of the inner segments remained dominated by the branch-point friction instead of the monomer friction, hence a framework based on the well-entangled polymers captured the relaxation of unentangled (due to the dilation effect) inner segments. In fact, the present case may be thought of as the limit of validity of the BoB model. Future work should be done with similar systems in order to explore the intriguing stress relaxation of this class of polymers. In addition, modeling should undergo further development in the direction of testing the above stretch coupling idea and predicting viscosity relaxation consistently in shear and extension and eventually advancing constitutive modeling. At the same time, measurements of polymer conformation *in situ* or *ex situ* (via quenching below glass temperature of deuterated samples and SANS measurements) and attempts to probe nonlinear material functions (including normal stresses) at higher rates will further advance the field.

Dendronized polymers (DP) are the natural extension of the concept of dendrimer but their architecture is such that molecular thickness cannot be neglected. In addition, based on their synthesis, they involve intra- and intermolecular interactions. In order to decode their mechanical properties, we presented a systematic investigation of the linear and nonlinear rheology of well-characterized first-, second-, and third-generation DPs in chapter 6. PGs were found to exhibit very long equilibration times due to their tendency to reduce gradients in monomer density. Aged PGs exhibited complex viscoelastic response dominated by the intermolecular bonding interactions, since entanglement interactions are at best weak. The linear viscoelastic data indicated the occurrence of a plateau modulus for DPs, which was lower than or comparable in value to that of the backbone (depending on generation g and degree of polymerization P_n). The intermolecular bonds and related molecular organization of DPs (liquid crystalline-like) were responsible for this modulus, whose extent in the frequency scale and actual value depended on both P_n and g. Eventually, the crossover of moduli marked the terminal relaxation and the very long relaxation times reflected the lifetime of the bonds. Their nonlinear response was akin to FENE chains without appreciable deformation and with weak shear thinning. The instantaneous maximum deformation was already saturated at the lowest shear rates, whereas Cox-Merz rule was validated. Overall, a Velcro-type analogy was invoked in order to describe the DPs behavior. DPs interpenetrate, however this does not constitute entanglement effects but rather enhanced molecular friction which appears to dominate viscoelasticity for both small and large P_n. The Velcro analogy was directly linked to the lateral surface of DPs with their exposed areas being in contact with each other, yielding an eventual highly cooperative motion. Hence, the combination of bonding interactions and topology controlled the linear and nonlinear viscoelastic response of DPs and at the same time offered the means to tailor these properties at wish.

The strength of interactions represents another degree of freedom that can be changed in order to adjust the mechanical properties of DPs. In order to explore this possibility, we investigated the linear and nonlinear rheological properties of a series of short dendronized polymers of first generation with increased molecular content of strong hydrogen bonding groups, from 0 to 25%. Different annealing protocols revealed an unusual dependency of the characteristic times on the thermal history of the samples. This was attributed to the correlation between the thermal history and the degree of interdigitation of the samples. Linear measurements revealed enhanced viscoelastic properties upon increase of the molecular content of UPy. Nonlinear uniaxial extension experiments showed a transition from ductile to brittle transition at the same distance from the glass temperature. This was attributed to the reduced capability of free ends for dissipating elastic energy as the UPy concentration increases. The incorporation of UPy groups inside PG1-40 DPs caused onset of strain hardening in nonlinear shear. Such a remarkable behavior was ascribed to strong intermolecular forces arising from the interaction of the locked brushes under shear (akin to the Velcro picture). Regarding the $g = 2$ and $g = 3$ DP samples with UPy groups in the interior (at $g = 1$ level) we found that already one dendron generation beyond g=1 effectively shielded intermolecular UPy interactions. The high degree of tunability of both linear and nonlinear properties and the unique nonlinear behavior in shear and extension makes these novel polymers with only 40 RUs promising candidates for the design of new functional materials. However, further investigation should address the possibility to add UPy groups at the periphery of DPs of larger generation than 1. Moreover, further work should be done on decoding the rheology of UPy-functionalized samples with degree of polymerization of the backbone larger than 50 repeating units. Finally, the observed ductile-to-brittle transition calls for further studies aimed at unambiguously elucidating its molecular origin.

Bibliography

(1) Colby, R. H.; Rubinstein, M., *Polymer Physics*; Oxford University Press: New York, 2003.

(2) De Gennes, P.-G.; Badoz, J., *Fragile Object, Soft matter, hard science, and the thrill of discovery*; Copernicus: Springer-Verlag, New York, Inc., 1996.

(3) Hosler, D.; Burkett, S. L.; Tarkanian, M. J. Prehistoric polymers: Rubber processing in ancient Mesoamerica. *Science* **1999**, *284*, 1988–1991.

(4) Staudinger, H. Die chemie der hochmolecularen stoffe im sinne der Kekuléschen strukurlehre. *Z. Angew. Chem.* **1929**, *42*, 37–40, 67–73.

(5) Gallé, F. World plastics outlook. *ICIS report* **2015**.

(6) Brunsveld, L.; Folmer, B. J. B.; Meijer, E. W.; Sijbesma, R. P. Supramolecular Polymers. *Chem. Rev.* **2001**, *101*, 4071–4097.

(7) Yang, L.; Xinxin, T.; Zhiqiang, W.; Zhang, X. Supramolecular polymers: historical development, preparation, characterization, and functions. *Chem. Rev.* **2015**, *115*, 7196–7239.

(8) Macosko, C. W., *Rheology: principles, measurements and applications*; Wiley-VCH, Ed., 1994.

(9) Larson, R. G., *Constitutive Equations for Polymer Melts and Solutions*; Butterworths Series in Chemical Engineering; Butterworth-Heinemann: 1988.

(10) Bird, R. B.; Armstrong, R. C.; Hassager, O., *Dynamics of polymeric liquids, Vol. 1: Fluid mechanics*; Wiley, Ed., 1987.

(11) Doi, M.; Edwards, S. F., *The Theory of Polymer Dynamics*; Clarendon Press: Oxford, 1986.

(12) De Gennes, P.-G., *Scaling-concepts in polymer physics*; Cornell University Press Ltd.: United Kingdom, 1979.

(13) Green, M. S.; Tobolsky, A. V. A new approach to the theory of relaxing polymeric media. *J. Chem. Phys.* **1946**, *14*, 80–94.

(14) Fetters, L. J.; Lohse, D. J.; Colby, R. H. Chapter 25: Chain dimensions and entanglement spacings. *Phys. Prop. Polym. Handb.* **2006**, 445–452.

(15) Reiner, M. The Deborah number. *Physics Today* **1964**, *17(1)*, 62.

(16) Marrucci, G.; Astarita, G. Significance of the Deborah number in steady flows. *Meccanica* **1967**, 141–143.

(17) Dealy, J. M. Weissenberg and Deborah numbers - Their definition and use. *Rheol. Bull.* **2010**, *79*, 14–18.

(18) Osaki, K. On the damping function of shear relaxation modulus for entangled polymers. *Rheol. Acta* **1993**, *32*, 429–437.

(19) Larson, R. G., *The structure and rheology of complex fluids*; Oxford University Press: New York, 1999.

(20) Hyun, K.; Wilhelm, M.; Klein, C. O.; Cho, K. S.; Nam, J. G.; Ahn, K. H.; Lee, S. J.; Ewoldt, R. H.; McKinley, G. H. A review of nonlinear oscillatory shear tests: analysis and application of large amplitude oscillatory shear (LAOS). *Prog. Polym. Sci.* **2011**, *36*, 1697–1753.

(21) Wilhelm, M. Fourier-Transform rheology. *Macromol. Mat. and Eng.* **2002**, *287*, 83–105.

(22) Cox, W. P.; Merz, E. H. Correlation of dynamic and steady flow viscosities. *J. Polym. Sci.* **1958**, *28*, 619–622.

(23) Kelly, P. A. Mechanics lecture notes - Part III, free on-line notes. **2012**, 330–334.

(24) Boger, D. V.; Walters, K., *Rheological phenomena in focus - Vol.4*; Elsevier, Ed.; Rheology series, Amsterdam, 1993.

(25) Miller, E.; Rothstein, J. P. Control of the sharkskin instability in the extrusion of polymer melts using induced temperature gradients. *Rheol. Acta* **2004**, *44*, 160–173.

(26) Keentok, M.; Xue, S.-C. Edge fracture in cone-plate and parallel plate flows. *Rheol. Acta* **1999**, *38*, 321–348.

(27) Zheng, R.; Tanner, R. I.; Fan, X.-J., *Injection Molding - Integration of theory and modeling methods*; Springer-Verlag: Berlin, Heidelberg, 2011.

(28) Hatzikiriakos, S. G.; Dealy, J. M. Wall slip of molten high density polyethylenes. II. Capillary rheometer studies. *Journal of Rheology* **1992**, *36*, 703–741.

(29) Tanner, R. I.; Keentok, M. Shear fracture in Cone-Plate Rheometry. *Journal of Rheology* **1983**, *27*, 47–57.

(30) Pollett, W. F. O. Rheological behaviour of continuously sheared polythene. *British Journal of Applied Physics* **1955**, *6*, 199–206.

(31) Meissner, J.; Garbella, R. W.; Hostettler, J. Measuring normal stress differences in polymer melt shear flow. *Journal of Rheology* **1989**, *33*, 843–864.

(32) Ashare, E., Ph.D. Thesis, University of Wisconsin, Madison, 1968, pp 50–52, 67–68, 105.

(33) Schweizer, T.; Schmidheiny, W. A cone-partitioned plate rheometer cell with three partitions (CPP3) to determine shear stress and both normal stress differences for small quantities of polymeric fluids. *Journal of Rheology* **2013**, *57*, 841–856.

(34) Doi, M. Explanation for the 3.4 power law of viscosity of polymeric liquids on the basis of the tube model. *Journal of polymer science, Polym. Lett. ed.* **1981**, *19*, 265–273.

(35) Marrucci, G. Dynamics of entanglements: A nonlinear model consistent with the Cox-Merz rule. *J. Non-Newtonian Fluid Mech.* **1996**, *62*, 279–289.

(36) Vlassopoulos, D. Macromolecular topology and rheology: beyond the tube model. *Rheol. Acta* **2016**, *55*, 613–632.

(37) Graham, R. S.; Likhtman, A. E.; McLeish, T. C. B. Microscopic theory of linear, entangled polymer chains under rapid deformation including chain stretch and convective constraint release. *Jornal of Rheology* **2003**, *47*, 1171–1200.

(38) Sefiddashti, M. H. N.; Edwards, B. J.; Khomami, B. Individual chain dynamics of polyethylene melt undergoing steady shear flow. *Journal of Rheology* **2015**, *59*, 119–153.

(39) Mead, D. W.; Larson, R. G.; Doi, M. A molecular theory for fast flows of entangled polymers. *Macromolecules* **1998**, *31*, 7895–7914.

(40) Roovers, J.; Toporowski, P. M. Synthesis of high molecular weight ring polystyrenes. **1983**, *16*, 843–850.

(41) Kapnistos, M.; Lang, M.; Vlassopoulos, D.; Pyckhout-hintzen, W.; Richter, D.; Cho, D.; Chang, T.; Rubinstein, M. Unespected power-law stress relaxation of entangled ring polymers. *Nature Mat.* **2008**, *7*, 997–1003.

(42) Lee, H. C.; Lee, H.; Lee, W.; Chang, T.; Roovers, J. Fractionation of cyclic polystyrene from linear precursor by HPLC at the chromatographic critical condition. *Macromolecules* **2000**, 8119–8121.

(43) Doi, Y.; Matsubara, K.; Ohta, Y.; Nakano, T.; Kawaguchi, D.; Takahashi, Y.; Takano, A.; Matsuhita, Y. Melt rheology of ring polystyrenes with ultrahigh puyrity. *Macromolecules* **2015**, *48*, 3140–3147.

(44) Watanabe, H.; Inoue, T.; Matsumiya, Y. Transient conformational change of bead-spring ring chain during creep process. *Macromolecules* **2006**, *39*, 5419–5426.

(45) Rubinstein, M. Dynamics of ring polymers in the presence of fixed obstacles. *Phys. Rev. Lett.* **1986**, *57*, 3023–3026.

(46) Yan, Z.-C.; Costanzo, S.; Jeong, Y.; Chang, T.; Vlassopoulos, D. Linear and Nonlinear Shear Rheology of a Marginally Entangled Ring Polymer. *Macromolecules* **2016**, *49*, 1444–1453.

(47) Milner, S. T.; McLeish, T. C. B. Parameter-Free Theory for Stress Relaxation in Star Polymer Melts. *Macromolecules* **1997**, *30*, 2159–2166.

(48) Lohse, D. J.; Milner, S. T.; Fetters, L. J.; Xenidou, M.; Hadjichristidis, N.; Mendelson, R. A.; Garcia-Franco, C. A.; Lyon, M. K. Well-defined, model long chain branched polyethylene. 2. Melt rheological behavior. *Macromolecules* **2002**, *35*, 3066–3075.

(49) Larson, R. G. Combinatorial Rheology of Branched Polymer Melts. *Macromolecules* **2001**, *34*, 4556–4571.

(50) Van Ruymbeke, E.; Muliawan, E. B.; Hatzikiriakos, S. G.; Watanabe, T.; Hirao, A.; Vlassopoulos, D. Viscoelasticity and extensional rheology of model Cayley-tree polymers of different generations. *Journal of Rheology* **2010**, *54*, 643–662.

(51) McLeish, T. C. B.; Larson, R. G. Molecular constitutive equations for a class of branched polymers: the pom-pom polymer. *Journal of Rheology* **1998**, *42.*

(52) McLeish, T. C. B. et al. Dynamics of Entangled H-Polymers: theory, Rheology and Neutron Scattering. *Macromolecules* **1999**, *32*, 6734–6758.

(53) McLeish, T. C. B. Tube theory of entangled polymer dynamics. *Advances in Physics* **2002**, *51*, 1379–1527.

(54) Snijkers, F.; Vlassopoulos, D.; Lee, H.; Yang, J.; Chang, T.; Driva, P.; Hadjichristidis, N. Start-up and relaxation of well-characterized comb polymers in simple shear. *Journal of Rheology* **2013**, *57*, 1079–1099.

(55) Pakula, T. Structure, dynamics and properties of materials with polymers having complex architectures. *Macromol. Symp.* **2004**, *214*, 307–315.

(56) Daniel, W. F.; Burdyńska, J.; Vatankhah-Varnoosfaderani, M.; Matyjaszewski, K.; Paturej, J.; Rubinstein, M.; Dobrynin, A. V.; Sheiko, S. S. Solvent-free, supersoft and superelastic bottlebrush melts and networks. *Nat. Mater.* **2015**, *15*, 183–189.

(57) Frauenrath, H. Dendronized Polymers - building a new bridge from molecules to nanoscopic objects. *Prog. Polym. Sci.* **2005**, *30*, 325–384.

(58) Schlüter, A. D.; Halperin, A.; Kröger, M.; Vlassopoulos, D.; Wegner, G.; Zhang, B. Dendronized polymers: molecular objects between conventional linear polymers and colloidal particles. *ACS Macro Lett.* **2014**, *3*, 991–998.

(59) Lehn, J. M. From supramolecular chemistry towards constitutional dynamic chemistry and adaptive chemistry. *Chem. Soc. Rev.* **2007**, *36*, 151–160.

(60) Bosman, A. W.; Sijbesman, R. P.; Meijer, E. W. Supramolecular polymers at work. *Materials Today* **2004**, *7*, 34–39.

(61) Cordier, P.; Tournilhac, F.; Soulié-Ziakovic, C.; Leibler, L. Self-healing and thermoreversible rubber from supramolecular assembly. *Nature* **2008**, *451*, 977–980.

(62) Sijbesma, R. P.; Meijer, E. W. Quadruple hydrogen bonded systems. *Chem. Comm.* **2003**, 5–16.

(63) Sijbesma, R. P.; Beijer, F. H.; Brunsveld, L.; Folmer, B. J. B.; Hirschberg, J. H. K. K.; Lange, R. F. M.; Lowe, J. K. L.; Meijer, E. W. Reversible polymers formed from self-complementary monomers using quadruply hydrogen bonding. *Science* **1997**, *278*, 1601–1604.

(64) Ducharme, Y.; Wuest, J. D. Use of hydrogen bonds to control molecular aggregation. Extensive, self-complementary arrays of donors and acceptors. *J. Org. Chem.* **1988**, *53*, 5787–5789.

(65) Söntiens, S. H. M.; Sijbesma, R. P.; Van Genderen, M. H. P.; Meijer, E. W. Stability and lifetime of quadrubly hydrogen bonded 2-ureido-4[1H]-pyrimidinone dimes. *J. Am. Chem. Soc.* **2000**, *122*, 7487–7493.

(66) Hilger, C.; Drager, M.; Stadler, R. Cooperative structure formation by combination of covalent and association chain polymers. 6. Molecular-origin of supramolecular self-assembling in statistical copolymers. *Macromolecules* **1992**, *25*, 2498–2501.

(67) Stadler, R. Thermoplastic elastomers via supramolecular self-assembling in random copolymers. *Kautschk Gummi Kunststoffe* **1993**, *46*, 619–628.

(68) Feldman, K. E.; Kade, M. J.; Meijer, E. W.; Hawker, C. J.; Kramer, E. J. Model transient networks from strongly hydrogen-bonded polymers. *Macromolecules* **2009**, *42*, 9072–9081.

(69) Rubinstein, M.; Semenov, A. N. Dynamics of entangled solutions of associating polymers. *Macromolecules* **2001**, *34*, 1058–1068.

(70) Kavassalis, T. A.; Noolandi, J. New view of entanglements in dense polymer systems. *Phys. Rev. Lett.* **1987**, *59*, 2674–2677.

(71) Kavassalis, T. A.; Noolandi, J. A New theory of entanglements and dynamics in dense polymer systems. *Macromolecules* **1988**, *21*, 2869–2879.

(72) Fetters, L. J.; Lohse, D. J.; D., R.; Witten, T. A.; Zirkel, A. Connection between polymer molecular weight, density, chain dimensions, and melt viscoelastic properties. *Macromolecules* **1994**, *27(17)*, 4639–4647.

(73) Fetters, L. J.; Lohse, D. J.; Graessley, W. W. Chain dimensions and entanglement spacings in dense macromolecular systems. *J. Polym. Sci.* **1999**, *37*, 1023–1033.

(74) Huang, Q.; Mednova, O.; Rasmussen, H. K.; Alvarez, N. J.; Skov, A. L.; Almdal, K.; Hassager, O. Concentrated polymer solutions are different from melts: role of entanglement molecular weight. *Macromolecules* **2013**, *46*, 5026–5035.

(75) Huang, Q.; Alvarez, N. J.; Matsumiya, Y.; Rasmussen, H. K.; Watanabe, H.; Hassager, O. Extensional rheology of entangled polystyrene solutions suggests importance of nematic interactions. *ACS Macro Lett.* **2013**, *2*, 741–744.

(76) Huang, Q.; Hengeller, L.; Alvarez, N. J.; Hassager, O. Bridging the Gap between Polymer Melts and Solutions in Extensional Rheology. *Macromolecules* **2015**, *48*, 4158–4163.

(77) Hirao, A.; Higashihara, T.; Nagura, M.; Sakurai, T. Successive synthesis of well-defined many arm star-branched polymers by an iterative methodology using a specially designed 1,1-diphenylethylene. *Macromolecules* **2006**, *39*, 6081–6091.

(78) Takano, A.; Nonaka, A.; Kadoi, O.; Hirahara, K.; Kawahara, S.; Isono, Y.; Torikai, N.; Matsushita, Y. Preparation and characterization of cyclic polystyrene with short poly(2-tert-blutylbutadiene) sequences. *Macromolecules* **2002**, *40*, 1582–1589.

(79) Cho, D.; Park, S.; Kwon, K.; Chang, T.; Roovers, J. Structural characterization of ring polystyrene by liquid chromatography at the critical condition and MALDI-TOF mass spectrometry. *Macromolecules* **2001**, *34*, 7570–7572.

(80) Hirao, A.; Matsuo, A. Synthesis of Chain-End-Functionalized Poly(methyl methacrylate)s with a Definite Number of Benzyl Bromide Moieties and Their Application to Star-Branched Polymers. *Macromolecules* **2003**, *36*, 9742–9751.

(81) Hirao, A.; Matsuo, A.; Watanabe, T. Precise Synthesis of Dendrimer-like Star-Branched Poly(methyl methacrylate)s up to Seventh Generation by an Iterative Divergent Approach Involving Coupling and Transformation Reactions. *Macromolecules* **2005**, *38*, 8701–8711.

(82) Hirao, A.; Sugiyama, K.; Tsunoda, Y.; Matsuo, A.; Watanabe, T. Precise synthesis of well-defined dendrimer-like star-branched polymers by iterative methodology based on living anionic polymerization. *Journal of Polymer Science Part A: Polymer Chemistry* **2006**, *44*, 6659–6687.

(83) Hirao, A.; Sugiyama, K.; Matsuo, A.; Tsunoda, Y.; Watanabe, T. Synthesis of well-defined dendritic hyperbranched polymers by iterative methodologies using living/controlled polymerizations. *Polymer International* **2008**, *57*, 554–570.

(84) Hirao, A.; Watanabe, T.; Ishizu, K.; Ree, M.; Jin, S.; Jin, K. S.; Deffieux, A.; Schappacher, M.; Carlotti, S. Precise Synthesis and Characterization of Fourth-Generation Dendrimer-like Star-Branched Poly(methyl methacrylate)s and Block Copolymers by Iterative Methodology Based on Living Anionic Polymerization. *Macromolecules* **2009**, *42*, 682–693.

(85) Van Ruymbeke, E.; Lee, H.; Chang, T.; Nikopoulou, A.; Hadjichristidis, N.; Snijkers, F.; Vlassopoulos, D. Molecular rheology of branched polymers: decoding and exploring the role of architectural dispersity through a synergy of anionic synthesis, interaction chromatography, rheometry and modeling. *Soft Matter* **2014**, *10*, 4762–4777.

(86) Guo, Y.; Van Beek, J. D.; Zhang, B.; Colussi, M.; Walde, P.; Zhang, A.; Kröger, M.; Halperin, A.; Schl"uter, A. D. Tuning polymer thickness: synthesis and scaling theory of homologous series of dendronized polymers. *J. Am. Chem. Soc.* **2009**, *131*, 11841–11854.

(87) Zhang, B.; Wepf, R.; Fischer, K.; Schmidt, M.; Besse, S.; Lindner, P.; King, B. T.; Sigel, R.; Schurtenberger, P.; Y., T.; Ding, Y.; Kröger, M.; Halperin, A.; Schlüter, A. D. The largest synthetic structure with molecular precision: towards a molecular object. *Angew Chem., Int. Ed.* **2011**, *50*, 737–740.

(88) Zhang, B.; Yu, H.; Schlüter, A. D.; Halperin, A.; Kröger, M. Synthetic regimes due to packing constraints in dendritic molecules confirmed by labelling experiments. *Nat. Commun.* **2013**, *4*, 1993.

(89) Bach, A.; Rasmussen, H. K.; Hassager, O. Extensional viscosity for polymer melts measured in the filament stretching rheometer. *Journal of Rheology* **2003**, *47*, 429–441.

(90) Rasmussen, H. K.; Bejenariu, A. G.; Hassager, O.; Auhl, D. Experimental evaluation of the pure configurational stress assumption in the flow dynamics of entangled polymer melts. *Journal of Rheology* **2010**, *54*, 1325–1336.

(91) Kolte, M. I.; Rasmussen, H. K.; Hassager, O. Transient filament stretching rheometer.2.Numerical simulation. *Rheologica Acta* **1997**, *36*, 285–302.

(92) Costanzo, S.; Huang, Q.; Ianniruberto, G.; Marrucci, G.; Hassager, O.; Vlassopoulos, D. Shear and Extensional Rheology of Polystyrene Melts and Solutions with the Same Number of Entanglements. *Macromolecules* **2016**, *49*, 3925–3935.

(93) Marín, J. M. R.; Huusom, J. K.; Alvarez, N. J.; Huang, Q.; Rasmussen, H. K.; Bach, A.; Skov, A. L.; Hassager, O. A control scheme for filament stretching rheometers with application to polymer melts. *Journal of Non-Newtonian Fluid Mechanics* **2013**, *194*, 14–22.

(94) Snijkers, F.; Vlassopoulos, D. Cone-partitioned-plate geometry for the ARES rheometer with temperature control. *Journal of Rheology* **2011**, *55*, 1167–1186.

(95) Read, D. J.; Auhl, D.; Das, C.; den Doelder, J.; Kapnistos, M.; Vittorias, I.; McLeish, T. C. B. Linking Models of Polymerization and Dynamics to Predict Branched Polymer Structure and Flow. **2011**, *333*, 1871–1874.

(96) Das, C.; Inkson, N. J.; Read, D. J.; Kelmanson, M. A.; McLeish, T. C. B. Computational linear rheology of general branch-on-branch polymers. *Journal of Rheology* **2006**, *50*.

(97) Das, C.; Read, D. J.; Auhl, D.; Kapnistos, M.; den Doelder, J.; Vittorias, I.; McLeish, T. C. B. Numerical prediction of nonlinear rheology of branched polymer melts. *Journal of Rheology* **2014**, *58*, 737–757.

(98) Van Ruymbeke, E.; Bailly, C.; Keunings, R.; Vlassopoulos, D. A General Methodology to Predict the Linear Rheology of Branched Polymers. *Macromolecules* **2006**, *39*, 6248–6259.

(99) Blackwell, R. J.; Harlen, O. G.; McLeish, T. C. B. Theoretical Linear and Nonlinear Rheology of Symmetric Treelike Polymer Melts. *Macromolecules* **2001**, *34*, 2579–2596.

(100) Marrucci, G. Relaxation by reptation and tube enlargement: A model for polydisperse polymers. *Journal of Polymer Science: Polymer Physics Edition* **1985**, *23*, 159–177.

(101) Daniels, D. R.; McLeish, T. C. B.; Crosby, B. J.; Young, R. N.; Fernyhough, C. M. Molecular rheology of comb polymer melts. 1. Linear viscoelastic response. *Macromolecules* **2001**, *34*, 7025–7033.

(102) Kapnistos, M.; Vlassopoulos, D.; Roovers, J.; Leal, L. G. Linear rheology of architecturally complex macromolecules: comb polymers with linear backbones. *Macromolecules* **2005**, *38*, 7852–7862.

(103) Ianniruberto, G. Extensional Flows of Solutions of Entangled Polymers Confirm Reduction of Friction Coefficient. *Macromolecules* **2015**, *48*, 6306–6312.

(104) Kirkwood, K. M.; Leal, L. G.; Vlassopoulos, D.; Driva, P.; Hadjichristidis, N. Stress relaxation of comb polymers with short branches. *Macromolecules* **2009**, *42*, 9592–9608.

(105) Bacova, P.; Hawke, L. G. D.; Read, D. J.; Moreno, A. J. Dynamics of branched polymers: a combined study by molecular dynamics, simulations and tube theory. *Macromolecules* **2013**, *46*, 4633–4650.

(106) Zhou, Q.; Larson, R. G. Direct molecular dynamics simulations of branch point motion in asymmetric star polymer melts. *Macromolecules* **2007**, *40*, 3443–3449.

(107) Zhang, A.; Zhang, B.; Wächtersbach, E.; Schmidt, M.; Schlüter, A. D. Efficient synthesis of high molar mass, first- to fourth- generation distributed dendronized polymers by the macromonomer approach. *Eur. J.* **2003**, *9*, 6083–6092.

(108) Pasquino, R.; Zhang, B.; Sigel, R.; Yu, H.; Ottiger, M.; Bertran, O.; Alemán, C.; Schlüter, A. D.; Vlassopoulos, D. Linear viscoelastic response of dendronized polymers. *Macromolecules* **2012**, *45*, 8813–8823.

(109) Honerkamp, J.; Weese, J. A nonlinear regularization method for the calculation of relaxation spectra. *Rheol. Acta* **1993**, *32*, 65–73.

(110) Kröger, M.; Schlüter, A. D.; Halperin, A. Branching defects in dendritic molecules: coupling efficiency and congestion effects. *Macromolecules* **2013**, *46*, 7550–7564.

(111) Kröger, M. Efficient algorithm for the dynamic creation of wormlike chains in solutions, brushes, melts and glasses. *Comput. Phys. Commun.* **1999**, *118*, 278–298.

(112) Kröger, M. Simple models for complex nonequilibrium fluids. *Phys. Rep.* **2004**, *390*, 453–551.

(113) Keentok, M.; Georgescu, A. G.; Sherwood, A. A.; Tanner, R. I. The measurement of the second normal stress difference for some polymer solutions. *Journal of Non-Newtonian Fluid Mechanics* **1980**, *6*, 303–324.

(114) Brown, E. F.; Burghardt, W. R.; H., K.; Venerus, D. C. Comparison of opticla and mechanical measurements of second normal stress difference relaxation following step strain. *Rheol. Acta* **1995**, *34*, 221–234.

(115) Adams, N.; Lodge, A. S. Rheological properties of concentrated polymer solutions II. A cone-and-plate and parallel-plate pressure distribution apparatus for determining normal stress differences in steady shear flow. *Phil. Trans. of the Royal Society of London* **1964**, *256*, 149–184.

(116) Schweizer, T. Measurement of the first and second normal stress differences in a polystyrene melt with a cone-partitioned plate tool. *Rheol. Acta* **2002**, *41*, 337–344.

(117) Baek, S.-G.; Magda, J. J. Monolithic rheometer plate fabricated using silicon micromachining technology and containing miniature pressure sensors for N1 and N2 measurements. *Journal of Rheology* **2003**, *47*, 1249–1260.

(118) Pollett, W. F. O.; Cross, A. H. A continuous-shear rheometer for measuring total stress in rubber-like materials. *Journal of Scientific Instruments* **1950**, *27*, 209–212.

(119) Schweizer, T.; van Meerveld, J.; Ottinger, H. C. Nonlinear shear rheology of polystyrene melt with narrow molecular weight distribution - Experiment and theory. *Journal of Rheology* **2004**, *48*, 1345–1363.

(120) Schweizer, T.; Bardow, A. The role of instrument compliance in normal force measurements of polymer melts. *Rheol. Acta* **2006**, *45*, 393–402.

(121) Schweizer, T.; Hostettler, J.; Mettler, F. A shear rheometer for measuring shear stress and both normal stress differences in polymer melts simultaneously: the MTR 25. *Rheol. Acta* **2008**, *47*, 943–957.

(122) Ravindranath, S.; Wang, S.-Q. Steady-state measurements in stress plateau region of entangled polymer solutions: Controlled-rate and controlled-stress modes. *Journal of Rheology* **2008**, *52*, 957–980.

(123) Christiansen, E. B.; Leppard, W. R. Steady state and oscillatory flow properties of polymer solutions. *Journal of Rheology* **1974**, *18*, 65–86.

(124) Gao, H. W.; Ramachandran, S.; Christiansen, E. B. Dependency of the steady-state and transient viscosity and first and second normal stress difference functions on molecular weight for linear mono and polydisperse polystyrene solutions. *Journal of Rheology* **1982**, *25*, 213–234.

(125) Eggers, H.; Schümmer, P. A new method for determination of normal stress differences in highly visco-elastic substances using a modified Weissenberg rheometer. *Journal of Rheology* **1994**, *38(4)*, 1169–1177.

(126) Gleissle, W. In *Rheology, vol.2*, Astarita, G., Marrucci, G., Nicolais, L., Eds.; Plenum: New York, 1980, p 457.

(127) Doi, M.; Edwards, S. F. Dynamics of concentrated polymer systems. Part 4. Rheological properties. *Journal of the Chemical Society - Faraday Transactions 2* **1979**, *75*, 38–54.

(128) Des Cloizeaux, J. Double reptation vs. simple reptation in polymer melts. *Europhys. Lett.* **1988**, *5*, 437–442.

(129) Tsenoglou, C. Network architecture and modulus of miscible heteropolyme blends. *J. Polym. Sci., Part B: Polym. Phys.* **1988**, *26*, 2329–2339.

(130) Viovy, J. L.; Rubinstein, M.; Colby, R. H. Constraint release in polymer melt - tube reorganization versus tube dilation. *Macromolecules* **1991**, *24*, 3587–3596.

(131) Likhtman, A. E.; McLeish, T. C. B. Quantitative theory for linear dynamics of linear entangled polymers. *Macromolecules* **2002**, *35*, 6332–6343.

(132) Likhtman, A. E.; Graham, R. S. Simple constitutive equation for linear polymer melts derived from molecular theory: the Rolie-Poly equation. *J. Non-Newtonian Fluid Mech.* **2003**, *114*, 1–12.

(133) Yaoita, T.; Isaki, T.; Masubuchi, Y.; Watanabe, H.; Ianniruberto, G.; Marrucci, G. Primitive chain network simulation of elongational flows of entangled linear chains: role of finite chain extensibility. *Macromolecules* **2011**, *44*, 9675–9682.

(134) Ianniruberto, G. Quantitative appraisal of a new CCR model for entangled linear polymers. *Journal of Rheology* **2015**, *59*, 211–235.

(135) Ianniruberto, G.; Brasiello, A.; Marrucci, G. Friction coefficient does not stay constant in nonlinear viscoelasticity. *Proc. 7th Annu. Eur. Rheol. Conf.* **2011**, *1*, 61.

(136) Yaoita, T.; Isaki, T.; Masubuchi, Y.; Watanabe, H.; Ianniruberto, G.; Marrucci, G. Primitive Chain Network Simulation of Elongational Flows of Entangled Linear Chains: Stretch/Orientation-induced Reduction of Monomeric Friction. *Macromolecules* **2012**, *45*, 2773–2782.

(137) Ianniruberto, G.; Brasiello, A.; Marrucci, G. Simulations of Fast Shear Flows of PS Oligomers Confirm Monomeric Friction Reduction in Fast Elongational Flows of Monodisperse PS Melts As Indicated by Rheooptical Data. *Macromolecules* **2012**, *45*, 8058–8066.

(138) Desai, P. S.; Larson, R. G. Constitutive model that shows extension thickening for entangled solutions and extension thinning for melts. *Journal of Rheology* **2014**, *58*, 255–279.

(139) Yaoita, T.; Masubuchi, Y.; Watanabe, H. Concept of stretch/orientation-induced friction reduction tested with a simple molecular constitutive equation. *Nihon Reoroji Gakkaishi* **2014**, *42*, 207–213.

(140) Wingstrand, S. L.; Alvarez, N. J.; Huang, Q.; Hassager, O. Linear and Nonlinear Universality in the Rheology of Polymer Melts and Solutions. *Phys. Rev. Lett.* **2015**, *115*, 078302.

(141) Dambal, A.; Kushwaha, A.; Shaqfeh, E. S. G. Slip-link simulations of entangled, finitely extensible, wormlike chains in shear flow. *Macromolecules* **2009**, *42*, 7168–7183.

(142) Smith, D. E.; Babcock, H. P.; Chu, S. Single-polymer dynamics in steady shear flow. *Science* **1999**, *283*, 1724–1727.

(143) Baumgaertel, M.; Schausberger, A.; Winter, H. H. The relaxation of polymers with linear flexible chains of uniform length. *Rheologica Acta* **1990**, *29*, 400–408.

(144) Auhl, D.; Ramirez, J.; Likhtman, A. E.; Chambon, P.; Fernyhough, C. Linear and nonlinear shear flow behavior of monodisperse polyisoprene melts with a large range of molecular weights. *Journal of Rheology* **2008**, *52*, 801–835.

(145) Snijkers, F.; Ratkanthwar, K.; Vlassopoulos, D.; Hadjichistidis, N. Viscoelasticity, nonlinear shear start-up, and relaxation of entangled star polymers. *Macromolecules* **2013**, *46*, 5702–5713.

(146) Ferry, J. D., *Viscoelastic Properties of Polymers*; Wiley, Ed., New York, 1980.

(147) Pasquino, R. et al. Viscosity of Ring Polymer Melts. *ACS Macro Letters* **2013**, *2*, 874–878.

(148) Roovers, J. The melt properties of ring polystyrenes. *Macromolecules* **1985**, *18*, 1359–1361.

(149) Roovers, J. Viscoelastic properties of polybutadiene rings. *Macromolecules* **1988**, *21*, 1517–1521.

(150) Mckenna, G.; Plazek, D. The viscosity of blends of linear and cyclic molecules of similar molecular mass. *Polym. Commun.* **1986**, *27*, 304–306.

(151) Halverson, J. D.; Grest, G. S.; Grosberg, A. Y.; Kremer, K. Rheology of ring polymer melts: from linear contaminants to ring-linear blends. *Phys. Rev. Lett.* **2012**, *108*, 038301.

(152) Li, Y.; Hsiao, K.-W.; Brockman, C. A.; Yates, D. Y.; Robertson-Anderson, R. M.; Kornfield, J. A.; San Francisco, M. J.; Schroeder, C. M.; McKenna, G. B. When Ends Meet: Circular DNA Stretches Differently in Elongational Flows. *Macromolecules* **2015**, *48*, 5997–6001.

(153) Carl, W. Configurational and rheological properties of cyclic polymers. *J. Chem. Soc., Faraday Trans.* **1995**, *91*, 2525–2530.

(154) Wiest, J. M.; Burdette, S. R.; Liu, T. W.; Bird, R. Effect of ring closure on rheological behavior. *Journal of Non-Newtonian Fluid Mechanics* **1987**, *24*, 279–295.

(155) Cifre, J. H.; Pamies, R.; Martínez, M. L.; de la Torre, J. G. Steady-state behavior of ring polymers in dilute flowing solutions via Brownian dynamics. *Polymer* **2005**, *46*, 267–274.

(156) Ianniruberto, G.; Marrucci, G. Convective constraint release (CCR) revisited. *Journal of Rheology* **2014**, *58*, 89–102.

(157) Chen, W. D.; Chen, J. Z.; An, L. J. Tumbling and tank-treading dynamics of individual ring polymers in shear flow. *Soft Matter* **2013**, *9*, 4312–4318.

(158) Marrucci, G.; Greco, F.; Ianniruberto, G. Possible role of force balance on entanglements. *Macromol. Symp.* **2000**, *158*, 57–64.

(159) Milner, S. T. Improved model of nonaffine strain measure. *Journal of Rheology* **2001**, *45*, 1023–1028.

(160) Larson, R. G.; Sridhar, T.; Leal, L. G.; McKinley, G. H.; Likhtman, A. E.; McLeish, T. C. B. Definitions of entanglement spacing and time constants in the tube model. *Journal of Rheology* **2003**, *47*, 809–818.

(161) Larson, R. G.; Desai, P. S. In *Annual Reviews*, Davis, S. H., Eds, M. P., Eds., Palo Alto, 2015; Vol. 47, pp 47–65.

(162) Schweizer, K. S. Private communication. **2016**.

(163) Liu, G.; Cheng, S.; Lee, H.; Ma, H.; Xu, H.; Chang, T.; Quirk, R. P.; Wang, S.-Q. Strain Hardening in Startup Shear of Long-Chain Branched Polymer Solutions. *Phys. Rev. Lett.* **2013**, *111*, 068302.

(164) Moorcroft, R. L.; M., F. S. Shear banding in time-dependent flows of polymers and wormlike micelles. *Journal of Rheology* **2014**, *58*, 103–147.

(165) Snijkers, F.; Pasquino, R.; Olmsted, D. P.; Vlassopoulos, D. Perspectives on the viscoelasticity and flow behavior of entangled linear and branched polymers. *J. Phys. Condens. Matter* **2015**, *27*, 1–25.

(166) Li, S. W.; Park, H. E.; Dealy, J. M.; Maric, M.; Lee, H.; Im, K.; Choi, H.; Chang, T.; Rahman, M. S.; Mays, J. Detecting Structural Polydispersity in Branched Polybutadienes. *Macromolecules* **2011**, *44*, 208–214.

(167) Torres, E.; Li, S.-W.; Costeux, S.; Dealy, J. M. Branching structure and strain hardening of branched metallocene polyethylenes. *Journal of Rheology* **2015**, *59*, 1151–1172.

(168) McLeish, T. C. B.; Clarke, N.; de Luca, E.; Hutchings, L. R.; Graham, R. S.; Gough, T.; Grillo, I.; Fernyhough, C. M.; Chambon, P. Neutron flow-mapping: Multiscale modelling opens a new experimental window. *Soft Matter* **2009**, *5*, 4426–4432.

(169) Nielsen, J. K.; Rasmussen, H. K.; Denberg, M.; Almdal, K.; Hassager, O. Nonlinear Branch-Point Dynamics of Multiarm Polystyrene. *Macromolecules* **2006**, *39*, 8844–8853.

(170) Tezel, A. K.; Oberhauser, J. P.; Graham, R. S.; Jagannathan, K.; McLeish, T. C. B.; Leal, L. G. The nonlinear response of entangled star polymers to startup of shear flow. *Journal of Rheology* **2009**, *53*, 1193–1214.

(171) Ruocco, N.; Dahbi, L.; Driva, P.; Hadjichristidis, N.; Allgaier, J.; Radulescu, A.; Sharp, M.; Lindner, P.; Straube, E.; Pyckhout-Hintzen, W.; Richter, D. Microscopic Relaxation Processes in Branched-Linear Polymer Blends by Rheo-SANS. *Macromolecules* **2013**, *46*, 9122–9133.

(172) Lentzakis, H.; Vlassopoulos, D.; Read, D. J.; Lee, H.; Chang, T.; Driva, P.; Hadjichristidis, N. Uniaxial extensional rheology of well-characterized comb polymers. *Journal of Rheology* **2013**, *57*, 605–625.

(173) Lentzakis, H.; Das, C.; Vlassopoulos, D.; Read, D. J. Pom-pom-like constitutive equations for comb polymers. *Journal of Rheology* **2014**, *58*, 1855–1875.

(174) Marrucci, G.; Ianniruberto, G. Interchain Pressure Effect in Extensional Flows of Entangled Polymer Melts. *Macromolecules* **2004**, *37*, 3934–3942.

(175) Wagner, M. H.; Rolón Garrido, V. H. Verification of the branch point withdrawal in elongational flow of a pom-pom polystyrene melt. *AIP Conference Proceedings* **2008**, *1027*.

(176) Van Ruymbeke, E.; Nielsen, J.; Hassager, O. Linear and nonlinear viscoelastic properties of bidisperse linear polymers: Mixing law and tube pressure effect. *Journal of Rheology* **2010**, *54*, 1155–1172.

(177) Nielsen, J. K.; Rasmussen, H. K.; Hassager, O. Stress relaxation of narrow molar mass distribution polystyrene following uniaxial extension. *Journal of Rheology* **2008**, *52*, 885–899.

(178) Hengeller, L.; Huang, Q.; Dorokhin, A.; Alvarez, N. J.; Almdal, K.; Hassager, O. Stress relaxation of bi-disperse polystyrene melts. *Rheologica Acta* **2016**, *55*, 303–314.

(179) Van Ruymbeke, E.; Orfanou, K.; Kapnistos, M.; Iatrou, H.; Pitsikalis, M.; Hadjichristidis, N.; Lohse, D. J.; Vlassopoulos, D. Entangled Dendritic Polymers and Beyond: rheology of Symmetric Cayley-Tree Polymers and Macromolecular Self-Assemblies. *Macromolecules* **2007**, *40*, 5941–5952.

(180) Huang, Q.; Costanzo, S.; Das, C.; Vlassopoulos, D. Stress growth and relaxation of dendritically branched macromolecules in shear and uniaxial extension. *Journal of Rheology* **2017**, *61*, 35–47.

(181) Park, S. J.; Desai, P. S.; Chen, X.; Larson, R. G. Universal relaxation behavior of entangled 1,4-polybutadiene melts in the transition frequency region. *Macromolecules* **2015**, *48*, 4122–4131.

(182) Bick, D. K.; McLeish, T. C. B. Topological Contributions to Nonlinear Elasticity in Branched Polymers. *Phys. Rev. Lett.* **1996**, *76*, 2587–2590.

(183) Verbeeten, W. M. H.; Peters, G. W. M.; Baaijens, F. P. T. Differential constitutive equations for polymer melts: the extended pom-pom model. *Journal of Rheology* **2001**, *45*, 823–843.

(184) Hawke, L. G. D.; Huang, Q.; Hassager, O.; Read, D. J. Modifying the pom-pom model for extensional viscosity overshoots. *Journal of Rheology* **2015**, *59*, 995–1017.

(185) Huang, Q.; Agostini, S.; Hengeller, L.; Shivokhin, M.; Alvarez, N. J.; Hutchings, L. R.; Hassager, O. Dynamic of strar polymers in fast extensional flow and stress relaxation. *Macromolecules* **2016**, *49*, 6694–6699.

(186) Snijkers, F.; Vlassopoulos, D. Appraisal of the Cox-Merz rule for well-characterized entangled linear and branched polymers. *Rheologica Acta* **2014**, *53*, 935–946.

(187) Ianniruberto, G.; Marrucci, G. Entangled melt of branched PS behave like linear PS in the steady state of fast elongational flows. *Macromolecules* **2013**, *46*, 267–275.

(188) Blackwell, R. J.; McLeish, T. C. B.; Harlen, O. G. Molecular drag-strain coupling in branched polymer melts. *Journal of Rheology* **2000**, *44*, 121–136.

(189) Alvarez, N. J.; Marín, J. M. R.; Huang, Q.; Michelsen, M. L.; Hassager, O. Creep Measurements Confirm Steady Flow after Stress Maximum in Extension of Branched Polymer Melts. *Phys. Rev. Lett.* **2013**, *110*, 168301.

(190) Hassager, O.; Mortensen, K.; Bach, A.; Almdal, K.; Rasmussen, H. K.; Pyckhout-Hintzen, W. Stress and neutron scattering measurements on linear polymer melts undergoing steady elongational flow. *Rheologica Acta* **2012**, *51*, 385–394.

(191) Schlüter, A. D.; Rabe, J. P. Dendronized Polymers: Synthesis, Characterization, Assembly at interfaces, and manipulation. *Angew. Chem., Int. Ed.* **2000**, *39*, 864–833.

(192) Shu, L.; Schlüter, A. D.; Ecker, C.; Severin, N.; Rabe, J. P. Extremely long dendronized polymers: synthesis, quantification of structure perfection, individualization, ans SFM manipulation. *Angew Chem., Int. Ed.* **2001**, *40*, 4666–4669.

(193) Kumari, M.; Gupta, S.; Achazi, K.; Böttcher, C.; Khandare, J.; Sharma, S. K.; Haag, R. Dendronized multifunctional amphiphilic polymers as efficient nanocarriers for biomedical applications. *Macromol. Rapid Commun.* **2015**, *36*, 254–261.

(194) Kochendoerfer, G. G. et al. Design and Chemical Synthesis of a Homogeneous Polymer-Modified Erythropoiesis Protein. *Science* **2003**, *299*, 884–887.

(195) Fuhrmann, G.; Grotzky, A.; Lukić, R.; Matoori, S.; Luciani, P.; Yu H. Zhang, B.; Walde, P.; Schlüter, A. D.; Gauthier, M. A.; Leroux, J.-C. Sustained gastrointestinal activity of dendronized polymer-enzyme conjugates. *Nat. Chem.* **2013**, *5*, 582–589.

(196) Huang, Y. Y.; Yang, X.; Feng, Y.; Verpoort, F.; Fan, Q. H. Chiral Ru/Ir bimetallic dendronized polymer catalysts constructed through sequential metal coordination and applied in asymmetric hydrogenation of quinaldine. *J. Mol. Catal. A: Chem.* **2014**, *393*, 150–155.

(197) Dziezok, P.; Sheiko, S. S.; Fischer, K.; Schmidt, M.; Möller, M. Cylindrical molecular brushes. *Angew. Chem., Int. Ed. Engl.* **1997**, *36*, 2812–2815.

(198) Wintermantel, M.; Gerle, M.; Fischer, K.; Schmidt, M.; Wataoka, I.; Urakawa, H.; Kajiwara, K.; Tsukahara, Y. Molecular bottlebrushes. **1996**, *29*, 978–983.

(199) Pakula, T.; Zhang, Y.; Matyjaszewski, K.; Lee, H.; Boerner, H.; Qin, S.; Berry, G. C. Molecular brushes as super-soft elastomers. *Polymer* **2006**, *47*, 7198–7206.

(200) Egorov, S. A.; Milchev, A.; Virnau, P.; Binder, K. A. New insight into the isotropic-nematic phase transition in lyotropic solutions of semiflexible polymers: density-functional theory tested by molecular dynamics. *Soft Matter* **2016**, *12*, 4944–4959.

(201) Cordova-Mateo, E.; Bertran, O.; Zhang, B.; Vlassopoulos, D.; Pasquino, R.; Schlüter, A. D.; Kröger, M.; Aleman, C. Interaction in dendronized polymers: intramolecular dominates intermolecular. *Soft Matter* **2014**, *10*, 1032–1044.

(202) Costanzo, S.; Scherz, L. F.; Schweizer, T.; Kröger, M.; Floudas, G.; Schlüter, A. D.; Vlassopoulos, D. Rheology and Packing of Dendronized Polymers. *Macromolecules* **2016**, *49*, 7054–7068.

(203) Zhu, Q.; Wu, J.; Tu, C.; Shi, Y.; He, L.; Wang, R.; Zhu, X.; Yan, D. Role of branching architecture in the glass transition of hyperbranched polyethers. *J. Phys. Chem. B* **2009**, *113*, 5777–5780.

(204) Sunder, A.; Bauer, T.; Mülhaupt, R.; Frey, H. Synthesis and thermal behavior of esterified aliphatic hyperbranched polyehter polyols. *Macromolecules* **2000**, *33*, 133–1337.

(205) Liu, H.; Wilén, C. E. Preparation and glass transition temperature of hyperbranched poly(allyl-Methyl-Maleate-Co-N-Propyl-Maleimide). *J. Appl. Polym. Sci.* **2005**, *97*, 1941–1947.

(206) Stutz, H. The glass temperature of dendritic polymers. *J. Polym. Sci., Part B: Polym. Phys.* **1995**, *33*, 333–340.

(207) Luo, X.; Xie, S. J.; Liu, J.; Hu, H. B.; Jiang, J.; Huang, W.; Gao, H. Y.; Zhou, D. S.; Lu, Z. Y.; Yan, D. Y. The relationship between the degree of branching and glass transition temperature of branched polyethylene: experiment and simulation. *Polym. Chem.* **2014**, *5*, 1305–1312.

(208) Liu, H.; Wilén, C. E. Extension of the chain-end, free volume theory for predicting glass temperature as a function of conversion in hyperbranched polymers obtained through one-pot approaches. *J. Polym. Sci., Part B: Polym. Phys.* **2004**, *42*, 1235–1242.

(209) Wooley, K. L.; Hawker, C. J.; Pochan, J. M.; Fréchet, J. M. J. Physical properties of dendritic macromolecules: a study of glass transition temperature. *Macromolecules* **1993**, *26*, 1514–1519.

(210) Kim, Y. H.; Webster, O. W. Hyperbranched polyphenylenes. *Prepr. (Am. Chem. Soc., Div. Polym. Chem.)* **1988**, *29*, 310–311.

(211) Zhang, A.; Okrasa, L.; Pakula, T.; Schlüter, A. D. Homologous series of dendronized polymethacrylates with a methyleneoxycarbonyl spacer between the backbone and dendritic side chain: synthesis, characterization, and some bulk properties. *J. Am. Chem. Soc.* **2004**, *126*, 6658–6666.

(212) Fox, T. G.; Flory, P. J. Second-order transition temperature and related properties of polystyrene. I. Influence of molecular weight. **1950**, *21*, 581–591.

(213) Hawker, C. J.; Farrington, P. J.; Mackay, M. E.; Wooley, K. L.; Fréchet, J. M. M. Molecular ball bearings: the unusual melt viscosity behavior of dendritic macromolecules. *J. Am. Chem. Soc.* **1995**, *117*, 4409–4410.

(214) Farrington, P.; Hawker, C. The melt viscosity of dendritic poly(benzyl-ether) macromolecules. *Macromolecules* **1998**, *31*, 5043–5050.

(215) Scherz, L.; Costanzo, S.; Vlassopoulos, D.; Schlüter, A. D. unpublished data.

(216) Rubinstein, M.; Colby, R. H.; Dobrynin, A. V. Dynamics of semidilute polyelectrolyte solutions. *Phys. Rev. Lett.* **1994**, *73*, 2776–2779.

(217) Odijk, T. Polyelectrolytes near the rod limit. *J. Polym. Sci., Polym. Phys. Ed.* **1977**, *15*, 477–483.

(218) Mikhailov, I. V.; Darinski, A. A.; Zhulina, E. B.; Borisov, O. V.; Leermakers, F. A. M. Persistence length of dendronized polymers: the self-consistent field theory. *Soft Matter* **2015**, *11*, 9367–9378.

(219) Guinier, A., *X-Ray diffraction in crystals, imperfect crystals and amorphous bodies*; Freeman: San Francisco, 1963.

(220) Grigoriadis, C.; Nese, A.; Matyjaszewski, K.; Pakula, T.; Butt, H. J.; Floudas, G. Dynamic Homogeneity by architectural design - bottlebrush polymers. *Macromol. Chem. Phys.* **2012**, *213*, 1311–1320.

(221) Riala, P.; Andreopoulou, A.; Kallistis, J.; Gitsas, A.; Floudas, G. Role of main chain rigidity and side-chain substitution on the supramolecular organization of rigid-flexible polymers. *Polymer* **2006**, *47*, 7241–7250.

(222) Dorgan, J. R.; Knauss, D. M.; Al-Muallen, H. A.; Huang, T.; D., V. Melt rheology of dendritically branched polystyrenes. *Macromolecules* **2003**, *36*, 380–388.

(223) Leibler, L.; Rubinstein, M.; Colby, R. H. Dynamics of reversible networks. *Macromolecules* **1991**, *24*, 4701–4707.

(224) Dalsin, S. J.; Hillmyer, M. A.; Bates, F. S. Linear rheology of polyolefin-based bottlebrush polymers. *Macromolecules* **2015**, *48*, 4680–4691.

(225) Bertran, O.; Zhang, B.; Schlüter, A. D.; Halperin, A.; Kröger, M.; Aléman, C. Computer simulation of dendronized polymers: organization and characterization at the atomistic level. *RSC Adv.* **2013**, *3*, 126–140.

(226) Beijer, F. H.; Sijbesma, R. P.; Kooijman, H.; Spek, A. L.; Meijer, E. W. Strong dimerization of ureidopyrimidinones via quadruple hydrogen bonding. *J. Am. Chem. Soc.* **1998**, *120*, 6761–6769.

(227) Yamauchi, K.; Lizotte, J. R.; Long, T. E. Thermoreversible poly(alkyl acrylates) consisting of self-complementary multiple hydrogen bonding. *Macromolecules* **2003**, *36*, 1083–1088.

(228) Lewis, C. L.; Stewart, K.; Anthamatten, M. The influence of hydrogen bonding side groups on viscoelastic behavior of linear and network polymers. *Macromolecules* **2014**, *47*, 729–740.

(229) Berret, J.-F.; Séréro, Y.; Winkelman, B.; Calvet, D.; Collet, A.; Viguier, M. Nonlinear rheology of telechelic polymer networks. *Journal of Rheology* **2001**, *45*, 477–492.

(230) Berret, J.-F.; Séréro, Y. Evidence of shear-induced fluid fracture in telechelic polymer networks. *Phys. Rev. Lett. 87*, 0483031–0483034.

(231) Séréro, Y.; Jacobsen, V.; Berret, J.-F.; May, R. Evidence of nonlinear chain stretching in the rheology of transient networks. *Macromolecules* **2000**, *33*, 1841–1847.

(232) Koga, T.; Tanaka, F.; Kaneda, I.; Winnik, F. M. Stress buildup under start-up shear flows in self-assembled transient networks of telechelic associating polymers. *Langmuir* **2009**, *25*, 8626–8638.

Acknowledgments

Sitting in my office during a warm winter afternoon, I was staring at the poster of the New York Philharmonic Orchestra on the wall, seeking for inspiration to complete my thesis, when a thought came to my mind: doing science is like attending a symphony; sometimes you are director of the orchestra, leading your collaborators, sometimes you are musician, playing your part in a team, or you may be just part of the audience, assessing the work of somebody else. Irrespective of your role, two elements are important in order to always enjoy the moment: first, you must like music; second, you cannot play alone.

When I look back at the work of the past three years, I really feel the importance of the help and encouragement of all people I met during my phD and I am grateful to each one of them for their contribution.

Particularly, I would like to thank my advisor, Dimitris for his guidance, teachings and availability. He has been a constant reference during my phD. His model always motivated me to work at my best.

I would like to acknowledge all my colleagues of the polymer group for the support in experiments and fruitful discussions.

I would like to thank all members of the European project Supolen, for giving me the opportunity to be part of a fantastic network that promoted my professional growth in science.

I am grateful to Prof. A. Dieter Schlüter, Dr. Leon Scherz, Dr. Thomas Schweizer and Prof. Martin Kröger for their collaboration on the project of dendronized polymers.

I would like to thank Prof. Ole Hassager and Dr. Qian Huang for their support with extensional measurements.

I would like to thank Prof. Giovanni Ianniruberto and Prof. Giuseppe Marrucci for modeling the rheology of polystyrene melts and solutions.

I would like to thank Dr. Chinmay Das for modeling the rheology of Caley-tree systems.

I would like to thank all the members of the machine shop of FORTH-IESL, for having built the homemade experimental tools needed for this thesis work.

Finally, I would like to thank my wife Angela, my parents and my family for their love, support and understanding.